

**“Mean Field Theory And Computer
Simulations On Non-Equilibrium
Phenomena In Complex Chemical
Systems.”**

Thesis submitted for the degree of
Doctor of philosophy (Sc.)

in

Chemistry (Physical)

by

Amit Das

University of Calcutta

2013

To My Family

Acknowledgements

I would start thanking my supervisor Jaydeb Chakrabarti for his constant support and invaluable guidance over the years which not only enriched my understanding of the subjects, but also was the key to develop myself as a good scientist. His incredible belief in me helped me to pursue diverse problems simultaneously which was very important for my development. I would also thank Dr. Ranjit Biswas who has been a wonderful mentor and collaborator. My special thanks go to Dr. Mahua Ghosh, our collaborator in the works on biomacromolecules, for introducing me to the world of biology. Her contributions as a mentor have been enormous in my development at later stages of my PhD. Thanks also to my thesis and PhD committee members Dr. Sanjoy Bandopadhyay, Indian Institute of Technology Kharagpur, and Professor Debshankar Ray, Indian Association for Cultivation of Sciences, Kolkata, respectively, for helpful comments and suggestions.

I have been really lucky to come across several brilliant minds during my days at St. Xavier's College (SXC), Kolkata, Rajabazar Science College (RSC), Kolkata, and S. N. Bose National Centre for Basic Sciences (SNBNCBS), Kolkata. I would always remember the statistical physics courses taken by Professor Jayanta K. Bhattacharjee and Professor Arup K. Raychaudhuri, the Director, SNBNCBS. I thank all of my teachers at the undergraduate and master's level, in particular, Dr. Ashish Nag (SXC) for transforming my views on physical chemistry and Dr. Swapan Chakrabarty (RSC) for a sound introduction to the world of statistical mechanics. Thanks to Professor Kamal Bhattacharya and Dr. Nikhil Guchhait (RSC) also for constant help and encouragement.

Great friends always make days fun and fruitful. I thank my fellow group-members, present and past: Samapan Sikdar, Paramita Saha, Suman Dutta and Arup Bhowmik. I would also thank my other friends who were part of my days of PhD in Chemical, Biological and Macromolecular Sciences department, SNBNCBS. Specifically, I would thank Snehasis Daschakrabarty who was my batch-mate and Hemanata Kashyap, a senior in the department with whom I shared my work-cubicle at early stages. Kinshuk Banerjee and Biswajit Das require special mention, who were my other cubicle-mates from the department later. Thanks to both of them for some great and memorable moments of both fun and serious scientific discussions. Tapas Sahoo, Neetik Mukherjee and Mithun Chaudhury have been wonderful friends over the years from my days at RSC. Finally, I would thank my close friends from

college days: Avisek Dutta, Kaustav Goswami, Shauvik De, Subhradip Paul, Debjit Roy, Sambit Gan, Saswata Chakrabarty, and Deep Sengupta.

My journey could not have sailed so far without the love and support of my family. No degree of thanks would be sufficient for my parents, Swapna and Banamali Das, to ensure that I get a great education. I also thank my younger brother Shubhajit, a budding physical chemist, for his constant support, comments and enticing discussions to disseminate my views onto various arenas, including, science, literature and of course music.

Finally, I would thank SBNCBS for providing me a wonderful research environment and facilities. I also thank Council of Scientific and Industrial Research, India for a research fellowship.

Amit Das

S. N. Bose National Centre for Basic Sciences,
Block JD, Sector III, Salt Lake,
Kolkata-700098, West Bengal, India.

Table of Contents

Chapter 1 Introduction	8
1.1 Dipolar solute rotation in different media	9
1.2 Solvation dynamics in nanoconfined fluids	12
1.3 Conformational fluctuations in biomacromolecules	15
1.4 Outline of the thesis	19
Chapter 2 Dipolar solute rotation in a supercritical polar fluid	20
2.1 Introduction	20
2.2 Wave vector dependent viscosity	22
2.2.1 Molecular hydrodynamic description for normal liquid	22
2.2.2 Molecular dynamics simulation	24
2.2.3 Extension to SC CHF_3	25
2.3 Generalization of SED model: Molecular hydrodynamic τ_R	27
2.4 Inclusion of solute-solvent interaction	28
2.5 Conclusion	30
Appendices	31
Chapter 3 Dipolar solute rotation in liquid media: effect of electrostatic solute-solvent interaction	37
3.1 Introduction	37
3.2 Common dipolar liquids	40
3.2.1 Molecular hydrodynamic friction and hydrodynamic rotation times	40
3.2.2 Friction due to long-ranged solute-solvent interaction	41
3.2.3 Rotation times including DF	46
3.2.4 Comparison with earlier theories	47
3.3 Generalization for ionic media	48
3.3.1 Wave vector dependent viscosity and molecular hydrodynamic τ_R	49
3.3.2 Electrostatic contribution to τ_R in ionic media	53
3.4 Quasi-universality of solute rotation in liquid solvents	56
3.5 Conclusion	59
Appendices	60
Chapter 4 Solvation dynamics in fluids under nano-meter scale confinement	72
4.1 Introduction	72
4.2 Dimensional crossover	77
4.2.1 Simulation details	77
4.2.2 Characterization of fluid structure under confinement	78
4.2.3 Crossover in equilibrium density fluctuations: Reflecting and repulsive walls	80
4.2.4 Crossover in dynamic density fluctuations: Reflecting and repulsive walls	81

4.2.5 Dependence of crossover on wall-fluid potential	83
4.3 Solvation dynamics under confinement	84
4.3.1 Simulation details	84
4.3.2 Mechanisms of confinement-induced slowing down	85
4.3.3 Effects of drying-wetting competition on SD.....	87
4.3.4 Implications of the results	90
4.4 Conclusion	91
Chapter 5 Conformational fluctuations in biomacromolecules	93
5.1 Introduction.....	93
5.2 The histogram based method for conformational thermodynamics	99
5.2.1 Protein-ligand binding	99
5.2.2 Metal-ion binding to protein.....	103
5.3 Conformational thermodynamics of CaM-peptide complexes	104
5.3.1 Simulation details	105
5.3.2 Methyl order parameters.....	105
5.3.3 Equilibrium correlations among dihedral angles.....	106
5.3.4 Histograms of dihedrals and convergence of thermodynamics	107
5.3.5 Conformational entropy.....	109
5.3.6 Conformational free energy.....	110
5.3.7 Thermodynamics at individual binding regions	111
5.3.8 Scaling of conformational entropy with methyl order parameters	113
5.3.9 Prediction.....	114
5.3.10 The HBM: merits, demerits and extensions	115
5.4 Conformational thermodynamics for Ca ²⁺ -ion binding to CaM.....	116
5.4.1 Dihedral correlations and histograms	117
5.4.2 Overall thermodynamics data.....	118
5.4.3 Conformational changes of the Ca ²⁺ binding loops.....	118
5.4.4 Changes in linker.....	121
5.4.5 Generalization of results on metal-ion binding to protein	122
5.5 Allosteric regulations in Ca ²⁺ binding to CaM	122
5.5.1 Dynamic correlations between dihedral angles	122
5.5.2 Dihedral auto- and cross correlations in CaM	123
5.5.3 Dynamic dihedral correlations and allosteric regulations	127
5.6 Conclusion	129
Appendices.....	131
Chapter 6 Thermodynamics of interfacial changes in a protein-protein complex.....	136
6.1 Introduction.....	136

6.2 Methods.....	138
6.2.1 Simulation details	138
6.2.2 Thermodynamics from HBM	138
6.2.3 HBM for interfacial water molecules	139
6.2.4 Dynamics of Interfacial water molecules	139
6.3 Results.....	140
6.4 Interpretation of results	147
6.5 Conclusion	149
References.....	150
List of Publications.....	165

Chapter 1 Introduction

Exploration of non-equilibrium phenomena in complex chemical systems lies at the heart of research in physical chemistry. The phrase ‘complex chemical systems’ applies for any multicomponent atomic or molecular system^{1, 2} containing interacting particles. Such systems are ubiquitous in nature, for instance, fluid-media in living systems host several dissolved or dispersed organic and inorganic molecules. The air surrounding us, which is a vast reservoir of various molecules of different species, also falls into this category. Solutions of fluorescent dyes, electrolytes, biomacromolecules, like protein, DNA, different interfaces and micelles all form instances of complex chemical systems. Development of such complex materials with specific physical and chemical properties constitutes an important branch of science and technology³.

In scientific literature the complex chemical systems are recognized by characteristic static and dynamic properties observed over broad range of length and timescales². Such characteristic properties often lead to highly specific and unique chemical phenomena, controlled by the diverse coupling among the different length and timescales. With increasing number of emergent complex chemical systems, molecular level understanding of their properties and these phenomena is becoming exceedingly important. Experiments allow direct exploration of structure and dynamics over different space and time windows. The theoretical approaches aided by computational techniques offer scope to procure knowledge essential for fundamental understanding of complex systems. Various experimental techniques have been employed in this regard, in conjunction with theory and computation^{2, 4} to extract structural and functional information about numerous emergent complex chemical systems during the past few decades.

The connection between the equilibrium structure and the underlying dynamics is an important feature of the complex chemical systems. The dynamics of constituent molecules in a system is determined by their spatial arrangements which are very important for their functional properties. Here lies the motivation for the studies of non-equilibrium processes in these complex materials which ultimately help to characterize the relationship between structure and functions. Different processes reveal different aspects of this relationship, of which three main classes of non-equilibrium phenomena are discussed in the present thesis: (i) solute rotation in different complex media, (ii) effects of nanometer scale confinement on dynamics of solvation in fluids and (iii) conformational dynamics in biomacromolecules.

We pursue the understanding of the above classes of non-equilibrium phenomena using theoretical and computational approaches. For the analytical calculations we work within the frame-work of mean field theory⁵. As the name suggests, Mean field theory^{5, 6} is a theoretical framework which approximates the many-body interactions in a system by an effective interaction so that any molecule feels a ‘mean field’ due to the other molecules. Thus, it reduces a many-body problem into an effective one-body problem and hence is enormously advantageous for the mathematical simplicity it brings in. Mean field theory is almost invariably the first approach adopted to explore any complex system. It is quite a useful description if the spatial fluctuations in the system are not significant. Such approximation leads to quantitative results when the range of interactions is infinite. For our purpose, we use the mean field theory to treat the long-ranged forces in the system. We perform several computer simulations to support our analytical results. The simulations on biomacromolecular systems are based on atomistic force-field based methods. All the theoretical and simulation methods are described in the relevant chapters where they have been employed.

In the three subsequent sections 1.1-1.3 of this chapter, we describe the backgrounds and unresolved aspects of these processes in the relevant complex chemical systems. We also briefly state our results and discuss the implications. The final section of this chapter gives an outline of the remaining part of the thesis.

1.1 Dipolar solute rotation in different media

Rotation of dissolved solute molecules in a fluid medium is a motion of fundamental category. Such rotation depends directly on the ability of the immediate surroundings of the solute to accommodate its new orientations. Any heterogeneity in the environment of the solute is captured by these rotational motions. Thus the dynamics of solute rotation has been one very important class of non-equilibrium process that supply valuable information regarding the nature of solute-solvent coupling⁷⁻⁹ and local environment of the solute. The rotational dynamics of a molecular rotor is typically expressed in terms of the rate of angular displacement around a specific molecular axis. For a spherical molecule one finds a unique rate of rotation, inverse of which gives the timescale of rotation. However, multiple timescales also are observed if the molecule itself possesses different rotational degrees of freedom, applicable for highly anisotropic molecules¹⁰ and biomacromolecules¹¹. The timescales can be lengthened if there is any specific interaction or complex formation between the solute and the solvent molecules^{12, 13}. Thus, these rotational rates or the associated timescales have proved useful tools to understand the local compactness of a

medium at a length scale of the order of the solute size. In addition such timescales often give valuable idea about mechanisms of certain reactions, especially in biomolecules, since binding can significantly retard these rotations.

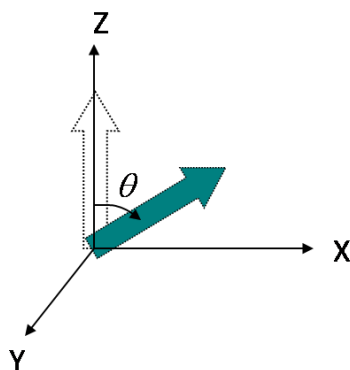


Figure 1.1: Rotation of a dipole. It is initially aligned to z-axis and then rotates about the y-axis. θ represents the angular displacement with respect to its initial orientation.

Figure 1.1 schematically shows the rotation of a dipole where the angular displacement is marked as θ , a time-dependent quantity, rate of change of which describes the rate of rotation. Measurements of the time dependent fluorescence anisotropy¹¹ $r(t)$ provides a method to track the rotation of a fluorescent solute. In such experiments the solute is excited using laser to create a dipole in a higher electronic state. This excited solute dipole then gradually relaxes to equilibrium via diffusive rotational motion. The time-dependent fluorescence emission intensity for such a dipole is anisotropic which is expressed in terms of $r(t)$. The conventional probes used in these experiments are aromatic fluorescent molecules, like coumarins, oxazines, anthracenes and many more. The observed $r(t)$ generally follows an exponential decay, given by $\exp(-t/\tau_R)$, with a characteristic time scale τ_R for the solute rotation. This is called the rotational correlation time, conventionally known as the rotation time. Sometimes multi-exponential decays are observed when one obtains via the time-integration of the normalized $r(t)$, an average τ_R , dominated by the longer time scale of the decay.

There are three major classes of well-studied solvent systems. In the first class fall the common liquid solvents having critical points much higher than ambient temperature (AT). These are the conventional solvents including the dipolar liquids, both protic (water and alcohols) and aprotic (acetone, acetonitrile, chloroform, formamide etc.), and the non-dipolar ones, like, the hydrocarbons (cyclohexane, benzene, toluene etc.)^{8, 14}. The observed τ_R in these solvents are a few tens of picoseconds (ps). Next class comprises of the supercritical

fluids¹⁵ with the fluid critical temperature near AT. Some examples are fluoroform, ethane, carbon-dioxide and nitrous oxide¹⁶⁻¹⁹. Average τ_R in these media are typically 5-10 ps. Finally, there are ionic media which are multicomponent systems themselves, namely, the ionic liquids²⁰ where the observed τ_R are about few nanoseconds (ns), electrolyte solutions^{12, 13, 21} with τ_R about few hundreds of ps and so on. The most popular fluorescent probe molecules have been the coumarin dyes, among which coumarin 153 is the one used mostly due to its non-reactive nature. It does not undergo any complexation with the solvent molecules in any of the above three varieties of solvent systems, thus providing reliable information about the local solvent structure and dynamics.

The average τ_R of a solute is conventionally understood by the Stokes-Einstein-Debye (SED) model^{8, 22}. It is a purely hydrodynamic model according to which the average τ_R for a spherical rotor, with volume V_p in a medium of viscosity η , is given under the stick boundary condition by

$$\tau_R = \frac{\eta V_p}{k_B T}, \quad (1.1)$$

where $k_B T$, the Boltzmann constant (k_B) times the absolute temperature. The conventional SED model has received enormous success in describing solute rotation in common polar solvents⁸, ionic liquids²³, electrolyte solutions¹³ and for biologically relevant moieties²⁴. In particular, η increases with increasing solvent density ρ . Thus, τ_R gets longer as ρ increases.

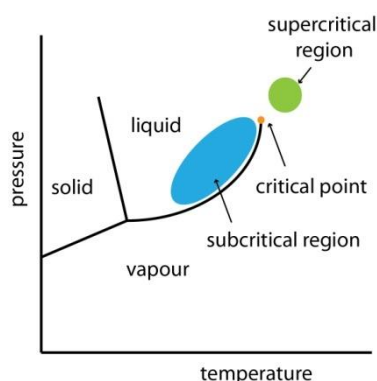


Figure 1.2: Phase diagram of a fluid. The supercritical and sub-critical regions are shown.

The experimentally observed solvent density dependence of τ_R in the supercritical fluids (Figure 1.2) is highly non-trivial. For instance, the observed τ_R for Coumarin 153, a dipolar solute, in supercritical fluoroform, a dipolar solvent, exhibit a non-monotonic

variation passing through a maximum around $\rho = 0.6\rho_c$ and a minimum at $\rho = \rho_c$, the critical density, followed by a monotonic increase for $\rho > \rho_c$. The SED model fails to explain this complex density dependence of τ_R . Our recent work²⁵, incorporating the solvent structural effects and solute-solvent interactions in the friction experienced by the rotating solute, satisfactorily describes the anomalous density-dependence of solute rotation within the SED-framework. The formulation and results are presented in chapter 2.

We extend^{26, 27} the above generalization of the SED model to answer the long-standing controversy on the decoupling of electrical part of rotational friction, termed as the dielectric friction²⁸, from dipolar solute rotation in various liquid systems. The controversy stems from the experimental finding for the common dipolar liquids⁸, the ionic liquids²³ and electrolyte solutions¹³ that hydrodynamic timescale matches the measured average rotation times in these complex media. This is surprising, for these experimental observations, suggest negligible dielectric friction even in presence of strong electrostatic solute-solvent interactions. This cannot be explained by the existing theories²⁹ which predict appreciably large dielectric friction. Our theory predicts a minimal contribution from the dielectric friction, and thus provides a microscopic explanation of how the dielectric friction gets decoupled from dipolar solute rotation in above liquid systems^{26, 27}. More importantly, our analyses suggest²⁷ the existence of a quasi-universality in solute rotation for a wide variety of solute-solvent combinations. We derive a macro-micro relation connecting a set of experimentally measurable quantities to the molecular arrangement of the solvent around a dissolved solute, and demonstrate that both the quasi-universality and the domination of hydrodynamics originate from one single source, that is, packing at liquid-like density. These calculations and results are given in chapter 3.

1.2 Solvation dynamics in nanoconfined fluids

Fluids under confinement represent a very important class of system relevant in various branches of science and technology, from biology³⁰ to tribology³¹. With increasing importance of physical and chemical processes in confined geometry³²⁻⁴³, fundamental understanding of confinement-induced effects on fluid properties has drawn considerable attention^{44, 45}. If the confinement is comparable to molecular size, measuring a few nanometers, the confined fluid undergoes drastic changes in static and dynamic properties^{46, 47}, while the dimensionality of the system crosses from three to two. In strong solvophilic confinements particle-movements become sluggish^{33, 47, 48} compared to the bulk, while strong solvophobic confinements tend to make particles to move faster than in the bulk^{46, 49}. The

understanding of this crossover in fluid properties is one of the most challenging problems. All the phenomena in nanoconfined fluids affect a broad range of physical and chemical processes in confined media³²⁻⁴³, ranging from extraction to catalysis in nanopores. Thus, study of the confinement-induced changes in fluid properties is both pedagogically and technologically important.

In a complex chemical system a fundamental step for most of the physical or chemical process is the solvation of the participating solute^{45, 50} by the solvent molecules. Any stabilizing interaction between a solute and surrounding solvent molecules is conventionally termed as solvation. The organization of the solvent molecules around the solute is a non-equilibrium process governed by the instantaneous solvent distribution and diffusion of the solvent molecules. Confinement affects both the fluid distribution as well as the diffusion significantly. Thus, solvation dynamics experience such confinement effects when the solute gets solvated in a confined fluid. Knowledge on modifications in solvation dynamics under confinement would supply valuable information on the possible changes in rates of various solvation-dependent processes, e.g. catalysis in nanoscale pores, charge- or proton-transfer reactions and associations of biomolecules.

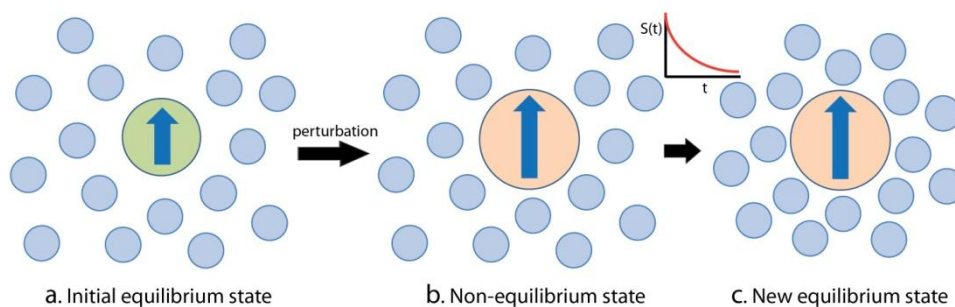


Figure 1.3: Schematic representation of solvation dynamics. The solute (larger circle) is perturbed from its (a) initial equilibrium solvated state via suddenly increasing its size or changing the dipole moment (vertical arrows inside circles) to create a (b) non-equilibrium situation. From this state the solvent molecules (smaller circles) move to reorganize themselves to reach a (c) new equilibrium state. Inset shows a schematic solvent response function $S(t)$.

Solvation dynamics is typically studied (Figure 1.3) via perturbing an equilibrated state of the solute and then measuring the time required for the solvent to reach a new equilibrium state from the initial equilibrium distribution. This time required, termed as the solvation time τ , is obtained in terms of the decay time-scale(s) of the time (t) dependent solvent response function⁴⁵ $S(t)$ which typically behaves like $\exp(-t/\tau)$ in the long-time limit. Dynamics of solvation of many fluorescent dyes have been widely studied in confined

fluids. The general picture emerging out of the observations from both experiments⁴⁵ and computer simulations⁵¹⁻⁵³ is as follows: In a bulk fluid the solvation is typically complete within tens of ps with one or two decay timescales in $S(t)$. In nanoconfined solvents, the solvation may extend from hundreds of ps to even ns. Recent computer simulations⁵¹⁻⁵³ also show such slowing of the solvation dynamics in various confined systems compared to the bulk. The most striking feature of this slowing down of solvation is that it happens in both solvophilic as well as solvophobic confinements. There has been no molecular-level understanding of this slowing down of solvation dynamics due to geometrical constraints imposed by the confinement.

The effects of confinement become more severe when the thermodynamic condition of the bulk-fluid phase surrounding the confined media is in the sub-critical region (Figure 1.2) near liquid-gas coexistence. The nature of surface becomes vital here which leads to changes in fluid phase behaviour^{54, 55}. Although, there exist many applications⁵⁶⁻⁵⁸ of the sub-critical liquids along with several studies on the surface induced phenomena^{55, 59-63}, not many studies have been performed to elucidate the roles of sub-critical solvents in solvation process. However, a simulation study⁶⁴ has shown that the density of the sub-critical solvent controls the solvation behaviour.

Our studies highlight several aspects of confinement-induced changes in solvent properties in absence and presence of solute to address above two classes of phenomena:

1. *Dimensional crossover in fluids:*

In a recent work we have studied⁶⁵ using extensive computer simulations the effects of nanoscale confinement on a fluid in a slit geometry far away from any coexistence point. We explain the dimensional crossover, observed in experiments^{46, 47}, in terms of modification in the long-wavelength behaviour of density response of the fluid due to geometrical constraints. We also show that the confining potential significantly affects the crossover behaviour. In a solvophobic slit the fluctuations increase as the confinement is made stronger. On the other hand, in a solvophilic confinement the fluctuation decreases significantly due to large attraction of the attractive walls under strong confinement.

2. *Solvation dynamics under nanoconfinement:*

We also study the solvation dynamics in a confined geometry where the bulk fluid-phase surrounding the confinement is specified. Two different phase-points are considered:

- (a) Far away from phase-transition– We study⁶⁶ via computer simulations the dynamics of solvation of a large solute in a fluid under nanometer scale confinement to provide microscopic mechanisms of the slowing down observed earlier. We find a single-

exponential $S(t)$ both in bulk and confinement to show that two fundamentally different aspects of the crossover is responsible for the slowing down in the presence of two kinds of walls. We show a sharp slowing down of solvation dynamics in solvophilic confinements due to suppression of fluid diffusion in the presence of solvophilic walls, along with slow solvent dynamics due to geometrical constraints. The solvation becomes slower than in the bulk in strong solvophobic confinements as well, but not as sharply as in the solvophilic case. This is due to the competition between reduction of dimensionality in solvent dynamics and faster in-plane solvent diffusion.

(b) Near the liquid-gas phase-coexistence– We further carry out computer simulations to study⁶⁷ the dynamics of solvation of a solvophilic solute in a solvophobic confinement, the confined solvent being in equilibrium with bulk liquid close to liquid-gas phase coexistence, far below the critical point. Under these circumstances evaporation takes place inside the pore, commonly known as capillary drying⁶¹. If a solvophilic solute particle is now inserted in such a dried solvophobic pore the solute tends to wet the pore via capillary condensation⁶⁸ posing a competition⁶² with the wall-mediated drying effect. This competition decides the fluid diffusion in the pore to affect solvation dynamics. We find that the solvent response inside the solvophobic confinement for the solvophilic solute is bi-exponential as in the bulk sub-critical liquid. The observed solvation timescales are significantly smaller under strong confinement compared to the bulk timescale indicating faster solvation in the pores. This is due to a low density fluid phase created via the competition between the drying by solvophobic walls and the surface-mediated wetting by solvophilic solute. The solvation timescale increases linearly with slit separation to approach the bulk value.

Details of all the calculations and results on dimensional crossover and solvation dynamics are included in chapter 4.

1.3 Conformational fluctuations in biomacromolecules

The biomacromolecules are highly flexible systems, with a huge number of internal degrees of freedom, having the capability to adopt numerous conformations. The fluctuations from one conformation to another plays very important role in various biological processes including molecular recognition, signal transduction, gene expression and so on⁶⁹⁻⁷². Reversible conformational switching of different biomacromolecules are important even technologically, for their application in several biosensing devices^{73, 74}. Nuclear Magnetic Resonance (NMR) relaxation experiments⁷⁵, fluorescence correlation spectroscopy coupled with Forster resonance energy transfer⁷⁶, multiphoton microscopy⁷⁷ and paramagnetic relaxation experiments⁷⁸ have been employed to explore conformational dynamics of

biomacromolecules. Molecular simulations⁷⁹⁻⁸³ have been important in this regard yielding microscopic information about conformational changes.

The primary focus of studies on conformations of biomacromolecules has been identification of a set of suitable variables to capture the conformational fluctuations. When a biomacromolecule participates in a binding event with another molecule, both the binding partners experience conformational changes⁸⁴ which stabilize the complex⁸⁵. These changes take place simultaneously at several pockets distributed over the entire surface of the biomacromolecules. The handling of such a large number of variables is extremely difficult. Moreover, the interactions in the system are also diverse, like van der Waals forces, electrostatic and hydrophobic interactions. These factors render the full characterization of the conformational fluctuations in biomacromolecules at microscopic level quite challenging^{86, 87}.

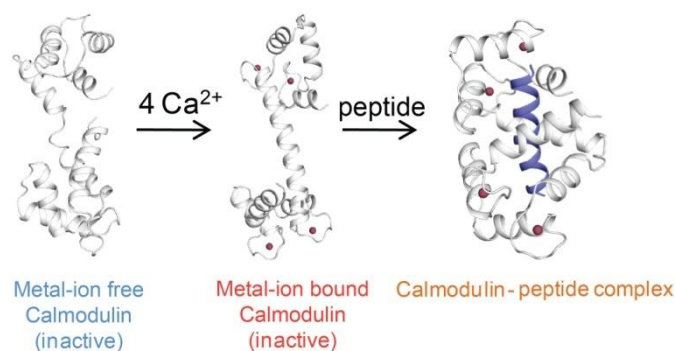


Figure 1.4: Example of conformational changes for specific function. Four Calcium (Ca^{2+})-ions (dots) bind to metal-free inactive Calmodulin, an eukaryotic cellular protein, and activates it for binding to peptides. Thus, Calmodulin participates in various cellular activities.

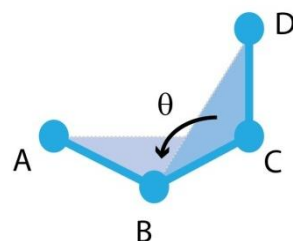


Figure 1.5: Illustration of a dihedral angle. Here the dihedral θ is defined as the angle between the planes with atoms A, B, C and the plane with atoms B, C and D. θ would change as relative positions of A and D change via rotation around the bond between B and C.

Proteins are important biomacromolecules with a huge diversity of their structures and functions. They often form complexes with metal-ions, ligands and other macromolecules⁸⁸ to adopt specific conformations for certain biological function (Figure 1.4). Importance of various backbone and side-chain dihedral angles⁸⁹ as suitable conformational variables have recently been highlighted⁹⁰ to describe protein conformations. A dihedral angle is given by the angle between two atomic planes constituted by four consecutive atoms as illustrated in Figure 1.5. By definition the dihedral angles are designed to trace the changes in rotational degrees of freedom which govern the conformational fluctuations. Moreover, the dihedrals are coarse-grained variables which give an advantage over the normal mode analyses with a significant reduction of number of working variables. We use the dihedral angles to describe following equilibrium and non-equilibrium aspects:

1. *Conformational thermodynamics:*

One significant aspect of the equilibrium conformational fluctuations is the estimation of thermodynamics of conformational changes upon complexation. This involves changes in both conformational entropy (ΔS_{conf}) and free energy (ΔG_{conf}) associated with the binding event⁹¹. The experimental methods, like, isothermal titration calorimetry (ITC)⁶⁹ providing the standard free energy and entropy changes of binding, can neither yield the conformational contributions nor resolve the changes at the level of individual variables or binding regions. NMR relaxation experiments⁹²⁻⁹⁵ provide an estimate of ΔS_{conf} . However, there has been no established experimental means of extracting ΔG_{conf} as yet, except UV resonance Raman measurements of conformational free energy landscapes⁹⁶. Histograms of the dihedral angles, obtained from all-atom molecular dynamics simulation trajectories have been used to estimate the ΔS_{conf} for proteins⁹⁷. Several computational techniques exist to estimate the ΔG_{conf} as well^{81, 82}. However, all these methods have been computationally very demanding and hence limited to small and medium sized biomacromolecules only.

We have recently developed⁸³ a theoretical approach, based on one dimensional histogram of dihedral angles, to estimate ΔG_{conf} and ΔS_{conf} for biomacromolecular complexes. These histograms are generated from all-atom molecular dynamics simulations of the binding molecules in explicit solvent in their free and bound states. Our approach is simple and computationally efficient compared to existing methods for its ability to provide both ΔG_{conf} and ΔS_{conf} simultaneously from the same histogram. ΔG_{conf} is obtained from the ratio of histogram maxima (equilibrium populations) in free and bound states, whereas ΔS_{conf} is estimated using the Gibbs formula⁹⁸. Moreover, our method allows us to estimate the thermodynamic changes in the individual binding regions.

We first illustrate our studies for protein-peptide binding where we show that the equilibrium fluctuations of dihedral angle represent the conformational thermodynamics obtained from NMR relaxation experiments⁷⁵. Next we consider⁹⁹ the case of a protein undergoing conformational changes upon binding to metal-ions^{100, 101}. We find different thermodynamic changes in different metal-binding sites where the ligands coordinating to the metal-ions play different roles in stabilizing the metal-ion bound protein-structure. Metal-ion binding induce large thermodynamic changes in distant part of the protein also via modification of secondary structural elements. The details of above method and the results are presented in chapter 5.

2. *Dynamic fluctuations of dihedral angles:*

Apart from the equilibrium aspects, we explore¹⁰² a very important non-equilibrium process allosteric regulation¹⁰³ in biomacromolecular systems. Allosteric regulation is defined as communication among distant sites in biomacromolecules which governs fundamental cellular processes, ranging from metabolism to gene expression. Such communication is an inherent capability of nearly all proteins¹⁰⁴ to regulate structural and dynamical changes at some part upon binding events at a distant part. Understanding such long-distance communication is a formidable experimental challenge, while the current theoretical explanation utilizes simplified models¹⁰⁵. We show that the distant site communications can be probed directly from the time-dependent correlations among the dihedral angles at different sites. We illustrate this for binding of multiple metal-ions to a protein where modifications in the dynamical correlation pattern upon the binding of metal-ions are interpreted in terms of allosteric regulations which explain experimental observations. We also discuss the connections between our observations and the existing understanding of allosteric regulation based on shift of populations among various conformational states¹⁰³. All these calculations and results are also included in chapter 5.

3. *Changes at biomacromolecular Interface:*

Another very important issue regarding biomacromolecular complexes is the changes at the interface. Recent experiments^{106, 107} suggest that structural modifications at the interfaces are vital for stability of the complexes and functions of the associated biomacromolecules. Although several qualitative aspects about such interfaces are known from structural data, quantification of the interfacial changes is lacking. In chapter 6 we study¹⁰⁸ in close detail the thermodynamics of conformational changes at the interface of a

protein-protein complex. ΔG_{conf} and ΔS_{conf} are calculated from the histograms of dihedral angles to show that the binding at interface is dominated by strong electrostatic interactions. We also show that the changes in the distribution of interfacial water molecules give rise to a substantial entropy contribution in binding of the proteins. The dynamics of the interfacial water molecules get arrested which demonstrates tight binding at the interface.

1.4 Outline of the thesis

The organization of the rest of this thesis is as follows: In chapter 2 we develop the molecular theory on dipolar solute rotation in a supercritical polar fluid to explain the experimentally observed non-monotonic solvent density dependence of average rotation times. We extend this theory in chapter 3 for dipolar solute rotation in various complex media, including common dipolar liquids, ionic liquids and electrolyte solutions to resolve the long-standing question regarding the role of dielectric friction in solute rotation.

In chapter 4 we provide a generic understanding for the experimentally observed confinement-induced dimensional crossover in various fluid properties. We also consider the dynamics of solvation of a large solute in a nanoconfined fluid to explore microscopic mechanisms of experimentally observed slowing down of solvation dynamics under confinement. Further we predict the solvation behaviour in a solvophobic pore placed in a sub-critical bulk fluid near liquid-gas coexistence, to capture the effects of competition between drying by the solvophobic walls and wetting by the solvophilic solute.

Chapters 5 and 6 consider conformational fluctuations in biomacromolecular systems. In chapter 5 we present our histogram-based method for estimation of entire conformational thermodynamics of biomacromolecular complexation from histogram of dihedral angles. We illustrate this method first for protein-peptide binding to show that dihedral histograms indeed provide the conformational thermodynamics obtained from NMR relaxation experiments. Further, we consider metal-ion binding to a protein where, apart from the thermodynamics, we also provide a route for direct probe of allosteric regulations via dynamic correlations among dihedral angles. Chapter 6 describes a study on biomacromolecular interface where we extend the histogram-based method for a protein-protein complex to highlight the important interactions dominating the binding at the interface. We generalize the histogram based method to compute interfacial water contributions to the thermodynamics. Estimation of the changes in dynamics of interfacial water molecules demonstrates tight binding at the biomacromolecular interface.

Chapter 2 Dipolar solute rotation in a supercritical polar fluid

2.1 Introduction

A fluid phase slightly above the gas-liquid critical temperature (see Figure 1.2) is broadly regarded as a supercritical (SC) fluid¹⁵. They are highly compressible offering large tunability of density by mild pressure variations. Pedagogically, the solvent-density dependence of several non-equilibrium rate processes near room temperature, can be studied in SC fluids like carbon dioxide, fluoroform, ethane etc. having critical temperature (T_c) close to the room temperature¹⁰⁹. Specifically, rotational dynamics of aromatic solutes in a SC fluid can supply valuable information regarding the nature of solute-solvent coupling⁷⁻⁹ and local environment of the solute.

The $r(t)$ -decay of Coumarin 153 (C153) in SC CHF_3 ($T_c=299$ K)¹⁰⁹ is single-exponential¹⁸ for all solvent densities. The observed τ_R is nearly temperature-insensitive with a non-monotonic variation between 5-9 ps as the fluid density (ρ) increases. In spite of large uncertainties, there is a clear maximum near $\rho_r (= \rho/\rho_c, \rho_c$ being the critical density of the fluid) = 0.6 with $\tau_R \sim 8$ ps and a minimum around $\rho_r = 1.0$ with $\tau_R \sim 5$ ps. Since η for a fluid, including the SC fluids, in general monotonically increases¹¹⁰ with density, the conventional SED model (Eq. 1.1) fails to explain the above complex density dependence.

The SED model has two major drawbacks: (1) Being based on purely continuum description of the molecular solvent, it does not consider the effects of solvent structure. The SC fluids have large compressibility. In a fluid composed of spherical molecules of diameter σ , the spatial arrangement of molecules can be described by the wave vector (k) dependent static structure factor^{5, 111, 112}, $S(k\sigma)$. Note that the compressibility is the long-wavelength limit of $S(k\sigma)$. Therefore, $S(k\sigma)$ may have a crucial role in the observed complex density dependence of τ_R . (2) The solute-solvent interaction has not been included in the above model. Several workers attempted^{7-9, 29, 113-115} to incorporate the effects of solute-solvent interaction on solute rotation. Especially, the concept of dielectric friction²⁸ has been invoked to address the change in the friction experienced by a rotating polar solute, due to electrostatic interactions. However, none of the above works conclusively support this picture. Relatively recent work¹¹⁴ suggests that the additional friction due to solute-solvent interaction is attributable to a static ‘electrostriction’ effect. This is believed to originate from the enhanced solvent-structure in the first solvation shell¹¹⁶ around the solute due to electrical interaction between the solute and the solvent molecules. Another interesting factor

encouraging the inclusion of solute-solvent interaction is the ‘local density augmentation’ (LDA)^{16, 117-121} observed during solvation in a SC solvent. As one approaches the critical density from low ρ_r , the solvent density around a dissolved solute becomes much larger than the bulk density of the SC solvent. This unusual enhancement of local density is termed as the LDA. For C153 in SC CHF_3 , the maximum in τ_R and LDA occurs¹⁰⁹ around the same ρ_r . This LDA is an outcome of strong solute-solvent coupling overcoming large length scale density fluctuations near critical point. Therefore, the solute-solvent interaction may have a significant role in solute rotation in a SC polar fluid. Note a modified SED model^{8, 22} includes the effects of solute-solvent interaction via two phenomenological parameters: a boundary condition factor and a solute shape-factor.

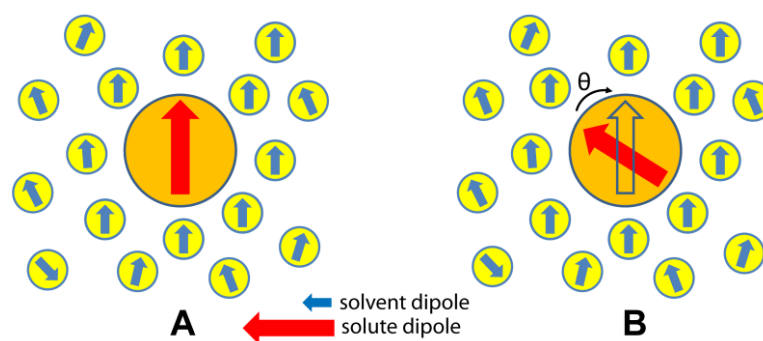


Figure 2.1: Pictorial description of solute-solvent interaction effects on solute rotation. Smaller circles with smaller arrows denote the solvent dipoles whereas larger circles with larger arrows denote the solute dipole. (A) The equilibrium condition with solute in its excited state. (B) After an angular displacement (θ) of the solute dipole in the background of solvent molecules.

In this chapter we introduce a molecular level theoretical framework²⁵ to calculate the τ_R of a dipolar solute in a dipolar fluid incorporating the contributions of both solvent structure and the solute-solvent dipolar interaction. Basically, the conventional SED theory is used with a couple of ramifications: (1) The hydrodynamic viscosity η is replaced with the wave vector dependent viscosity $\eta(k\sigma)$ of the fluid which brings in $S(k\sigma)$ directly into the picture. This is done based on molecular hydrodynamic arguments leading to an analytical expression of $\eta(k\sigma)$ which is verified via MD simulations. We also show how to extract the experimental η for a SC fluid from $\eta(k\sigma)$. This modification to SED model captures qualitatively the experimentally observed non-trivial density dependence of τ_R in SC CHF_3 . (2) The effect of the solute-solvent interaction is included by considering the rotational

relaxation of the excited solute in fluorescence depolarization experiments. In such experiments, anisotropy in polarization is created by photo-exciting a dissolved solute. This anisotropy in polarization subsequently relaxes to a new equilibrium via rotational diffusion of the solute. Let us consider a small angular displacement of the solute dipole from its final solvent-equilibrated orientation in the background of the solvent dipoles (shown schematically in Figure 2.1). The solute dipole would then tend to relax back to its equilibrium orientation by rotational diffusion under the action of torque generated via the solute-solvent interaction.

The organization of this chapter is as follows: In section 2.2 we describe the theoretical formulations of $\eta(k\sigma)$ for SC fluid. Section 2.3 shows the calculation of molecular hydrodynamic τ_R of C153 in SC CHF₃ from $\eta(k\sigma)$. The effects of solute-solvent electrostatic interactions in τ_R are included in section 2.4. We conclude in section 2.5. At the end of the chapter the appendices are given which include the details of theoretical calculations.

2.2 Wave vector dependent viscosity

In this section we introduce the molecular hydrodynamic description of $\eta(k\sigma)$ and then illustrate the calculation for a normal liquid. The theory is verified by MD simulations on a Lennard-Jones liquid. Finally, we calculate $\eta(k\sigma)$ for SC CHF₃.

2.2.1 Molecular hydrodynamic description for normal liquid

According to molecular hydrodynamics, the transverse current autocorrelation function $C_{\perp}(k\sigma, t)$ is defined for a normal liquid as $C_{\perp}(k\sigma, t) = k^2 \langle j_{\perp}^k(t) j_{\perp}^{-k}(0) \rangle$ where $j_{\perp}^k(t)$ is the Fourier component of the transverse current. $C_{\perp}(k\sigma, t)$ is known to be related to the shear viscosity η of the fluid¹¹¹:

$$C_{\perp}(k\sigma, t) = \omega_0^2 e^{-\nu k^2 t} \quad (2.1)$$

where t denotes the time, $\omega_0^2 = k^2(k_B T/m)$, $\nu = \eta/\rho m$ and m , the mass of a fluid molecule. Integrating both sides of Eq. 2.1 over the entire time range we get the wave vector dependent viscosity given by¹²²

$$\eta(k\sigma) = \frac{\rho m}{k^2} \left[\frac{1}{\omega_0^2} \int_0^{\infty} C_{\perp}(k\sigma, t) dt \right]^{-1} \quad (2.2)$$

Fick's law¹¹¹ for diffusive motion states that the current:

$$\mathbf{j}(\mathbf{r}, t) = -D\nabla\rho(\mathbf{r}, t) \quad (2.3)$$

where $\rho(\mathbf{r}, t)$ is the time dependent microscopic solvent density at position \mathbf{r} , D being the self-diffusion coefficient of the fluid. Now, Eq. 2.3 yields in the Fourier space for the transverse current, $j_{\perp}^k(t) = ik_{\perp}D\rho_k(t)$, k_{\perp} being the transverse component of \mathbf{k} (parallel to z axis). Multiplying both sides by $j_{\perp}^{-k}(0)$ and taking average over initial conditions¹¹¹, we obtain

$$\langle j_{\perp}^k(t)j_{\perp}^{-k}(0) \rangle = k_{\perp}^2 D^2 \langle \rho_k(t)\rho_{-k}(0) \rangle. \quad (2.4)$$

It is known¹¹¹ that: $\rho_k(t) = \rho_k e^{-Dk^2 t}$, ρ_k being the Fourier component of the microscopic solvent density. Inserting this in Eq. 2.4 leads to, $\langle j_{\perp}^k(t)j_{\perp}^{-k}(0) \rangle = k_{\perp}^2 D^2 S(k\sigma) e^{-Dk^2 t}$, where static structure factor¹¹¹, $S(k\sigma) = \langle \rho_k \rho_{-k} \rangle$. Thus, we reach at a molecular hydrodynamic expression of $C_{\perp}(k\sigma, t)$, following its definition¹¹¹

$$C_{\perp}(k\sigma, t) = k^2 \langle j_{\perp}^k(t)j_{\perp}^{-k}(0) \rangle = k^2 k_{\perp}^2 D^2 S(k\sigma) e^{-Dk^2 t} \quad (2.5)$$

Putting Eq. 2.5 in Eq. 2.2 and performing the integration one obtains,

$$\eta(k\sigma) = \frac{\rho k_B T}{k_{\perp}^2 D S(k\sigma)}. \quad (2.6)$$

We set $k_{\perp}^2 = 6\pi\rho r_0$ (ρ being the bulk density and r_0 , the molecular radius of the fluid) to arrive at the final expression of wave vector dependent viscosity,

$$\eta(k\sigma) = \frac{k_B T}{6\pi D r_0 S(k\sigma)} \quad (2.7)$$

We can also derive the weakly interacting limit of diffusion⁵, from the expression of $\eta(k\sigma)$: The isothermal compressibility of the fluid¹¹¹ is given by $\chi_T = (\rho k_B T)^{-1} \lim_{k \rightarrow 0} S(k\sigma)$. So, $\eta(k\sigma \sim 0) = k_B T / 6\pi r_0 D S(k\sigma \sim 0) = 1 / (6\pi r_0 D \rho \chi_T)$. Rearranging this we get $D = \Gamma_d / \rho^2 \chi_T$ where $\Gamma_d = \rho / 6\pi r_0 \eta$, a density dependent dissipative coefficient⁵.

Note that Eq. 2.7 yields

$$\eta(k\sigma) / \eta(k'\sigma) = S(k'\sigma) / S(k\sigma) \quad (2.8)$$

for wave vectors $k\sigma$ and $k'\sigma$. In the long-wavelength $k\sigma \sim 0$ limit where $S(k\sigma)$ has a minimum¹¹¹ (inset, Figure 2.2a), an expansion yields, $\eta(k\sigma) \propto (1 - bk^2\sigma^2)$ where b depends

on the curvature of $S(k\sigma)$ near $k\sigma \sim 0$. Such small $k\sigma$ behaviour of $\eta(k\sigma)$ has been reported earlier^{24, 122}.

2.2.2 Molecular dynamics simulation

Both sides of Eq. 2.8 can be computed from Molecular Dynamics simulations which can provide direct test of the wave vector dependent viscosity. We consider to this end, for simplicity, a Lennard-Jones (LJ) system at normal liquid condition. The interaction potential between a pair of LJ liquid molecules at separation r is given by $4\varepsilon[(\sigma/r)^{12} - (\sigma/r)^6]$, ε being the interaction strength parameter¹¹¹. Our simulation system involves 216 LJ particles using the argon units¹¹¹ [$\varepsilon = 120$ K in k_B unit, diameter $\sigma = 3.4$ Å and molecular mass 40 a.m.u], adopting microcanonical (fixed number of particles N , volume V and total energy E) ensemble¹¹¹. A simple cubic simulation box is used of side $L = 6.46\sigma$ with the periodic boundary condition on all sides. The density of the system is taken at $\rho\sigma^3 = 0.8$ and the average temperature at $k_B T/\varepsilon \sim 0.8$ (96 K). The equations of motion are integrated using the Verlet algorithm¹²³, the time-step for integration being 0.028 ps.

We calculate $\eta(k\sigma)$ from the simulation by Eq. 2.2, with $C_{\perp}(k\sigma, t) = k^2 \langle j_{\perp}^k(t) j_{\perp}^{-k}(0) \rangle$ and $j_{\perp}^k(t) = \sum_i v_i^{\perp}(t) e^{-ikz_i(t)}$, $v_i^{\perp}(t)$ being the transverse component of the velocity of the i th particle at time t and $z_i(t)$, its z -coordinate at time t . Finally, we can write: $C_{\perp}(k\sigma, t) = k^2 \langle \sum_i v_i^{\perp}(0) e^{-ikz_i(0)} \sum_j v_j^{\perp}(t) e^{ikz_j(t)} \rangle$. Here, the angular brackets represent an average over 1000 independent initial configurations. $S(k\sigma)$ has been calculated from the Fourier transform (FT) of the pair correlation function^{111, 123} obtained via the simulations.

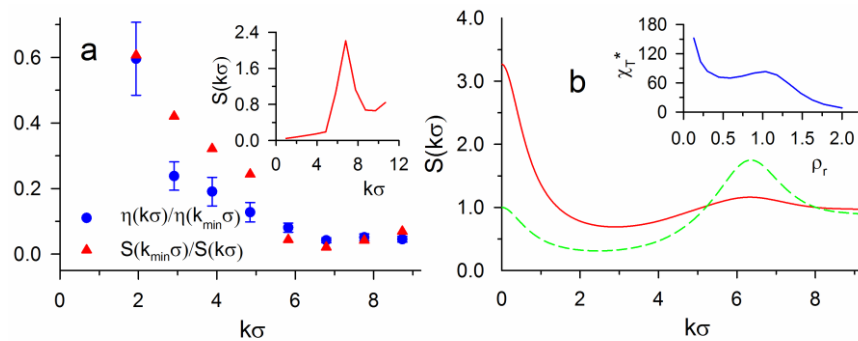


Figure 2.2: Wave vector dependent viscosity and structure factors. (a) $\eta(k\sigma)/\eta(k_{\min}\sigma)$ (filled circles with error bars) and $S(k_{\min}\sigma)/S(k\sigma)$ (open triangles, the solid line is drawn only as a guide to the eyes) as a function of $k\sigma$, both calculated from MD simulation, for LJ liquid for $\rho\sigma^3 = 0.8$ at 96K. **Inset:** $S(k\sigma)$ of the same system calculated from our simulation. **(b)** $S(k\sigma)$ as function of $k\sigma$ for SC CHF_3 at 310 K at two densities,

$\rho_r = 0.74$ (the solid line) and at $\rho_r = 2.0$ (the dotted line). Inset: Scaled compressibility χ_T^* of SC CHF₃ at 310 K as a function of ρ_r .

The finiteness of the simulated system-size restricts us to explore the $k\sigma \sim 0$ limit¹²². The minimum accessible wave vector in our simulation is $k_{\min}\sigma = 2\pi\sigma/L$, L being the side-length of the simple-cubic simulation box. The inset in Figure 2.2a shows $S(k\sigma)$ from the simulations. Figure 2.2a shows a comparison between $\eta(k\sigma)/\eta(k_{\min}\sigma)$ (circles with error bars) and $S(k_{\min}\sigma)/S(k\sigma)$ (open triangles), both computed from the simulations. Both the plots are similar in appearance with almost the same rate of decrease from the maximum value of unity at the smallest wave vector, which is consistent to the low wave vector expansion. The discrepancy between the two plots is more pronounced for low wave vector region which could be due to finite size effects in the simulations¹²³.

2.2.3 Extension to SC CHF₃

Hydrodynamic results being insensitive to the detailed molecular interactions, we expect the hydrodynamic description of $\eta(k\sigma)$ in terms of $S(k\sigma)$ to be valid for SC polar fluids also. We calculate $S(k\sigma)$ using the standard liquid state theory¹¹¹ and obtain its $k\sigma \sim 0$ limit as a theoretical estimate of χ_T . Here, $S(k\sigma)$ is computed using the Ornstein-Zernike (OZ)^{111, 112} relation: $S(k\sigma) = [1 - \rho C(k\sigma)]^{-1}$, $C(k\sigma)$ being the Fourier transform (FT) of $C(r)$, the spatial direct correlation function of the fluid. In our calculation we assume that the solvent-solvent interaction consists of hard core part of diameter σ and a long-ranged dipolar contribution due to a dipole moment of magnitude μ located at the centre of a solvent molecule. $C(r)$ is expressed as a combination of the short-ranged and long-ranged part for the polar fluid. For the former, we use the Percus-Yevick (PY)^{111, 112} form $C^{PY}(r)$ for hard sphere potential. The long-ranged part $C^{LR}(r)$ is considered within mean-field approximation where the many-body correlations are replaced by a simple form based on the pair-potentials. Here we derive $C^{LR}(r)$ from angle averaged Mayer's function^{111, 112} based on standard dipolar potential. Thus,

$$C(r) = C^{PY}(r) + C^{LR}(r) \quad (2.9)$$

$$\begin{aligned} \text{where} \quad C^{PY}(r) &= c_0 + c_1(r/\sigma) + c_3(r/\sigma)^3 && \text{for } r < \sigma \\ &= 0 && \text{for } r > \sigma \end{aligned} \quad (2.10)$$

$$\text{and} \quad C^{LR}(r) = 2\mu^4 / 9(k_B T)^2 r^6 \quad (2.11)$$

The three coefficients c_0 , c_1 and c_3 in $C^{PY}(r)$, are functions of the packing-fraction $p = (\pi/6)\rho\sigma^3$, and given by: $c_0 = -(1+2p)^2/(1-p)^4$, $c_1 = 6p(1+0.5p)^2/(1-p)^4$ and $c_3 = 0.5pc_0$. Inset of Figure 2.2b shows $\chi_T^*(= \chi_T\mu^2/\sigma^6)$ for a typical isotherm. Our estimate for the critical point from the divergence of χ_T is: $T_c^*(= k_B T_c \sigma^3/\mu^2) = 0.29$ and $\rho_c^* = 0.25$ which are in good agreement with the experimental numbers¹¹⁰. The details of all these calculations are given in Appendix A.

Subsequently, we perform calculations at a supercritical temperature¹²⁴. We show the calculated $S(k\sigma)$ of SC CHF₃ ($\sigma = 3.5 \text{ \AA}$)¹¹⁰ in Figure 2.2b at two densities above and below ρ_c . In general, two peaks can be observed in $S(k\sigma)$: one around $k\sigma \sim 0$ in a region dominated by fluid compressibility and another around $k\sigma \sim 2\pi$, dictated by the molecular packing. For low ρ_r , the peak at $k\sigma \sim 0$ predominates which gradually disappears with increasing ρ_r along with the concomitant enhancement of the packing-driven peak.

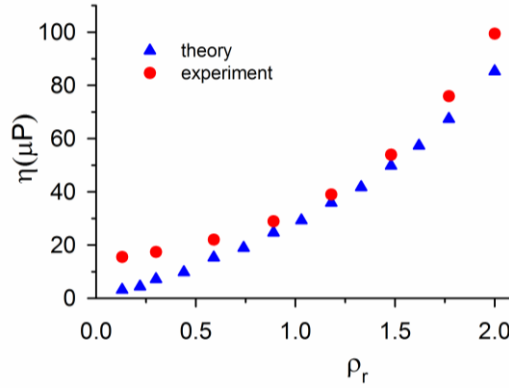


Figure 2.3: Shear viscosity of SC CHF₃. Experimental (circles) and theoretical (triangles) η at 310 K as a function of ρ_r .

We use this $S(k\sigma)$ and experimentally observed¹¹⁰ D to obtain $\eta(k\sigma)$ for SC CHF₃. It is found that the experimentally observed shear viscosity of SC CHF₃ is well reproduced (see Figure 2.3) by an integration of $\eta(k\sigma)$ over the entire range of wave vectors: $\bar{\eta} = (1/4\pi) \int \eta(k\sigma) d\mathbf{k}\sigma / \int d\mathbf{k}\sigma$ where, the factor $1/4\pi$ takes care of the degeneracy of the choice of the transverse direction. Here, for numerical purpose, the integration range was taken from $k\sigma = 0$ up to $k\sigma = 10$. We note that a larger upper limit does not alter the value of $\bar{\eta}$. The experimentally observed viscosity¹¹⁰ is thus an average momentum transfer in a given layer of fluid over all possible length scales. This rationalizes the extension of the molecular hydrodynamic expression for the $\eta(k\sigma)$ for SC CHF₃.

2.3 Generalization of SED model: Molecular hydrodynamic τ_R

Let us now consider the generalization of the SED theory via replacement of η by $\eta(k\sigma)$. Recalling the SED expression (Eq. 1.1): $\tau_R = \eta V_p / k_B T$, we can define the rate of rotational relaxation $\omega = 1/\tau_R = k_B T / \eta V_p$. Introducing $\eta(k\sigma)$ we get the wave vector dependent rate, $\omega(k\sigma) = k_B T / \eta(k\sigma) V_p$. Now, the different peaks in $S(k\sigma)$ for SC CHF₃, both sharp and broad, appearing at different regions of wave vectors, create different wave vector-windows for $\omega(k\sigma)$. We average the $\omega(k\sigma)$ over the wave vectors under a given structure factor peak to produce an average rate: $\tilde{\omega}_{av,\alpha} = \int_{\alpha} \omega(k\sigma) d\mathbf{k}\sigma / \int_{\alpha} d\mathbf{k}\sigma$ for the α th peak. The rotation time for the α th peak is then, $\tilde{\tau}_{R,\alpha} = 1/\tilde{\omega}_{av,\alpha}$. Here, each of the structure factor peaks (Figure 2.2b) will give rise to a time scale implying an over-all multi-exponential rotational relaxation. For example, at low density region ($\rho_r < 1$), $S(k\sigma)$ has a single prominent peak around $k\sigma \sim 0$ but no such peak at larger wave vectors. This implies a single-exponential relaxation, τ_R being governed by the single peak. In the higher density region ($\rho_r > 1$), the relaxation would be bi-exponential with two time scales because of two peaks in $S(k\sigma)$, τ_R being a weighted average of the two. However, the present formalism does not allow calculating the weights of these separate time scales.

Figure 2.4a shows both $\tilde{\tau}_{R,1}$ and $\tilde{\tau}_{R,2}$ of C153 ($V_p = 246 \text{ \AA}^3$ and excited state dipole moment $\mu_0 = 13.4 \text{ D}$)¹²⁵ in SC CHF₃ at 310 K as a function of ρ_r , while the experimental data at two temperatures 302 K and 310 K are shown in inset. At very low densities, $k\sigma \sim 0$ being the only peak of $S(k\sigma)$, $\tilde{\tau}_{R,1}$ is the only relevant time scale. Interestingly, it shows all the features of the experimental density dependence of rotation time with the maximum at $\rho_r = 0.59$, agreeing qualitatively with the experimental data. Appearance of this maximum can be explained by a minimum in compressibility (see inset of Figure 2.2b). Such a minimum also justifies the LDA becoming maximum near $\rho_r = 0.6$. $\tilde{\tau}_{R,1}$ becomes minimum at $\rho_r = 1.03$, with good agreement with the experimental finding. This minimum is explained by the maximum in compressibility at $\rho_r = 1.03$.

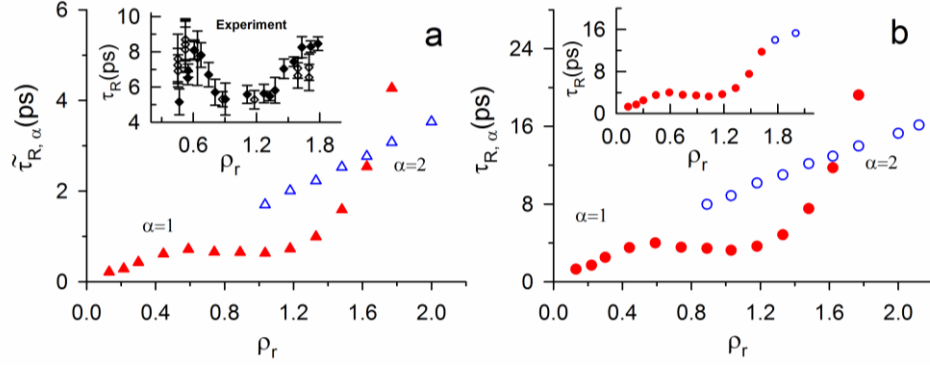


Figure 2.4: Estimated rotation time data. (a) Molecular hydrodynamic rotation times of C153 in SC CHF₃ at 310 K as a function of ρ_r : Filled and open triangles represent the $\tilde{\tau}_{R,1}$ (from $k\sigma \sim 0$ peak) and $\tilde{\tau}_{R,2}$ ($k\sigma \sim 2\pi$ peak) respectively. Inset: The experimentally observed time scales with error bars at 302K (filled) and 310 K (diamonds), respectively. (b) Rotation times after inclusion of solute-solvent polar interaction: Filled and open circles represent the $\tau_{R,1}$ and $\tau_{R,2}$ respectively. Inset: the lower time scale of $\tau_{R,1}$ and $\tau_{R,2}$, the symbols being identical as before.

The packing dominated peak appears for densities above $\rho_r = 1$, giving rise to $\tilde{\tau}_{R,2}$ that increases linearly with ρ_r . In this regime the packing dominated contribution of $S(k\sigma)$ remains almost unchanged with density implying $\tilde{\tau}_{R,2} \propto 1/D$. According to the Enskog's description¹¹¹, $D = [3/(8\rho\sigma^2 g(\sigma))](k_B T/\pi m)^{1/2}$ for a fluid where $g(\sigma)$ is the radial distribution function at contact, m being the mass of a molecule. $g(\sigma)$ being weakly sensitive to ρ_r in this density regime, we get $\tilde{\tau}_{R,2} \propto 1/D \propto \rho_r$. Note that in the density range $0 < \rho_r < 1.6$, $\tilde{\tau}_{R,1}$ and $\tilde{\tau}_{R,2}$ do not differ significantly from each other, although $\tilde{\tau}_{R,1} < \tilde{\tau}_{R,2}$. However, $\tilde{\tau}_{R,1}$ increases rapidly at very high densities ($\rho_r > 1.6$) where the fluid becomes highly incompressible. The experimental τ_R in these densities does not show such rapid increase, rather is comparable in trend with $\tilde{\tau}_{R,2}$.

2.4 Inclusion of solute-solvent interaction

It is evident from the earlier section that although the molecular hydrodynamic timescales successfully capture the experimentally observed non-monotonic density dependence, the timescale values are only qualitative. Therefore, we next include the contributions from solute-solvent electrostatic interactions which could contribute significantly. The torque on the solute dipole undergoing rotational relaxation, as shown in Figure 2.1, is determined by the electrostatic interaction energy, $U(\theta)$ of the rotating photo-

excited dipolar solute as a function of its orientation θ (with respect to the laboratory frame z -axis), due to the solvent dipoles in the first solvation shell (see Appendix B). $U(\theta)$ depends on two factors: (1) the solute-solvent dipolar interaction potential[†] and (2) the solvent orientation distribution in the first solvation shell. The solvent orientation is characterized by $\rho_{10}(t)$, the projection of the solvent orientation distribution for spherical harmonic $l=1$. Since we are considering the perturbation from the final equilibrium orientation of the solute and relaxation back to the same equilibrium state, we use over-damped equation of motion for all the relevant dynamical variables. Note that the solvent orientation distribution undergoes relaxation as well, the rate being dictated by the solvent rotational diffusion D_R . The fluctuating torque is then given by $-\partial U(\theta)/\partial\theta$, where $U(\theta) = -u_0\rho_{10}(t)\rho_0 \cos\theta$ (see Appendix B) where $\rho_0 = 1/4\pi$, the bulk value of the orientation profile. The over-damped equation of motion (EOM) of the solute dipole: $\Gamma_{rot} \dot{\theta} = -\partial U(\theta)/\partial\theta$ where Γ_{rot} is the rotational frictional coefficient^{126, 127}. For small angular displacement from the final equilibrium state and $t < D_R^{-1}$, the solution is $\theta(t) = \theta(0)e^{-\omega t}$. Here $\omega = u_0\rho_0\rho_{10}(0)/\Gamma_{rot}$, the angular frequency of rotation which is the relaxation rate of the orientational correlation function. Hence, we identify $\tau_R = 1/\omega = \eta V_p M / k_B T$ where[‡] $M = \pi(6k_B T R^3 / \mu_0 \mu)^2 (1 - 2\mu^2 \rho / 9k_B T)$, R being the solute-solvent interaction length in the first solvation shell (see Appendix B). This expression is similar to the SED-expression, with the friction experienced by the solute dipole being modified by a factor of M over the hydrodynamic friction. Therefore, the solute-solvent interaction contributes non-additively to the hydrodynamic friction. Now, inserting the $k\sigma$ -dependence we get the modified wave vector dependent rotational relaxation frequency: $\omega(k\sigma) = k_B T / \eta(k\sigma) V_p M$, and follow the similar averaging over peaks of $S(k\sigma)$ to calculate the new time scales $\tau_{R,1}$ and $\tau_{R,2}$. To calculate M we use $R = R_0 + r_0$, R_0 and r_0 being the solute and solvent radii respectively.

[†] Note that the total solute-solvent interaction contains an orientation independent short-ranged component in addition to the asymmetric (dipolar) component given by. However, the short-ranged component does not contribute to the torque acting on the solute because the latter (torque) is determined by the angle-dependent interaction alone.

[‡] Here an obvious restriction arises, out of the mean field approximations we imposed in our formulation, to allow only positive values of the factor M that, $2\mu^2 \rho / 9k_B T < 1$.

Figure 2.4b shows the $\tau_{R,1}$ and $\tau_{R,2}$. The maximum in $\tau_{R,1}$ is now at 4 ps at $\rho_r = 0.59$ and the minimum is at 3.24 ps at $\rho_r = 1.03$. The $\tau_{R,2}$ values ranges between 9 ps and 16 ps for $\rho_r \geq 1.6$. Interestingly, the experimental τ_R of C153 compares well to the lower of the two calculated time scales. In particular the large time scale given by $\tau_{R,1}$ has not been reported in the experiments for $\rho_r \geq 1.6$. Thus identification of τ_R with $\tau_{R,1}$ for low density and that with $\tau_{R,2}$ at high density produce semi-quantitative agreement with the experimental data, shown in inset of Figure 2.4b.

2.5 Conclusion

In conclusion, we have developed a theoretical understanding of the rotational relaxation, for large polar solutes in polar SC solvents, incorporating the solvent structure via wave vector dependent shear viscosity and then the solute-solvent interaction. Here we extend the SED picture to incorporate the molecular interactions explicitly. The SED model, in its conventional form can qualitatively produce the experimental data with the simple replacement of η by $\eta(k\sigma)$. However, for a semi-quantitative agreement one needs to include the solute-solvent interaction. Apart from extracting the time scales that compare well with the experimental data, the present theory explains the possible causes behind this remarkable density dependence of rotation of a polar solute in a SC polar fluid. In particular, the rotational relaxation of the solute at low solvent densities is essentially governed by fluid compressibility. We predict that at very high densities, where the packing dominates the solvent structure, the time scales increase linearly. We expect that a more explicit treatment⁷ of the solute-solvent interaction would yield a better agreement to the experimental rotation times. Even though we restrict our discussion to rotation of C153 in SC fluoroform for the availability of experimental data, the present theoretical framework is applicable to rotation of a polar solute in a polar solvent in general. Moreover, such framework can be used to find the rotation time in other systems having different solute-solvent interactions and different solvent structures, like electrolytes, ionic liquids, to name only a few.

Appendices

A. Determination of critical point of fluid and calculation of $S(k\sigma)$ of the SC fluid.

The critical point of the fluid is determined¹²⁴ by the divergence of χ_T^* defined as $(1/\rho k_B T) \lim_{k\sigma \rightarrow 0} S(k\sigma)$. Therefore, the inverse compressibility $B_T^* = 1/\chi_T^* = 0$ at the critical point. $S(k\sigma)$ has been calculated from $C(k\sigma)$, the Fourier transform of $C(r)$. The short-ranged part of $C(r)$ is $C^{PY}(r)$, defined in 2.2.3, and the long-ranged attractive part $C^{LR}(r)$ for the polar fluid is derived by angle-averaging the Mayer's function^{111, 112}: $C^{LR}(r, \theta, \theta') = [e^{-\beta v(r, \theta, \theta')} - 1]$, where, $v(r, \theta, \theta')$ is the potential energy of interaction between two fluid dipoles with orientations θ and θ' in the laboratory frame. We derive $v(r, \theta, \theta')$ from the standard dipole-dipole potential¹²⁸, the potential energy of interaction between two fluid dipoles given by,

$$v(\mathbf{r}, \Omega) = \frac{1}{r^3} [\boldsymbol{\mu} \cdot \boldsymbol{\mu} - 3(\boldsymbol{\mu} \cdot \hat{\mathbf{r}})(\boldsymbol{\mu} \cdot \hat{\mathbf{r}})], \quad (2.12)$$

where, $\boldsymbol{\mu} = \mu \boldsymbol{\Omega}$, $\boldsymbol{\Omega}(\theta, \phi)$ being the unitary vector pointing along the direction of a fluid dipole in the laboratory frame; $\hat{\mathbf{r}}(\vartheta, \varphi)$ is the unit vector along \mathbf{r} , the separation vector between two dipoles. We carry out the dot products and integrate over all the angular coordinates, ϑ and φ of the separation \mathbf{r} . We integrate over the azimuthal coordinates, ϕ & ϕ' of the dipoles also, retain only the polar coordinates θ & θ' , to get θ & θ' $v(r, \theta, \theta') = -\mu^2 \cos \theta \cos \theta' / r^3$. We expand the exponential in $C^{LR}(r, \theta, \theta')$ under mean field theory² approximation, retaining up to the quadratic term:

$$C^{LR}(r, \theta, \theta') \approx -\beta v(r, \theta, \theta') + (\beta v(r, \theta, \theta'))^2, \quad (2.13)$$

Finally, integrating $C^{LR}(r, \theta, \theta')$ over θ and θ' we find $C^{LR}(r) = 2\beta^2 \mu^4 / 9r^6$.

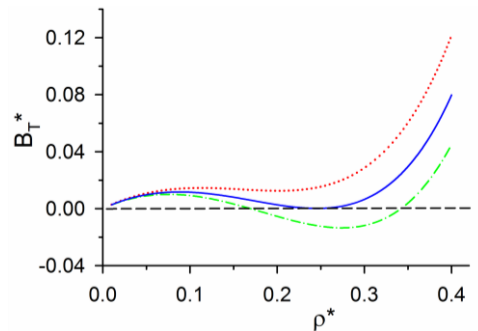


Figure A1: Estimation of critical point of a polar fluid. Plot of B_T^* as a function of ρ^* at three different temperatures, $T^* = 0.28$ (the dash-dot curve) below the T_c^* , $T^* = 0.30$ (the

dotted curve) above the T_C^* , and at $T^* = T_C^* = 0.29$ (the solid curve). Note that, B_T^* at T_C^* , becomes zero for $\rho^* = 0.25$.

To calculate the $S(k\sigma)$ of SC CHF₃ ($T_c = 299$ K)¹¹⁰, we use $\mu = 2.47$ D, higher than its gas phase value of 1.65 D (such high value is reported¹¹⁰) and $\sigma = 3.5$ Å, also taken from Song et al¹¹⁰. The $k\sigma \sim 0$ mode is calculated analytically by integration of $C(r)$ over the entire space. In Figure A1, we show the plot of B_T^* as a function of fluid density, $\rho^* = \rho\sigma^3$ at three different temperatures, $T^* = k_B T \sigma^3 / \mu^2$: one above ($T^* = 0.30$) and one below ($T^* = 0.28$) the critical temperature T_C^* and another at $T_C^* = 0.29$. We get the critical density, $\rho_C^* = 0.25$ which is fairly comparable with the corresponding experimental value¹¹⁰ of 0.2. The other non-zero $k\sigma$ modes of $C(k\sigma)$ has been calculated numerically.

B. Calculation of the interaction energy $U(\theta)$ of the rotating solute.

Following similar treatment as described above, we can write down the dipolar interaction potential $V_{dip}(R, \theta, \theta')$, between the solute dipole (μ_0) with polar orientation θ and a solvent dipole (μ) with polar orientation θ' (both in the laboratory frame) with a separation R , as

$$V_{dip}(R, \theta, \theta') = -u_0 \cos \theta \cos \theta', \quad (2.14)$$

where $u_0 = \mu_0 \mu / R^3$.

As the solute relaxes back to its final equilibrium orientation, the solvent also relaxes. The solvent relaxation is given by the equation of continuity¹¹¹ for the solvent orientation profile $\rho(\theta', t)$:

$$\frac{\partial \rho(\theta', t)}{\partial t} + \frac{\partial j}{\partial \theta'} = 0 \quad (2.15)$$

j being the current associated with the rotational diffusion of the solvent, defined as:

$$j = -D_R \rho(\theta', t) \nabla_{\theta'} \mu \quad (2.16)$$

where μ is the chemical potential and D_R , the coefficient of rotational diffusion of the solvent. We use the following definition for μ :

$$\mu = \frac{\delta F[\rho(\theta', t)]}{\delta \rho(\theta', t)}, \quad (2.17)$$

F being the density functional free energy¹¹¹ as a functional of $\rho(\theta', t)$. Also, we define $\rho_{10}(t)$, the projection of the solvent orientation distribution for spherical harmonic $l = 1$ as

$$\rho_{10}(t) = \int d(\cos \theta') \cos \theta' \rho(\theta', t) / \rho_0 \quad (2.18)$$

where ρ_0 is the bulk value of the orientation profile given by $\rho_0 = 1/4\pi$.

In the calculation of μ from Eq. 2.17, we generalize the equilibrium density functional¹¹¹ F for non-equilibrium fluctuations in the solvent orientation distribution. The equilibrium free energy that describes equilibrium changes in the solvent orientation distribution $\rho(\theta')$ from its bulk value ρ_0 is:

$$\begin{aligned} \beta F[\rho(\theta')] = & \int d(\cos \theta') \rho(\theta') \left[\ln \left(\frac{\rho(\theta')}{\rho_0} \right) - 1 \right] - \frac{1}{2} \int d(\cos \theta') d(\cos \theta'') C(\theta', \theta'') [\rho(\theta') - \rho_0] [\rho(\theta'') - \rho_0] \\ & + \beta \int d(\cos \theta') \rho(\theta') \mathcal{V}_{dip}(R, \theta') \end{aligned} \quad (2.19)$$

where, $\beta = 1/k_B T$ and $C(\theta', \theta'')$ is the two particle direct orientational correlation function between solvent molecules having orientations θ' and θ'' . Note that the solvent molecules also possess spherically symmetric interaction potential. However, the correlations due to spherically symmetric potential are irrelevant for $\rho(\theta')$. We simply replace $\rho(\theta')$ by $\rho(\theta', t)$ in Eq. 2.19.

We use the mean field¹¹¹ expression for $C(\theta', \theta'') \approx -\beta v(\theta', \theta'')$ where $v(\theta', \theta'')$ is the long-ranged dipolar interaction potential between solvent molecules with separation r , given by

$$v(\theta', \theta'') = -\frac{\mu^2 \cos \theta' \cos \theta''}{r^3} \quad (2.20)$$

The solvent-solvent correlation is truncated at the mean interparticle separation a_s defined as

$$\frac{4}{3} \pi a_s^3 \rho = 1 \quad (2.21)$$

where ρ denotes bulk solvent density. Using Eqs. 2.16, 2.17 and 2.19 we get

$$j = -D_R \frac{\partial \rho(\theta', t)}{\partial \theta'} - D_R \rho(\theta', t) \lambda \rho_{10}(t) \sin \theta' - D_R \rho(\theta', t) \frac{\partial \mathcal{V}_{dip}(R, \theta')}{\partial \theta'} \quad (2.22)$$

where $\lambda = \rho_0 \beta \mu^2 / a_s^3$. From Eq. 2.22 we can easily arrive at,

$$\frac{\partial j}{\partial \theta} = D_R \rho_0 \rho_{10}(t) \cos \theta' - D_R \rho_0 \rho_{10}(t) u_0 \cos 2\theta' \quad (2.23)$$

where we have used $\rho(\theta', t)/\rho_0 = \rho_{10}(t) \cos \theta'$. Inserting Eq. 2.23 in 2.15 we finally find a solution for

$$\rho_{10}(t) = \rho_{10}(0) e^{-D_R t}. \quad (2.24)$$

We now calculate the angle dependent interaction energy. Considering only the solvent molecules in the first solvation shell, the angle-dependent interaction energy is given by:

$$U(\theta) = \int V_{dip}(R, \theta, \theta') \rho(\theta', t) d(\cos \theta') = -u_0 \cos \theta \int \cos \theta' \rho(\theta', t) d(\cos \theta') \quad (2.25)$$

Inserting Eq. 2.18 in Eq. 2.25 we can write

$$U(\theta) = -u_0 \rho_{10}(t) \rho_0 \cos \theta \quad (2.26)$$

The fluctuating torque on the solute dipole is then given by $-\partial U(\theta)/\partial \theta$. We recall the overdamped EOM of the solute dipole⁵:

$$\Gamma_{rot} \dot{\theta} = -\frac{\partial U(\theta)}{\partial \theta} \quad (2.27)$$

which with the help of Eq. 2.26 becomes in small θ limit,

$$\dot{\theta} = -\frac{u_0 \rho_0 \rho_{10}(t)}{\Gamma_{rot}} \theta \quad (2.28)$$

Therefore we find the solution:

$$\theta(t) = \theta(0) \exp \left[-\frac{u_0 \rho_0}{\Gamma_{rot}} \int_0^t \rho_{10}(t') dt' \right]. \quad (2.29)$$

Inserting Eq. 2.24 in 2.29 we get

$$\theta(t) = \theta(0) \exp \left[-\frac{u_0 \rho_0 \rho_{10}(0)}{\Gamma_{rot} D_R} (1 - e^{-D_R t}) \right] \quad (2.30)$$

As long as $t < D_R^{-1}$, we can linearize the second exponential in Eq. 2.30 to get $\theta(t) = \theta(0) \exp[-\omega t]$, where $\omega = u_0 \rho_0 \rho_{10}(0)/\Gamma_{rot}$. The rotational relaxation of the solute can be characterized by the correlation function: $C_r(t) = \langle \theta(t) \theta(0) \rangle$ where $\langle \rangle$ denotes an average over initial angular orientations of the solute dipole in the laboratory frame. Insertion of the

solution of $\theta(t)$ here, gives: $C_r(t) = \langle \theta(0)^2 \rangle e^{-\omega t}$. Now, comparing the relaxation of this correlation function with the fluorescence depolarization, we identify the rotation time of the solute as $\tau_R = 1/\omega = \Gamma_{rot}/u_0\rho_0\rho_{10}(0)$.

We now define $\rho_{10}(0) = \rho_{10}$ which is calculated by minimizing $F[\rho(\theta')]$ in Eq. 2.19 with respect to $\rho(\theta')$. The minimization condition $\delta\beta F[\rho(\theta')]/\delta\rho(\theta') = 0$ yields within the framework of classical density functional theory¹¹¹ (DFT):

$$\frac{\rho(\theta')}{\rho_0} = e^{-\beta V_{dip}(R,\theta')} \exp\left[\int d(\cos\theta'')\mathcal{C}(\theta',\theta'')\{\rho(\theta'')-\rho_0\}\right] \quad (2.31)$$

Note that we are working at a temperature few percent (1~3%) above the critical point of the solvent, where the fluctuations of solvent orientation is much less pronounced than those at the critical point. In addition, the presence of moderate solute-solvent dipolar interaction ($u_0 \sim k_B T$) further reduces the orientation fluctuations. In this limit of small solvent orientation fluctuations, implying $[\rho(\theta') - \rho_0]/\rho_0 \ll 1$, we expand the second exponential in the right hand side of Eq. 2.31 and retain only the linear term to obtain

$$\frac{\rho(\theta')}{\rho_0} = e^{-\beta V_{dip}(R,\theta')} \left[1 + \int d(\cos\theta'')\mathcal{C}(\theta',\theta'')\{\rho(\theta'')-\rho_0\}\right] \quad (2.32)$$

Using the mean field expression of $\mathcal{C}(\theta',\theta'') \approx -\beta v(\theta',\theta'')$ again in Eq. 2.32 we arrive at

$$\frac{\rho(\theta')}{\rho_0} = e^{-\beta V_{dip}(R,\theta')} \left[1 - \beta \int d(\cos\theta'')v(\theta',\theta'')\{\rho(\theta'')-\rho_0\}\right] \quad (2.33)$$

We now multiply both sides in Eq.2.33 by $\cos\theta'$, integrate and use Eqs.2.18 and 2.19 yielding

$$\rho_{10} = \int d(\cos\theta')\cos\theta' e^{-\beta V_{dip}(R,\theta')} + \frac{\rho_0\beta\rho_{10}\mu^2}{a_s^3} \int d(\cos\theta')\cos^2\theta' e^{-\beta V_{dip}(R,\theta')} \quad (2.34)$$

Rearranging Eq. 2.34 we get

$$\rho_{10} = \frac{\int d(\cos\theta')\cos\theta' e^{-\beta V_{dip}(R,\theta')}}{1 - \frac{\rho_0\beta\mu^2}{a_s^3} \int d(\cos\theta')\cos^2\theta' e^{-\beta V_{dip}(R,\theta')}} \quad (2.35)$$

Eq. 2.14 is then inserted in Eq. 2.35. After this, linearization with respect to u_0 , subsequent integrations and use of Eq. 2.21 lead to the final expression of the required orientation distribution

$$\rho_{10} = \frac{2\beta u_0/3}{1 - 2\beta\mu^2 \rho/9}. \quad (2.36)$$

Chapter 3 Dipolar solute rotation in liquid media: effect of electrostatic solute-solvent interaction

3.1 Introduction

The SED model^{8, 22} in Eq. 1.1 can be recast as

$$\tau_R = \frac{\Gamma_{rot}^{hyd}}{6k_B T}, \quad (3.1)$$

where the hydrodynamic rotational friction^{127, 129} $\Gamma_{rot}^{hyd} = 6\eta V_p$. Even though the conventional SED model has received enormous success in describing solute rotation in common polar solvents⁸, ionic liquids²³, electrolyte solutions¹³ and for biologically relevant moieties²⁴, it completely breaks down while explaining the non-monotonic density dependence of τ_R observed in supercritical fluids. Our generalization²⁵ of the SED model, described in the previous chapter, incorporating the solvent structural effects in the friction experienced by the rotating solute rather satisfactorily describes the non-monotonic density-dependence. Following this approach²⁵, the generalized expression of the hydrodynamic friction becomes: $\Gamma_{rot}^{hyd}(k\sigma) = 6\eta(k\sigma)V_p$ involving the wave vector dependent viscosity²⁵ $S(k\sigma)$ which contains the molecular information of the solvent via the static structure factor $S(k\sigma)$ ¹¹¹. The success of the generalized SED model naturally raises the following question: Why does the simple and purely hydrodynamic SED model works so well for complex media? $\Gamma_{rot}^{hyd}(k\sigma)$ takes into account the solvent-solvent interactions in $S(k\sigma)$, while the solute-solvent interactions enter only through V_p , the excluded volume of the solvent due to the presence of the solute. Since the friction arises due to the solute-solvent coupling at the molecular level, the total rotational friction Γ_{rot} should contain the effects from both the short-ranged and long-ranged solute-solvent interactions.

The solute-solvent long-ranged electrostatic interactions become operational when the solute and the solvent are charged or having permanent electrical moment. Nee and Zwanzig²⁸ explored, within a continuum model description, the connection between the rotational friction and the dielectric response of a liquid. When a polar solute rotates in a polar medium, there is a redistribution of the polarization field generated by the solute in its surrounding solvent. This redistribution is not instantaneous, rather takes time, thus imparting a friction on the solute against the motion, termed as the “dielectric friction (DF)”. The early theoretical approaches^{28, 29, 130-133} addressing DF included the solvent effects through continuum dielectric constant and dielectric relaxation time. The solute in all these theories

has been a point dipole in a spherical cavity. Recent works^{7, 115, 134-136} consider an extended charge distribution model (ECDM) of a solute molecule where the constituent atoms with individual partial charges are distributed in an asymmetric ellipsoidal cavity. In spite of realistic elements, the ECDM received limited applications for two principal reasons: the high sensitivity on the cavity radius¹³⁴ and the somewhat arbitrary truncation of the number of terms used in the expression of DF^{113, 134}. Both these factors are highly system specific, varying for different solute-solvent combinations. Moreover, the solvent is still considered as a dielectric continuum without any microscopic details.

Although the concept of DF has been a key to understand ion-transport¹³⁷⁻¹⁴² and other non-equilibrium phenomena in polar media in general²⁹, its role in solute rotation is still a matter of considerable debate⁸. $r(t)$ measurements of C153 in various polar liquids show⁸ that τ_R increases linearly with the solvation time τ_s and consequently, viscosity of the solvent. SED model is found to work quite well in most of these cases. τ_R in a polar medium is observed to be slightly larger than that in a non-polar medium of similar viscosity. It is tempting to interpret the additional slowing down of τ_R in terms of extra DF operating in the system. The conventional van der Zwan and Hynes (VZH) theory¹³², used widely to estimate the dielectric contributions towards the rotational friction, shows that DF depends linearly on τ_s . Calculations for C153 in the aprotic solvents using this model yield⁸ dielectric contributions around 10-20% of the total friction. Similar estimation for the monohydroxy alcohols indicates even larger contributions of DF due to larger τ_s for the alcohols compared to those for the aprotic solvents of similar polarity. However, the enhancement of experimental τ_R is not as large as predicted by the existing DF theories^{28, 132}. Such discrepancy calls for a proper microscopic theory of DF on solute rotation.

The observations on dipolar solute rotation in ionic media, namely, ionic liquids (IL) and the electrolyte solutions (ES) possessing interactions even long-ranged than dipolar interactions, render the situation even more interesting. ILs are highly viscous and often have ions containing large alkyl chains¹⁴³ and permanent dipole moment¹⁴⁴. The dipolar solute rotation in ILs is then expected to be controlled by coupling between the medium viscosity and solute-IL dipole-dipole and dipole-ion interactions. $r(t)$ -measurements using fluorescent probes report $\tau_R \sim$ a few ns^{23, 145-148}, one or two orders of magnitude larger than that in regular liquid solvents⁸. The electrical interactions in an ES are very similar as in dipolar ILs. They are more viscous compared to the neat liquid component¹³. Consequently, much slower solute rotation ($\tau_R \sim$ hundreds of ps) is observed in an ES¹³ than in regular liquids.

Systematic investigations on dipolar probe C153 show²³ that in the dipolar ILs the τ_R is well explained by the SED model. In case of ES, the concentration dependent τ_R values, as observed¹³ using coumarin 334 (C334, another dipolar solute) in solutions of LiNO₃ in dimethyl sulphoxide (DMSO), are exactly reproduced by Eq. 1.1 with solution viscosities as inputs. These observations seem to suggest insignificant DF even in these ionic media. Given the validity of the SED description for solute rotation in common dipolar solvents, the question then naturally arises: Is there a common mechanism that decouples the solute rotation from the friction due to electrostatic solute-medium interactions?

Recent computer simulations^{29, 114} reveal that the enhancement in Γ_{rot} on a solute in a dipolar medium can be attributed to a static “electrostriction” effect, arising from enhanced structure in the first solvation shell via solute-solvent electrostatic interactions. Keeping this in mind, in the present chapter, we develop a theoretical formalism²⁶ to estimate the DF in a polar medium due to increased solvent ordering around the solute via the long-ranged solute-solvent interactions. The hydrodynamic friction has been taken into account via $\eta(k\sigma)$ introduced in the previous chapter. We derive an expression for τ_R of a dipolar solute in a dipolar solvent, where the relevant parameters have been obtained from microscopic considerations. Both the solute and the solvent are treated as point dipoles embedded in the centre of hard spheres to keep the calculation analytically tractable. Our main finding is that the DF have marginal effects on solute rotation, allowing an overwhelming dominance of Γ_{rot}^{hyd} in τ_R . In this way, we provide a molecular level explanation for the validity of the well-known SED description for solute rotation in common dipolar solvents. We generalize the molecular theory to ILs and ES, with an emphasis on a possible common mechanism for the decoupling between solute rotation and DF. Our calculations²⁷ show that viscosity and τ_R are dominated by the packing driven peak of the experimental $S(k\sigma)$. This motivates us to consider only the packing driven peaks of $S(k\sigma)$ for different media, obtained from analytical liquid state theories¹¹¹. Our results agree well with the experimental data. Here we again find negligible DF contributions to solute rotation.

This interesting similarity of DF for solute rotation in all the liquid media of varying interaction could be attributed to the short-range repulsive interaction that governs the solvent packing around the solute at liquid density. This leads us to construct a quantity which reflects the insensitivity of solute rotation to the details of solute-solvent interaction. This factor, we term, the quasi-universality factor and is defined as $\lambda = \tau_R r_0 D / V_p$ where r_0 and D are respectively the molecular radius and the translational self-diffusion coefficient of the solvent. Note here, τ_R and D are experimentally accessible quantities, while r_0 and V_p can be obtained from molecular modelling. λ is further connected to the microscopic solvent

structure and thereby constitute a macro-micro relation. We find that λ remains very similar for a wide variation of solute-solvent interactions which confirms the quasi-universality. The reason behind this universality can be traced to the fact that solute rotation is governed by the local friction which in turn is dominated by the packing-driven interactions.

The rest of chapter is organized as follows: Section 3.2 includes the calculations of Γ_{rot}^{hyd} , the DF and finally τ_R for a dipolar solute in common dipolar solvents. The calculations are extended in section 3.3 for the ionic media. Section 3.4 describes the quasi-universality of solute rotation in various liquid media. We conclude in section 3.5 and then present the appendices containing the details of various calculations.

3.2 Common dipolar liquids

In this section we formulate our theory for common dipolar liquids. First, the calculations on Γ_{rot}^{hyd} and hydrodynamic contributions to τ_R are described. Next we show how the DF can be included in the theory to calculate Γ_{rot} . Finally the τ_R are estimated with both hydrodynamic and electrostatic contributions. The obtained theoretical τ_R are compared with the experimental data on C153 in common dipolar solvents.

3.2.1 Molecular hydrodynamic friction and hydrodynamic rotation times

Let us first calculate the rotation time for a dipolar solute in a dipolar liquid from the molecular hydrodynamic friction $\Gamma_{rot}^{hyd}(k\sigma)$. We consider the case of C153 in acetonitrile at ambient condition as a representative example. From Eq. 2.7, the wave vector dependent viscosity for a liquid solvent²⁵ in the limit of slip boundary condition¹¹¹, appropriate for normal liquids, is: $\eta(k\sigma) = k_B T / 4\pi r_0 D S(k\sigma)$. Here, we model acetonitrile as a fluid consisting of hard spheres of diameter σ with central point dipole, of dipole moment $\mu = 3.5 D^{125}$. $S(k\sigma)$ could be obtained experimentally via neutron or x-ray scattering experiments, computer simulations or liquid state theories¹¹¹ as shown in the previous chapter. Our calculated $S(k\sigma)$ from liquid state theories, shown in Figure 3.1, reveals the only peak (nearest-neighbour) around the wave vector $k\sigma \approx 2\pi$ which according to molecular hydrodynamics, represent the governing wave vector modes for shear waves in a liquid¹⁴⁹⁻¹⁵¹. Therefore, the average viscosity is given by²⁵, $\bar{\eta} = \int \eta(k\sigma) d\mathbf{k}\sigma / \int d\mathbf{k}\sigma$, integrating over the wave vectors spanning the nearest-neighbour peak. Using the values of r_0 and D for acetonitrile^{8, 152}, we find $\bar{\eta} = 0.29$ cP at 300 K, which is close to the experimental shear viscosity⁸, 0.34 cP.

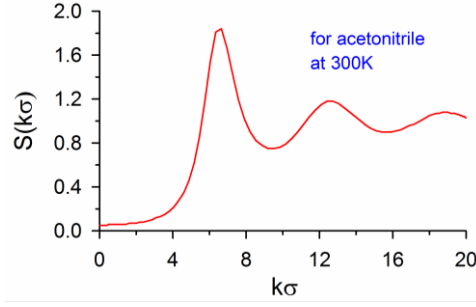


Figure 3.1: Representative static structure factor of a common dipolar liquid acetonitrile.

One can use $\bar{\eta}$ in place of η in the SED expression to estimate the hydrodynamic rotation time: $\tau_R^{hyd} = \bar{\eta}V_p/k_B T$. τ_R^{hyd} can also be estimated from the wave vector dependent rate of rotational relaxation²⁵: $\tilde{\omega}(k\sigma) = k_B T / \eta(k\sigma) V_p$, as in the previous chapter. The average rate of rotational relaxation is defined by integrating over the wave vectors under the $k\sigma \approx 2\pi$ peak of $S(k\sigma)$: $\tilde{\omega}_{av} = \int \tilde{\omega}(k\sigma) d\mathbf{k}\sigma / \int d\mathbf{k}\sigma$. The average rotation time can then be identified as: $\tau_R^{hyd} = 1/\tilde{\omega}_{av}$. Using $V_p = 246 \text{ \AA}^3$ for C153, we find $\tau_R^{hyd} = 17$ ps and 19 ps from the above two descriptions respectively, which are faster by $\sim 20\%$ from that measured (22 ps) in experiments⁸. Since the two descriptions produce results differing so little, for simplicity, onwards we use the first one.

3.2.2 Friction due to long-ranged solute-solvent interaction

Let us now include the long-ranged solute-solvent interactions in the total rotational friction. The torque acting on a rotating dipolar solute, as shown in chapter 2, $f(t) = -\partial U(\theta)/\partial \theta$ where θ is the time-dependent solute-orientation with respect to the laboratory frame z -axis, $U(\theta)$ being the solvent-orientation averaged solute-solvent dipolar interaction potential energy²⁵. For simplicity, we consider first the solvent molecules in the first solvation shell. The interaction potential $V_{dip}(R_s, \theta, \theta')$ between the dipolar solute and a dipolar solvent molecule at separation $R_s = r_0 + R_0$, integrated over all possible solvent orientation θ' and weighted by the solvent orientational density $\rho(\theta', t)$ in the first solvation shell, provides

$$U(\theta) = \int V_{dip}(R_s, \theta, \theta') \rho(\theta', t) d(\cos \theta') \quad (3.2)$$

where R_0 is the solute radius. Note, $U(\theta)$ has got implicit time dependence via the time-dependent solvent density $\rho(\theta', t)$. $V_{dip}(R_s, \theta, \theta')$, for the photo-excited solute dipole becomes²⁵

$$V_{dip}(R_s, \theta, \theta') = -u_0 \cos \theta \cos \theta', \quad (3.3)$$

where $u_0 = \mu_0 \mu / R_s^3$, the solute-solvent interaction strength. The normalized projection of $\rho(\theta', t)$ for spherical harmonics $l=1$ and $m=0$ is given by

$$\rho_{10}(t) = \int d(\cos \theta') Y_1^0(\cos \theta') \rho(\theta', t) / \rho_0 \quad (3.4)$$

where $\rho_0 = 1/4\pi$, the bulk orientational solvent density. Here, $\rho_{10}(t)$ approximately determines the solvent response towards the photo-excitation of the solute dipole, which is proportional to the solvent polarization. Using Eqs. 3.2-2.18, one obtains

$$U(\theta) = -u_0 \rho_{10}(t) \rho_0 \cos \theta \quad (3.5)$$

The microscopic expression for the time dependent total torque, in the limit of small angular displacements, then becomes

$$f(t) = u_0 \rho_{10}(t) \rho_0 \sin \theta \approx u_0 \rho_{10}(t) \rho_0 \theta. \quad (3.6)$$

The DF $\delta\Gamma_{rot}$ due to long-ranged solute-solvent interaction is subsequently determined by the memory function^{111, 153} $M(t)$, the auto-correlation function of the time-dependent fluctuating torque which is the orthogonal projection^{111, 153} of the total torque $f(t)$. $M(t)$ is related to the auto-correlation function of the total torque, $\phi(t) = \langle f(t)f(0) \rangle / I^2 \langle \dot{\theta}(0)\dot{\theta}(0) \rangle$, by the Mori-Zwanzig formalism^{111, 153}:

$$\frac{1}{\tilde{M}(s)} = \frac{1}{\tilde{\phi}(s)} + \frac{1}{s} \quad (3.7)$$

where $\tilde{M}(s)$ and $\tilde{\phi}(s)$ denote the Laplace transforms of $M(t)$ and $\phi(t)$ respectively, at a complex frequency s . Here, I denotes the moment of inertia of the rotating body about the axis of rotation. Using the equipartition theorem we obtain

$$\phi(t) = \frac{\langle f(t)f(0) \rangle}{Ik_B T}, \quad (3.8)$$

which, after using Eq. 3.6, takes the following form

$$\phi(t) = \frac{u_0^2 \rho_0^2}{Ik_B T} \langle \rho_{10}(t) \rho_{10}(0) \theta(t) \theta(0) \rangle. \quad (3.9)$$

Note that $\phi(t)$ has coupling between the fast mode $\rho_{10}(t)$, describing the orientational relaxation of the solvent and slow mode $\theta(t)$, describing the rotational motion of the solute. For rotation of a massive and large polar solute in fast polar solvents, the relaxation time scales of $\rho_{10}(t)$ and $\theta(t)$ are widely separated. Hence, under decoupling approximation¹⁵⁴ one can write

$$\phi(t) \approx \frac{u_0^2 \rho_0^2}{Ik_B T} \langle \rho_{10}(t) \rho_{10}(0) \rangle \langle \theta(t) \theta(0) \rangle, \quad (3.10)$$

Now, the lag in solvent response towards solute rotation can be linked to the solvent reorganization time via the following approximate relation: $\rho_{10}(t) = \rho_{10}(0) e^{-t/\tau_s}$. Considering the equation of motion for θ we find (Appendix A):

$$\phi(t) = B e^{-\lambda t} \quad (3.11)$$

where $B = \frac{u_0^2 \rho_0^2 \rho_{10}(0)^2}{Ik_B T}$ and $\lambda = \left(\frac{u_0 \rho_0 \rho_{10}(0)}{\Gamma_{rot}} + \frac{1}{\tau_s} \right)$.

Insertion of the Laplace transform of Eq. 3.11: $\tilde{\phi}(s) = B/(s - \lambda)$, in Eq. 3.7 leads to

$$\tilde{M}(s) = \frac{Bs}{(s - \lambda)s + B}. \quad (3.12)$$

which can further be expressed as

$$\tilde{M}(s) = \frac{B}{\sqrt{\lambda^2 - 4B}} \left[\frac{s_+}{s - s_+} - \frac{s_-}{s - s_-} \right], \quad (3.13)$$

s_+ and s_- being the roots of the equation, $s^2 - \lambda s + B = 0$, given by $s_{\pm} = (\lambda \pm \sqrt{\lambda^2 - 4B})/2$. Here s_- gives a divergent exponential in $t \rightarrow \infty$ limit, implying an unphysical situation. Therefore, integrating around the pole at s_+ , we have the inverse Laplace transform

$$M(t) = \frac{B}{\sqrt{\lambda^2 - 4B}} s_+ e^{-s_+ t} \quad (3.14)$$

Now, we calculate $\delta\Gamma_{rot}$ by the time-integral of the memory function $M(t)$:

$$\delta\Gamma_{rot} = \frac{I}{2} \int_0^\infty M(t) dt = \frac{I}{2} \frac{B}{\sqrt{\lambda^2 - 4B}}, \quad (3.15)$$

In the limit of weak solute-solvent coupling (*i.e.*, $\lambda^2 > B$), insertion of the expressions of B and λ in Eq. 3.15 produces

$$\delta\Gamma_{rot} = \frac{[u_0 \rho_0 \rho_{10}(0)]^2}{2k_B T} \left(\frac{u_0 \rho_0 \rho_{10}(0)}{\Gamma_{rot}} + \frac{1}{\tau_s} \right)^{-1}. \quad (3.16)$$

Eq. 3.16 is a self-consistent expression for $\delta\Gamma_{rot}$ since $\Gamma_{rot} = \Gamma_{rot}^{hyd} + \delta\Gamma_{rot}$ with solution given by

$$\delta\Gamma_{rot} = \frac{\frac{[u_0 \rho_0 \rho_{10}(0)]^2}{2k_B T} \Gamma_{rot}^{hyd} \tau_s}{u_0 \rho_0 \rho_{10}(0) \tau_s + \Gamma_{rot}^{hyd} - \frac{[u_0 \rho_0 \rho_{10}(0)]^2}{2k_B T} \tau_s}. \quad (3.17)$$

Note Eq. 3.17 connects $\delta\Gamma_{rot}$ to the orientational static solvent structure around the solute, ρ_{10} and the average solvation time, τ_s . The total friction now becomes

$$\Gamma_{rot} = \Gamma_{rot}^{hyd} \left[1 - \frac{(u_0 \rho_0 \rho_{10}(0))^2 \tau_s}{2k_B T (\Gamma_{rot}^{hyd} + u_0 \rho_0 \rho_{10}(0) \tau_s)} \right]^{-1}. \quad (3.18)$$

Expansion of Eq. 3.18 in the weak solute-solvent coupling limit produces the following first order term:

$$\Gamma_{rot} = \Gamma_{rot}^{hyd} \left[1 + \frac{(u_0 \rho_0 \rho_{10}(0))^2 \tau_s}{2k_B T (\Gamma_{rot}^{hyd} + u_0 \rho_0 \rho_{10}(0) \tau_s)} \right] \quad (3.19)$$

where $\rho_{10}(0) = (2u_0/3k_B T)[1 - 2\mu^2 \rho_b/9k_B T]^{-1}$, obtained in the Appendix B in the previous chapter from a equilibrium DFT for the classical systems, ρ_b being the bulk solvent density.

Now, we recast Eq. 3.19 as

$$\Gamma_{rot} = \Gamma_{rot}^{hyd} [1 + J] \quad (3.20)$$

where $J = (u_0 \rho_0 \rho_{10}(0))^2 \tau_s [2k_B T (\Gamma_{rot}^{hyd} + u_0 \rho_0 \rho_{10}(0) \tau_s)]^{-1}$, the solute-solvent dipolar coupling factor. Note that, J is essentially the ratio $\delta\Gamma_{rot}/\Gamma_{rot}^{hyd}$, diminishing with increasing hydrodynamic friction.

Next, we extend our calculations to take into account the effects of solvent molecules beyond the first solvation shell around the solute. We find the expression of the coupling factor (Appendix B): $J = (3\rho_b I_R \tau_s / 8\pi k_B T) [\Gamma_R^{hyd} + \mathcal{U}_0(0)\tau_s]^{-1}$ where $I_R = (2\pi)^{-6} \int d\mathbf{k} |V_{dip}^{110}(\mathbf{k})|^2 |\rho_{10}(\mathbf{k}, 0)|^2$ and $\mathcal{U}_0(t) = -\sqrt{3/4\pi} (2\pi)^{-3} \int V_{dip}^{110}(\mathbf{k}) \rho_{10}(\mathbf{k}, t) d\mathbf{k}$. Here $V_{dip}^{110}(\mathbf{k})$ and $\rho_{10}(\mathbf{k}, t)$ denotes the Fourier components of the solute-solvent dipolar interaction potential and the normalized solvent density distribution around the solute, respectively. We calculate $\rho_{10}(\mathbf{k}, 0)$ by using the DFT treatment (Appendix C).

In Figure 3.2a, we illustrate the behaviours of $V_{dip}^{110}(\mathbf{k})$ and $\rho_{10}(\mathbf{k}, 0)$. These two quantities govern the interaction terms $\mathcal{U}_0(0)$ and I_R to decide the values of J . We consider the case of C153 in acetonitrile, using the excited state dipole moment of C153 to be¹²⁵ $\mu_0 = 14$ D and van der Waals radius¹²⁵ $R_0 = 3.9$ Å. Figure 3.2a shows the plot of $|V_{dip}^{110}(\mathbf{k})|^2$ at different wave vectors. It decays from maximum near $k\sigma \approx 0$ mode. We show in Figure 3.2b, the profile of $\rho_{10}(\mathbf{k})$ for the same system exhibiting a similar behaviour to $|V_{dip}^{110}(\mathbf{k})|^2$. From the nature of these two at different wave vectors, it is quite clear that the dominant electrical contributions towards the friction come from the long-wavelength *i.e.* $k\sigma \approx 0$ mode. This actually reflects the long-ranged nature of the solute-solvent interaction.

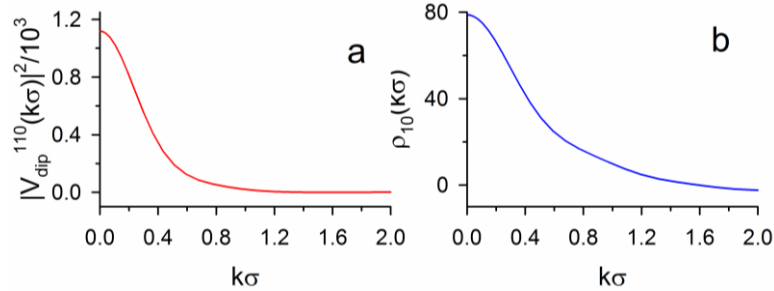


Figure 3.2: Angular components of solute-solvent interaction potential (a) $|V_{dip}^{110}(k\sigma)|^2$ and solvent density around the solute (b) $\rho_{10}(k\sigma)$. Both are shown for C153 in acetonitrile, at different wave vectors.

The details of estimated DF for C153 in various polar liquids, both aprotic and the alcohols are presented in Figure 3.3. Here the solvent parameters we use in our calculations are: the solvent $D^{152, 155-159}$, $\mu^{125, 160-162}$, static dielectric constants ϵ_0^{125} , r_0^8 and τ_s^8 . For these calculations, we replace Γ_{rot}^{hyd} in Eq. 3.20 by that averaged over the wave vector window around the nearest-neighbour modes. Figure 3.3a shows $\delta\Gamma_{rot}$ as a function of τ_s while the

hydrodynamic part Γ_{rot}^{hyd} is shown in Figure 3.3b. Note the difference in scales of the vertical axes in these two panels. We find that for most of the aprotic solvents DF is nearly zero barring the cases of DMSO and propylene carbonate (PC) both of which have dipole moments larger than 4 D. The alcohols also exhibit comparatively larger DF. In Figure 3.3c we show the ratio $\delta\Gamma_{rot}/\Gamma_{rot}^{hyd} = J$ which turn out to be too small in all the cases to generate any considerable dielectric contribution. J accounts for at most $\sim 1\text{-}2\%$ of the total friction, even for solvents like the alcohols supporting observations of Horng et al⁸. A closer inspection reveals that Γ_{rot}^{hyd} is always very large compared to the product $I_R\tau_s$ in the numerator of J , rendering it small.

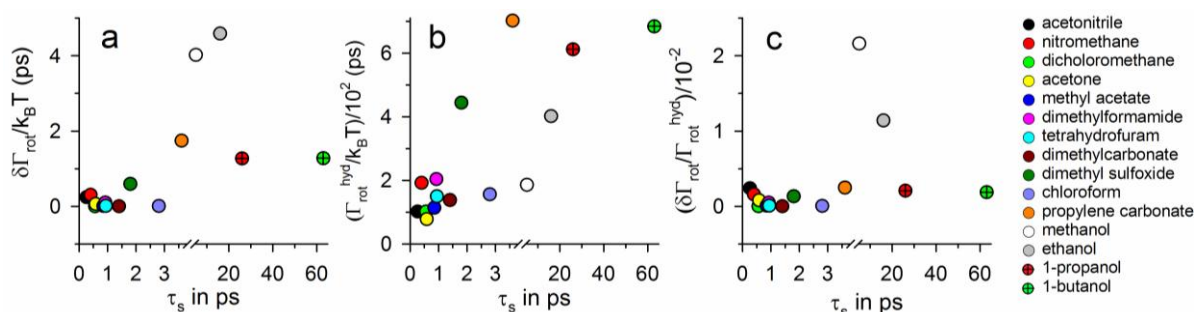


Figure 3.3: Friction data for common dipolar liquids. (a) $\delta\Gamma_{rot}$ and (b) Γ_{rot}^{hyd} and (c) $\delta\Gamma_{rot}/\Gamma_{rot}^{hyd}$, all as functions of τ_s for C153 in aprotic polar liquids and in alcohol solvents. The solvation times have been taken from Horng et al⁸.

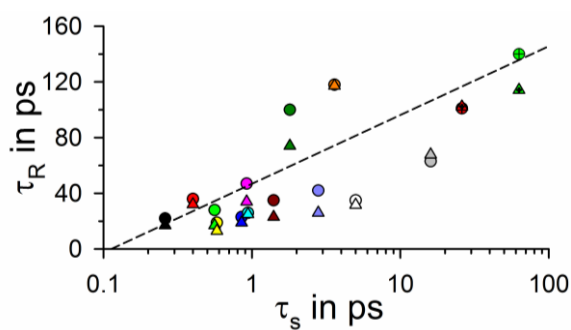


Figure 3.4: Experimental⁸ (circles) and calculated (triangles) τ_R of C153 in aprotic polar solvents and alcohols, as a function of experimental⁸ τ_s . Colour codes same as Figure 3.3. The best linear fit through the experimental points are shown by the dotted straight line.

3.2.3 Rotation times including DF

Let us now discuss the rotation times. We can rewrite Eq. 3.20 as

$$\tau_R = \tau_R^{hyd} [1 + J]. \quad (3.21)$$

Figure 3.4 shows the experimental⁸ (circles) and calculated (triangles) τ_R of C153 in the polar liquids depicted in Figure 3.3, as a function of experimental τ_s . From the data in Figure 3.4, it is clear that the calculated τ_R agree reasonably well with the experimental values. Further, Figure 3.4 indicates a linear dependence¹⁶³⁻¹⁶⁵ between τ_R and τ_s , shown by the best fit line through the experimental data. Such behaviour can be rationalized by noting that in general we have $\Gamma_{rot}^{hyd} \gg \mathcal{U}_0(0)\tau_s$, true for all the liquids we study here. Under these circumstances, Eq. 3.21 can be approximated as

$$\tau_R = \tau_R^{hyd} + \frac{3\rho_b I_R}{48\pi(k_B T)^2} \tau_s, \quad (3.22)$$

showing a linear dependence between τ_R and τ_s . Typically in dipolar solvents τ_s is proportional to solvent viscosity η . So the linear dependence in Eq. 3.22 implies that τ_R is also proportional to η which is observed in experiments. In most of the dipolar solvents, the pre-factor of the term containing τ_s is too small to contribute significantly to τ_R . However, if the pre-factor is large due to large solute-solvent coupling this additional dependence could be observed.

3.2.4 Comparison with earlier theories

Our estimated values of DF are smaller in magnitude than those obtained from the VZH theory. The differences between the VZH and our results are more significant for the alcohol solvents. Interestingly, a common point of both the frameworks lies in the inclusion of the solute-solvent interaction and τ_s to determine the DF. In the VZH approach, the solute-solvent interaction is incorporated in terms of experimentally observed fluorescence Stokes shift¹²⁵. It has been experimentally observed that C153 exhibits larger τ_s in alcohol solvents compared to the same in aprotic solvents of equivalent polarity, probably due to solute-solvent specific interactions and/or solvent-solvent interactions. It is to be mentioned here that computer simulation studies¹⁶⁶ have indicated presence of such interactions, even though effects of these interactions have not been reflected strongly in the solvatochromic shift¹²⁵ of C153 in protic polar solvents. Therefore, the VZH description, based directly on the Stokes shift values and τ_s , predicts larger friction for alcohols than aprotic solvents. In the present theory, the solute-solvent interactions are considered using a microscopic model

of the interactions where in principle the Stokes shift values can also be used. It is indeed true that in common to the VZH approach the DF in the present theory is related to the τ_s . However, the difference here is that the dependence on τ_s is non-linear and enters through a self-consistent manner (Eq. 3.17). This non-linear dependence on τ_s reduces the magnitude of DF significantly compared to that predicted by the VZH approach. Even in the linearized version (Eq. 3.22), the pre-factor of τ_s for these solute-solvent systems is rather small.

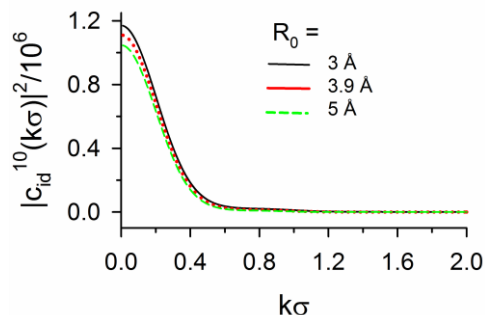


Figure 3.5: Solute-solvent correlation for ionic solutes in dipolar solvent. $|c_{id}^{10}(k\sigma)|^2$ as a function of $k\sigma$, for ionic solutes in acetonitrile. The solute here is modelled as a hard sphere with a unit positive charge embedded at the centre. We show the data for three values of the solute radius with insignificant dependence for solutes larger than solvents.

Similar self-consistent treatment of DF, as in our calculation, done in the context of ion-transport in a polar medium to obtain the DF¹³⁷⁻¹⁴² shows substantial contribution of the long-ranged forces. The solute-solvent long-ranged interaction in those cases is of ion-dipole type, much stronger compared to the dipole-dipole interaction. Figure 3.5 shows the longitudinal component of wave vector dependent direct correlation function^{142, 167}, $c_{id}^{10}(k\sigma)$ plotted for an ionic solute placed in acetonitrile. For a univalent cationic solute of size comparable to C153, the value of $|c_{id}^{10}(k\sigma)|^2$ is about 1000 times larger than $|V_{dip}^{110}(k\sigma)|^2$ (Figure 3.2a) at $k\sigma \approx 0$. Since the principal electrical contribution to friction arises from the $k\sigma \approx 0$ mode, clearly the DF would be important for ion translation but not so significant for solute rotation in a dipolar solvent.

3.3 Generalization for ionic media

Here we generalize the theory developed in the previous section for the ionic solvents, namely the IL and the ES to compute the DF. We follow similar steps as in section 3.2: First we consider the hydrodynamic contributions from $\eta(k\sigma)$ and then extend the equations 3.2.2

for IL and ES. Finally, the rotation times are calculated and compared with the experimental data.

3.3.1 Wave vector dependent viscosity and molecular hydrodynamic τ_R

We present our analyses based on $\eta(k\sigma)$ for ILs and ES in this section.

(a) Ionic liquids

To calculate $\eta(k\sigma)$ for the ILs we need the structure factors. The total structure factor $S_{tot}(k\sigma)$ of an IL is obtained combining the partial structure factors¹⁶⁸, $S_{ij}(k\sigma)$: $S_{tot}(k\sigma) = \sum_{i,j} \sqrt{x_i x_j} S_{ij}(k\sigma)$ where x_i is the mole fraction of the i th ion ($i, j = 1$ (cation) and 2 (anion)). The experimental $S_{tot}(k\sigma)$ of different ILs, measured via small angle x-ray scattering experiments^{168, 169}, are different from the $S(k\sigma)$ of normal liquids¹¹¹ due to pre-peaks at lower wave vectors ($0 < k\sigma < 2\pi$) apart from the packing driven $k\sigma \approx 2\pi$ peak. These pre-peaks have also been observed in several simulation studies¹⁷⁰⁻¹⁷³ and are believed to be manifestations of long-range charge-ordering in ILs¹⁷². The pre-peak intensities vary with alkyl chain-length as shown by studies on ILs with $[\text{Im}_{n1}^+]$ and $[\text{Pr}_{n1}^+]$ cations (see Tables for names^{168, 169}). For $n < 8$ typically one pre-peak is present, whereas another pre-peak appears only for $n \geq 8$ and becomes stronger even than the other pre-peak for $n=10$.

We calculate $\eta(k\sigma)$ for three pyrrolidinium ILs ($n = 4, 6$ and 10) using the experimental¹⁶⁸ $S_{tot}(k\sigma)$, for which the experimental viscosities and τ_R are known²³. Considering the similarities of the experimentally observed ionic partial structure factors¹⁶⁸, radii²³ and self-diffusivities^{144, 174}, we define an average molecular radius $\bar{r}_0 = (r_1 + r_2)/2$ and average self-diffusion coefficient $\bar{D} = (D_1 + D_2)/2$ for each IL, r_i and D_i denoting the radius and self-diffusion coefficient of i th ion. Therefore, for an IL $\eta(k\sigma) = k_B T / 4\pi \bar{r}_0 \bar{D} S_{tot}(k\sigma)$. The viscosity contribution from the α -th peak in $S_{tot}(k\sigma)$ is calculated as²⁵, $\bar{\eta}_\alpha = \int_\alpha \eta(k\sigma) d\mathbf{k}\sigma / \int_\alpha d\mathbf{k}\sigma$ integrating from $k\sigma = k_L^{(\alpha)}$ to $k\sigma = k_R^{(\alpha)}$, covering the entire peak. For instance, in case of $[\text{Pr}_{41}^+][\text{Tf}_2\text{N}^-]$, we set $k_L^{(1)} = 5.1$ and $k_R^{(1)} = 7.4$ for the pre-peak, while $k_L^{(2)} = 7.4$ and $k_R^{(2)} = 11.0$ for the $k\sigma \approx 2\pi$ peak.

The overall average viscosity is obtained as $\bar{\eta} = \sum_\alpha c_\alpha \bar{\eta}_\alpha$ where $c_\alpha = h_\alpha / \sum_\alpha h_\alpha$, the combining weight factors and h_α , the height of the α th peak. Table 3.1 shows that $\bar{\eta}$ for the

above three ILs agree reasonably well with their experimental viscosities. For $n=4$ and 6, we find that the $k\sigma \approx 2\pi$ peak contributions are dominating ($>85\%$ of the $\bar{\eta}$), while it is the major contributor ($\sim 50\%$) for $n=10$. These clearly show the dominance of the nearest-neighbour peak over the pre-peaks which is not surprising, for the viscosity is determined by the momentum transfer between the adjacent layers. The molecular hydrodynamic friction, $\Gamma_{rot}^{hyd}(k\sigma) = 6V_p\eta(k\sigma)$, defines the wave vector dependent rate of rotational relaxation²⁵: $\tilde{\omega}(k\sigma) = k_B T / \eta(k\sigma) V_p$. The corresponding average rate is defined as²⁵: $\tilde{\omega}_{av} = \int \tilde{\omega}(k\sigma) d\mathbf{k}\sigma / \int d\mathbf{k}\sigma$. The molecular hydrodynamic rotation time is then given by $\tau_R^{hyd} = 1/\tilde{\omega}_{av} \approx \bar{\eta} V_p / k_B T$. The calculated τ_R^{hyd} of C153 in these three ILs (Table 3.1) agree well with the experimental data²³.

The dominance of the $k\sigma \approx 2\pi$ peak contributions in $\bar{\eta}$ calculated from the experimental $S_{tot}(k\sigma)$ indicates that the viscosity can be extracted from a model of the $k\sigma \approx 2\pi$ peak in $S_{tot}(k\sigma)$. To this end, we theoretically calculate the $S_{tot}(k\sigma)$, using the known Percus-Yevik form¹¹¹ for short-ranged repulsive interactions and treating the long-ranged electrostatic interactions at the mean-field level^{25, 26} (Appendix C) that is known to capture the $k\sigma \approx 2\pi$ peak¹¹¹ reasonably well. We consider the ILs to be composed of hard spheres with unit point charges at centres, a dipolar ion having an additional central point dipole. Further, we assume only dipolar cations and choose ILs having no specific interaction with C153. Table 3.1 shows that the $\bar{\eta}$ and τ_R^{hyd} values for the three pyrrolidinium ILs discussed above, calculated from the $k\sigma \approx 2\pi$ peak of the theoretical $S_{tot}(k\sigma)$ (numbers in parenthesis), agree well with the experimental data.

Next we consider the ILs for which no experimental $S_{tot}(k\sigma)$ are available, focusing only on the $k\sigma \approx 2\pi$ peak. In Figure 3.6a, we illustrate the theoretical $S_{ij}(k\sigma)$ and $S_{tot}(k\sigma)$ for $[\text{Im}_{41}^+][\text{PF}_6^-]$. The calculated $\bar{\eta}$ values of these dipolar ILs (Table 3.2) from the $k\sigma \approx 2\pi$ peak of $S_{tot}(k\sigma)$ agree quite well with the experimental²³ η which justify our model calculations. The τ_R^{hyd} values (Table 3.2) too are quite close to the respective experimental τ_R .

Table 3.1: Viscosities and τ_R^{hyd} of C153 in three *N*-methyl(*N*-alkyl)pyrrolidinium ([Pr_{n1}⁺]) ILs with anion bis(trifluoromethylsulfonyl)imide ([Tf₂N⁻]) at 298 K, whose experimental structure factors are known.

Name of ILs	$\bar{\eta}$ (cP) (calc.)	$\bar{\eta}_\alpha$ (cP) from $k\sigma \approx 2\pi$ peak	η (cP) (expt)	$\Delta\eta$ (%) ^a	τ_R^{hyd} (ns) (calc.)	τ_R (ns) (expt.)	$\Delta\tau_R$ (%) ^b	<i>J</i>
[Pr ₄₁ ⁺][Tf ₂ N ⁻]	50	43(64) ^c	70	29(9)	3.0(3.8)	3.4	12(12)	0.0002
[Pr ₆₁ ⁺][Tf ₂ N ⁻]	57	49(66)	93	39(29)	3.4(3.9)	5.7	40(32)	0.0031
[Pr _{10,1} ⁺][Tf ₂ N ⁻] ^d	155	78(111)	145	7(23)	9.2(6.6)	9.0	2(27)	-

$${}^a \Delta\eta = \frac{|\eta^{expt} - \bar{\eta}|}{\eta^{expt}} \times 100 \quad {}^b \Delta\tau_R = \frac{|\tau_R^{expt} - \tau_R^{hyd}|}{\tau_R^{expt}} \times 100$$

^c The results in the parenthesis are from the theoretically calculated structure factors. In addition, we use the dipole moments¹⁴⁴, static dielectric constants¹⁷⁵, ionic radii²³ and self-diffusivities^{174, 176} of the ILs for calculations.

^d In this case, the dipole moment of the cation is too high (~ 16 D)¹⁴⁴ for the mean-field approximation to be valid.

Table 3.2: Viscosities and τ_R^{hyd} of C153 in other ILs at 298 K.

Name of ILs ^a	$\bar{\eta}$ (cP) (calc.)	η (cP) (expt)	$\Delta\eta$ (%)	τ_R^{hyd} (ns) (calc.)	τ_R (ns) (expt.)	$\Delta\tau_R$ (%)	<i>J</i>
[Im ₄₁ ⁺][Tf ₂ N ⁻]	33	41	20	2.0	2.6	23	0.0010
[Pr ₃₁ ⁺][Tf ₂ N ⁻]	42	53	21	2.5	2.6	4	0.0002
[Im ₄₁ ⁺][BF ₄ ⁻]	52	75	31	3.1	4.3	28	0.0068
[N _{ip311} ⁺][Tf ₂ N ⁻]	71	105	32	4.2	4.4	5	0.0002
[N _{ip411} ⁺][Tf ₂ N ⁻]	99	130	24	5.9	7.9	25	0.0002
[N _{ip611} ⁺][Tf ₂ N ⁻]	129	139	7	7.7	7.8	1	0.0021
[Im ₄₁ ⁺][PF ₆ ⁻]	149	187	20	8.9	12.0	26	0.0024

^a The cation [Im₄₁⁺] is 1-Butyl-3-methylimidazolium and [N_{ipn11}⁺] is (dimethyl)(isopropyl)(alkylammonium); the anion [BF₄⁻] is tetrafluoroborate and [PF₆⁻] is hexafluorophosphate.

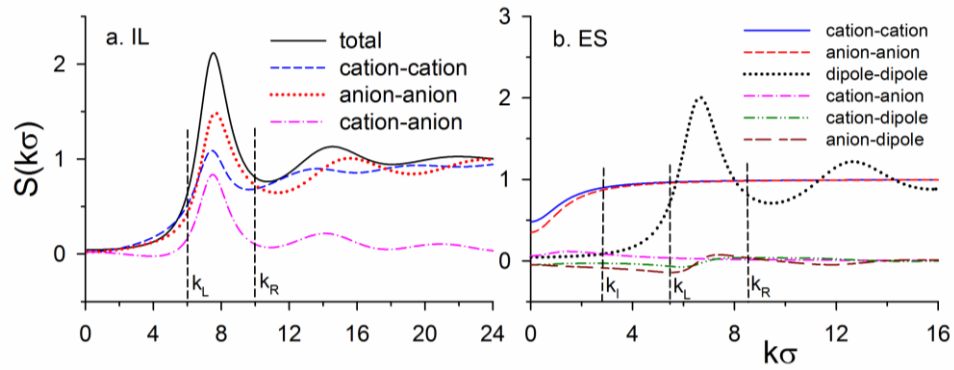


Figure 3.6: The theoretical static structure factors. For (a) IL $[\text{Im}_{41}^+][\text{PF}_6^-]$ and (b) 0.5 M LiNO_3 in DMSO at 298 K. In both cases we show the total as well as partial structure factors. In panel a, the range over which we carry out the integrations on total structure factor for calculation of viscosities is marked by the quantities k_L and k_R . In panel b, such integration ranges are marked, for the ionic components by k_I and for the dipolar component by k_L and k_R . In case of the electrolyte solutions the calculations are done using the ionic radii¹¹⁶ r_1 , r_2 and molecular radius⁸ r_3 , dipole moment¹²⁵ μ and static dielectric constant¹²⁵ ϵ_0 of DMSO.

(b) Electrolyte Solutions

Here we focus on the LiNO_3 -DMSO solution since a systematic experimental investigation on rotation of a neutral dipolar solute C334 in this ES, is available¹³. Moreover, C334 does not show any solute-solvent specific interaction in this ES. However, no experimental or simulated structure factor of this ES system is known. Therefore, we model this ES as a ternary mixture¹⁷⁷ of oppositely charged hard spheres representing the ions and dipolar hard spheres representing the dipolar solvent to calculate the $S_{ij}(k\sigma)$ (Appendix D). Here also the long-ranged interactions are treated at the mean-field level. The ionic components (Figure 3.6b) have only one significant mode around $k\sigma \approx 0$ with no structure near $k\sigma \approx 2\pi$. This compressibility mode²⁵ can be attributed to weak screening at low concentrations ($c \sim 0.1$ -1 M here) leading to a small inverse Debye screening length¹¹¹ $\kappa_D\sigma \sim 1$. The dipolar component in Figure 3.6b is similar to the $S(k\sigma)$ for normal liquids. The cross-terms nearly vanish (Figure 3.6b) rendering only the self terms significant.

The partial viscosity $\bar{\eta}_i$ due to the i th component is defined as $\bar{\eta}_i = \int_{\alpha} \eta_i(k\sigma) dk\sigma / \int_{\alpha} dk\sigma$ where $\eta_i(k\sigma) = k_B T / 4\pi r_i D_i S_{ii}(k\sigma)$. We fix $\alpha \equiv k\sigma \approx 0$ mode for the ionic components ($i = 1, 2$) and $\alpha \equiv k\sigma \approx 2\pi$ mode for the dipolar solvent ($i = 3$).

Integrating over the different ranges depicted in Figure 3.6b ($k\sigma = 0$ to $k\sigma = k_L$ for $i = 1, 2$ and from $k\sigma = k_L$ to $k\sigma = k_R$ for $i = 3$), the average viscosity of the ES: $\bar{\eta} = \sum_i x_i \bar{\eta}_i$ where x_i is the mole fraction of the i th species. The calculated $\bar{\eta}$ (Figure 3.7a) at several concentrations agree quite well with the experimental viscosities¹³. The τ_R^{hyd} of a solute in an ES can be obtained as: $\tau_R^{hyd} = \sum_i x_i / \omega_{av,i}$ where $\omega_{av,i} = \int_{\alpha} \omega_i(k\sigma) d\mathbf{k}\sigma / \int_{\alpha} d\mathbf{k}\sigma$, defined for the i th species in solution. The agreement of the calculated τ_R^{hyd} values of C334 to the experimental¹³ τ_R (Figure 3.7b) is also quite well. Both $\bar{\eta}$ and deviate from the experimental data at large c values which can be attributed to formation of ion-pairs, triple-ions etc¹⁷⁸, modifying the average solvent structure.

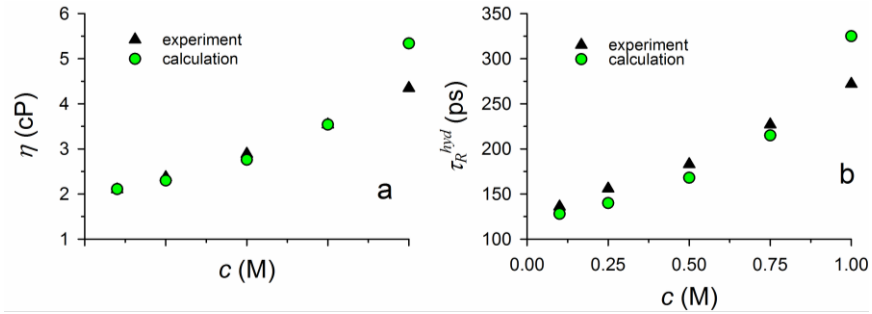


Figure 3.7: Viscosities and rotation times in ES. Comparison of (a) experimental and calculated η of solutions of LiNO_3 in DMSO and (b) experimental τ_R and calculated τ_R^{hyd} of C334 ($V_p = 252 \text{ \AA}^3$)¹³ in the solutions of LiNO_3 in DMSO, both at 298 K. For these calculations we calculate the concentration dependent ionic self-diffusivities D_i using Onsager equation¹⁷⁹ with ionic conductivities at infinite dilution¹⁸⁰ as inputs.

3.3.2 Electrostatic contribution to τ_R in ionic media

According to section 3.2.2, the DF ($\delta\Gamma_{rot}$) acting on a rotating dipolar solute can be expressed as²⁶

$$\delta\Gamma_{rot} = \Gamma_{rot} - \Gamma_{rot}^{hyd} = \mathcal{J}\Gamma_{rot}^{hyd} = \Gamma_{rot}^{hyd} \left(\frac{3\rho_b I_R \tau_s}{8\pi k_B T [\Gamma_{rot}^{hyd} + \mathcal{U}_0(0)\tau_s]} \right). \quad (3.23)$$

The solute-solvent interaction has been treated here at the mean-field level replacing the solute-solvent correlation simply by the interaction potential¹¹¹. Equation 3.23 clearly reveals the non-linear coupling between DF and Γ_{rot}^{hyd} . In addition, $\delta\Gamma_{rot}$ possesses complex dependence on τ_s , showing an implicit connection to solvent dielectric response. This is

important because nowhere in this theory we explicitly connect Γ_{rot} with solvent polarization relaxation. $\mathcal{U}_0(0)$ incorporates all the important medium-interactions in $\delta\Gamma_{rot}$. The overall rotation time is given by Eq. 3.21 in terms of J .

In order to use the above formalism (Eq. 3.21, 3.23), developed above for a dipolar liquid, in case of IL and ES, we calculate $\mathcal{U}_0(0)$ and I_R for these media and determine J . For dipolar solute rotation in an IL we find (see Appendix E),

$$\begin{aligned} \mathcal{U}_0^{IL}(t) = & -\sqrt{3/4\pi}(2\pi)^{-3} \left[\rho_0 \int V_{s1}^{110}(\mathbf{k}) \rho_1^{10}(\mathbf{k}, t) d\mathbf{k} + \rho_0 \int V_{sd}^{110}(\mathbf{k}) \rho_1^{10}(\mathbf{k}, t) d\mathbf{k} \right. \\ & \left. + 2\pi \int V_{s2}^{110}(\mathbf{k}) \rho_2^{10}(\mathbf{k}, t) d\mathbf{k} \right] \end{aligned} \quad (3.24)$$

where $\rho_0 = 1/4\pi$. $V_{si}^{110}(\mathbf{k})$ denotes the Fourier component of the interaction potential between the solute and the i th ionic species; $\rho_i^{10}(\mathbf{k}, t)$, the normalized projection of the local density of the i th species around the solute for spherical harmonics $l=1$ and $m=0$; and $V_{sd}^{110}(\mathbf{k})$, the Fourier component of the dipole-dipole part of the solute-IL interaction potential. Similarly, for an ES (Appendix F)

$$\mathcal{U}_0^{ES}(t) = -\sqrt{3/4\pi}(2\pi)^{-3} \left[2\pi \sum_{i=1,2} \int V_{si}^{110}(\mathbf{k}) n_i^{10}(\mathbf{k}, t) d\mathbf{k} + \rho_0 \int V_{sd}^{110}(\mathbf{k}) n_3^{10}(\mathbf{k}, t) d\mathbf{k} \right] \quad (3.25)$$

where the local ionic densities are denoted by n_i ($i=1$ for cation and 2 for anion) and density of the dipolar solvent by n_3 . Here $V_{si}^{110}(\mathbf{k})$ and $V_{sd}^{110}(\mathbf{k})$ correspond to solute-ion and solute-dipolar solvent interactions respectively.

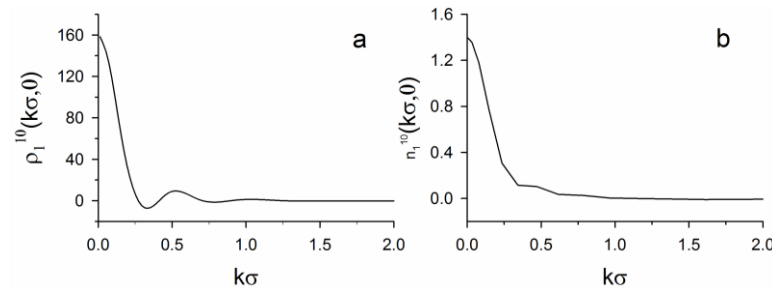


Figure 3.8: The wave vector dependent solvent density profiles around the solute. (a) IL $[\text{Im}_{41}^+][\text{PF}_6^-]$ and (b) 1M LiNO_3 in DMSO at 298 K.

We calculate the equilibrium solvent local densities using the classical DFT (Appendix G). Figure 3.8 illustrates representative density profiles in IL and ES. The panel a

shows the behaviour of the dipolar cation density $\rho_1^{10}(\mathbf{k},0)$ for $[\text{Im}_{41}^+][\text{PF}_6^-]$ around C153 (solute radius $R_0 = 3.9 \text{ \AA}$ and excited state dipole moment $\mu_0 = 14 \text{ D}$)¹²⁵. In panel b we show the cationic density profile $n_1^{10}(\mathbf{k},0)$ for 1M LiNO_3 in DMSO around C334 ($R_0 = 4.1 \text{ \AA}$ and $\mu_0 = 13 \text{ D}$)^{13, 181}.

We show the ratio $J = \delta\Gamma_{rot} / \Gamma_{rot}^{hyd}$ for C153 in dipolar-ILs in Tables 3.1 and 3.2, calculated using experimental^{23, 125} τ_s , μ_0 and R_0 . J does not exceed 1%, suggesting complete domination of Γ_{rot}^{hyd} . Due to unavailability of experimental τ_s for C334 in LiNO_3 -DMSO, we use the τ_s (2.1 ns) observed²¹ for C334 in 1M NaClO_4 -DMSO solution with similar viscosity (4.7 cP)²¹ to that of 1M LiNO_3 -DMSO (4.35 cP)¹³. Here we find a very similar $J \sim 1\%$ as in the ILs. The calculated τ_R s of C153 in ILs (Figure 3.9) are within 1% of the corresponding τ_R^{hyd} . Both the calculated and experimental τ_R depend linearly on τ_s indicating a viscosity-scaling of these average inverse rates, as observed for common dipolar solvents²⁶. In case of ES, for C334 in 1M LiNO_3 -DMSO we calculate $\tau_R = 328 \text{ ps}$, $\sim 1\%$ larger than the corresponding $\tau_R^{hyd} = 325 \text{ ps}$.

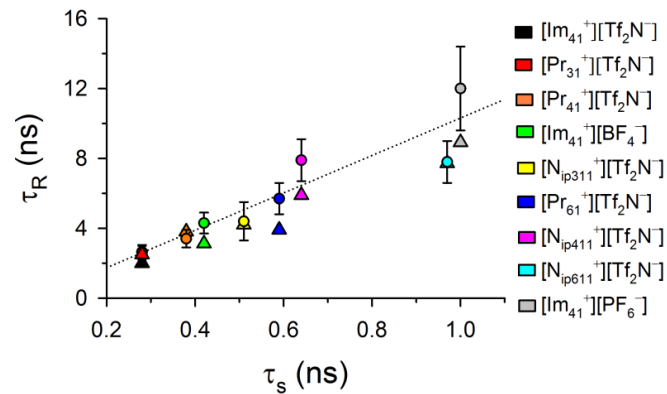


Figure 3.9: Rotation time data in ILs. The experimental (circles) τ_R with error bars and calculated (triangles) τ_R of C153 in nine ionic liquids as functions of τ_s . The dotted line represents the best linear fit through the experimental data.

In dipolar liquids also we observe very small J ($\sim 1\%$) for dipolar solute rotation²⁶. Here we find in IL and ES, even long-ranged solute-solvent electrostatic interactions fail to generate appreciable DF. The reason can be demonstrated from Eq. 30. The criterion for significant J is: $\mathcal{U}_0^{II}(0)\tau_s \gg \Gamma_{rot}^{hyd}$. Although in ILs we get ~ 10 - 100 times larger $\mathcal{U}_0^{II}(0)$ than its analogue $\mathcal{U}_0(0)$ in dipolar liquids²⁶ and much higher τ_s than that in dipolar solvents, the

product $\mathcal{U}_0^{\text{IL}}(0)\tau_s$ (Figure 3.10a) is never comparable to $\Gamma_{rot}^{\text{hyd}}$ (Figure 3.10b) which is also very large (~ 1000 times of that in dipolar liquids) due to high medium viscosity. This analysis also provides a microscopic explanation for the experimental observation that dipolar solute rotation in ILs follow essentially the same dependence on the temperature-reduced viscosity (η/T) as in the common dipolar solvents²³. For an ES at low electrolyte concentration, the ion-ordering around the solute is smaller than that in an IL (Figure 3.8) because of ion solvation by the dipolar medium. Consequently, $\mathcal{U}_0^{\text{ES}}(0)$ is quite small so that even subsequent multiplication by a large τ_s fails to make the product dominate over $\Gamma_{rot}^{\text{hyd}}$. Consequently, the Γ_{rot} for a dipolar solute in an ES appears to be similar to that in a neat dipolar medium but viscosity-scaled.

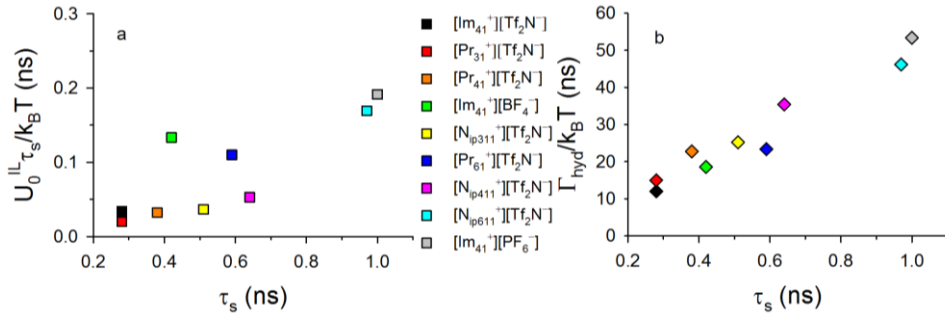


Figure 3.10: Components of friction in ILs. (a) The product $\mathcal{U}_0^{\text{IL}}(0)\tau_s/k_B T$ and (b) $\Gamma_{rot}^{\text{hyd}}/k_B T$ for C153 in nine ILs (marked in the figure by colours).

3.4 Quasi-universality of solute rotation in liquid solvents

The present calculations clearly show that the solute-solvent excluded volume and the hydrodynamic viscosity are enough to understand the rotation of a spherical solute as the long-ranged interactions get decoupled. This decoupling leads us to write, $\tau_R \approx \tau_R^{\text{hyd}} = 1/\tilde{\omega}_{av}$, where $\tilde{\omega}_{av} = \int \tilde{\omega}(k\sigma) d\mathbf{k}\sigma / \int d\mathbf{k}\sigma$. Using $\tilde{\omega}(k\sigma) = k_B T / \eta(k\sigma) V_p$ and $\eta(k\sigma) = k_B T / 4\pi r_0 D S(k\sigma)$ one can write

$$\lambda = \tau_R r_0 D / V_p = 1/4\pi S_{av} = \gamma \quad (3.26)$$

where $S_{av} = \int S(k\sigma) d\mathbf{k}\sigma / \int d\mathbf{k}\sigma$. This integral will be dominated by the peak in $S(k\sigma)$. Equation 3.26 relates experimental quantities to the microscopic solvent structure and thus constitutes a macro-micro relationship. Note, a similar relation as Eq. 3.26 can be derived from the SED expression: $\tau_R = \eta V_p / k_B T$ and Stokes-Einstein relation¹¹¹ for self-diffusion

of a tagged solvent particle: $D = k_B T / 4\pi r_0 \eta$ that $\lambda = \tau_R r_0 D / V_p = 1/4\pi$ which follows from Eq. 3.26 with $S_{av} = 1$, valid for extremely low density solvent condition.

First we calculate γ from the solvent structure factors. For ILs we calculate S_{av} from the weighted average (as in case of $\bar{\eta}$) of different peak contributions in the experimental $S_{tot}(k\sigma)$. We find for the three pyrrolidinium ILs $\gamma \sim 0.05, 0.06$ and 0.09 for $n=4, 6, 10$ respectively, while from the theoretical $S_{tot}(k\sigma)$ of the ILs, we get $\gamma \sim 0.07$. Therefore γ appears to be similar for different ILs. Nearly the same value of γ (~ 0.06) is obtained from theoretical²⁶ $S(k\sigma)$ for liquid solvents of diverse interactions like hydrocarbons (non-dipolar), aprotic dipolar liquids and alcohols (protic dipolar). In fact $\gamma \sim 0.06$ even for a purely hard sphere system indicating that γ is primarily determined by the repulsive part of the total interaction and is rather insensitive to the long-ranged interactions.

We need to estimate λ from experimental data to check its equality with γ . We consider near-spherical solutes with known τ_R in above liquid solvents and ILs. In Figure 3.11a, we show λ values for C153 as a function of τ_R in different solvents. We use \bar{r}_0 and \bar{D} to estimate λ for ILs, while r_0 , estimated from the van der Waals volumes⁸ and experimental^{152, 155, 156} D are used for common liquids. Although the range of observed τ_R in common liquids is fairly large (~ 10 - 150 ps)⁸, that of λ is quite narrow: 0.05 - 0.12 . In ILs, though the τ_R are much larger²³ λ -range is fairly narrow (0.06 - 0.10). This remarkable similarity and small spread of λ values for a single solute C153 in solvents of such diverse interactions clearly suggest a quasi-universal character of C153-rotation in liquid media.

It is interesting to check if this quasi-universality of λ holds even for non-dipolar solutes. This is important because γ is expected to be insensitive to the microscopic details of solute-solvent interactions. In Figure 3.11a, we show λ for two non-dipolar solutes PTP¹⁴ with $\lambda \sim 0.07$ - 0.14 in liquids and DMDPP¹⁴⁵ with $\lambda \sim 0.07$ - 0.08 in three ILs. Thus, the quasi-universal nature holds here as well. Some highly non-spherical solutes exhibit different regimes of this quasi-universality: $\lambda \sim 0.09$ - 0.20 for pyrenes and anthracenes in common liquids¹⁹ and $\lambda \sim 0.02$ - 0.05 for perylene¹⁴⁶ and aminoquinoline¹⁴⁷ in different ILs. These variations may be partly attributed to the shape anisotropy and could be incorporated via suitable shape-factors.

Due to the difference in partial structure factors of different components in an ES one needs to further generalize the calculations of λ and γ . Here τ_R is given by: $\tau_R = \sum_i x_i / \omega_{av,i}$ where $\omega_{av,i} = \int_{\alpha} \omega_i(k\sigma) d\mathbf{k}\sigma / \int_{\alpha} d\mathbf{k}\sigma$, for the i th component in the medium. Using $\omega_i(k\sigma) = k_B T / \eta_i(k\sigma) V_p$ and $\eta_i(k\sigma) = k_B T / 4\pi r_i D_i S_{ii}(k\sigma)$ we find

$$\lambda' = \tau_R / V_p = (1/4\pi) \sum_i x_i / r_i D_i S_{av,ii} = \gamma'. \quad (3.27)$$

which connects solute properties (τ_R and V_p) to the medium properties: structure factors and self-diffusion coefficients. Figure 3.11b shows the λ' values for C334, DMDPP and DPP¹², in LiNO₃-DMSO solutions at different concentrations c along with γ' computed for the ES at each c . As c increases from 0.1 to 1M, the observed τ_R of all three solutes^{12, 13} increases, the same trend being present in λ' . Here again, λ' at $c < 1$ M agree quite well with γ' , while the agreement worsens at higher concentrations presumably for changes in average solvent structure for the ion-pairs, triple-ions etc¹⁷⁸ appearing at such concentrations.

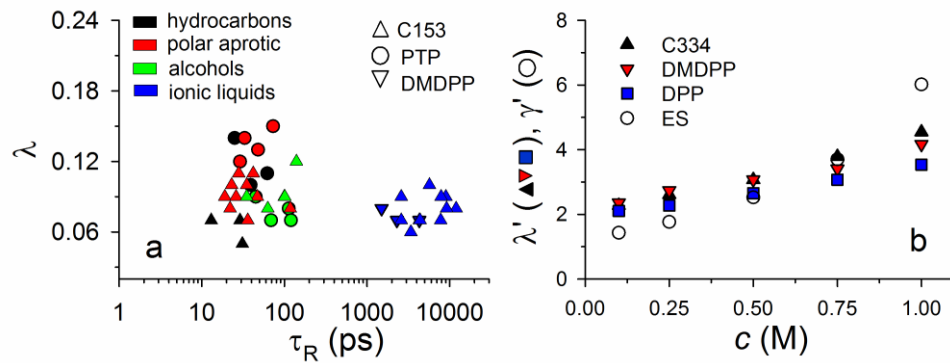


Figure 3.11: Data on λ for various solute-solvent combinations. (a) λ vs. τ_R plot for five solutes: C153, PTP (*p*-terphenyl) and DMDPP (2,5-dimethyl-1,4-dioxo-3,6-diphenylpyrrolo[3,4-*c*]pyrrole) in various liquid solvents: hydrocarbons (black), polar aprotic (red), alcohols (green) and ionic liquids (blue). (b) Plot of λ' for three solutes C334, DMDPP and DPP (1,4-dioxo-3,6-diphenylpyrrolo[3,4-*c*]pyrrole) as a function of c in solutions of LiNO₃ in DMSO at 298K along with the values of γ' for the solvent. Here λ' and γ' defined by Eq. 3.27 are made dimensionless by multiplying both with σD_3 where D_3 is the self-diffusion coefficient of the dipolar solvent and σ , the average molecular diameter of the components in ES.

3.5 Conclusion

In conclusion, in this chapter, we have developed a microscopic theory that systematically includes the effects of solute-solvent dipole-dipole interactions and solvent structure on average rotation time of a polar solute in a polar solvent. We find that the rotational relaxation of a dipolar solute in a polar medium is governed by the hydrodynamics, having little dependence on the long-ranged solute-solvent interaction. We thus provide a molecular basis for the SED model which has been obtained from purely hydrodynamic consideration.

We generalize our theory for ionic liquids and electrolyte solutions to show that decoupling of DF from solute rotation occurs even in ionic media via the non-linear dependence of DF on Γ_{rot}^{hyd} and an overwhelming domination of Γ_{rot}^{hyd} . The fact that repulsive part of the interaction largely determines the liquid structure makes solute rotation insensitive to the mean-field effect generated via the solute-solvent long-ranged interactions. This insensitivity leads to quasi-universality in solute rotation and thus provides a microscopic explanation for the experimental observation that dipolar solute rotation in ILs and ES follow the same correlation as established for common dipolar solvents. Note, the present theory considers only the solute-solvent combinations with no specific interaction (such as H-bonding). The effects of shape anisotropies of solute and solvent molecules or solution inhomogeneity are also ignored. Despite these lacunae, the present analytical scheme provides a resolution to the debate regarding the role of DF in solute rotation.

Finally, the approach described in this chapter can be extended to rotation of realistic solutes in any solvent in general. One needs to this end, a proper description of the solvent static structure factor and an appropriate solute-solvent interaction model. Generally, the solute-solvent interaction can be expressed as: $V(\mathbf{r}-\mathbf{R}, \theta, \theta') = \sum_{l_1, l_2, m} V^{l_1 l_2 m}(\mathbf{r}-\mathbf{R}) Y_{l_1}^m(\cos \theta) Y_{l_2}^m(\cos \theta')$. Inclusion of the higher harmonics ($l_1, l_2 > 1$) will take care of the contributions from the finite charge distributions over the solute and the solvent molecules systematically. Similar expressions can be written for the fluctuating solvent density and the solvent-solvent static correlations. This kind of modelling would be very similar to the extended charge distribution model¹³⁴ considered earlier. Note that the coupling parameter J depends on a competition between Γ_{rot}^{hyd} and the product $\mathcal{U}_0(0)\tau_s$. The modified treatment will affect the solute-solvent interaction strength $\mathcal{U}_0(0)$, resulting in very different value of the DF. However, the calculation scheme will be numerically quite intensive, loosing

analytical simplicity of the present one. The scenario could be simplified for an uncharged multipolar solute in a non-dipolar solvent having only higher multipole moments. The solute-solvent interaction term $V^{l_1 l_2 m}(\mathbf{r} - \mathbf{R})$ in such cases will fall off quite fast as a function of $|\mathbf{r} - \mathbf{R}|$. In such cases, the rotational friction will be dominated by the packing of the solvent around the solute.

Appendices

A. Equation of motion and orientational correlation function for solute rotation

The EOM for solute rotation can be written as

$$\Gamma_{rot} \dot{\theta} = -\frac{\partial U(\theta)}{\partial \theta} + \xi(t) \quad (3.28)$$

where $\xi(t)$ denotes the fluctuating torque arising out of all possible sources including short-ranged and long-ranged forces and the terms non-linear in θ . Here^{5, 111} $\langle \xi(t) \rangle = 0$ and $\langle \xi(t) \xi(0) \rangle = 2\Gamma_{rot} k_B T \delta(t)$. Considering the initial equilibrium distribution of the solvent around the rotating solute, we can write Eq. 3.28 in Fourier space:

$$i\omega \Gamma_{rot} \theta(\omega) = u_0 \rho_0 \rho_{10}(0) \rho_0 \theta(\omega) + \xi(\omega), \quad (3.29)$$

and subsequently

$$\langle \theta(\omega) \theta(-\omega) \rangle = \frac{2k_B T}{\Gamma_{rot} [\omega^2 + (u_0 \rho_0 \rho_{10}(0) / \Gamma_{rot})^2]}, \quad (3.30)$$

which, upon inverse Fourier transformation, becomes

$$\langle \theta(t) \theta(0) \rangle = \frac{k_B T}{u_0 \rho_0 \rho_{10}(0)} \exp \left[-\frac{u_0 \rho_0 \rho_{10}(0)}{\Gamma_{rot}} t \right]. \quad (3.31)$$

Therefore, the normalized profile for orientational correlation function for solute

$$\frac{\langle \theta(t) \theta(0) \rangle}{\langle \theta(0) \theta(0) \rangle} = \exp \left[-\frac{u_0 \rho_0 \rho_{10}(0)}{\Gamma_{rot}} t \right] \quad (3.32)$$

B. Calculation of the solute-solvent dipolar coupling factor J including contributions from beyond the first solvation shell

Here we calculate the coupling factor after considering the solvent molecules in the immediate neighbourhood and beyond. To this end, we write the average dipolar solute-solvent interaction energy as

$$U(\theta) = \int V_{dip}(|\mathbf{r} - \mathbf{R}|, \theta, \theta') \rho(\mathbf{r}, \theta', t) d\mathbf{r} d(\cos \theta') \quad (3.33)$$

where $V_{dip}(|\mathbf{r} - \mathbf{R}|, \theta, \theta')$ is space-dependent form of dipolar interaction potential between the photo-excited solute dipole and a solvent dipole, with a separation $|\mathbf{r} - \mathbf{R}|$. $\rho(\mathbf{r}, \theta', t)$ denotes the time dependent solvent density distribution. Here, \mathbf{r} and \mathbf{R} denote the position vectors of the solvent molecule and the solute molecule, respectively. Now, $V_{dip}(|\mathbf{r} - \mathbf{R}|, \theta, \theta')$ can be written as²⁵

$$V_{dip}(|\mathbf{r} - \mathbf{R}|, \theta, \theta') = -\frac{\mu_0 \mu}{|\mathbf{r} - \mathbf{R}|^3} \cos \theta \cos \theta'. \quad (3.34)$$

One can expand $V_{dip}(|\mathbf{r} - \mathbf{R}|, \theta, \theta')$ as a function of spherical harmonics¹⁸²

$$V_{dip}(|\mathbf{r} - \mathbf{R}|, \theta, \theta') = \sum_{l_1, l_2, m} V_{dip}^{l_1 l_2 m}(|\mathbf{r} - \mathbf{R}|) Y_{l_1}^m(\cos \theta) Y_{l_2}^m(\cos \theta') \quad (3.35)$$

where

$$V_{dip}^{l_1 l_2 m}(|\mathbf{r} - \mathbf{R}|) = \int V_{dip}(|\mathbf{r} - \mathbf{R}|, \theta, \theta') Y_{l_1}^m(\cos \theta) Y_{l_2}^m(\cos \theta') d(\cos \theta) d(\cos \theta'). \quad (3.36)$$

As it turns out, $V_{dip}^{110}(|\mathbf{r} - \mathbf{R}|)$ is the leading component of $V_{dip}(|\mathbf{r} - \mathbf{R}|, \theta, \theta')$ that couples with $\rho_{10}(\mathbf{r}, t)$. Therefore, we obtain for the interaction energy

$$U(\theta) = \sqrt{3/4\pi} \cos \theta \int V_{dip}^{110}(|\mathbf{r} - \mathbf{R}|) \rho_{10}(\mathbf{r}, t) d\mathbf{r} \quad (3.37)$$

using¹⁸² $Y_1^0(\cos \theta) = \sqrt{3/4\pi} \cos \theta$. Setting, $|\mathbf{R}| = 0$, implying the solute being located at the origin, we can write Eq. 3.37 in Fourier space using the Parseval's relation¹⁸²:

$$U(\theta) = \sqrt{3/4\pi} (2\pi)^{-3} \cos \theta \int V_{dip}^{110}(\mathbf{k}) \rho_{10}(\mathbf{k}, t) d\mathbf{k} \quad (3.38)$$

Eq. 3.38 can be rewritten as

$$U(\theta) = -\mathcal{U}_0(t) \cos \theta \quad (3.39)$$

where

$$\mathcal{U}_0(t) = -\sqrt{3/4\pi}(2\pi)^{-3} \int V_{dip}^{110}(\mathbf{k}) \rho_{10}(\mathbf{k}, t) d\mathbf{k}, \quad (3.40)$$

the solute-solvent interaction strength, weighted by the solvent distribution. Therefore, the torque on the rotating solute becomes

$$f(t) \approx \mathcal{U}_0(t)\theta(t) \quad (3.41)$$

in small θ limit. The autocorrelation function of $f(t)$, under the decoupling approximation:

$$\phi(t) = \frac{3\rho_b}{4\pi k_B T} (2\pi)^{-6} \int d\mathbf{k} |V_{dip}^{110}(\mathbf{k})|^2 \langle \rho_{10}(\mathbf{k}, t) \rho_{10}(-\mathbf{k}, 0) \rangle \langle \theta(t) \theta(0) \rangle \quad (3.42)$$

Here, for the solvent density modes we use $\rho_{10}(\mathbf{k}, t) = \rho_{10}(\mathbf{k}, 0) e^{-t/\tau_s}$. For the auto-correlation of the angular variable, through analysis of the equation of motion (Appendix A), we get

$$\frac{\langle \theta(t) \theta(0) \rangle}{\langle \theta(t) \theta(0) \rangle} = \exp \left[-\frac{\mathcal{U}_0(0)}{\Gamma_{rot}} t \right] \quad (3.43)$$

where $\mathcal{U}_0(0) = -\sqrt{3/4\pi}(2\pi)^{-3} \int V_{dip}^{110}(\mathbf{k}) \rho_{10}(\mathbf{k}, 0) d\mathbf{k}$. Using this normalized profile in Eq. 3.42, we arrive at

$$\phi(t) = B e^{-\lambda t} \quad (3.44)$$

where $B = \frac{3\rho_b}{4\pi k_B T} (2\pi)^{-6} \int d\mathbf{k} |V_{dip}^{110}(\mathbf{k})|^2 |\rho_{10}(\mathbf{k}, 0)|^2$ and $\lambda = \left(\frac{\mathcal{U}_0(0)}{\Gamma_{rot}} + \frac{1}{\tau_s} \right)$. Finally, we

calculate the memory function as described earlier, using Eq. 3.44 and derive the long-range part of the rotational friction:

$$\delta\Gamma_{rot} = \frac{3\rho_b}{8\pi k_B T} (2\pi)^{-6} \int d\mathbf{k} |V_{dip}^{110}(\mathbf{k})|^2 |\rho_{10}(\mathbf{k}, 0)|^2 \left(\frac{\mathcal{U}_0(0)}{\Gamma_{rot}} + \frac{1}{\tau_s} \right)^{-1}. \quad (3.45)$$

This leads to the following expression of total friction

$$\Gamma_{rot} = \Gamma_{rot}^{hyd} \left[1 + \frac{3\rho_b I_R \tau_s}{8\pi k_B T (\Gamma_{rot}^{hyd} + \mathcal{U}_0(0) \tau_s)} \right] \quad (3.46)$$

where $I_R = (2\pi)^{-6} \int d\mathbf{k} |V_{dip}^{110}(\mathbf{k})|^2 |\rho_{10}(\mathbf{k}, 0)|^2$. Therefore, the modified dipolar coupling parameter J becomes:

$$J = \frac{3\rho_b I_R \tau_s}{8\pi k_B T (\Gamma_{rot}^{hyd} + \mathcal{U}_0(0)\tau_s)} \quad (3.47)$$

C. Calculation of $\rho_{10}(\mathbf{k})$ for a dipolar liquid around the dipolar solute

To evaluate $\rho_{10}(\mathbf{k})$ we evaluate $\rho_{10}(\mathbf{r})$ using equilibrium DFT as described in Appendix B of the previous chapter. The density functional free energy $F[\rho(\mathbf{r}, \theta)]$ is given by:

$$\begin{aligned} \beta F[\rho(\mathbf{r}, \theta)] = & \int d\mathbf{r} d(\cos \theta) \rho(\mathbf{r}, \theta) \left[\ln \left(\frac{\rho(\mathbf{r}, \theta)}{\rho_b/4\pi} \right) - 1 \right] \\ & - \frac{1}{2} \int d\mathbf{r} d\mathbf{r}' d(\cos \theta) d(\cos \theta') C(|\mathbf{r} - \mathbf{r}'|, \theta, \theta') [\rho(\mathbf{r}, \theta) - \rho_b/4\pi] [\rho(\mathbf{r}', \theta') - \rho_b/4\pi] \\ & + \beta \int d\mathbf{r} d(\cos \theta) \rho(\mathbf{r}, \theta) V_{dip}(|\mathbf{r} - \mathbf{R}|, \theta = 0, \theta') \end{aligned} \quad (3.48)$$

where, $C(|\mathbf{r} - \mathbf{r}'|, \theta, \theta')$ is the two particle direct correlation function (DCF) between solvent molecules at positions \mathbf{r} and \mathbf{r}' having orientations θ and θ' . Minimization of $F[\rho(\mathbf{r}, \theta)]$, with respect to the constraint for N solvent molecules

$$\int d\mathbf{r} d(\cos \theta) \rho(\mathbf{r}, \theta) = N, \quad (3.49)$$

yields $\delta\beta F/\delta\rho + \lambda(\delta/\delta\rho)\int d\mathbf{r} d(\cos \theta) \rho(\mathbf{r}, \theta) = 0$, λ being the Lagrange's multiplier. The differentiations give

$$\begin{aligned} \ln \left(\frac{\rho(\mathbf{r}, \theta)}{\rho_b/4\pi} \right) = & \int d\mathbf{r}' d(\cos \theta') C(|\mathbf{r} - \mathbf{r}'|, \theta, \theta') \{ \rho(\mathbf{r}, \theta') - \rho_b/4\pi \} \\ & - \beta V_{dip}(|\mathbf{r} - \mathbf{R}|, \theta) - \lambda \end{aligned} \quad (3.50)$$

For small fluctuations: $[\rho(\mathbf{r}, \theta) - \rho_b/4\pi]/(\rho_b/4\pi) = \delta\rho(\mathbf{r}, \theta)/(\rho_b/4\pi) \ll 1$, Eq. 3.50 yields

$$\begin{aligned} \frac{\delta\rho(\mathbf{r}, \theta)}{\rho_b/4\pi} = & \int d\mathbf{r}' d(\cos \theta') C(|\mathbf{r} - \mathbf{r}'|, \theta, \theta') \{ \rho(\mathbf{r}, \theta') - \rho_b/4\pi \} \\ & - \beta V_{dip}(|\mathbf{r} - \mathbf{R}|, \theta) - \lambda \end{aligned} \quad (3.51)$$

Multiplying both sides of Eq. 3.51 by $Y_1^0(\cos \theta')$, integrating over $\cos \theta'$ we obtain using Eq.2.18

$$\begin{aligned} \frac{\rho_{10}(\mathbf{r})\rho_0}{\rho_b/4\pi} &= \int d\mathbf{r}' d(\cos\theta') d(\cos\theta'') Y_1^0(\cos\theta') C(|\mathbf{r}-\mathbf{r}'|, \theta', \theta'') \delta\rho(\mathbf{r}, \theta'') \\ &\quad - \beta \int d(\cos\theta') Y_1^0(\cos\theta') V_{dip}(|\mathbf{r}-\mathbf{R}|, \theta') \end{aligned} \quad (3.52)$$

Again, multiplying both sides of Eq. 3.52 by $e^{-i\mathbf{k}\cdot\mathbf{r}}$, integrating over \mathbf{r} and using the convolution theorem¹⁸²

$$\begin{aligned} \frac{\rho_{10}(\mathbf{k})\rho_0}{\rho_b/4\pi} &= \int d(\cos\theta') d(\cos\theta'') Y_1^0(\cos\theta') C(\mathbf{k}, \theta', \theta'') \rho(\mathbf{k}, \theta'') \\ &\quad - \beta \int d(\cos\theta') Y_1^0(\cos\theta') V_{dip}(\mathbf{k}, \theta') \end{aligned} \quad (3.53)$$

Here the surviving component of the Fourier mode of the DCF, $C(\mathbf{k}, \theta', \theta'')$ is given by $C^{110}(\mathbf{k}) = \int C(r, \theta', \theta'') e^{-i\mathbf{k}\cdot\mathbf{r}} Y_1^0(\cos\theta') Y_1^0(\cos\theta'') d\mathbf{r} d(\cos\theta') d(\cos\theta'')$. We can write within mean-field approximation²⁵: $C(r, \theta', \theta'') = C^{PY}(r) + C^{LR}(r)$ as in Appendix A of chapter 2. $C^{LR}(r)$ is obtained by angle-averaging of $C^{LR}(r, \theta', \theta'') = (\beta\mu^2/r^3) \cos\theta' \cos\theta''$, denoting the long-ranged part²⁵. Finally, we get from Eq. 3.53,

$$\frac{\rho_{10}(\mathbf{k})\rho_0}{\rho_b/4\pi} = (\rho_0/2\pi) C^{110}(\mathbf{k}) \rho_{10}(\mathbf{k}) - \beta V_{dip}^{10}(\mathbf{k}) \quad (3.54)$$

where $V_{dip}^{10}(\mathbf{k}) = \sqrt{3\pi} V_{dip}^{110}(\mathbf{k})$. Rearrangement of Eq. 3.54 leads to

$$\rho_{10}(\mathbf{k}) = \frac{-\rho_b \beta V_{dip}^{10}(\mathbf{k})}{1 - \rho_b C^{110}(\mathbf{k})/8\pi^2} \quad (3.55)$$

D. Calculation of the Static structure factors

(i) Ionic liquid

We model an IL as a binary mixture of hard spheres (HS)¹⁸³, each with a charge embedded at the centre. For a dipolar ion, there is an additional dipole at the centre of the HS. The spatial direct correlation function^{111, 112} (SDCF) between the i th and j th ion ($i=1$ for cation, 2 for anion) can be written as: $C_{ij}(r) = C_{ij}^{PY}(r) + C_{ij}^{LR}(r)$, where $C_{ij}^{PY}(r)$ is the hard core part given by the Percus-Yevick form for binary mixture of hard spheres¹⁸³ and $r = |\mathbf{r}_i - \mathbf{r}_j|$. The long-ranged part $C_{ij}^{LR}(r)$ is treated at the mean-field level¹¹¹. For simple

ions: $C_{ij}^{LR}(r) = -\beta q_i q_j / \epsilon r$, the standard Coulombic form. For the dipolar ions with dipole moment μ we write $C_{ij}^{LR}(r) = -\beta q_i q_j / \epsilon r + 2\beta^2 \mu^4 / 9\epsilon r^6$, q_i , the charge on the i th ion and ϵ , the dielectric constant of the medium. Here the second term denotes the dipolar part calculated as in Appendix A of chapter 2. For the ion-dipole interactions $C_{ij}^{LR}(r) = \beta q_i \mu / 3\pi\epsilon r^2$, the projections of standard ion-dipole interaction potential¹⁸⁴ $v_{ij}(r) = -(q_i \mu / \epsilon r^2) \cos \theta \cos \theta'$ between the i th ion with polar angle θ and j th dipolar ion with orientation θ' (both in the laboratory frame) for spherical harmonics $l_1 = 1$, $l_2 = 1$ and $m = 0$. From $C_{ij}(r)$ we calculate $C_{ij}(k\sigma)$ and hence $S_{ij}(k\sigma)$, the partial structure factors using the OZ relation^{2,3}. The total static structure factor is then obtained as: $S_{tot}(k\sigma) = \sum_{i,j} \sqrt{x_i x_j} S_{ij}(k\sigma)$ where x_i is the mole fraction of the i th ion.

(ii) Electrolyte solution

We model the solution of a 1:1 electrolyte to be a ternary mixture, the components being the cations, the anions and the dipolar solvent molecules. The mole-fractions of the ions are the same to maintain electro-neutrality. We label the components in the following fashion: the cations as 1, the anions as 2 and the dipoles as 3. For salt concentrations 0.1M to 1M, the ionic mole-fractions turn out to be $\sim 0.001-0.01$. As a result, the hard core contributions are negligible to ionic SDCFs $C_{ij}(r)$ ($i, j = 1, 2$), owing to very small packing fraction p . Here we use the hypernetted chain closure by Attard et al¹⁸⁵ to calculate the ionic SDCFs, via solving the OZ relation. We use the asymptotic form¹⁸⁵ of total correlation function $h_{ij}(r) = -\beta q_i q_j e^{-\kappa r} / \epsilon r$. Here, $\kappa = \kappa_D \left[1 - (\kappa_D \sigma)^2 / 2 + (\kappa_D \sigma)^3 / 6 \right]^{-1/2}$, the modified screening length in terms of the inverse Debye screening length¹¹¹ $\kappa_D = \left[(4\pi\beta / \epsilon) \sum_i c_i q_i^2 \right]^{1/2}$ where σ is the average molecular diameter of the components in ES and c_i , the concentration of the i th ion. The SDCFs for ion-dipole ($i, j = 1, 3$) and the dipole-dipole interactions ($i, j = 3$) are calculated as described in previous section. The hard sphere part $C_{ij}^{HS}(r)$ are adopted from the work by Hoshino et al¹⁷⁷ on structure factors for a ternary mixture of hard spheres. $S_{ij}(k\sigma)$ s are calculated using the method for ternary mixtures described in Hoshino et al¹⁷⁷.

E. Calculation of dielectric friction

(i) Ionic liquid

For an IL made of dipolar cation ($i=1$) and simple anion ($i=2$), the average solute-solvent interaction energy can be written, via an extension of Eq.3.37, as,

$$U(\theta) = \sqrt{3/4\pi} \cos \theta \left[\rho_0 \int V_{s1}^{110}(\mathbf{r} - \mathbf{R}) \rho_1^{10}(\mathbf{r}, t) d\mathbf{r} + \rho_0 \int V_{sd}^{110}(\mathbf{r} - \mathbf{R}) \rho_1^{10}(\mathbf{r}, t) d\mathbf{r} \right. \\ \left. + 2\pi \int V_{s2}^{110}(\mathbf{r} - \mathbf{R}) \rho_2^{10}(\mathbf{r}, t) d\mathbf{r} \right] \quad (3.56)$$

where $V_{si}^{110}(\mathbf{r} - \mathbf{R})$ denotes the leading component of the interaction potential between the dipolar solute and the i th ionic species in the medium; and $V_{sd}^{110}(\mathbf{r} - \mathbf{R})$, the same between dipolar solute and a dipolar ion. Setting, $|\mathbf{R}| = 0$, we can write Eq. 3.56 in Fourier space:

$$U(\theta) = \sqrt{3/4\pi} (2\pi)^{-3} \cos \theta \left[\rho_0 \int V_{s1}^{110}(\mathbf{k}) \rho_1^{10}(\mathbf{k}, t) d\mathbf{k} + \rho_0 \int V_{sd}^{110}(\mathbf{k}) \rho_1^{10}(\mathbf{k}, t) d\mathbf{k} \right. \\ \left. + 2\pi \int V_{s2}^{110}(\mathbf{k}) \rho_2^{10}(\mathbf{k}, t) d\mathbf{k} \right] \quad (3.57)$$

Eq. 3.57 can be expressed as

$$U(\theta) = -\mathcal{U}_0^{\text{IL}}(t) \cos \theta \quad (3.58)$$

where

$$\mathcal{U}_0^{\text{IL}}(t) = -\sqrt{3/4\pi} (2\pi)^{-3} \left[\rho_0 \int V_{s1}^{110}(\mathbf{k}) \rho_1^{10}(\mathbf{k}, t) d\mathbf{k} + \rho_0 \int V_{sd}^{110}(\mathbf{k}) \rho_1^{10}(\mathbf{k}, t) d\mathbf{k} \right. \\ \left. + 2\pi \int V_{s2}^{110}(\mathbf{k}) \rho_2^{10}(\mathbf{k}, t) d\mathbf{k} \right] \quad (3.59)$$

the time dependent solute-solvent interaction strength, weighted by the solvent distribution.

Therefore, the torque on the rotating solute given by $f(t) = -\partial U(\theta)/\partial \theta$ becomes

$$f(t) \approx \mathcal{U}_0^{\text{IL}}(t) \theta(t) \quad (3.60)$$

in small θ limit. The autocorrelation function of $f(t)$, under the decoupling approximation:

$$\phi(t) = \frac{\langle \mathcal{U}_0^{\text{IL}}(t) \mathcal{U}_0^{\text{IL}}(0) \rangle \langle \theta(t) \theta(0) \rangle}{I k_B T} \quad (3.61)$$

where I denotes the moment of inertia of the rotating body about the axis of rotation. We now calculate $\langle \mathcal{U}_0^{\text{IL}}(t) \mathcal{U}_0^{\text{IL}}(0) \rangle$ and $\langle \theta(t) \theta(0) \rangle$ separately. We write

$$\begin{aligned}
\langle \mathcal{U}_0^{\text{IL}}(t) \mathcal{U}_0^{\text{IL}}(0) \rangle &= \frac{3\rho_b}{4\pi I k_B T} (2\pi)^{-6} \times \\
&\left\langle \left(\int d\mathbf{k} [\rho_0 V_{s1}^{110}(\mathbf{k}) \rho_1^{10}(\mathbf{k}, t) + \rho_0 V_{sd}^{110}(\mathbf{k}) \rho_1^{10}(\mathbf{k}, t) + 2\pi V_{s2}^{110}(\mathbf{k}) \rho_2^{10}(\mathbf{k}, t)] \right) \right. \\
&\times \left. \left(\int d\mathbf{k}' [\rho_0 V_{s1}^{110}(\mathbf{k}') \rho_1^{10}(\mathbf{k}', t) + \rho_0 V_{sd}^{110}(\mathbf{k}') \rho_1^{10}(\mathbf{k}', t) + 2\pi V_{s2}^{110}(\mathbf{k}') \rho_2^{10}(\mathbf{k}', t)] \right) \right\rangle \quad (3.62)
\end{aligned}$$

Here, for the solvent density modes we use $\rho_i^{10}(\mathbf{k}, t) = \rho_i^{10}(\mathbf{k}, 0) e^{-t/\tau_s}$ to get

$$\langle \mathcal{U}_0^{\text{IL}}(t) \mathcal{U}_0^{\text{IL}}(0) \rangle = \frac{3\rho_b I_R}{4\pi I k_B T} e^{-t/\tau_s} \quad (3.63)$$

where I_R contains all the self- and cross-terms in Eq. 3.62 resulting from the multiplication. Using the EOM (Eq.3.28) we arrive at

$$\frac{\langle \theta(t) \theta(0) \rangle}{\langle \theta(0) \theta(0) \rangle} = \exp \left[-\frac{\mathcal{U}_0^{\text{IL}}(0)}{\Gamma_{rot}} t \right] \quad (3.64)$$

The rest of the treatment is similar to that for the dipolar liquids²⁶ once all the multicomponent contributions are accounted for in I_R . We get the DF

$$\delta \Gamma_{rot} = \frac{3\rho_b I_R}{8\pi k_B T} \left(\frac{\mathcal{U}_0^{\text{IL}}(0)}{\Gamma_{rot}} + \frac{1}{\tau_s} \right)^{-1} \quad (3.65)$$

Eq. 3.65 portrays the self-consistency for $\delta \Gamma_{rot}$ as $\Gamma_{rot} = \Gamma_{rot}^{hyd} + \delta \Gamma_{rot}$. Solution of Eq. 3.65 leads to the following expression of total friction

$$\Gamma_{rot} = \Gamma_{rot}^{hyd} \left[1 - \frac{3\rho_b I_R \tau_s}{8\pi k_B T (\Gamma_{rot}^{hyd} + \mathcal{U}_0^{\text{IL}}(0) \tau_s)} \right]^{-1} \quad (3.66)$$

We find that $J = (3\rho_b I_R \tau_s / 8\pi k_B T) [\Gamma_{rot}^{hyd} + \mathcal{U}_0^{\text{IL}}(0) \tau_s]^{-1} \ll 1$ for all the ILs and hence we can linearize Eq. 3.66 to write

$$\Gamma_{rot} = \Gamma_{rot}^{hyd} [1 + J]. \quad (3.67)$$

Hence, $\delta \Gamma_{rot} = \Gamma_{rot} - \Gamma_{rot}^{hyd} = J \Gamma_{rot}^{hyd}$.

(ii) Electrolyte solution

In this case, we have three components: cation, anion and the dipolar liquid. Therefore, the average solute-solvent interaction energy is given in Fourier space by

$$U(\theta) = \sqrt{3/4\pi}(2\pi)^{-3} \cos \theta \left[2\pi \int V_{s1}^{110}(\mathbf{k}) n_1^{10}(\mathbf{k}, t) d\mathbf{k} + 2\pi \int V_{s2}^{110}(\mathbf{k}) n_2^{10}(\mathbf{k}, t) d\mathbf{k} \right. \\ \left. + \rho_0 \int V_{sd}^{110}(\mathbf{k}) n_3^{10}(\mathbf{k}, t) d\mathbf{k} \right] \quad (3.68)$$

Here $V_{si}^{110}(\mathbf{k})$ and $V_{sd}^{110}(\mathbf{k})$ denote the Fourier components of the dipole-ion part and dipole-dipole part of the solute-solvent interactions, respectively. Note, here we use n_i instead of ρ_i to denote the densities of the components. Equation 3.68 can readily be written as

$$U(\theta) = -\mathcal{U}_0^{\text{ES}}(t) \cos \theta \quad (3.69)$$

where

$$\mathcal{U}_0^{\text{ES}}(t) = -\sqrt{3/4\pi}(2\pi)^{-3} \left[2\pi \sum_{i=1,2} \int V_{si}^{110}(\mathbf{k}) n_i^{10}(\mathbf{k}, t) d\mathbf{k} + \rho_0 \int V_{sd}^{110}(\mathbf{k}) n_3^{10}(\mathbf{k}, t) d\mathbf{k} \right] \quad (3.70)$$

The rest of the calculation is similar to that for IL to arrive at the same expression of DF as Eq. 3.65 where the quantities that would be different are $\mathcal{U}_0^{\text{ES}}(t)$ and I_R .

E. Calculation of equilibrium solvent density profiles around solute

(i) Ionic liquid

We get $\rho_i^{10}(\mathbf{r})$ from DFT treatment similar as Appendix B. The free energy $F[\rho_i(\mathbf{r}, \theta')]$, is given by

$$\beta F[\rho_i(\mathbf{r}, \theta')] = \int d\mathbf{r} d(\cos \theta') \rho_1(\mathbf{r}, \theta') \left[\ln \left(\frac{\rho_1(\mathbf{r}, \theta')}{\rho_b/4\pi} \right) - 1 \right] + \int d\mathbf{r} d(\cos \theta') \rho_2(\mathbf{r}, \theta') \left[\ln \left(\frac{\rho_2(\mathbf{r}, \theta')}{\rho_b} \right) - 1 \right] \\ - \frac{1}{2} \int d\mathbf{r} d\mathbf{r}' d(\cos \theta') d(\cos \theta'') C_{11}^{d-d}(|\mathbf{r} - \mathbf{r}'|, \theta', \theta'') \delta\rho_1(\mathbf{r}, \theta') \delta\rho_1(\mathbf{r}', \theta'') \\ - \frac{1}{2} \sum_{i,j \geq 1} \int d\mathbf{r} d\mathbf{r}' d(\cos \theta') d(\cos \theta'') C_{ij}^{i-i}(|\mathbf{r} - \mathbf{r}'|, \theta', \theta'') \delta\rho_i(\mathbf{r}, \theta') \delta\rho_j(\mathbf{r}', \theta'') \\ - \frac{1}{2} \int d\mathbf{r} d\mathbf{r}' d(\cos \theta') d(\cos \theta'') C_{11}^{i-d}(|\mathbf{r} - \mathbf{r}'|, \theta', \theta'') \delta\rho_1(\mathbf{r}, \theta') \delta\rho_1(\mathbf{r}', \theta'') \\ - \frac{1}{2} \int d\mathbf{r} d\mathbf{r}' d(\cos \theta') d(\cos \theta'') C_{12}^{i-d}(|\mathbf{r} - \mathbf{r}'|, \theta', \theta'') \delta\rho_1(\mathbf{r}, \theta') \delta\rho_2(\mathbf{r}', \theta'') \\ + \beta \int d\mathbf{r} d(\cos \theta') \rho_1(\mathbf{r}, \theta') V_{s1}(|\mathbf{r} - \mathbf{R}|, \theta = 0, \theta') + \beta \int d\mathbf{r} d(\cos \theta') \rho_2(\mathbf{r}, \theta') V_{s2}(|\mathbf{r} - \mathbf{R}|, \theta = 0, \theta') \\ + \beta \int d\mathbf{r} d(\cos \theta') \rho_1(\mathbf{r}, \theta') V_{sd}(|\mathbf{r} - \mathbf{R}|, \theta = 0, \theta') \quad (3.71)$$

where $\delta\rho_1(\mathbf{r},\theta') = [\rho_1(\mathbf{r},\theta') - \rho_b/4\pi]$ and $\delta\rho_2(\mathbf{r},\theta') = [\rho_2(\mathbf{r},\theta') - \rho_b]$, the superscripts denoting the solvent-solvent interaction types: $d-d$ (dipole-dipole), $i-i$ (ion-ion) and $i-d$ (ion-dipole). Note, for $i=2$, the polar angle $\theta'=0$ since it has no dipole where $\rho_i^{10}(\mathbf{r})$ is defined by the polar angle associated with the radius vector. Minimization of $F[\rho_i(\mathbf{r},\theta')]$, with respect to the constraints

$$\int d\mathbf{r}d(\cos\theta')\rho_i(\mathbf{r},\theta') = N_i, \quad (3.72)$$

where N_i is the number of i th ion type in medium ($N_1=N_2$ for electroneutrality) yields two separate equations for two species. For the dipolar cation:

$$\delta\beta F/\delta\rho_1 + \lambda_1(\delta/\delta\rho_1)\int d\mathbf{r}d(\cos\theta')\rho_1(\mathbf{r},\theta') = 0, \quad (3.73)$$

λ_1 being the Lagrange's multiplier for species 1, which in limit $\delta\rho(\mathbf{r},\theta')/(\rho_b/4\pi) \ll 1$ yields

$$\begin{aligned} \ln\left(\frac{\rho_1(\mathbf{r},\theta')}{\rho_b/4\pi}\right) &\approx \frac{\delta\rho_1(\mathbf{r},\theta')}{\rho_b/4\pi} = \int d\mathbf{r}'d(\cos\theta'')C_{11}^{d-d}(|\mathbf{r}-\mathbf{r}'|,\theta'',\theta'')\delta\rho_1(\mathbf{r}',\theta'') \\ &+ \int d\mathbf{r}'d(\cos\theta'')C_{11}^{i-i}(|\mathbf{r}-\mathbf{r}'|,\theta'',\theta'')\delta\rho_1(\mathbf{r}',\theta'') + \frac{1}{2}\int d\mathbf{r}'d(\cos\theta'')C_{12}^{i-i}(|\mathbf{r}-\mathbf{r}'|,\theta'',\theta'')\delta\rho_2(\mathbf{r}',\theta'') \\ &+ \int d\mathbf{r}'d(\cos\theta'')C_{11}^{i-d}(|\mathbf{r}-\mathbf{r}'|,\theta'',\theta'')\delta\rho_1(\mathbf{r}',\theta'') + \frac{1}{2}\int d\mathbf{r}'d(\cos\theta'')C_{12}^{i-d}(|\mathbf{r}-\mathbf{r}'|,\theta'',\theta'')\delta\rho_2(\mathbf{r}',\theta'') \\ &- \beta V_{s1}(|\mathbf{r}-\mathbf{R}|,\theta=0,\theta') - \beta V_{sd}(|\mathbf{r}-\mathbf{R}|,\theta=0,\theta') - \lambda_1. \end{aligned} \quad (3.74)$$

Using the definitions in Eq. 2.18 for $\rho^{10}(\mathbf{r})$ and Eq. 3.36 for $C^{110}(|\mathbf{r}-\mathbf{R}|)$ in Eq. 3.74 we obtain:

$$\begin{aligned} \rho_1^{10}(\mathbf{r}) &= \frac{2}{3}\rho_b\sqrt{3/4\pi}\left[\int d\mathbf{r}'C_{11}^{d-d,110}(|\mathbf{r}-\mathbf{r}'|)\rho_1^{10}(\mathbf{r}') + \int d\mathbf{r}'C_{11}^{i-d,110}(|\mathbf{r}-\mathbf{r}'|)\rho_1^{10}(\mathbf{r}') \right. \\ &\left. + \frac{1}{2}\int d\mathbf{r}'C_{12}^{i-d,110}(|\mathbf{r}-\mathbf{r}'|)\rho_2^{10}(\mathbf{r}') - \beta V_{s1}^{10}(|\mathbf{r}-\mathbf{R}|) - \beta V_{sd}^{10}(|\mathbf{r}-\mathbf{R}|)\right] \end{aligned} \quad (3.75)$$

Next, in a similar fashion from Eq. 3.71 and 3.72 we can write for the anion

$$\delta\beta F/\delta\rho_2 + \lambda_2(\delta/\delta\rho_2)\int d\mathbf{r}d(\cos\theta')\rho_2(\mathbf{r},\theta') = 0, \quad (3.76)$$

λ_2 being the Lagrange's multiplier for the anionic species. Equation 3.76 gives us, through the same analysis as described above for the cation that

$$\rho_2^{10}(\mathbf{r}) = \frac{2}{3} \rho_b \sqrt{3/4\pi} \left[\frac{1}{2} \int d\mathbf{r}' C_{12}^{i-d,110}(|\mathbf{r}-\mathbf{r}'|) \rho_1^{10}(\mathbf{r}') - \beta V_{s2}^{10}(|\mathbf{r}-\mathbf{R}|) \right] \quad (3.77)$$

Now, Eq. 3.75 and 3.77 are self-consistent equations for $\rho_1^{10}(\mathbf{r})$ and $\rho_2^{10}(\mathbf{r})$ respectively which are solved iteratively using the appropriate DCFs. Finally, Fourier transform gives the $\rho_i^{10}(\mathbf{k})$ s.

(ii) Electrolyte solution

For an ES, we can write down the free energy functional as

$$\begin{aligned} \beta F[n_i(\mathbf{r}, \theta')] &= \sum_{i=1,2} \int d\mathbf{r} d(\cos \theta') n_i(\mathbf{r}, \theta') \left[\ln \left(\frac{n_i(\mathbf{r}, \theta')}{n_i^b} \right) - 1 \right] + \int d\mathbf{r} d(\cos \theta') n_3(\mathbf{r}, \theta') \left[\ln \left(\frac{n_3(\mathbf{r}, \theta')}{n_3^b / 4\pi} \right) - 1 \right] \\ &\quad - \frac{1}{2} \sum_{i,j=1,2(i \neq j)} \int d\mathbf{r} d\mathbf{r}' d(\cos \theta') d(\cos \theta'') C_{ij}^{i-i}(|\mathbf{r}-\mathbf{r}'|, \theta', \theta'') \delta n_i(\mathbf{r}, \theta') \delta n_j(\mathbf{r}', \theta'') \\ &\quad - \frac{1}{2} \int d\mathbf{r} d\mathbf{r}' d(\cos \theta') d(\cos \theta'') C_{33}^{d-d}(|\mathbf{r}-\mathbf{r}'|, \theta', \theta'') \delta n_3(\mathbf{r}, \theta') \delta n_3(\mathbf{r}', \theta'') \\ &\quad - \frac{1}{2} \sum_{i=1,2} \int d\mathbf{r} d\mathbf{r}' d(\cos \theta') d(\cos \theta'') C_{i3}^{i-d}(|\mathbf{r}-\mathbf{r}'|, \theta', \theta'') \delta n_i(\mathbf{r}, \theta') \delta n_3(\mathbf{r}', \theta'') \\ &\quad + \beta \sum_{i=1,2} \int d\mathbf{r} d(\cos \theta') n_i(\mathbf{r}, \theta') V_{si}(|\mathbf{r}-\mathbf{R}|, \theta = 0, \theta') \\ &\quad + \beta \int d\mathbf{r} d(\cos \theta') n_3(\mathbf{r}, \theta') V_{sd}(|\mathbf{r}-\mathbf{R}|, \theta = 0, \theta') \end{aligned} \quad (3.78)$$

where $\delta n_i(\mathbf{r}, \theta') = [n_i(\mathbf{r}, \theta') - n_i^b]$ for the ions ($i=1,2$) and $\delta n_3(\mathbf{r}, \theta') = [n_3(\mathbf{r}, \theta') - n_3^b / 4\pi]$ for the dipolar solvent with n_i^b being the bulk density for the i th species. The minimization conditions:

$$\int d\mathbf{r} d(\cos \theta') \rho_i(\mathbf{r}, \theta') = N_i, \quad \text{for the ions where } N_1 = N_2 \quad (3.79)$$

$$\text{and,} \quad \int d\mathbf{r} d(\cos \theta') n_3(\mathbf{r}, \theta') = N_d \quad \text{for the dipolar solvent} \quad (3.80)$$

Minimization of free energy with respect to the constraints in Eq. 3.79 and 3.80 gives:

$$\delta \beta F / \delta n_i + \lambda_i (\delta / \delta n_i) \int d\mathbf{r} d(\cos \theta') n_i(\mathbf{r}, \theta') = 0, \quad \text{for } i = 1, 2, 3 \quad (3.81)$$

λ_i being the Lagrange's multiplier for i th species. Rest of the treatment is very similar to the IL case. We finally arrive at the following self-consistent expressions for the local densities:

$$n_i^{10}(\mathbf{r}) = \frac{2}{3} n_i^b \sqrt{3/4\pi} \left[\frac{1}{2} \int d\mathbf{r}' C_{i3}^{i-d,110}(\mathbf{r}-\mathbf{r}') n_3^{10}(\mathbf{r}') - \beta V_{si}^{10}(|\mathbf{r}-\mathbf{R}|) \right] \quad \text{for } i = 1, 2 \quad (3.82)$$

and

$$n_3^{10}(\mathbf{r}) = \frac{2}{3} n_3^b \sqrt{3/4\pi} \left[\int d\mathbf{r}' C_{33}^{d-d,110}(\mathbf{r}-\mathbf{r}') n_3^{10}(\mathbf{r}') + \frac{1}{2} \sum_{i=1,2} \int d\mathbf{r}' C_{i3}^{i-d,110}(\mathbf{r}-\mathbf{r}') n_i^{10}(\mathbf{r}') - \beta V_{sd}^{10}(|\mathbf{r}-\mathbf{R}|) \right] \quad (3.83)$$

Using DCFs obtained in Appendix C-(ii), we solve Eq. 3.82 and 3.83 in iterative manner to obtain the spatial $n_i^{10}(\mathbf{r})$ and the Fourier components $n_i^{10}(\mathbf{k})$. Here we have used an average molecular diameter for all the components for simplicity.

Chapter 4 Solvation dynamics in fluids under nano-meter scale confinement

4.1 Introduction

Recently fluids in nanometer (nm) scale confinements have drawn considerable attention as important media in various branches of science and technology^{37, 38, 40-43}. Several experiments focus on the dimensional crossover from 3D to 2D behaviour, observed when a fluid is kept under a confinement of about a nm. In an enclosed environment many static and dynamic properties of the fluid alter dramatically⁴⁴ compared to the bulk, like self-diffusion, refractive index, mechanical relaxation and so on. Such changes lead to confinement-induced effects on physical and chemical processes in fluid phase.

Confined water has been quite extensively studied in the recent past: Surface force measurements show that water molecules confined to a film of three to four molecular diameters (\sim a nm) thickness, undergo ordering similar to a solid⁴⁷. The mechanical relaxation timescale, for dissipating the stress against an external strain, becomes almost an order of magnitude larger⁴⁷ compared to the corresponding bulk value under a confinement less than a nm. The melting temperature of water drops significantly when confined in silica nano-pores of diameter \sim 3 nm as revealed by Raman scattering measurements¹⁸⁶. Water confined in reverse micelles (RM) of diameter \sim nm has a static dielectric constant (ϵ_0) 3-4 times lower¹⁸⁷ than the bulk value (\sim 80)³⁵. Sudden jumps in the viscosity η and diffusion coefficient D have been observed³³ in case of linear alkanes and alcohols in organosilicate nano-pores of diameter less than 2 nm. Measurements of refractive index (n) and the equilibrium film-thickness of cyclohexane confined within two mica plates have shown a sudden transition from a 3D bulk fluid to a 2D adsorbate for plate separation around couple of nm. This transition is accompanied with significant enhancement in fluctuations of n , changes in phase-transition temperatures and normalized enthalpies, lowering of critical temperature and anomalous fast self diffusion⁴⁶. However, the changes in fluid properties under confinement depend on the nature of the confining potential. Li et al⁴⁸ have studied water in sub-nanometer confinements where the viscosity increases substantially in a hydrophilic environment but having not so much effect in a hydrophobic confinement. There have been a number of theoretical studies on confinement induced effects. Schoen and co-workers¹⁸⁸ have reported on extensive grand-canonical Monte-Carlo (GCMC) simulation¹²³ to calculate static properties of confined fluid and shows their sensitivity to the wall structure. A weighted density functional theory of a 2D fluid has also been derived¹⁸⁹ as a limiting case

of the corresponding functional for an inhomogeneous 3D fluid within linearized approximation. The 3D to 2D crossover under confinement has been studied extensively near the critical point¹⁹⁰⁻¹⁹². However, the question how the confinement-induced crossover takes place in various fluid properties, even far from critical point, has remained largely unaddressed.

The rates of various non-equilibrium processes are also highly affected in confined media. Solvation is one such process which governs nearly all chemical reactions in fluid-phase^{45, 50}. Any stabilizing interaction leading to the organization of the solvent molecules around a solute is conventionally termed as solvation. Therefore, study of solvation dynamics (SD) under confinement is extremely important for understanding chemical reactions in confined media, ranging from catalysis in nanopores³⁷ to charge-transfer in biomolecules¹⁹³.

Conventionally, SD is studied via monitoring the relaxation of solvent distribution around the solute after a perturbation of the solute-solvent interaction^{30, 45, 53, 194} from an existing equilibrium solvated state. The solvent response to the perturbation is given by¹²⁴

$$S(t) = \frac{\Delta\bar{U}(t) - \Delta\bar{U}(\infty)}{\Delta\bar{U}(0) - \Delta\bar{U}(\infty)}. \quad (4.1)$$

Here

$$\Delta\bar{U}(t) = \int d^3r [U_{pert}(\mathbf{r} - \mathbf{R})\rho(\mathbf{r}, t) - U_{unpert}(\mathbf{r} - \mathbf{R})\rho(\mathbf{r}, t = 0)]. \quad (4.2)$$

where $U_{unpert}(\mathbf{r} - \mathbf{R})$ and $U_{pert}(\mathbf{r} - \mathbf{R})$ are the interaction potentials between the solute at position \mathbf{R} and a solvent molecule at position \mathbf{r} before and after the perturbation. $\rho(\mathbf{r}, t)$ is the time-dependent local solvent density¹²⁴ around the solute particle. Eq. 4.2 can be rewritten as:

$$\begin{aligned} \Delta\bar{U}(t) = \int d^3r \{ & U_{pert}(\mathbf{r} - \mathbf{R})[\rho(\mathbf{r}, t) - \rho(\mathbf{r}, t = 0)] \\ & - [U_{unpert}(\mathbf{r} - \mathbf{R}) - U_{pert}(\mathbf{r} - \mathbf{R})]\rho(\mathbf{r}, t = 0) \}. \end{aligned} \quad (4.3)$$

Simple hydrodynamic results¹¹¹ show that the Fourier components of $[\rho(\mathbf{r}, t) - \rho(\mathbf{r}, t = 0)]$ decay as $\exp[-Dk^2t]$ for wave vector k . Consequently, the solvent relaxation represented by $S(t)$ shows typical exponential dependence¹²⁴, $\exp[-t/\tau]$, τ being the solvation timescale, governed primarily by D . Since D is dramatically altered in confinement, SD also is affected by confinement. Several studies exist on SD of fluorescent dyes in confined fluids. The confining frameworks have been diverse^{30, 45, 195, 196}, for instance, solvophilic lipid vesicles

and RM¹⁹⁴; and solvophobic carbon nanotubes³⁷, sol-gel glasses¹⁹⁷ and silica nano-pores⁵². In a bulk fluid τ is generally tens of ps⁴⁵, whereas in solvophilic nanoconfinements^{30, 45}, τ may extend from hundreds of ps to even ns. For instance, the longest timescale for a dye coumarin 480 turns out to be about 10 ns in spherical water-pools of aqueous AOT (dioctyl sodium sulfosuccinate) RMs (solvophilic) of 1-10 nm diameter¹⁹⁸, in sharp contrast to a sub-ps solvation timescale observed for the same dye in bulk water¹⁹⁹. The solvation time for coumarin dyes increase typically by factor of 2 to 3 in solvophobic nanopores^{196, 200}. Recent computer simulations⁵¹⁻⁵³ also show such slowing of the SD in various confined systems compared to the bulk. Although these studies bring out various aspects of solvation in confinement in details, there is, as yet, no general understanding of how the confinement-induced changes in solvent properties bring about the slowing down of SD under confinement.

The effects of confinement become severe when the thermodynamic condition of the surrounding bulk fluid falls in the sub-critical region of the phase diagram (Figure 1.2). It is well known that presence of any surface drastically alters the phase behaviour of a sub-critical fluid⁶². If a solvophobic surface is placed in a bulk sub-critical liquid, close to the liquid-gas phase coexistence, it stabilizes the coexisting low density gas-phase in vicinity of the surface. This surface-mediated evaporation in a solvophobic pore is commonly known as capillary drying⁶¹. The diffusion of the fluid molecules becomes much faster in a dried solvophobic pore compared to the surrounding bulk liquid. On the other hand, a solvophilic surface, placed in the bulk gas, induces the high density coexisting liquid phase near the surface. This surface-mediated wetting inside a pore is called the capillary condensation⁶⁸ which slows down the fluid diffusion. The typical interfacial width between the gas and the liquid phases induced by surfaces near the bulk phase-coexistence extends to several nms^{201, 202} that becomes comparable to the size of the nanoconfinement. If a solvophilic solute particle is inserted in a dried solvophobic nanoscale pore, the solute tends to wet the pore, posing a competition^{62, 203, 204} with the wall-mediated drying. This competition decides the fluid diffusion in the pore which in turn affects the SD. Therefore, the studies on how the SD responds to this competition would throw light on surface-induced effects on various physical and chemical processes in a sub-critical nanoconfined solvent. Despite many applications⁵⁶⁻⁵⁸ of the sub-critical liquids and several studies on capillary drying and condensation phenomena^{55, 59-63}, there have not been many attempts to elucidate the roles of sub-critical solvents in solvation process. Recent MD simulations⁶⁴ on SD in a bulk Stockmayer fluid show that the density of the sub-critical fluid phase controls the solvation behaviour. Thus,

SD under confinement near bulk phase-coexistence has remained largely unexplored to the best of our knowledge.

In this chapter we study the three different aspects of nanoconfined fluids. First we study, using computer simulations, the dimensional crossover in fluids under nanoscale confinements where the surrounding bulk fluid is far away from any phase transition point. The wave vector (k) dependent fluctuations in density govern majority of properties of a fluid including static quantities like ε_0 and $n^{\dagger\dagger}$, as well as long-time dynamic quantities like η , D and so forth¹¹¹. Hence, the crossover in all such properties should be generically related to that in density fluctuations. We calculate⁶⁵ the fluctuation in number of particles N in a slit of parallel walls with a fixed volume V at absolute temperature T at the same chemical potential μ as in the bulk shown schematically in Figure 4.1. The fluctuation is defined as:

$$\Delta = \langle (N - \langle N \rangle)^2 \rangle / \langle N \rangle, \quad (4.4)$$

the angular brackets representing ensemble averages generated by GCMC simulations^{123, 205}.

The generality of experimentally observed crossover, independent of system specific details, leads us to consider a model LJ fluid with model wall-fluid potential to capture qualitatively the generic effect of confinement. We show⁶⁵ that Δ undergoes a crossover from 3D to 2D behaviour without any accompanying phase-transition below a confinement extending only a few molecular diameters, measuring about a nm, the same length scale of crossover observed in the experiments. The crossover in Δ can be understood from the suppression of the density fluctuations in the system in direction perpendicular to the slit, beyond the wavelength given by the length scale of the confinement. The dynamic density fluctuations, given in terms of the Van Hove correlation function (VHCF), computed from MD simulations with initial conditions chosen from the GCMC configurations, also exhibit⁶⁵ similar crossover in the in-plane diffusivity D_{\parallel} . However, the crossover is dependent on the confining potential: 3D to 2D crossover in Δ and D_{\parallel} for a fluid in solvophobic slit is significantly different from that in solvophilic pore due to strong layering of the fluid-particles near the wall by large wall attraction in the later case. We relate our observations to experimental observations on different fluid properties dependent on density fluctuations.

^{††} For instance, ε_0 of a dipolar fluid is related to the long-wavelength limit of the dipole moment density $\mathbf{M}(\mathbf{k})$ of the system: $(\varepsilon_0 - 1) / \varepsilon_0 = 4\pi\rho \int_0^{\infty} dt \langle \mathbf{M}_{\mathbf{k}} \mathbf{M}_{-\mathbf{k}} \rangle / Nk_B T$. Now, $\mathbf{M}(\mathbf{k}) \propto \rho(\mathbf{k})$ which connects ε_0 with the long-wavelength limit of density fluctuation. The refractive index $n = \sqrt{\varepsilon_0}$, is also related to density fluctuations.

Next we consider SD of a spherical non-polar solute in the confined LJ fluid. Although SD in general gets slower under confinement^{30, 45} there is a caveat in the existing interpretation of the data. The surrounding equilibrium bulk-phases have not been clearly specified in all these cases. This leads us to consider the SD when the bulk is well-specified. Moreover, we observe that D_{\parallel} suddenly exceeds the bulk-value in strong solvophobic confinement, while D_{\parallel} becomes very small compared to bulk under strong solvophilic confinements⁶⁵. This prompts us to examine any subtle interplay between the heterogeneous solvent distribution and D_{\parallel} leading to slowing down of SD in confined geometry, irrespective of the nature of the confining potential. The choice of a non-polar system to study SD is not so restrictive, for the long-time SD is primarily governed by non-polar interactions in the system¹²⁴. The model system also offers a scope to single out the effects of confinement avoiding the various complicating factors of realistic systems. At a phase point, far away from any phase transition, we show⁶⁶ that two fundamentally different aspects of the dimensional crossover are responsible for the confinement-induced slowing down of SD in presence of two kinds of walls. The confined geometry reduces the solvent relaxation due to restricted dynamics which alone slows down the SD. The reduced dimension of solvent dynamics adds up to slower D_{\parallel} in a solvophilic confinement to result in a sharp increase in solvation timescale. On the other hand, slowing down of the dynamics due to reduced dimensionality competes with the faster diffusion in a solvophobic slit, resulting in marginal slowing down in solvation time.

Another phase point is taken⁶⁷ at a sub-critical temperature where the fluid is confined in a solvophobic slit in equilibrium with the bulk sub-critical liquid, close to liquid-gas phase coexistence. Here SD in confinement becomes faster compared to the bulk liquid, but not driven by the gas-like diffusion in the dried solvophobic pore. This can be explained as an outcome of the competition between the wall-induced evaporation effect trying to make diffusion faster and condensation in the pore due the solvophilic solute increasing the density creating an opposite effect. SD slows down linearly as the slit separation increases. Finally, we discuss the implications of our results in the light of confinement effects on various chemical processes in confined geometry.

The rest of the chapter is organized as follows: In section 4.2 we consider the dimensional crossover in nanoscale confinements. Section 4.3 includes the studies on SD under confinement. Then we conclude in section 4.4.

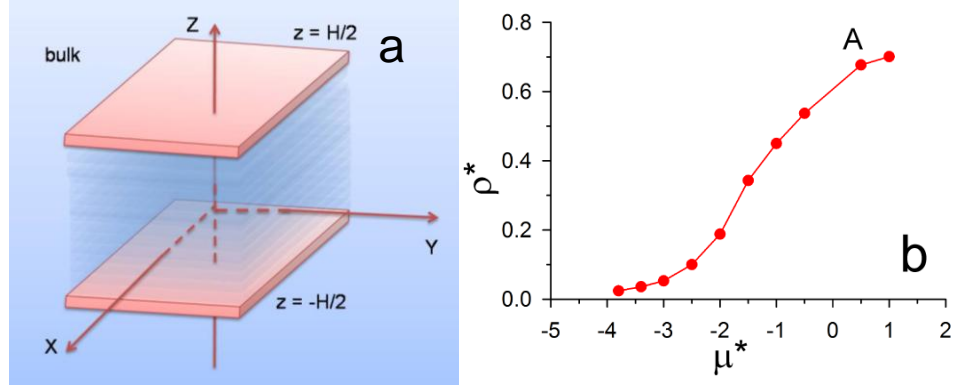


Figure 4.1: System details and phase diagram. (a) Schematic diagram of the simulated slit placed in bulk fluid. (b) ρ^* ($= \rho\sigma^3$) vs. μ^* plots for bulk fluid at $T^*=2.0$. The working phase-point is point 'A' ($\mu^*=0.4$, $\rho^*=0.67$).

4.2 Dimensional crossover

In this section, we first present the details of the simulations. Then we discuss the structure of the confined fluids in terms of density profiles and in-plane radial distribution functions. Next, we consider the crossover behaviour of Δ in different type of slits which is followed by the results of crossover in D_{\parallel} .

4.2.1 Simulation details

For the studies on dimensional crossover, the model fluid is taken in a rectangular simulation box with two parallel plates placed at a separation H on the z -axis at $z = -H/2$ and $z = H/2$ (Figure 4.1a), with fixed box lengths along x and y axes ($L_x = L_y = 20\sigma$, σ being the particle diameter). Here, the periodic boundary condition is applied along x and y directions only. We consider a truncated LJ potential with a cut-off radius $L_x/2$ as the interparticle interaction: $u_{LJ}(r) = 4\varepsilon[(\sigma/r)^{12} - (\sigma/r)^6]$, ε being the interaction strength and r , the interparticle separation. Due to large cut-off we have not added any corrections due to truncation. The confining potential type is varied: hard walls only reflecting the colliding particles; repulsive walls with wall-fluid interaction for a particle at z : $u_{w-f}(z - H/2) = 4\varepsilon'(\sigma/|z - H/2|)^{10}$ and attractive walls: $u_{w-f}(z - H/2) = 4\varepsilon'[(\sigma/|z - H/2|)^9 - (\sigma/|z - H/2|)^3]$ where $\varepsilon' = 10\varepsilon$.

We calculate the fluid density profiles in the direction normal to the slits (z -axis) given by $\rho(z)^* = N(z)\sigma^3/A\Delta z$ where $N(z)$ is the number of particles in a particular fluid-segment of width Δz located at z and A , the area of the x - y plane. We calculate the radial

distributions functions (RDF) ¹¹¹, describing the probability of finding two particles at a given separation. The in-plane 2D RDF¹⁸⁸ is defined as $g(r_{\parallel}) = \langle N(r_{\parallel}) / 2\pi r_{\parallel} \Delta r_{\parallel} \rho_{2D}^l(z)n \rangle$ for a layer at z of width Δz ($\leq \sigma$) with n particles where $r_{\parallel} = \sqrt{x^2 + y^2}$, layer-density $\rho_{2D}^l(z) = n/A$. For a wider layer ($\Delta z \geq \sigma$), we compute the 3D $g(r) = \langle N(r) / 4\pi r^2 \Delta r \rho_{3D}^l n \rangle$ where $r = \sqrt{x^2 + y^2 + z^2}$, layer-density $\rho_{3D}^l = n/A\Delta z$.

In the MD simulations, we adopt NVE ensemble (constant N , volume V and total energy E) using the Verlet algorithm¹²³ to integrate the equations of motion with time-step 0.005 LJ units ($\tau_0 = (m\sigma^2/\varepsilon)^{1/2} \sim 2.8 \times 10^{-12}$ s for Argon where m is the mass of Argon atom)¹¹¹. We calculate T from fluctuations of kinetic energy and μ by inserting test particles¹²³. The mean values of the T and μ in MD runs agree to those of the GCMC simulations. Furthermore, these quantities remain similar also for different initial conditions chosen from equilibrated GCMC configurations. The self part of in-plane VHCF²⁰⁶ are computed:

$$G_s(r_{\parallel}, t) = (1/N) \left\langle \sum_i \delta(\mathbf{r}_{\parallel} - \mathbf{r}_{\parallel}^i(0) + \mathbf{r}_{\parallel}^i(t)) \right\rangle, \quad (4.5)$$

where \mathbf{r}_{\parallel} is the space variable parallel to the walls (along x - y plane) and $\mathbf{r}_{\parallel}^i(t)$, the position of the i th particle along x - y plane at time t . In the long-time limit, the VHCF is Gaussian: $G_s(r_{\parallel}, t) \approx (1/4\pi D_{\parallel} t) \exp[-r_{\parallel}^2 / 4D_{\parallel} t]$.

4.2.2 Characterization of fluid structure under confinement

Figure 4.1b shows the ρ - μ diagram obtained from GCMC simulations for the bulk fluid in absence of any solute. The diagram confirms that there is no phase transition²⁰⁷ at LJ temperature $T^*(=k_B T/\varepsilon)=2.0$ where the point ‘A’, with chemical potential¹²³ $\mu^*(= \mu/k_B T) = 0.4$, represent the phase point of our interest for dimensional crossover. The behaviour of $\rho(z)^*$ is shown in Figure 4.2 for different wall types which exhibit layering similar to those in earlier studies^{48, 188, 189}. We characterize the structure of different layers from the RDFs. Structurally, the wall-adjacent layers for any type of wall assume 2D behaviour as suggested by $g(r_{\parallel})$, shown in Figure 4.3a. For reflecting walls, at $H = 4\sigma$, the central region is a fluid-segment of one diameter width, the corresponding $g(r_{\parallel})$ revealing 2D structure (Figure 4.3b). For $H > 4\sigma$, central region of uniform density appears which gets extended as confinement is relaxed. We calculate the 3D $g(r)$ in that region, for instance, $|z| < 3$ in Figure 4.2c and $|z| < 6$

in Figure 4.2e. Unlike the bulk 3D $g(r)$, the $g(r)$ for the central region drops off to small values at large r till $H = 10\sigma$ (Figure 4.3c), characterizing a finite spatial extent (perpendicular to the wall). At sufficiently large H ($H \geq 12\sigma$), the central region approaches the 3D limit with proper asymptotic behaviour, $g(r) \sim 1$ for large r . These features of the central region are qualitatively same for the other wall types as well. The well-formed central region resembles the bulk-like inner-core of water inside large reverse micelles¹⁹⁴. The other layers formed in between the central region and the wall-adjacent layers behave quite similarly as a 2D fluid.

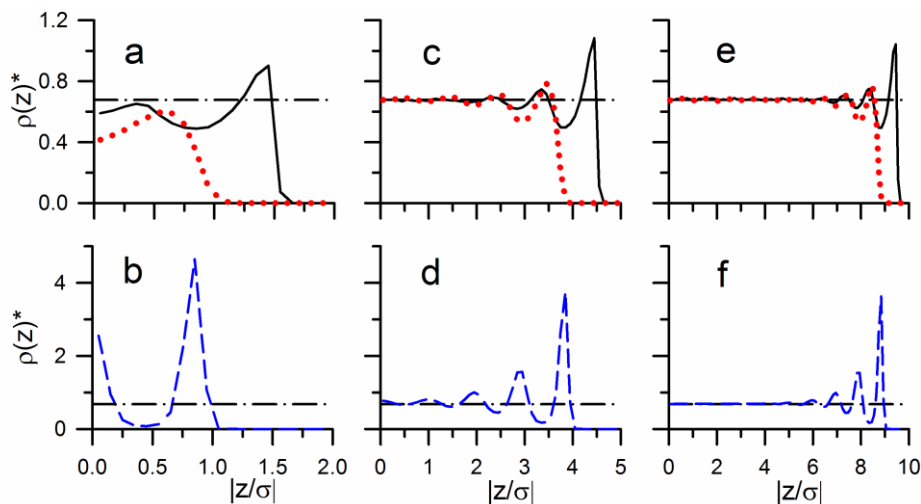


Figure 4.2: Density profile in the slits: $\rho(z)^*$ in reflecting (solid), repulsive (dotted) and attractive (dashed) slits for different H : (a), (b) 4σ , (c), (d) 10σ and (e), (f) 20σ . Dash-dot lines mark the bulk density. Profiles shown here are for the half-slit width along z and they are symmetric about z axis.

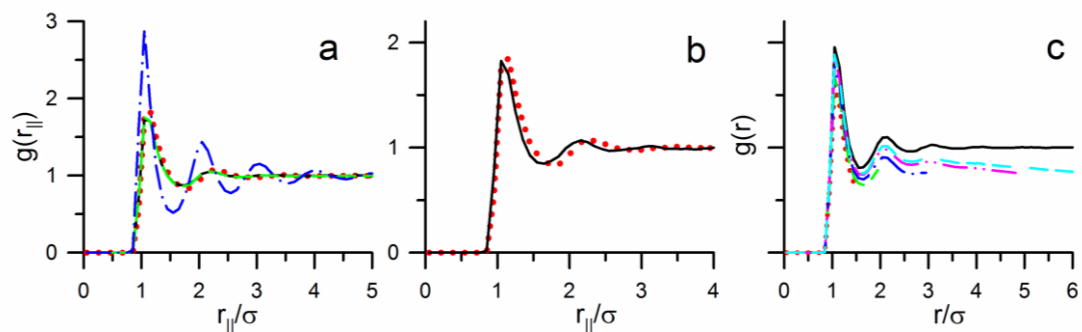


Figure 4.3: Structure of fluid in confinement. (a) $g(r_{||})$ for wall-adjacent layers at $H = 10\sigma$ for reflecting (solid), repulsive (dashed), attractive (dash-dot) slits and the pure 2D case (dotted). $g(r)$ s for the central region in a reflecting slit at (b) $H = 4\sigma$, along with pure 2D $g(r_{||})$ (dotted), (c) $H = 8\sigma$ (dotted), 10σ (dashed), 12σ (dash-dot), 16σ (dash-dot-dot) and 20σ (dash-dash-dash). The solid line represents the bulk 3D $g(r)$.

4.2.3 Crossover in equilibrium density fluctuations: Reflecting and repulsive walls

The bulk 3D and 2D limits of Δ , shown in Figure 4.4a are evaluated from the bulk simulations of a 3D fluid and 2D disks respectively at the same μ and T . Figure 4.4a shows Δ as a function of H for reflecting and repulsive walls. Δ exhibits a clear 3D to 2D crossover in case of reflecting walls: A steep rise in Δ takes place around a critical separation $H_c = 4\sigma$ where the structural crossover takes place in the central region as well. Similar crossover is observed for the repulsive walls also. The intimate connection of crossover in Δ and the structural changes at the central region is illustrated by Figure 4.4b, showing the behaviour of Δ calculated over the central regions. The striking similarity of these plots with those in Figure 4.4a confirms that the central fluid layer holds the key to this crossover. The constant volume specific heat^{123, 205} C_V as a function of H are featureless for both kind of walls (Figure 4.4c), ruling out any thermodynamic phase-transition associated with the crossover. This crossover in Δ qualitatively matches the sudden increase in fluctuations in refractive index of cyclohexane confined between solvophobic mica plates with separation just below 2 nm ($\sim H_c$), measured from surface force experiments⁴⁶. Thus, H_c matches with the length scale at which the jumps in τ , ϵ_0 , η , D and n are observed in experiments^{33, 35, 46, 47}.

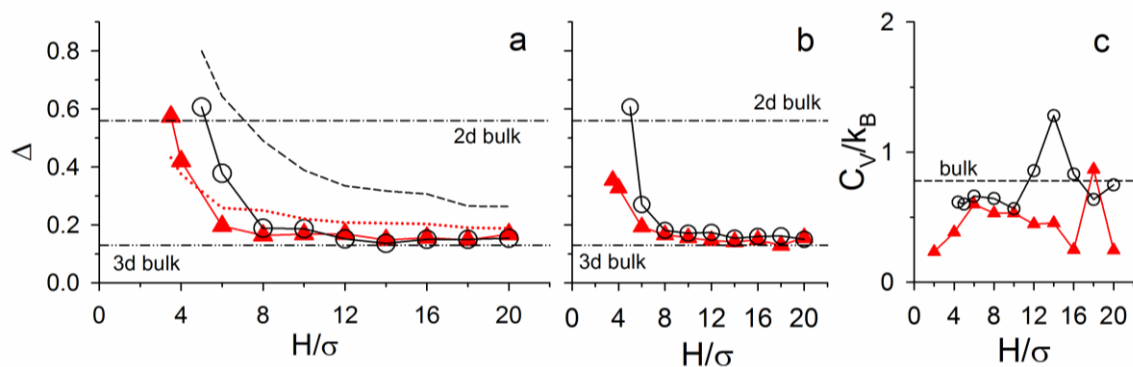


Figure 4.4: Different quantities in slits as functions of H : (a) Δ , reflecting (triangles: simulation; dotted line: theory) and repulsive (circles: simulation; dashed line: theory); (b) Δ in the central region, reflecting (triangles) and repulsive (circles). (c) C_V , reflecting (triangles) and repulsive (circles).

The crossover in Δ around H_c can be made more explicit within a simple theoretical treatment focusing on the long-wavelength cut-off due to the confinement. Δ is given by the long-wavelength ($k\sigma \approx 0$) limit of the static structure factor $S(k\sigma)$ in bulk¹¹¹. $S(k\sigma)$ can be calculated from the liquid direct correlation function $c(r)$ via the OZ relation¹¹¹. Within mean-

field approximations for LJ fluids, the $c(r)$ is split into correlations due to the short-ranged hard core, given by the Percus-Yevick form¹¹¹ $C^{PY}(r)$ for $r < \sigma$ and an attractive tail, $C^{LR}(r) = -4(\varepsilon/k_B T)(\sigma/r)^6$ for $r \geq \sigma$. In a slit geometry, we integrate over \mathbf{r}_{\parallel} in $c(r)$ to yield $c(z)$. We compute $S(k_z \sigma)$, k_z being the transverse component of wave vector, using the OZ relation: $S(k_z \sigma) = [1 - \rho c(k_z \sigma)]^{-1}$ where ρ is the average fluid density in the slit obtained from GCMC simulations. We ignore the density inhomogeneity near the walls which is a good approximation here, since the homogeneous central region, showing the crossover, encompasses majority of the slit. The spatial integration for the Fourier Transform of $c(z)$ to calculate $c(k_z \sigma)$ becomes restricted as z runs from zero to $H/2$ corresponding to a minimum wave vector $k_z^{\min} \sigma = 2\pi/H$. Here, Δ is defined by the value of $S(k_z^{\min} \sigma)$. The comparison of simulation and theoretical results for reflecting walls (Figure 4.4a) reveals nearly quantitative agreement. This indicates that the crossover is a manifestation of cut-off in long-wavelength density fluctuations due to geometrical constraint. The repulsive slit results also show good qualitative agreement between simulations and the theoretical estimate (Figure 4.4a). This is because the fluid layers in this case are formed away from the walls due to their repulsive nature, creating geometrical constraint similar to reflecting walls.

4.2.4 Crossover in dynamic density fluctuations: Reflecting and repulsive walls

The crossover shows up in the dynamic density fluctuations as well, as demonstrated in Figure 4.5a by the long-time ($t \sim 100$ times larger than the diffusion time scale required for a tagged particle to traverse the length of its diameter) behaviour of $-\ln G_s(r_{\parallel}, t)$ as a function of r_{\parallel}^2 for different values of H . The plots, shown for the reflecting slits, are straight lines with slopes changing from 2D to 3D limit with a sudden change above $H = 4\sigma$. Note that the crossover in D_{\parallel}^* ($= D_{\parallel} [m/\sigma^2 \varepsilon]^{1/2}$) almost coincides with that in Δ . D_{\parallel}^* , for both the reflecting and repulsive walls (Figure 4.5b), become maximum at the smallest value of H and drops around $H = 6\sigma$ to meet the bulk 3D value. Physically, under maximum confinement, there is only one fluid layer resembling 2D fluid where the self-diffusion is faster compared to the 3D situation. The in-plane diffusivity drops, as the confinement is relaxed to accommodate multiple fluid layers, due to contributions from inter-layer diffusion. Figure 4.5c shows D_{\parallel}^* for the central layer which indicates that the crossover in D_{\parallel}^* is primarily due to the central region. Similar faster diffusion than bulk have been observed for cyclohexane in mica pores of a few nm width from NMR measurements²⁰⁸, for water in

carbon nanotubes using flow measurements⁴⁹ and in earlier simulations²⁰⁹. This trend, however, is absent in the shear viscosity data of water from Atomic Force Microscopy (AFM) experiments with a hydrophobic graphite substrate⁴⁸. This could be due to the fact that the geometry of a spherical tip sliding close to a planar solid does not represent the strong confinement limit.

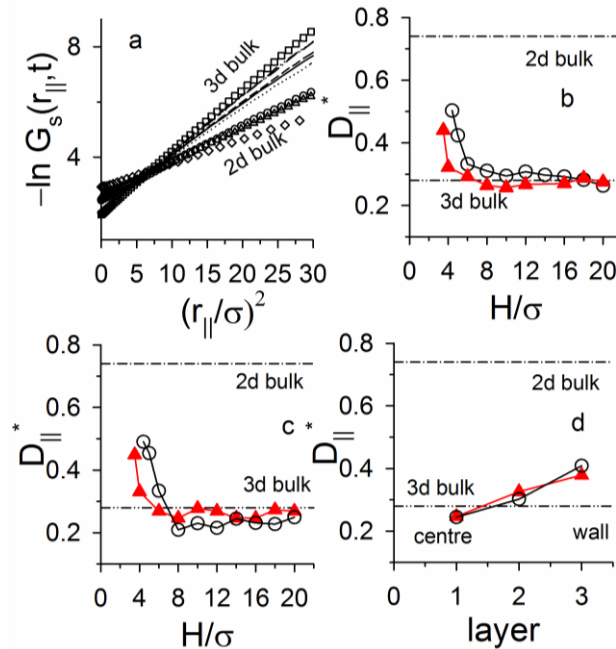


Figure 4.5: Dynamic density fluctuations in solvophobic slits. (a) long-time limit of $-\ln G_s(r_{\parallel}, t)$ vs. r_{\parallel}^2 in reflecting slits for $H = 3.5\sigma$ (triangles), 4σ (circles), 6σ (dotted), 8σ (solid), 10σ (dashed), 16σ (dash-dot) and 20σ (dash-dot-dot) along with the corresponding 2D (diamonds) and 3D (squares) limits. **(b)** D_{\parallel}^* for reflecting (triangles) and repulsive (circles) slits. **(c)** D_{\parallel}^* of only the central region in a slit with reflecting (triangles) and repulsive (circles) walls. **(d)** Layer wise value of D_{\parallel}^* in a slit of $H=14\sigma$ with reflecting (triangles) and repulsive (circles) walls. The left-most layer is the central region and the right-most one is for the wall-adjacent layer. The middle one is for a layer in between the two.

We extract the in-plane diffusion coefficient for different layers as well. In Figure 4.5d we show the D_{\parallel}^* data for different layers for a reflecting and repulsive slit with $H=14\sigma$. There are only three different layers present in the slits with these walls: the central region, the wall-adjacent layer and the layer in between. Nearly 3D bulk like diffusion is observed in the central region. The relatively faster in-plane diffusion observed in the wall adjacent layer compared to the other layers is probably due to the fact that unlike other layers, the particles

in this layer are in contact with the smooth wall in one side which makes the particles to move faster compared to those which are in between two layers of particles.

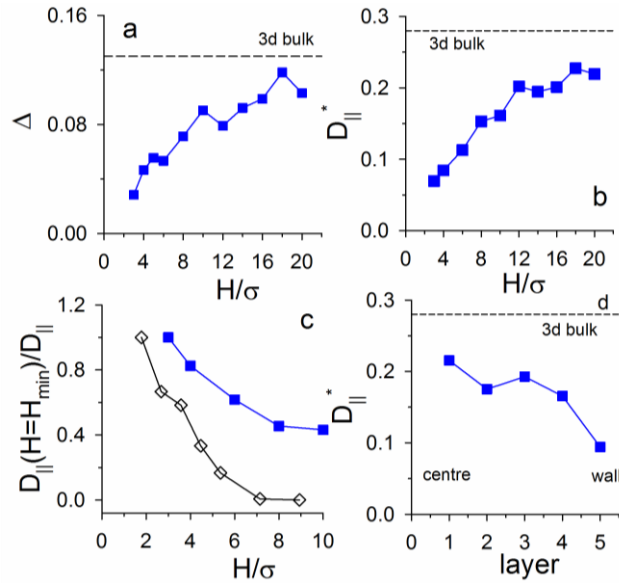


Figure 4.6: Different variables for the attractive slits as functions of H : (a) Δ , (b) $D_{||}^*$ and (c) calculated $D_{||}^*(H_{\min})/D_{||}^*(H)$ (squares) with a similar quantity $\eta(H)/\eta(H_{\min})$ for confined water⁴⁸ (diamonds). (d) Layer wise value of $D_{||}^*$ in a slit of $H=14\sigma$ with attractive walls. The left-most layer is the central region and the right-most one is for the wall-adjacent layer. The data in between are for the middle layers.

4.2.5 Dependence of crossover on wall-fluid potential

Let us now consider the effect of different wall-particle interaction on the crossover. The case of the attractive walls is different compared to the reflecting and repulsive walls. Due to attractive nature of the walls, the density in the fluid layers close to the wall becomes very high. This suppresses the fluctuation in the system which is reflected in very low values of Δ in the extreme confinement limit ($H \sim 3\sigma$) far from the bulk 2D value (Figure 4.6a). Unlike the reflecting and repulsive slits, here Δ gradually approaches the 3D limit for large H from low values. The dependence of Δ on H (Figure 4.6a) agrees qualitatively with the observed trends in ε_0 for the water pool confined inside hydrophilic cavities of RMs³⁵. Under the strong confinements, $D_{||}^*$ is about an order of magnitude smaller for the attractive slit (Figure 4.6b), compared to those for the reflecting and repulsive walls. Variation of $D_{||}^*$ is in agreement with the earlier simulation reports on water in hydrophilic silica pores^{48, 210}. Figure 4.6c shows the trends of the inverse of $D_{||}^*$, qualitatively in agreement with the observations of estimated viscosity (η) of water confined between an AFM tip and hydrophilic surfaces⁴⁸.

The layer-wise diffusion is shown in Figure 4.6d for $H=14\sigma$. Note, here we get five distinct layers in total. D_{\parallel}^* gradually decreases from the central to the wall-adjacent layer. The diffusivity in the central region is near the 3D bulk value while the particles in the high-density layer close to the wall are almost immobilized due to the attractive wall-fluid potential resulting in almost zero diffusivity.

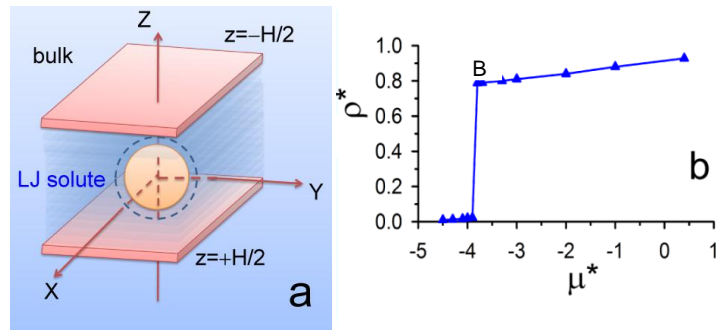


Figure 4.7: Schematic diagram of the simulated slit with solute. The LJ solute particle is placed at the centre of the slit. The dotted line around solute marks its change in size as the perturbation. (b) ρ^* vs. μ^* plots for bulk fluid at $T^*=0.9$ (triangles). The working phase-point is B ($\mu^*=-3.7$ and $\rho^*=0.79$).

4.3 Solvation dynamics under confinement

First we summarize the details of simulations and calculations. Then the results on confinement effects on SD in solvophobic and solvophilic slits are presented to highlight different mechanisms of slowing down. Afterwards, we show how SD is modified from that in a bulk sub-critical solvent, in presence of competition between drying effect of solvophobic slit and wetting effect of solvophilic solute. Finally, we compare our results with various realistic systems to discuss some future implications of the observations.

4.3.1 Simulation details

The simulated system for SD (Figure 4.7a) is very similar to that in Figure 4.1a with the additional solute particle with diameter 3σ fixed at the middle of the box. The solute is solvophilic interacting with the solvent particles via $U(|\mathbf{r} - \mathbf{R}|) = u_{LJ}(|\mathbf{r} - \mathbf{R}|; a\varepsilon, b\sigma)$ where $a = \sqrt{2}$ and $b = 2$, determined from the Lorentz-Berthelot mixing rules²¹¹. For the high temperature studies we use same parameters as above for wall-fluid interactions. For the low temperature studies (Figure 4.7b) we set $\varepsilon' = 5\varepsilon$ where our simulations are stable with the solvophobic slits.

To calculate the $S(t)$ we first run equilibrium MD from stored GCMC configurations at the average μ and T same as that of the respective GCMC runs⁶⁵. After equilibration of the dynamics we increase the solute diameter by 5% (shown by dotted circle in Figure 4.7a) which acts as the perturbation to study the SD using Eq. 4.1. Such change in solute-size is fundamental in any solute-excitation process leading to chemical reactions²¹²⁻²¹⁵. The solvent is in equilibrium before the perturbation and relaxes to the new equilibrium after the perturbation. The averages represented by the overhead lines in Eq. 4.1, equivalent to the averages over solvent density as in Eq. 4.2, are performed in simulation by averaging over 400 trajectories. Each such trajectory is generated from an equilibrium snapshot chosen from the GCMC runs. In general, $S(t)$ contains a short-time Gaussian part⁴⁵ followed by multi-exponential decay given by $\sum_i a_i \exp[-t/\tau_i]$ where the a_i s are the amplitudes and τ_i s are the associated decay timescales, obtained by suitable fitting procedure. The error in τ has been estimated from the error of the fitting parameters.

4.3.2 Mechanisms of confinement-induced slowing down

Let us now consider effects of confinement on SD when the bulk fluid surrounding the slits is at point ‘A’ on Figure 4.1b. We observe two different regions in $S(t)$ in bulk fluid (solid line in Figure 4.8a): A short-time (<1ps) Gaussian component is followed by a single-exponential decay of $S(t)$, as shown in the inset of Figure 4.8a, having a time-scale $\tau \sim 5$ ps within the error bars (Figure 4.8b). We ensure, as a check of consistency, that in all cases we get back the bulk-behaviour as the walls are removed far apart ($H=20\sigma$).

The single exponential behaviour of $S(t)$ remains similar in confined fluid as in the bulk, shown in Figure 4.8a by the dashed (solvophilic) and dotted (solvophobic) lines. However, the effects of the confinement on the values of τ are significant particularly in solvophilic slits compared to those in solvophobic ones. Figure 4.8b shows τ -data along with the error bars. As the solvophilic confinement is made stronger by reducing H from $H=20\sigma$, τ remains similar to that in the bulk up to $H=5\sigma$. We observe a sharp jump in τ around $H \sim 4\sigma$ (circles in Figure 4.8b). At the strongest confinement ($H=4\sigma$) we find $\tau=20$ ps which is about four times slower than the bulk. This qualitatively matches with earlier observations of SD^{45, 51}. At the strongest confinement the solute experiences the sharp layers with liquid structure. The fluid diffusion in these layers would govern the SD. We have shown in 4.2.5 that such strong layering in presence of the attractive walls (Figure 4.2b) leads to slower D_{\parallel} compared to the bulk diffusion. The slowing down of τ is similar to that in D_{\parallel} . However,

the detailed features show qualitative differences: D_{\parallel} decreases gradually⁶⁵ from the bulk 3D behavior with decrease in H from 20σ (Figure 4.6b), whereas τ values show a sharp jump under strong confinement conditions.

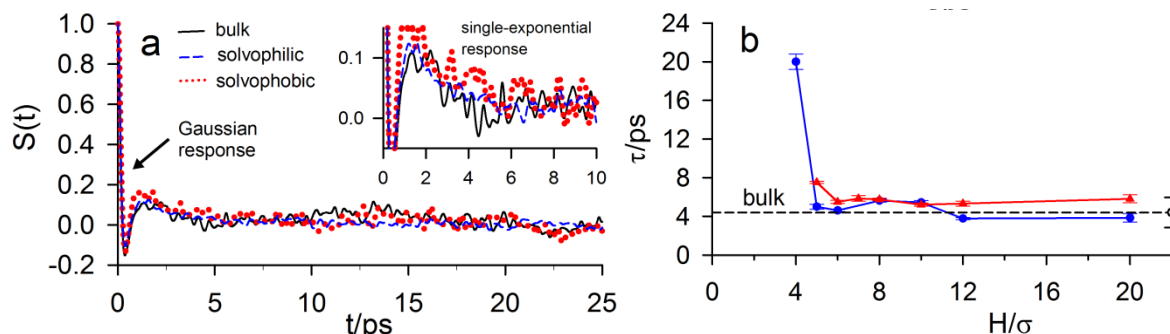


Figure 4.8: Solvation data at point A: (a) $S(t)$, in bulk (solid) and in solvophobic (dotted) and solvophilic (dashed) slits with $H=12\sigma$. (b) τ as function of H , with the error bars, in solvophobic (triangles) and solvophilic (circles) slits. The bulk timescale marked by dashed line through the open circle with error bar.

Although the increase in τ in solvophobic slits is marginal (triangles in Figure 4.8b), it occurs around $H=5\sigma$, similar length scale where dimensional crossover has been shown in 4.2.3 in solvophobic slits. We find $\tau=8$ ps at the strongest confinement ($H=5\sigma$) which is slightly slower than the bulk in agreement qualitatively with earlier results^{51, 196, 200} on SD in solvophobic confinements. Unlike the solvophilic case there is no jump in the τ values for small H . Such marginal slowing down of SD in the solvophobic slits is interesting for our earlier results show that under similar condition D_{\parallel} gets faster than the bulk diffusion by a factor of two (Figure 4.5b) with a sharp jump at $H=5\sigma$.

The contrasting qualitative behaviors of τ and D_{\parallel} indicate that further confinement-induced effects are important to understand SD under strong confinements. The confinement restricts the solvent motion in the z -direction, hindering the solvent relaxation in that direction. For instance, the solvent forms distinct layers in the strongest solvophilic confinement (Figure 4.2a). Under strongest solvophobic confinement, the solvent forms a single layer of about two diameter thickness inside the pore (Figure 4.2b). All these layers exhibit the fluid properties resembling a quasi-2D system⁶⁵. Thus, the solvation of solute of diameter 3σ is due to solvent response from these strong layers of restricted z -motion. To assess the possible effects of this reduced dimensionality on SD we simulate the SD from the GCMC equilibrated snapshots of the quasi-2D system at $H=5\sigma$ without the solvophobic

walls. The system is shown schematically in Figure 4.9. The solvophobic walls are removed (Figure 4.9) so that the particles do not feel any effect of wall. We update the x and y coordinates of the particles, but keep the z -coordinates fixed. Thus, we completely cut off the z -component of the solvent response. Then we ensure proper equilibration of the system in the MD run with these restrictions and calculate $S(t)$ as usual by averaging over hundreds of trajectories. We find slower (~ 3 -times) SD here than the bulk 3D case. This observation confirms that reduction of solvent response along z -direction alone leads to the slower solvation than bulk. In presence of solvophobic walls this slowing effect competes with the higher in-plane diffusivity resulting in marginal increase in τ . In solvophilic slits this effect adds up with slower diffusion resulting in much sharper change in τ .

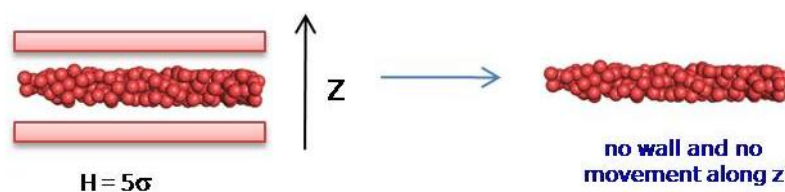


Figure 4.9: Scheme for the system simulated to understand the effects of walls.

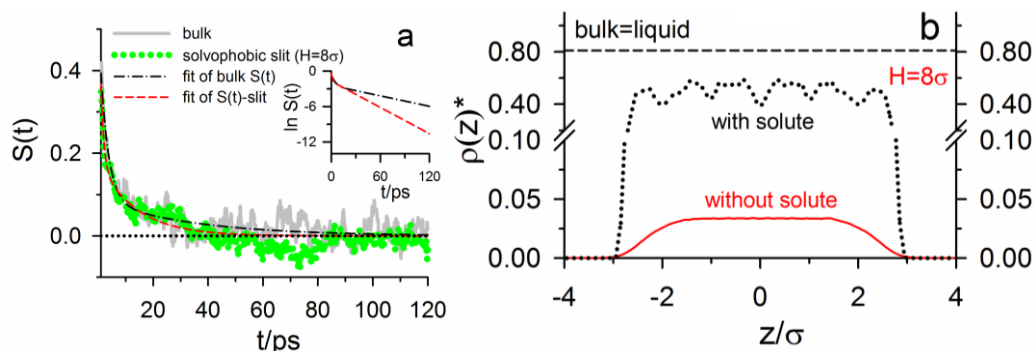


Figure 4.10: $S(t)$ and density profiles at point B. (a) Solvent response functions $S(t)$, in bulk (solid) and in solvophobic (dotted) slit with $H=8\sigma$. Bi-exponential fits to both data are shown: dash-dot line for the bulk $S(t)$ and the dashed line for the $S(t)$ in slit. The zero line is highlighted in the figure. Inset, comparison of the logarithm of the fitted $S(t)$ data for the two cases. (b) Density profiles $\rho(z)^*$ in the same slit in presence (dotted) and absence (solid) of solute.

4.3.3 Effects of drying-wetting competition on SD

Our studies on SD in solvophobic slits placed in a bulk sub-critical fluid near liquid-gas coexistence are performed at a sub-critical isotherm at $T^*=0.9$ (Figure 4.7b) which is well below the critical temperature of LJ fluids ($T_c^*=1.3$)¹²⁴. The liquid-gas phase-coexistence accompanies a sharp change in density around the coexistence chemical

potential²⁰⁷ $\mu_{coex}^* = -3.9$. We consider $\mu^* = -3.7$, just above μ_{coex}^* (marked ‘B’ in Figure 4.7b), corresponding to liquid bulk phase.

Next we discuss the behaviour of bulk SD. $S(t)$ for the bulk liquid phase has three regions: the Gaussian component, followed by a bi-exponential decay (the solid line in Figure 4.10a), with timescales $\tau_1 = 3.2$ ps and $\tau_2 = 40$ ps. Such behaviour of $S(t)$ has been observed earlier for ambient non-polar solvents²¹⁶. τ_1 has been interpreted as the timescale originated from the solvent-cage expansion²¹⁷ following the initial Gaussian response and τ_2 as the longer diffusive relaxation timescale.

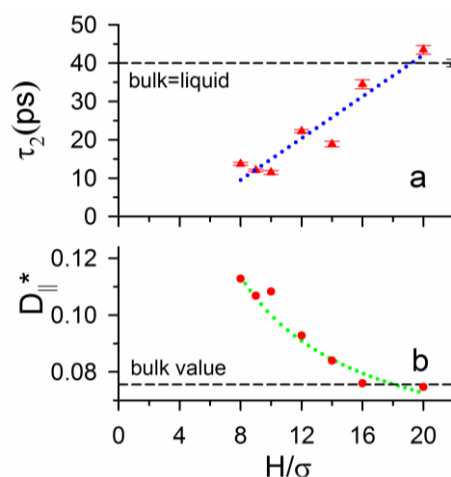


Figure 4.11: Solvation Data at point B. (a) solvation timescale τ_2 in solvophobic slits placed in bulk sub-critical liquid. The dotted lines indicate the linear fit to the data. (b) D_{\parallel}^* at different H . A fit line is shown to highlight the $1/H$ dependence. The bulk limits are marked in both panels by dashed line.

Let us now consider the SD data in a solvophobic slit. The observed $S(t)$ show bi-exponential decay as in the bulk liquid with which the slit is in equilibrium. We show one such representative case for the strongest confined situation $H_{min} = 8\sigma$, by the dotted line in Figure 4.10a. Here SD is somewhat faster than the bulk as is evident from the zero line in the figure. This is also clear from the comparison of logarithm of the fitted $S(t)$ data in the inset of Figure 4.10a. The initial slopes in the inset reflect the smaller timescale which are similar in the two cases. Here $\tau_1 \sim 2$ ps and $\tau_2 \sim 14$ ps which is about 1/3-rd of the value in the bulk liquid. Interestingly, this τ_2 is considerably longer compared to the diffusive timescale in the coexisting bulk gas-phase (~ 1 ps) which is stabilized by the solvophobic slit in absence of the solvophilic solute. This longer τ_2 occurs due to formation of a meta-stable fluid phase (Figure 4.7b) in the slit, with a density profile as shown by the dotted line in Figure 4.10b, via

competition between the wetting effect around the solvophilic solute and the drying effects by the solvophobic walls. This competition enhances the mean density inside the slit up to ~ 0.45 , much higher than the density at dried condition (~ 0.03) in the solvophobic slit without the solute (solid line in Figure 4.10b), but much less than the coexisting bulk liquid density.

We now look at the effect of changing H on the timescales. Out of the two timescales observed in the $S(t)$, τ_1 is nearly unaffected by confinement, as observed in earlier experiments⁴⁵. It remains about 2-3 ps which is very similar to that in the bulk $S(t)$. However, τ_2 rises almost linearly with H , approaching the bulk-behaviour beyond $H=16\sigma$ (Figure 4.11a). Figure 4.11b shows that the D_{\parallel} in solvophobic slits, estimated in presence of the solute, attains maximum at the strongest confinement where the mean-density in the slit is minimum. With increasing H , D_{\parallel} linearly decreases as $1/H$ (fit shown in Figure 4.11b) to approach the bulk value beyond $H=16\sigma$. The observations of larger D_{\parallel} in solvophobic confinement compared to that in bulk liquid is qualitatively similar to our earlier observations⁶⁵.

The dependences of D_{\parallel} and τ_2 on H can be understood from simple qualitative arguments. The diffusion of fluid molecules in weak interaction limit is given by D_0/χ_T where the χ_T is the isothermal compressibility and D_0 is the Stoke diffusion of a tagged particle⁵. By definition $\chi_T = -(1/V)(\partial P/\partial V)_T$ where P is the pressure and V is the volume of the system. If two walls are at separation $H=2\sigma$, no solvent particle can enter the slit. For $H > 2\sigma$, the available volume for the solvent particles in the pore $V=L^2(H-2\sigma)$. For low H the density in the pore is much smaller than the bulk liquid where we ignore the effect of correlations. In such a case, $\chi_T = L^2(H-2\sigma)/Nk_B T$. Therefore, we can write $D_{\parallel} = D_0 Nk_B T / L^2(H-2\sigma)$ which indicates a $1/H$ -dependence of D_{\parallel} , as shown by the fitted line in Figure 4.11b. Comparing the exponential behaviours of $[\rho(\mathbf{r},t) - \rho(\mathbf{r},t=0)]$ and $S(t)$, given in section 4.1, we can write $\tau = 1/(Dk^2)$. Since, the majority of the solvent response comes from the solvent movements in the first few coordination spheres of the solute corresponding to $k\sigma \approx 1$, we get in slit geometry where the relevant diffusion is in planes parallel^{65, 210} to the walls of the slit: $\tau \approx \sigma^2 / D_{\parallel}$. Thus we can write here $\tau_2 \approx \sigma^2 / D_{\parallel} = \sigma^2 L^2(H-2\sigma)/(D_0 Nk_B T)$. This clearly indicates a linear relation between τ_2 and H as we observe in Figure 4.11a.

4.3.4 Implications of the results

Let us now discuss various perspectives of our observations on confinement induced changes in SD. The mechanisms of slowing of SD we bring out here would control various chemical reactions in confined geometry. One important class of chemical reaction, for instance, is charge-transfer (CT) or proton-coupled electron-transfer in biological systems¹⁹³. Effects of SD on rates of CT reactions have been studied widely in biomimetic systems, like, RMs which show⁴⁵ qualitatively similar slowing of rate as confinement becomes stronger. Although such systems, for instance, the fluorescent dyes in an associative solvent like water, are very complex with complicated interactions, both the RM and the reacting species are solvophilic. Our results on the solvophilic confinement show that one contribution to the observed slowing down in the rates of CT reactions in these systems is due to slow SD in response to the suppression of fluid diffusion under strong confinement. Interestingly, considering the four times slowing of SD in a slit geometry, one would expect ~12 times slowing down in a confining framework in all directions, like that in a spherical RM which is qualitatively similar to the experimentally observed (10 to 100 times) slowing down⁴⁵. Fluid-phase reactions in carbon nanotubes³⁷ using metal nanoparticles as catalysts in alcohol solvents, like, methanol have drawn lot of attention recently where the confining frameworks are solvophobic. The reaction rates and the yields are found to be enhanced significantly in the nanotubes³⁷ compared to the bulk. This phenomenon can be qualitatively explained from our observations with solvophobic slits. Here SD is slower, but the in-plane fluid diffusion is faster than the bulk case. As a result the reacting particles encounter each other at a faster rate, even before they are solvated by the medium.

It would be interesting to discuss our results of 4.3.3 in light of the earlier observations with sub-critical water confined in solvophobic environment. Several studies^{204, 218} on the phase behaviour and fluctuations of water molecules near hydrophobic surfaces in nanoscale slits to show similar evaporation effects as we have seen here. However, the presence of a single hydrophilic site resists²⁰⁴ the evaporation and leads to similar competition we have observed. This competition has been interpreted^{203, 219} in terms of changes in density fluctuation behaviour of water molecules near a hydrophobic surface via the hydrophilic interaction which plays very important part in deciding the phase behaviour of water at a biomolecular interface. Our simplified model captures all these essential physics. Our results reflect the dynamical aspects of solvation affected by such competing interactions. In general biomolecular surfaces are heterogeneous having both types of interactions. Solvation plays very important role in associations of biomolecules²⁰³ where two

such surfaces with competing interactions come in close vicinity. Our results on solvation dynamics may be helpful to understand the kinetics of such biomolecular and macromolecular associations. Moreover, the fixed solute approximation would be useful for large solutes²¹², like the biomolecules and different macromolecules in general where the movement of solute is much slower compared to the solvent molecules. The perturbation chosen here in terms of change in solute size also would be applicable for the macromolecular solutes, since any perturbations leading to chemical reactions always accompany changes in shape and conformation of the participating solvated species.

The most interesting aspect of our results on SD under solvophobic confinement, in equilibrium with a sub-critical bulk liquid, is the faster SD under strong confinement and its linear approach to bulk behaviour with increasing H . This behaviour is in sharp contrast to the confinement induced slowing down where the confined fluid is far away from any phase-transition. Our results also clearly show that experimental observation of this slowing of SD cannot be rationalized without precise specification of the surrounding equilibrium bulk fluid. More interestingly, the solvation of solvophilic solute in a solvophobic pore in equilibrium sub-critical liquid near phase-coexistence offers a wonderful scope for tuning of solvation timescales which may be useful in controlling chemical and physical processes in the confined media. In particular, the sub-critical liquid in solvophobic confinements, like, carbon nanotubes, graphene nanochannels, sol-gel matrix, could be attractive media for controlling the chemical reactions, namely, large scale catalysis, charge-transfer, nanoparticle synthesis and physical processes, for instance, industrial scale separations and extractions, and so on.

4.4 Conclusion

In conclusion, we have shown that the dimensional crossover in static density fluctuations for a confined fluid can be understood from the modifications in long-wavelength response of the fluid due to confinement-induced geometrical constraints. The dynamic density fluctuations also show the signature of this crossover. Our results provide a clear relation between the crossover of different physical properties and the length scale of confinement although the detailed nature of the crossover is sensitive to the confining potential. Thus, we suggest a possible general mechanism for the crossover in large number of diverse static and long-time dynamical quantities under confinement.

We also show that the SD of a solute in a nanoconfined fluid is affected by the dimensional crossover in fluid properties. In fact, two different aspects of crossover in

solvophilic and solvophobic slits lead to different mechanisms of slowing down of SD observed in several confined systems. There is sharp slowing down of solvation timescale in solvophilic slits due to suppression of fluid diffusion by the attractive walls, in addition to the restricted solvent dynamics in confining direction. The slowing down of SD is marginal in solvophobic slits which can be explained via a competition between two opposite effects: reduction of dimensionality in solvent dynamics and faster solvent diffusion in narrow repulsive slits. Experiments and further theoretical investigations are required to verify the suggested mechanisms which could shed important light on solvation dominated chemical processes under confinement.

Finally we examine the effects on surface-induced phase transition on the SD of a solute in a fluid confined in solvophobic environment when the bulk is a sub-critical liquid close to the liquid-gas phase coexistence. The solvent response is bi-exponential as in the bulk liquid. This happens due to the formation of a meta-stable high density phase by the wetting induced by the solvophilic solute in competition with the drying effects of the solvophobic walls. However, SD slows down linearly to approach the bulk character as the confinement becomes weaker. Thus, we bring out clearly how geometric constraints, in combination with the influences of the confining potential, nature of solute and the thermodynamic state of the surrounding bulk fluid lead to a dramatic behavior of the SD in a nanoconfined fluid. Our results would help in further theoretical and experimental investigations on nanoconfined fluids with well-specified surrounding bulk fluid phase.

Chapter 5 Conformational fluctuations in biomacromolecules

5.1 Introduction

Biomacromolecules are large flexible molecules which exist in numerous possible conformations in biological environments. Fluctuations among these conformations are of fundamental importance from various perspectives, like, structure, function and applications. Specific conformations are required for thermodynamic stability of biomacromolecules. One classic example of such conformational fluctuation is the folding of proteins into its native conformation²²⁰. The biomacromolecules need to adopt suitable conformations in general to participate in molecular recognition, signal transduction, gene expression and so on⁶⁹⁻⁷². Furthermore, subtle conformational changes of different biomacromolecules have been utilized in various nano-biotechnological applications^{73, 74, 221}. Thus, microscopic understanding of conformational changes in biomacromolecules is important from both biological and technological standpoints.

The biomacromolecules, like proteins, are characterized by a large number of internal degrees of freedom which specify the conformations. When a biomacromolecule binds with a binding partner, these large molecules themselves experience conformational changes, to stabilize the complex⁸⁵, along with the changes in surrounding solvent⁸⁴. Not only that these changes take place simultaneously over different binding regions consisting of large number of conformational variables, but also the interactions between different groups of atoms are diverse. A microscopic understanding of biomacromolecular binding at the level of the binding regions, essential for understanding most of the biophysical and biochemical processes in detail, is thus one of the most challenging problems^{86, 87}.

The most important equilibrium aspect of conformational fluctuations is the thermodynamic characterization including both entropy and free energy contributions⁹¹. Experimentally, the binding entropy and the binding free energy for biomacromolecular complexes have been measured by isothermal titration calorimetry (ITC)⁶⁹. However, this macroscopic method cannot yield the information on the changes of individual binding regions. With the advent of NMR relaxation experiments⁹²⁻⁹⁵ to measure the conformational entropy costs in biomacromolecular complexes, the role of conformational changes in the binding regions has been emphasized. Computer simulations provide a useful route to extract thermodynamic data at the microscopic level in controlled manner⁸¹. The computer simulations²²²⁻²²⁵ to estimate the conformational entropy from the normal modes²²⁶ associated

with atomic vibrations or quasi-harmonic (QH) analyses²²⁷ have been numerically very challenging, while the approaches based on purely statistical scoring functions from the crystal structure databases^{228, 229} are devoid of microscopic details. Atomic Cartesian coordinates often are not suitable to capture all possible bond rotations, thus providing poor estimates²³⁰ of conformational entropy. Furthermore these methods are often limited due to huge collective motional correlations inherent to changes in atomic Cartesian coordinates.

Recently, the protein dihedral angles have been widely used as the conformational variables. Multidimensional histograms of the dihedral angle distributions have been constructed to estimate the conformational entropy⁹⁷. However, such calculations are computationally demanding thus limiting the applicability to small systems only. A detailed approach⁷⁹ incorporating correlations among the dihedral angles up to different order (pair-wise correlations, three-point correlations and beyond) has shown that ~80% of the conformational entropy for different small molecules could be recovered by neglecting all sorts of correlations. In biomacromolecules, the long-ranged dihedral correlations have been found^{90, 231} to be negligible except some short-ranged correlations among the side-chain torsions. These observations practically illustrate the importance of completely reduced one-dimensional histograms^{80, 232} based on a single dihedral angle. A recent Monte-Carlo based approach⁹⁸ has considered a fixed-backbone implicit solvent model to probe the contributions of side-chain entropies towards the binding entropy for protein-ligand interactions. Their estimates correlate quite well with the ITC data²³³ for several Calmodulin-target peptide complexes.

Accurate and efficient estimation of conformational free energy is quite challenging till date. The conformational states of a small biomacromolecule have been explored via UV resonance Raman measurements⁹⁶ where the free energy difference between two states has been calculated by the population ratios of those two states. Computational methodologies for calculation of conformational free energies are of two types: 1) estimating the absolute free energies of a conformational state; and 2) evaluating the free energy differences between two states. One recent example of the former class is the reference system method²³⁴. It is an implicit solvent model based on the description of a reference system for a biomacromolecule using the internal or Cartesian coordinates. Though this method gives good measures of conformational free energies for dipeptides, application to larger systems is computationally very costly. There are a number of methods belonging to the latter class. For instance, the confinement method²³⁵, a variation of the normal mode analyses and the deactivated morphing method²³⁶, based on non-physical transformations between two conformational

states where all the interactions are turned off before the change. Non-equilibrium MD simulations⁸² have been employed, based on differential fluctuation theorem²³⁷, to evaluate free energy differences with implicit solvent contributions. Explicit solvent MD simulations²³⁸ have also been used to calculate the free energy differences between two conformational states of a polymer chain, using a path variable connecting two states on the configurational phase space. A Common limitation of all these approaches is their inefficiency to study medium to large biomacromolecular systems and focus on individual binding regions.

The dynamic conformational fluctuations control various fundamental non-equilibrium processes in biological systems including allosteric regulations²³⁹. The remarkable ability of biomacromolecules to transmit responses over large distances is known as allosteric regulation which governs a host of cellular processes, ranging from signal transduction to gene expression²⁴⁰⁻²⁴³. For example, binding of a ligand at one sub-unit of a protein affects the subsequent ligand binding at another sub-unit through propagation of change in protein shape or conformation far away from the first ligand binding site¹⁰³. Recent experiments²⁴⁴⁻²⁴⁹ indicate that even in absence of any structural changes, the ligand-induced modifications of dynamic fluctuations of a protein can link two sites via allosteric regulation.

The current understanding of allosteric regulation is based on population shift experienced by the biomacromolecule into different conformational states^{104, 105, 250} upon ligand binding. This shift occurs through the participation of a large number of dynamically coupled conformational degrees of freedom. The simplest system showing dynamical coupling are a set of coupled harmonic oscillators. However, the conformational degrees of freedom are much more complex in nature. In fact, experimental characterization of the dynamic coupling among conformational degrees of freedom has been quite challenging, despite several techniques to probe conformational dynamics of biomacromolecules⁷⁵⁻⁷⁸. NMR experiments have been widely used to probe allostery²⁵¹. Changes in intrinsic dynamics at allosteric sites, observed via measurement of NMR relaxation rates of backbone motions, have been a good marker of dynamic-driven allostery in proteins^{244, 245}. A solution-NMR residual dipolar coupling analysis have shown that significant rotational motions of different sub-domains control the allosteric regulation in a heat-shock protein²⁵². Covariance analysis of NMR chemical shifts has been used²⁵³ to study the coupling between residues which participate in allosteric regulation in a protein during ligand binding events. Using this method, other dynamics-driven allosteric networks have also been identified from the inter-residue chemical shift correlations. However, the nature of dynamic coupling among

allosteric degrees of freedom revealing a complete molecular picture has remained elusive. A microscopic characterization of dynamics of the conformational variables is thus of primary importance to understand the allosteric events.

In the absence of detailed knowledge on dynamic coupling among the conformational degrees of freedom, the processes responsible for population shift are taken to be Markovian so that the transition to a conformational state depends only on the previous one²⁵⁴. Although the Markovian model has been tested for few biomacromolecules in the long-time limit using a Master equation approach¹⁰⁵, its validity needs the knowledge of all the dynamical variables associated with the processes²⁵⁴ which is a really difficult task. Apart from the Markovian model of population shift, various other techniques have been employed to understand the mechanism of allosteric regulation in biomacromolecules. Many of the approaches²⁵⁵⁻²⁶² are based on different network-models of biomacromolecules to highlight allosteric pathways for conformational transitions. Such models have also formed the basis of normal-mode analyses²⁵⁷ to describe allosterically regulated large domain motions, induced by ligand-binding, in biomacromolecules. Despite revealing important insight to allosteric regulation^{256, 260}, the coarse-grained network models lack any atomistic detail. However, there are a number of atomistic approaches, like models^{263, 264} based on fluctuations of distances between different parts in a biomacromolecule; structure-based statistical mechanical model²⁶⁵ based on large backbone and side-chain entropic contributions as driving factors of allosteric transitions in proteins; statistical coupling analysis²⁶⁶ to map the equilibrium correlations among parts of biomacromolecules; cross-correlation matrices²⁶⁷ between position vectors of C_{α} atoms of different residues; force distribution analysis²⁴¹; and investigation²⁶⁸ of evolutionarily conserved pathways of allosteric signal transmission via energy propagation. The distance fluctuation matrices and the correlation maps, although point at key allosteric sites or correlated regions in biomacromolecules, cannot reveal the nature of dynamic correlation between allosterically coupled dynamical variables. Since the biomacromolecules feature a wide distribution of timescales of various kinds of motions, the temporal behaviour of such correlations could be very important for specific allosteric events occurring in a given time-domain. Recent studies^{79-83, 90, 105, 269, 270} have shown that the dihedral angles are convenient variables to microscopically describe conformations of biomacromolecules, including the conformational thermodynamics⁸³ and allosteric regulation in proteins^{105, 269, 270}. However, these studies do not directly address the dynamic coupling of the dihedral angles.

In the present chapter, we study both the equilibrium and non-equilibrium aspects of conformational fluctuations. We extract thermodynamics of the conformational changes from the one-dimensional histograms of the dihedral angles. These histograms can be sampled efficiently from the equilibrium trajectories from all-atom MD simulations of a biomacromolecular complex and its components in their respective free states, all being in an explicit solvent. The connection between the underlying thermodynamics and the histogram can be understood as follows: Since the histograms can be treated as the probability of finding the system in a given conformation, they can be interpreted as given by the Boltzmann factors of the corresponding effective free energies; while the entropies are given by the Gibbs formula⁹⁸. The histogram-based method (HBM)⁸³ can yield both the information simultaneously from a single set of simulations, unlike the existing expensive computation methodologies which provide the entropy and free energy separately. Moreover, the HBM is capable of yielding the conformational thermodynamics data for each binding regions in the complex.

We apply the HBM⁸³ to experimentally well studied Calmodulin-peptide complexes. Calcium (Ca^{2+}) saturated Calmodulin (CaM) is the primary mediator of target protein activities responding to changes in intracellular calcium levels²⁷¹. CaM belongs to the class of EF-hand proteins. EF-hand²⁷² is a helix-loop-helix structural motif that generally binds a Ca^{2+} ion via the loop. CaM has two globular domains: N-terminal (N-domain) and the C-terminal domain (C-domain). Each domain has two EF-hands, I and II in the N-domain and III and IV in the C-domain (Figure 5.1a). Two domains are connected via a linker region consisting of 29 residues (residues 68-92). Metal-free (apo) CaM, upon Ca^{2+} -saturation, undergoes subtle conformational changes^{273, 274} in the metal-bound (holo) form (Figure 5.1a) with the linker becoming a long helix and thus exposing the target-binding hydrophobic faces of CaM for target peptides⁶⁹. Moreover, the linker gets deformed to wrap around the peptides (Figure 5.1b) which are CaM-binding sequences of large number of proteins including several regulatory enzymes^{275, 276} e.g. protein kinases, phosphodiesterases, cyclases etc. Here we consider five such peptides: CaM-binding sequences of smooth muscle myosin light chain kinase (smMLCK)²⁷⁷, the neuronal and endothelial nitric oxide synthases (nNOS and eNOS respectively)²⁷⁸, the calmodulin kinase I (CaMKI)⁶⁹ and the calmodulin kinase kinase (CaMKK)²⁷⁹. For all these CaM-peptide complexes the ITC data^{69, 233, 277} and conformational entropy changes (ΔS_{conf}) measured via NMR relaxation experiments are known^{75, 233, 280, 281}. According to observations, the total changes in conformational entropy (ΔS_{conf}^{tot}) is linearly correlated with the total binding entropy (ΔS_{bind}^{tot}) for the complexes. Recent work⁷⁵ shows

that ΔS_{conf} for CaM and the target peptides are linearly related to $\langle \Delta S_{Me}^2 \rangle$, the average changes in residue-weighted methyl group order-parameters S_{Me}^2 which describes the rotational freedom of the methyl group. We estimate ΔS_{conf} of the complexes and the components correctly and recover the experimental observations. Further, we estimate the conformational free energy cost of binding to predict different contributions of the individual binding regions of CaM. Our calculations show that the deformations in linker helix to wrap around the peptides cost huge free energy and entropy. The unfavourable changes are outweighed by the favourable changes at different binding regions dominated by the interactions among the charged residues and the hydrophobic residues.

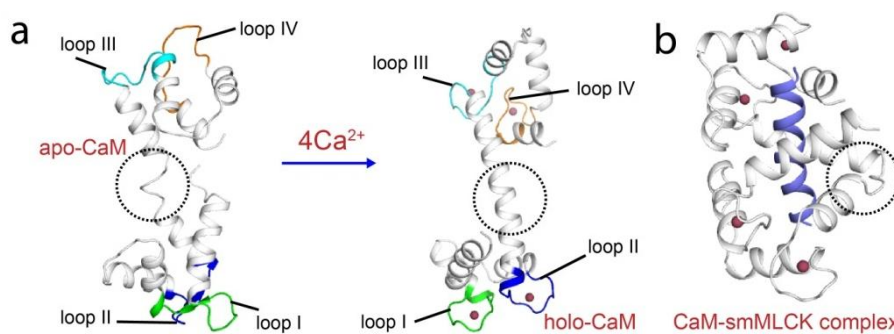


Figure 5.1: Binding events of CaM. (a) Apo- to holo- transition of CaM using cartoon representations. The EF-hand loops are coloured: I (purple), II (yellow), III (pink) and IV (cyan). The part of linker that undergoes loop to helix transformation is marked by circle. (b) CaM bound to a target peptide (blue), smMLCK.

We also consider the Ca²⁺-ion binding to apo-CaM. Despite several experimental^{100, 101, 282} and theoretical studies^{283, 284} on such binding events, the conformational thermodynamics of CaM upon Ca²⁺-ion binding is largely unexplored. Using the HBM we estimate the contributions from individual metal-binding sites to the conformational thermodynamics along with the role of the individual residues in bringing about the thermodynamic changes in the conformation space. We find four metal-ion binding sites in CaM have different conformational free energy and entropy changes with the major share of the changes due to the coordinating residues to the Ca²⁺-ions. The non-coordinating residues in the vicinity of the binding sites also undergo thermodynamic changes. We find substantial thermodynamic changes in the linker where modification of the secondary structural element takes place (Figure 5.1a). Finally, we correlate these results with the experimentally measured binding data and discuss the broad implications of our studies.

The dynamic correlation between the non-equilibrium fluctuations of different degrees of freedom have been studied in great detail via time-dependent correlation functions

(TDCF) for various non-equilibrium systems^{65, 111, 254, 285}. The TDCF between two variables describes how the changes in a physical quantity affect the other quantities after certain time. The TDCF remains non-zero till a timescale called dynamic correlation time (τ). Such TDCF has not been explored in details in the context of dynamical variables associated with the biomacromolecules. We extract the TDCF of the dihedral angles in a protein from the temporal evolution of all-atom MD trajectories. Our primary objective is to probe directly the dynamic correlation among the conformational variables participating in allosteric regulation. We illustrate the TDCFs of the dihedral angles in the case of Ca^{2+} ion binding to apo-CaM which is known to involve certain allosteric events. We show that a number of dihedrals exhibit long-ranged temporal correlation with non-exponential behaviour. Further, a sub-set of dynamically cross-correlated dihedrals of distant residues is affected via binding of Ca^{2+} ions to CaM, indicating their involvement in allosteric regulation. Our approach, based on dynamic correlations, provides a significant advancement to understand allosteric regulation of biomacromolecules without any assumption on the underlying dynamical processes.

The rest of the present chapter is organized as follows: We describe the HBM for a protein-ligand binding and its extensions in Section 5.2. The results on conformational thermodynamics for CaM-peptide complexes are presented, along with a prediction and discussions on merits and demerits of HBM in 5.3. Conformational thermodynamics for binding of Ca^{2+} ions to CaM is considered in 5.4. Section 5.5 deals with the allosteric regulations in CaM. We conclude in 5.6.

5.2 The histogram based method for conformational thermodynamics

In this section we illustrate the theoretical basis of HBM for protein-ligand binding and its extensions.

5.2.1 Protein-ligand binding

For a system with conformational variable set $\{\xi_i\}$, the normalized probability distribution is given by:

$$P(\{\xi_i\}) = \frac{1}{Z} \exp[-\mathcal{H}(\{\xi_i\})/k_B T] \quad (5.1)$$

where k_B is the Boltzmann constant, T the absolute temperature, $\mathcal{H}(\{\xi_i\})$, the Hamiltonian and Z , the partition function of the system. The reduced probability distribution for a given conformational variable ξ can be obtained by integrating over the other variables in Eq. 5.1:

$$P(\xi_i = \xi) = (1/Z) \int \exp[-\mathcal{H}(\{\xi_i\})/k_B T] \delta(\xi_i - \xi) \Pi d\xi_i = (1/Z) \exp[-G(\xi)/k_B T] \quad (5.2)$$

which defines the effective free energy $G(\xi)$ or the potential of mean force¹¹¹ associated with ξ .

We consider $\xi \equiv (\theta, \tau)$ where θ and τ are the dihedral angles for protein p and ligand l respectively. Subsequently, we use the subscripts $p+l$, p and l to indicate quantities associated with the complex, the protein and the ligand respectively, while the superscripts c and f to denote the bound and free state respectively. We define the following effective free energies from Eq. 5.2:

$$P_{p+l}^c(\xi) = \frac{1}{Z} \exp[-G_{p+l}^c(\xi)/k_B T], \quad P_p^f(\theta) = \frac{1}{Z} \exp[-G_p^f(\theta)/k_B T]$$

$$\text{and} \quad P_l^f(\tau) = \frac{1}{Z} \exp[-G_l^f(\tau)/k_B T] \quad (5.3)$$

Therefore, the free energy change for ξ due to complexation is

$$\Delta G_{conf}(\xi) = -k_B T \ln \left[\frac{P_{p+l}^c(\xi)}{P_p^f(\theta) P_l^f(\tau)} \right]. \quad (5.4)$$

The correlation between any two dihedral angles ξ_i of i th residue and ξ'_j of j th residue is defined as⁸⁰

$$C_{\xi\xi'}(s) = \langle \cos \xi_i \cdot \cos \xi'_j \rangle - \langle \cos \xi_i \rangle \langle \cos \xi'_j \rangle \quad (5.5)$$

where the $s = |i - j|$ and the angular brackets denote ensemble average. If correlations are negligibly small, the conformational variables can be considered independent. Then we write, $G_{p+l}^c(\xi) = G_p^c(\theta) + G_l^c(\tau)$ and $P_{p+l}^c(\xi) = P_p^c(\theta) \cdot P_l^c(\tau)$ to give us from Eq. 5.4:

$$\Delta G_{conf}(\xi) = -k_B T \ln \left[\frac{P_p^c(\theta)}{P_p^f(\theta)} \right] - k_B T \ln \left[\frac{P_l^c(\tau)}{P_l^f(\tau)} \right] \quad (5.6)$$

so that the thermodynamics is given separately in terms of the individual dihedrals. If we sum over all the dihedral angles of protein and ligand we get the total conformational free energy change:

$$\Delta G_{conf}^{tot} = -k_B T \sum_{\theta} \ln \frac{P_p^c(\theta)}{P_p^f(\theta)} - k_B T \sum_{\tau} \ln \frac{P_l^c(\tau)}{P_l^f(\tau)} = \Delta G_{conf}^{prot} + \Delta G_{conf}^{lig}. \quad (5.7)$$

We can express ΔG_{conf}^{tot} differently to illustrate the nature of approximations in our calculations. Let $z(\xi)$ be the partition function corresponding to effective free energy $G(\xi) = -k_B T \ln z(\xi)$. Therefore, $z(\xi) = \exp(-G(\xi)/k_B T) = P(\xi)Z$, from Eq. 5.3, $P(\xi)$ being the probability distribution for ξ . Defining $z(\xi)$ for the protein variables θ and ligand variables τ in free and complex states we can write

$$-k_B T \ln \Pi_{\theta} \left[\frac{z_p^c(\theta)}{z_p^f(\theta)} \right] - k_B T \ln \Pi_{\tau} \left[\frac{z_l^c(\tau)}{z_l^f(\tau)} \right] = -k_B T \sum_{\theta} \ln \frac{P_p^c(\theta)}{P_p^f(\theta)} - k_B T \sum_{\tau} \ln \frac{P_l^c(\tau)}{P_l^f(\tau)} \quad (5.8)$$

which, using Eq. 5.7, simplifies to

$$\Delta G_{conf}^{tot} = -k_B T \ln \left[\frac{Z_p^c(\theta) Z_l^c(\tau)}{Z_p^f(\theta) Z_l^f(\tau)} \right] \quad (5.9)$$

where $Z_p^c(\theta) = \Pi_{\theta} z_p^c(\theta)$ and so on. The term in square brackets in Eq. 5.9 is the conformational contribution to the equilibrium binding constant. Here we assume that the other degrees of freedom like bond angles and bond vibrations change very little in the complex compared to the free states and they are decoupled from the dihedral angles, thus cancelling out from the ratio in Eq. 5.9. The ratio of partition functions in Eq. 5.9 resembles that used earlier²⁸⁶ to define the standard free energy of binding of a receptor to a ligand. However, we consider here only a restricted set of internal degrees of freedom associated with equilibrium fluctuations of the dihedrals. Since we focus only on the conformational part of the thermodynamics we do not consider the solvation components, although the effects of solvent on dihedral distributions have been taken into account through explicit solvent molecules. We also ignore the external contributions to the thermodynamics as in Marlow et al⁷⁵.

The normalized probability distribution of a protein dihedral θ is given by the histograms $H_p^c(\theta)$ and $H_p^f(\theta)$ and that for a ligand dihedral by $H_l^c(\tau)$ and $H_l^f(\tau)$ in the bound and the free state, respectively. They can be generated from equilibrium trajectories obtained by molecular simulations. The peak of the histogram defines the equilibrium value of the relevant dihedrals. Then the equilibrium conformational free energy cost associated with any protein dihedral θ is

$$\Delta G_{conf}^{eq}(\theta) = -k_B T \ln [H_{p,\max}^c(\theta) / H_{p,\max}^f(\theta)] \quad (5.10)$$

where the subscript ‘max’ denotes the maximum of histogram. Such a treatment is sufficient since the population at the base of a peak is insignificant (1-10%) compared to that at the maximum for a typical histogram.

The free energy contributions from the neighbourhood of the maximum can be accounted for within a QH expansion about the maximum. We expand a histogram $H(\theta)$ about the maximum at $\theta = \theta_0$ up to the quadratic term: $H(\theta) = H_{max} - (1/2)H''(\theta_0)(\theta - \theta_0)^2$ where $H''(\theta_0) = |C(\theta_0)|$, the curvature near the maximum. Therefore, the effective free energy for θ can be written using Eq. 5.3 as:

$$G(\theta)/k_B T = -\ln[H_{max} - (1/2)C(\theta_0)(\theta - \theta_0)^2] - \ln Z. \quad (5.11)$$

Equation 5.11 can be rearranged to give $G(\theta)/k_B T = -\ln[ZH_{max}] - Bx^2$ where $x = \theta - \theta_0$ and $B = C(\theta_0)/2H_{max}$. For $Bx^2 \ll 1$, we get $G(\theta)/k_B T = -\ln[ZH_{max}] - Bx^2$. This can be further approximated as $G(\theta)/k_B T = -\ln[ZH_{max}] - \exp[-Bx^2] + 1$ to yield

$$G(\theta)/k_B T = -\ln[eZH_{max}] - \exp[-Bx^2] \quad (5.12)$$

Considering contributions from all x , Eq. 5.12 can be written as: $\tilde{G}(\theta)/k_B T = -\ln[eZH_{max}] - \int_{-\infty}^{+\infty} \exp[-Bx^2] dx$. This integration essentially implies that the contributions around the peak have been taken into account at QH level. The integration gives the modified free energy

$$\tilde{G}(\theta)/k_B T = -\ln[ZH_{max} \exp(\sqrt{\pi/B}) + 1]. \quad (5.13)$$

The corresponding free energy difference is then

$$\Delta\tilde{G}_{conf}(\theta)/k_B T = -\ln[H_{p,max}^c(\theta)/H_{p,max}^f(\theta)] - \left(\sqrt{\pi/B_p^c} - \sqrt{\pi/B_p^f} \right). \quad (5.14)$$

Similar expressions like Eq. 5.10 and 5.14 can be written for the ligand dihedrals as well.

For multi-modal histograms we compute the free energies by taking average, weighted by the maximum values of the peaks. For a particular dihedral ξ with multi-modal histograms in both free and complex states, the free energy cost is given by $\sum_{i,j} c_{ij} \Delta G_{ij}$ where

$\Delta G_{ij} = -k_B T \ln(H_{max,j}^c / H_{max,i}^f)$ representing the free energy cost for transition from i th peak in free state to j th peak in the complex state and $c_{ij} = H_{max,i}^f H_{max,j}^c / (\sum_i H_{max,i}^f + \sum_j H_{max,j}^c)$, the respective weights.

The conformational entropy for a particular dihedral can be estimated directly using the Gibbs entropy formula, given for a dihedral ξ by

$$S_{conf}(\xi) = -k_B \sum_i H_i(\xi) \ln H_i(\xi) \quad (5.15)$$

where the sum is taken over the histogram bins i with a non-zero value of $H_i(\xi)$. Therefore, the conformational entropy change for the dihedral is

$$\Delta S_{conf}(\xi) = -k_B \left[\sum_i H_i^c(\xi) \ln H_i^c(\xi) - \sum_i H_i^f(\xi) \ln H_i^f(\xi) \right]. \quad (5.16)$$

In the QH-limit, the entropy associated with the histogram of any dihedral ξ can be expressed in terms of the entropy of a harmonic oscillator fitted to the peak. The frequency of the oscillator of mass μ and force constant k is given by $\omega = \sqrt{k/\mu} = \sqrt{C/\mu}$. So, entropy is given by $S_{conf}(\xi) = k_B [1 + \ln(2\pi k_B T / h \sqrt{C/\mu})]$, h being the Planck's constant. If C_f and C_c are the curvatures near maxima for the dihedral-histogram in free and complexed states respectively, we have

$$\Delta S_{conf}(\xi) = (1/2)k_B \ln(C_f / C_c) \quad (5.17)$$

For multi-peak histograms QH entropies are obtained by weighted average over the peaks with finite curvature around the maxima.

The thermodynamics of conformational changes of a given residue are finally obtained by adding all the associated dihedral contributions. ΔG_{conf} and ΔS_{conf} of a given region are computed by adding the contributions of all residues in that region. Similarly, the total changes are calculated by adding all residue contributions.

5.2.2 Metal-ion binding to protein

We can write down the free energy cost for dihedral θ for apo- to holo-transition of the protein as

$$\Delta G_{conf}(\theta) = G_{holo}(\theta) - G_{apo}(\theta) = -k_B T \ln[P_{holo}(\theta) / P_{apo}(\theta)], \quad (5.18)$$

where the respective states are indicated by the appropriate subscripts. To arrive at Eq. 5.18 we assume the total partition function Z of the system to remain unchanged in the apo- and the holo-state. These two states differ only by (i) the Ca^{2+} ions and (ii) a few added counter ions that replace some water molecules to maintain constant N . The replacement of water molecules with ions may lead to difference in Z between apo- and holo-state. However, this

difference is proportional to the ratio of fugacities¹¹¹ of the added ions (including Ca^{2+}) and replaced waters, given by $z = \exp(\mu_{ion}/k_B T) \exp(-\mu_{water}/k_B T)$ where μ 's are chemical potentials of the respective species. Since the densities of the ions (ρ_{ion}) are too small, we have $\mu_{ion} \sim \ln \rho_{ion} \rightarrow -\infty$ and hence $z \sim 0$, indicating that the difference in Z between the two states can be safely neglected. This is further supported by very small difference in ionic strengths between the apo-CaM system (0.26) and the holo-CaM system (0.29) simulated here. The total free energy change is then

$$\Delta G_{conf}^{tot} = -k_B T \sum_{\theta} \ln [P_{holo}(\theta) / P_{apo}(\theta)]. \quad (5.19)$$

Here, the contributions from other variables like bond angles, bond vibrations etc. are considered to remain similar in apo- and holo-states since metal-ion binding only alters the secondary and/or tertiary structure of the protein. Consequently, they get decoupled from the dihedrals and their distributions cancel from the ratio in Eq. 5.19. Thermodynamics of solvation are not considered as we focus only on the conformational changes. However, the solvent-effects on conformation have been incorporated via the explicit solvent. The total equilibrium conformational free energy difference in terms of histograms is given from Eq. 5.19 by

$$\Delta G_{conf}^{tot} = -k_B T \sum_{\theta} \ln [H_{holo}^{\max}(\theta) / H_{apo}^{\max}(\theta)], \quad (5.20)$$

The conformational entropy change for any dihedral is obtained from Eq. 5.16:

$$\Delta S_{conf}(\theta) = -k_B \left[\sum_i H_i^{holo}(\theta) \ln H_i^{holo}(\theta) - \sum_i H_i^{apo}(\theta) \ln H_i^{apo}(\theta) \right]. \quad (5.21)$$

5.3 Conformational thermodynamics of CaM-peptide complexes

In this section we discuss the conformational thermodynamics of CaM-peptide complexes. First we describe the details of the simulations. Then the results in the following order are presented on methyl order parameters, dihedral correlations, histograms, conformational entropy and conformational free energy. Then we discuss changes at different binding regions, scaling between methyl order parameters and conformational entropy and predictions using HBM. Finally we discuss different merits, demerits and possible routes to extend the HBM.

5.3.1 Simulation details

For CaM-peptide complexes, we perform all atom MD simulation of the free protein, free peptide and the complex in explicit water. Simulations are done with the NAMD program²⁸⁷ at 308K and 1 atm pressure in isothermal-isobaric (*NPT*) ensemble under standard protocols²⁸⁸, using the CHARMM force-field²⁸⁹, periodic boundary conditions and 1 femtosecond time-step. TIP3P model is used for solvent water molecules. Electroneutrality is maintained via addition of counter-ions (Na^+ or Cl^-). The particle-mesh Ewald method²⁹⁰ is used to treat the long-ranged electrostatic forces. The initial configurations are chosen from following protein data bank (PDB) entries: 1CDL (smMLCK), 1NIW (eNOS), 2O60 (nNOS), 2L7L (CaMKI), 1CKK (CaMKK) and 1CLL (free CaM). The peptide coordinates in the complexes are taken as the initial configurations of the free peptide simulations. We keep the number of total particles including water, pressure and temperature fixed for each case to make the simulated ensembles equivalent. We run 50 ns long simulations to capture most of the protein motions and peptide motions relevant for binding. The equilibration is ensured in any run by monitoring the root mean square deviation of the biomacromolecules, shown in the Figure A1 in Appendix. We analyze the data at two levels: First, we consider the trajectories up to 10 ns since the conformational entropy is dominated primarily by sub-ns side-chain motions^{75, 233}, and calculate the histograms for the dihedral angles from equilibrated configurations sampled beyond 2 ns. Subsequently, we consider the longer 50 ns trajectory and compare data with the shorter run. The dihedral angles are calculated from angle between the relevant atomic planes⁸⁹ given by the Cartesian coordinates of the associated atoms.

5.3.2 Methyl order parameters

By definition S_{Me}^2 of a methyl group increases from zero to unity as its rotation about the long-axis gets restricted indicating lowering of entropy. We compare our calculated methyl group (Figure A2) order-parameters $S_{Me}^2(\text{calc})$ (method in Appendix A) to the experimental data $S_{Me}^2(\text{exp})$ ⁷⁵ in Figure 5.2a (CaM) and 5.2b (peptide) for a representative case: eNOS-complex. Most of the Ala, Met, Val and Thr methyls are close to the perfect correlation line ($S_{Me}^2(\text{exp})=S_{Me}^2(\text{calc})$) or within the $S_{Me}^2(\text{exp})=S_{Me}^2(\text{calc})\pm 0.2$ region, indicating reasonable agreement between the theoretical and experimental values. There are some overestimations, mostly for the Leu methyls, as expected for force-field based MD simulations^{291, 292}. Results of other complexes are shown in Figure A3 and A4.

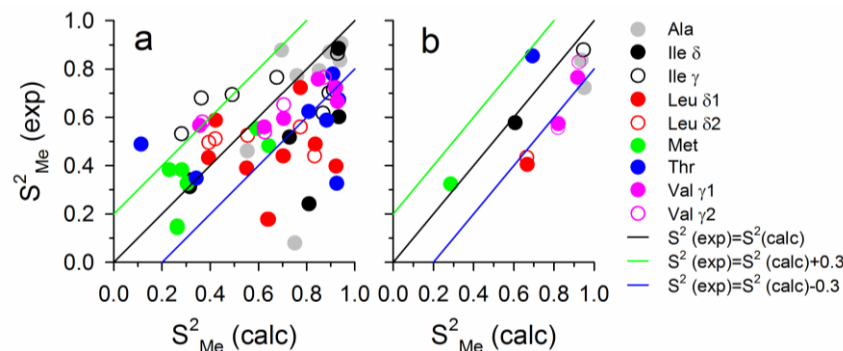


Figure 5.2: Methyl order parameter data. S^2_{Me} are shown for different types of methyls (a) CaM and (b) peptide in the eNOS-complex. Here, the experimental data $S^2_{Me}(\text{exp})$ are plotted against the theoretical $S^2_{Me}(\text{calc})$ values. The straight lines show $S^2_{Me}(\text{exp}) = S^2_{Me}(\text{calc})$ (solid), $S^2_{Me}(\text{exp}) = S^2_{Me}(\text{calc}) + 0.2$ (dotted) and $S^2_{Me}(\text{exp}) = S^2_{Me}(\text{calc}) - 0.2$ (dashed) situations.

5.3.3 Equilibrium correlations among dihedral angles

We choose the backbone dihedrals ϕ , ψ and the side-chain dihedrals χ_1 , χ_2 , χ_3 , χ_4 and χ_5 . Figure 5.3a-c show the equilibrium correlations (Eq. 5.5) among different dihedrals. The correlation data among different dihedrals in CaM (Figure 5.3a) and peptides (Figure 5.3b) in various complexes and the cross-correlations between CaM and peptide dihedrals (Figure 5.3c) indicate nearly zero correlations among the dihedrals which is consistent with the earlier observations^{80, 231}.

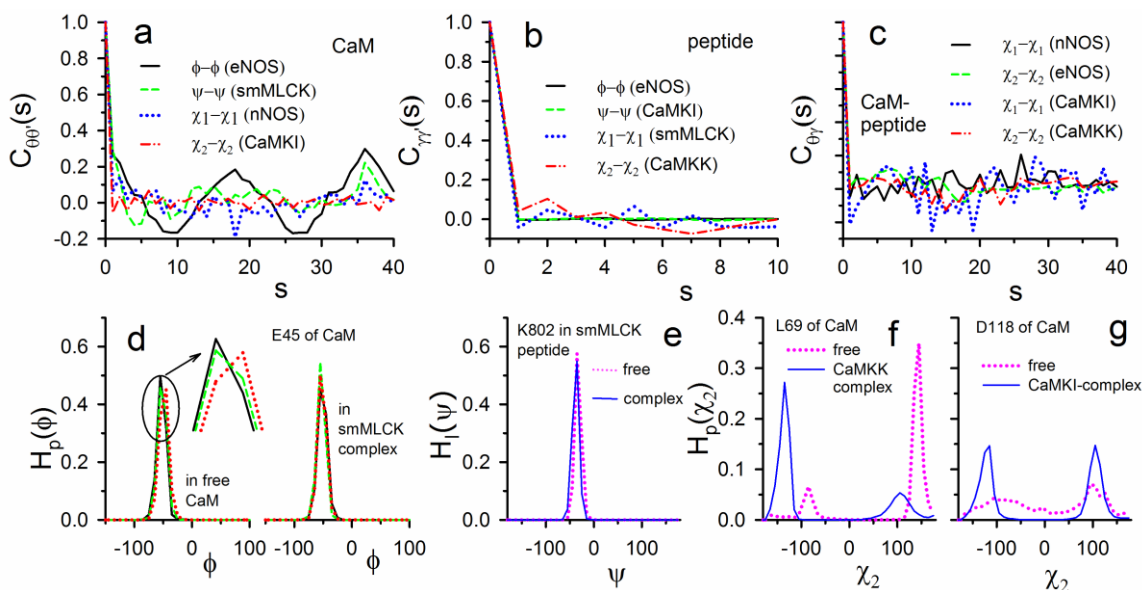


Figure 5.3: Equilibrium dihedral correlations and histograms. (a-c) ξ - ξ' correlations $C_{\xi\xi'}(s)$ (Eq. 5.5) where ξ and ξ' are dihedral angles from two residues and s is the

difference between their locations. (a) Dihedrals of CaM in different complexes: $\xi = \xi' = \phi$ in the eNOS-complex (solid line), ψ in smMLCK-complex (dashed), χ_1 angles in nNOS-complex (dotted) and χ_2 in CaMKI-complex (dash-dot). (b) Dihedrals of peptides in different complexes: $\xi = \xi' = \phi$ in the eNOS-complex (solid line), ψ in CaMKI-complex (dashed), χ_1 angles in smMLCK-complex (dotted) and χ_2 in CaMKK-complex (dash-dot). (b) Cross-correlations among side-chain dihedrals ξ from protein and ξ' from peptide: $\xi = \xi' = \chi_1$ in nNOS-complex (solid), χ_2 in eNOS-complex (dashed), χ_1 in CaMKI-complex (dotted) and χ_2 in CaMKK-complex (dash-dot). Representative histograms of (d) ϕ of Glu45 of CaM in free and bound form in smMLCK-complex. The inset shows the near-peak region for the free case. In each case three convergent histograms are shown in solid, dashed and dotted lines sampled from different parts of the MD-trajectory; (e) ψ of Lys802 of smMLCK peptide in free (dotted) and CaM-bound form (solid). Multi-modal histograms are shown for (f) χ_2 of CaM residue Leu69 in free and bound form in CaMKK complex and (g) χ_2 of CaM residue Asp118 in free and bound form in CaMKI complex.

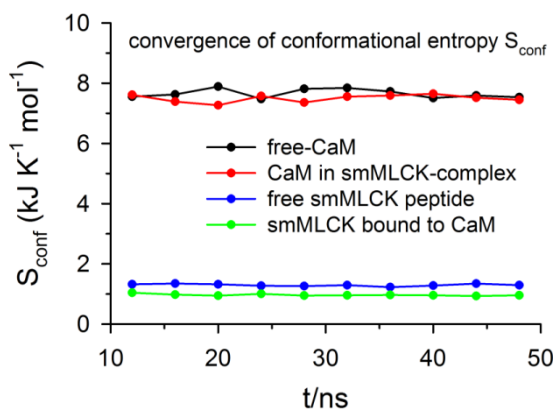


Figure 5.4: The convergence of conformational entropy during the simulation. A representative case of smMLCK complex is shown. The CaM and peptide contributions individually remain almost invariant with time demonstrating the robustness of the histogram technique. The errors in calculated S_{conf} for free CaM ($0.05 \text{ kJ K}^{-1}\text{mol}^{-1}$) and for CaM in the complex ($0.04 \text{ kJ K}^{-1}\text{mol}^{-1}$) are quite small. The errors in the peptide-data are nearly zero.

5.3.4 Histograms of dihedrals and convergence of thermodynamics

In absence of significant correlations, we consider the histograms of the individual dihedrals for the calculation of thermodynamics. The histograms are calculated over 10 sets of equilibrated configurations each having 1000 samples from different parts of the trajectory. Figure 5.3d shows three such histograms in free and complex states for the

dihedral angle ϕ of CaM-residue Glu45 in smMLCK-complex. The similarities of these histograms indicate the convergence of thermodynamic quantities calculated based on them, for instance, conformational entropies (Figure 5.4). Due to equivalence of the samples we compute the overall changes in entropy and free energy via a flat average over the entire equilibrium trajectory. All the backbone dihedrals exhibit sharply single-peaked histograms with the maxima around the equilibrium values in the initial configuration (PDB coordinates). Histograms of ψ dihedral of a peptide residue Lys802 of smMLCK peptide are shown in Figure 5.3e. Multi-modal histograms have been mostly observed for the side-chain dihedrals, as illustrated in Figure 5.3f for χ_2 of CaM residue Leu69 and Figure 5.3g for χ_2 of CaM residue Asp118, indicating different rotameric states.

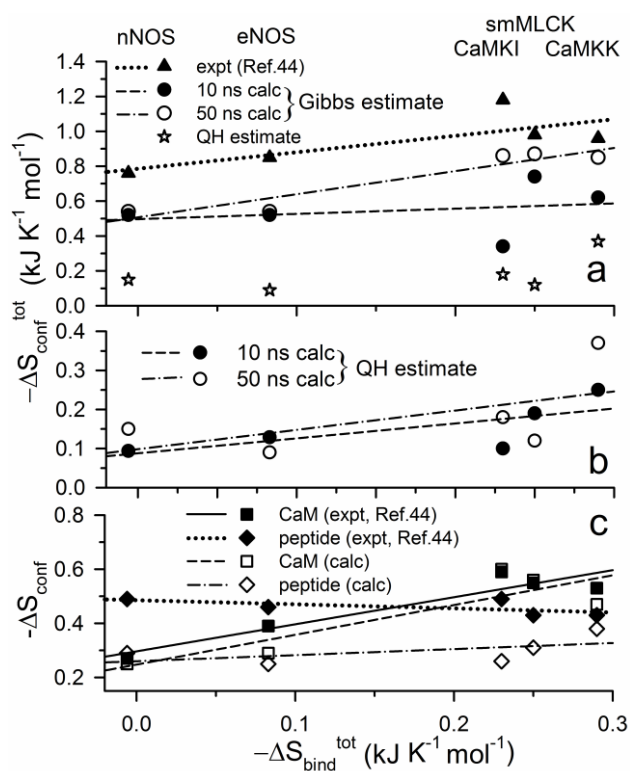


Figure 5.5: Conformational entropy data. (a-b) Comparison of theoretical and experimental ΔS_{conf}^{tot} for CaM-peptide binding plotted against the experimental ΔS_{bind}^{tot} from ITC measurements²³³: (a) Calculated ΔS_{conf}^{tot} (Gibbs formula) from the 10 ns runs (filled circles), the 50 ns runs (open circles) along with the experimental ΔS_{conf}^{tot} (Marlow et al⁷⁵) (filled triangles). The lines represent the best linear fits: 10 ns (dashed), 50 ns (dash-dot) and the experimental data (dotted). The stars represent the 50 ns ΔS_{conf}^{tot} data in QH-limit. (b) Calculated ΔS_{conf}^{tot} from 10 ns simulations (filled circles) and 50 ns simulations (open circles) using QH approximation. The best linear fits: 10 ns (dashed,

m=0.39, R²=0.53) and 50 ns (dash-dot, m=0.47, R²=0.32). (c) The conformational entropy contributions of the components from 50 ns run plotted against ΔS_{bind}^{tot} : CaM contributions (open squares) with the best fit line (dashed) and peptide contributions (open diamonds) with the best fit line (dash-dot). The corresponding experimental data⁷⁵ are also shown for CaM contributions (filled squares) with the best fit line (solid) and peptides (filled diamonds) with best fit line (dotted).

5.3.5 Conformational entropy

In Figure 5.5, we compare our calculated total conformational entropies ΔS_{conf}^{tot} of the complex with the available experimental results. First we consider the results calculated using the Gibbs formula (Eq. 5.16) (Figure 5.5a). Here we compare the 10 ns and 50 ns data with the experimental ΔS_{conf}^{tot} (filled triangles) reported in Marlow et al⁷⁵. Both the theoretical and experimental ΔS_{conf}^{tot} are plotted against the corresponding ΔS_{bind}^{tot} from ITC²³³, showing linear correlations between ΔS_{conf}^{tot} and ΔS_{bind}^{tot} . The 10 ns data (filled circles) can account for the experimental trend (filled triangles) except for CaMKI and CaMKK. However, the best fit correlation line has slope $m = 0.3$ and linear correlation coefficient $R = 0.3$ which are far from the experimental data ($m = 0.95$ and $R = 0.75$). The 50 ns data (open circles) provide an overall better estimate for all cases where the correlation line ($m = 1.3$ and $R = 0.95$) agree quite well with the experimental data. One reason of the underestimation by the 10 ns data for CaMKI and CaMKK could be the fact that the initial configurations for simulations in these two cases are NMR determined structures. For other complexes the initial structures are from crystallographic data where the 10 ns and 50 ns data hardly make any difference. NMR-data generate an ensemble of structures, unlike the only structure obtained from crystallography. Therefore, equilibration of the solution-NMR structures may not have been completed properly in the 10 ns simulation run. Figure 5.5a further shows that ΔS_{conf}^{tot} from QH approximation (Eq. 5.17) (open stars) leads to underestimation, although the linear correlation between ΔS_{conf}^{tot} and ΔS_{bind}^{tot} is observed here as well (Figure 5.5b).

The ΔS_{conf} (in $\text{kJ K}^{-1} \text{mol}^{-1}$) for all the side-chain dihedrals in the complexes showing multi-peak histograms are -0.43 (nNOS), -0.23 (eNOS), -0.57 (CaMKI), -0.56 (smMLCK) and -0.58 (CaMKK) obtained using the Gibbs formula. Such multi-modal histograms contribute more than 60% of the total conformational entropy stabilizations of the complexes, indicating the importance of the redistributions of populations among various side-chain rotamers in the binding. In Figure 5.5c, we report the contributions of the CaM and peptide separately in the complexes, estimated from the 50 ns runs. The CaM contributions show

good agreement between the theoretical (open squares) and the experimental data (filled squares). The best fit theoretical line (dashed, $m = 1.1$, $R = 0.88$) almost quantitatively matches the experimental correlation line (solid, $m = 1.0$, $R = 0.94$)⁷⁵. We find CaM in CaMKI to be entropically most stabilized and least stabilized in nNOS which support the same experimental observations⁷⁵. In the same line for the peptide, we get similar entropic stabilization for all the cases.

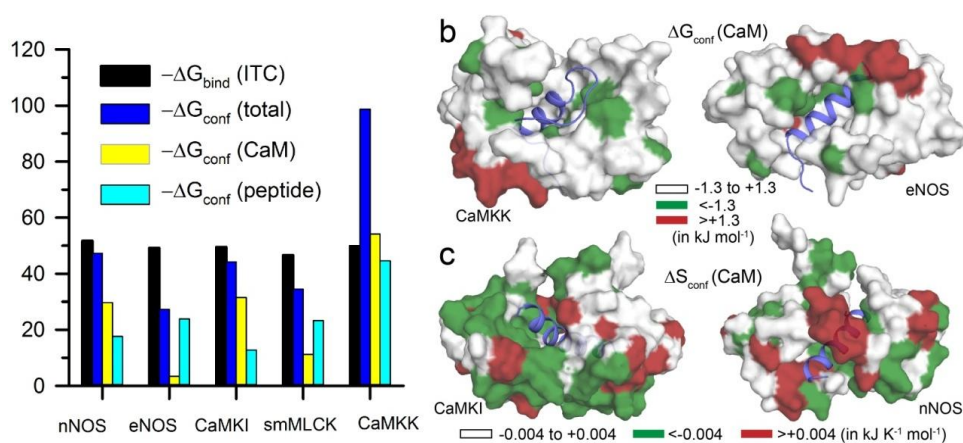


Figure 5.6: Conformational free energy data. (a) Calculated ΔG_{conf}^{tot} and the individual protein and peptide contributions along with the experimental ΔG_{bind}^{tot} . All data are in kJ mol⁻¹. Surface representations of CaM-peptide complexes showing the residue-wise (b) ΔG_{conf} of CaM for the cases where the protein is most stabilized (CaMKK) and least stabilized (eNOS); (c) ΔS_{conf} of CaM in most ordered (CaMKI) and disordered (nNOS) complexes. The stabilized residues are green and destabilized ones are red. The residues undergoing minor changes are white. Peptide is in violet cartoon representation.

5.3.6 Conformational free energy

The total conformational free energy changes ΔG_{conf}^{tot} calculated from histogram maxima (Eq. 5.10) and the contributions of the components are shown in Figure 5.6a along with the experimental total binding free energy cost²³³ ΔG_{bind}^{tot} . The $-\Delta G_{bind}^{tot}$ values fall in a very narrow window (45-52 kJ mol⁻¹). Our estimated $-\Delta G_{conf}^{tot}$ also lie in a similar range (27-47 kJ mol⁻¹) for four complexes except CaMKK where the extent of stabilization is nearly double. This separates out CaMKK from the others which may be a signature of its opposite binding orientation compared to other four: While binding to CaM, N-terminal of four of the peptides interact with the C-terminal of CaM, except CaMKK for which C-terminal of the peptide interacts with the N-terminal of the protein and so on²⁷⁹. We also estimate the

contributions to ΔG_{conf}^{tot} due to finite width of the histograms using Eq. 5.14, to be only 1-5% of the estimate from histogram maxima for all the complexes except smMLCK for which this difference is ~15%. Although it seems from ΔG_{bind}^{tot} -data that all the peptides exhibit similar affinity to CaM, the conformational contributions of the components bring out a different picture. The protein is conformationally most stabilized in CaMKK-complex, while least stabilized in eNOS-complex. The peptide, on the other hand, is stabilized similarly in all the cases except in CaMKK-complex.

Table 5.1: Conformational thermodynamics of different highly stabilized peptide binding regions of CaM in the complexes. The residue numbers according to the PDB indices are listed. The conformational free energy and entropy contributions of these binding regions are shown along with their percentages of charged and polar residue contributions (CPRC) and hydrophobic residue contributions (HRC).

peptide	CaM residues	ΔG_{conf} (kJ mol ⁻¹)			ΔS_{conf} (kJ K ⁻¹ mol ⁻¹)		
		Total	CPRC (%)	HRC (%)	Total	CPRC (%)	HRC (%)
nNOS	11-19, 36-41, 42-50, 84-92	-18.2	43	24	-0.1	31	29
eNOS	11-19, 117-123	-6.5	64	14	-0.05	76	4
CaMKI	7-10,36-41, 42-50, 52-55, 71-76, 84-92, 105-116	-32.9	57	26	-0.44	68	15
smMLCK	11-19, 36-41, 52-55, 84-92, 105-116, 117-123	-9.0	59	14	-0.27	65	12
CaMKK	7-10, 11-19, 36-41, 42-50, 52-55, 84-92, 105-116, 124-128	-41.3	49	27	-0.24	49	22
DAPK2	11-19, 35, 36-41, 42-50,124-128	-17.9	64	15	-0.24	55	23

5.3.7 Thermodynamics at individual binding regions

The thermodynamic changes at each protein residue are shown by surface representations in Figure 5.6b-c for the most and least stabilized complexes, both free-energetically and entropically. In Figure 5.6b, CaMKK and eNOS complexes are shown, where the green residues are stabilized, the red residues are destabilized and the white residues undergo a marginal change in conformational free energy. In Figure 5.6c we show

the entropy changes for CaMKI and nNOS complexes where the green residues are ordered while the red residues are disordered in the bound protein compared to the free state. Similar surface representations showing residue-level changes of the other complexes are included in Figure A5.

Next we examine closely the changes in the peptide binding regions (PBR) of CaM. If any atom of a protein residue comes within a distance of 5 Å of a peptide atom, we consider the corresponding residue to be part of the PBR. The thermodynamic contribution of a PBR is obtained by summing over the contributions of the residues that are part of the PBR. Different PBRs show different degree of thermodynamic stabilizations. The residues in linker helix responsible for the wrapping the peptide, constitute the most destabilized PBRs. The deformation of linker helix occurs for different peptides at slightly different locations where a coiled region is formed due to loss of secondary structure element. For instance, in nNOS-complex the coil is produced over the residues 77-83 ($\Delta G_{\text{conf}} = +19.8 \text{ kJ mol}^{-1}$ and $\Delta S_{\text{conf}} = +0.07 \text{ kJ K}^{-1} \text{ mol}^{-1}$), whereas it is 73-76 for smMLCK ($\Delta G_{\text{conf}} = +11.7 \text{ kJ mol}^{-1}$ and $\Delta S_{\text{conf}} = 0.0 \text{ kJ K}^{-1} \text{ mol}^{-1}$) and 76-81 for CaMKK ($\Delta G_{\text{conf}} = +20.6 \text{ kJ mol}^{-1}$ and $\Delta S_{\text{conf}} = +0.08 \text{ kJ K}^{-1} \text{ mol}^{-1}$). For the other two complexes these regions are residues 77-83 with the changes being for eNOS ($\Delta G_{\text{conf}} = +15.6 \text{ kJ mol}^{-1}$ and $\Delta S_{\text{conf}} = +0.08 \text{ kJ K}^{-1} \text{ mol}^{-1}$) and CaMKI ($\Delta G_{\text{conf}} = +12.8 \text{ kJ mol}^{-1}$ and $\Delta S_{\text{conf}} = +0.12 \text{ kJ K}^{-1} \text{ mol}^{-1}$).

The huge free energy cost at the destabilized PBR is compensated by the favourable changes at the other PBRs and the peptides. The changes at the most stabilized PBRs for different complexes are shown in Table 5.1. Furthermore, CaM being an acidic protein interacting with all these peptides rich with basic residues, the electrostatic contributions are also expected to play an important role. We analyze from our calculations the contributions of these protein-peptide interactions in some highly stabilized PBRs. It is quite apparent from Table 5.1 that the charged and polar residue contributions dominate in all the cases, for both conformational free energy as well as entropy. The highly stabilized common binding regions in all the complexes are CaM-residues 11-19 (EFKEAFSLF), 36-41 (MRSLGQ), 42-50 (NPTEAELQD), 52-55 (INEV), 84-92 (EIREAFRVF) and 105-116 (LRHVMHNLGEKL). Evidently, these PBRs are rich in charged (E, D, R, K, H) and polar (S, Q, N, T) residues making it the dominating stabilizing factor in CaM-peptide complexes. Table 5.1 also shows that there are stabilized residues with hydrophobic side-chains (F, A, L, I, V, M) as well, undergoing substantial conformational stability in the binding, as pointed out earlier from structural analyses⁶⁹ and recent NMR studies²⁸⁰.

5.3.8 Scaling of conformational entropy with methyl order parameters

The agreement between our results on ΔS_{conf} and those of Marlow et al.⁷⁵ has got a strong implication. Marlow et al.⁷⁵ connects the NMR data on $\langle \Delta S_{Me}^2 \rangle$, the average changes of residue weighted S_{Me}^2 , to ΔS_{conf} for several CaM-peptide complexes. By definition, $\langle \Delta S_{Me}^2 \rangle = n_{CaM} \langle \Delta S_{Me}^2 \rangle^{CaM} + n_{pep} \langle \Delta S_{Me}^2 \rangle^{peptide}$ where n_{CaM} and n_{pep} are the numbers of residues in CaM and peptide respectively. $\langle \Delta S_{Me}^2 \rangle^{CaM} = \langle S_{Me}^2 \rangle_c^{CaM} - \langle S_{Me}^2 \rangle_f^{CaM}$ and $\langle \Delta S_{Me}^2 \rangle^{peptide} = \langle S_{Me}^2 \rangle_c^{peptide} - \langle S_{Me}^2 \rangle_f^{peptide}$ where the average is taken over the available methyl groups in the respective system. The underlying assumption is that $\langle \Delta S_{Me}^2 \rangle$ is a measure of conformational disorder at any residue so that S_{Me}^2 is a dynamical proxy for conformational entropy. This identification heavily relies on the linearity of $(\Delta S_{bind}^{tot} - \Delta S_{sol})$ with experimental $\langle \Delta S_{Me}^2 \rangle$ (ΔS_{sol} being the calculated solvent contribution⁷⁵) as shown in Figure 5.7a (dotted line, $m=-0.039$) that leads to linear dependence of ΔS_{conf}^{tot} on $\langle \Delta S_{Me}^2 \rangle$ with the same slope.

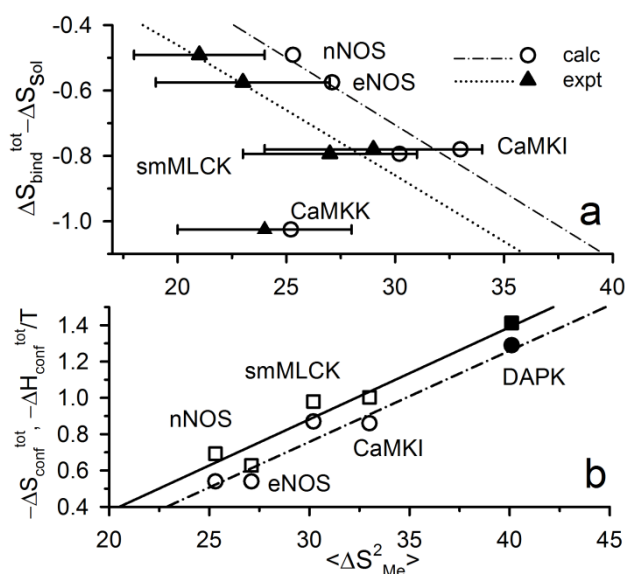


Figure 5.7: Conformational entropy and methyl order parameters. (a) $(\Delta S_{bind}^{tot} - \Delta S_{sol})$, taken from Marlow et al.⁷⁵, plotted against experimental⁷⁵ (triangles with error bars) and our calculated (open circles) values of $\langle \Delta S_{Me}^2 \rangle$. CaMKK is an outlier to the experimental best fit line (dotted, $m=-0.039$, $R=0.97$) as well as the best fit through the calculated data (dash-dot, $m=-0.042$, $R=0.98$). **(b)** Plot of $-\Delta S_{conf}^{tot}$ (circles) and $-\Delta H_{conf}^{tot}/T$ (squares) vs. $\langle \Delta S_{Me}^2 \rangle$ from our calculations excluding CaMKK. Both the best fit lines (dash-dot for $-\Delta S_{conf}^{tot}$ and solid for $-\Delta H_{conf}^{tot}/T$) show a linear relationship.

ΔS_{conf}^{tot} and solid for $-\Delta H_{conf}^{tot}/T$) have $m=0.05$. The solid symbols represent the data for the CaM-DAPK2 complex.

We calculate $\langle \Delta S_{Me}^2 \rangle$ from our simulation data on S_{Me}^2 in order to check whether we could recover the experimentally observed linearity between $(\Delta S_{bind}^{tot} - \Delta S_{sol})$ and $\langle \Delta S_{Me}^2 \rangle$. The estimation of $\langle \Delta S_{Me}^2 \rangle$ from simulation is somewhat tricky. Although $\langle S_{Me}^2 \rangle_c^{CaM}$ and $\langle S_{Me}^2 \rangle_f^{CaM}$ remain very similar over the entire equilibrium trajectory, $\langle S_{Me}^2 \rangle_c^{peptide}$ and $\langle S_{Me}^2 \rangle_f^{peptide}$ converge slowly with convergence achieved typically beyond 12 ns (Figure A6). Such slow convergence is probably due to the presence of fewer methyl groups than in protein. The convergence for smMLCK is the poorest, for it has the least number (8) of methyl groups. This slow convergence for peptides leads to pronounced variations in $\langle \Delta S_{Me}^2 \rangle$ arising due to large multiplicative factors ($n_{CaM} = 148$ and $n_{pep} \sim 20$). Therefore, we consider only the long-time part of the trajectory to estimate $\langle \Delta S_{Me}^2 \rangle$. The $(\Delta S_{bind}^{tot} - \Delta S_{sol})$ from Marlow et al⁷⁵ is linear with our calculated $\langle \Delta S_{Me}^2 \rangle$ (dash-dot line in Figure 5.7a, $m = -0.042$) excluding the data for CaMKK which is an outlier in the experimental plot as well. A microscopic justification for the use of S_{Me}^2 as a dynamical proxy of conformational entropy in Marlow et al⁷⁵ is provided by Figure 5.7b showing the linearity between our estimated ΔS_{conf}^{tot} (open circles) from dihedral distributions and simulated $\langle \Delta S_{Me}^2 \rangle$ (dash-dot line) with very similar slope ($m = -0.050$). Since, our calculated ΔG_{conf}^{tot} values are very similar for different complexes except CaMKK, the conformational enthalpy changes $\Delta H_{conf}^{tot} (= \Delta G_{conf}^{tot} + T\Delta S_{conf}^{tot})$ should also have the same linearity with $\langle \Delta S_{Me}^2 \rangle$ as ΔS_{conf}^{tot} for thermodynamic consistency. We find this indeed is the case in Figure 5.7b, also showing the plot of $\Delta H_{conf}^{tot}/T$ values (open squares) of the complexes, excluding the outlier CaMKK.

5.3.9 Prediction

We apply our approach to make predictions on the conformational thermodynamics of binding of a target peptide from death associated protein kinase (DAPK2)²⁹³ to CaM. Here, the S308D mutant of DAPK2 has been considered with a high resolution crystal structure

(PDB ID 1ZUZ) and known ITC data ($\Delta G_{bind}^{tot} = -39.5 \text{ kJ mol}^{-1}$ and $\Delta S_{bind}^{tot} = -0.28 \text{ kJ K}^{-1} \text{ mol}^{-1}$ at 300K)²⁹³. However, nothing is known regarding the conformational entropies of this system to the best of our knowledge. We perform 20 ns runs for this complex and the free peptide as we have seen earlier that shorter runs are sufficient to capture the conformational thermodynamics if crystal structures are employed as starting configurations. The residue-wise S_{Me}^2 data are given in Figure A7. We find $\Delta S_{conf}^{tot} = -1.29 \text{ kJ K}^{-1} \text{ mol}^{-1}$ using the Gibbs formula where the CaM and peptide contributions are -0.98 and $-0.31 \text{ kJ K}^{-1} \text{ mol}^{-1}$ respectively. The ΔS_{conf}^{tot} value follow the same linear scaling with $\langle \Delta S_{Me}^2 \rangle$ as the other complexes as shown by the closed circle in Figure 5.7b. We get $\Delta G_{conf}^{tot} = -38.1 \text{ kJ mol}^{-1}$ with CaM and peptide contributions being -15.4 and $-22.7 \text{ kJ mol}^{-1}$, respectively. These free energy values are very similar to the case of smMLCK. The calculated ΔH_{conf}^{tot} (filled square) falls, just like ΔS_{conf}^{tot} , on the line drawn for other complexes in Figure 5.7b. Residues 77-83 constitute the maximum destabilized PBR in DAPK2-complex with very similar changes as earlier: $\Delta G_{conf} = +21.2 \text{ kJ mol}^{-1}$ and $\Delta S_{conf} = +0.02 \text{ kJ K}^{-1} \text{ mol}^{-1}$. Surface representations of CaM-DAPK2-complex are included in Figure A5 where contributions of different CaM-residues are shown. The changes of highly stabilized PBRs are listed in Table 5.1 along with the associated contributions of charged and hydrophobic residues.

5.3.10 The HBM: merits, demerits and extensions

Efficiency of any computational method depends on the simulation length to generate a convergent thermodynamics. The present method is highly advantageous from that point of view as indicated by the convergence of the histograms and conformational entropy (Figure 5.4) obtained from different parts of trajectory. The convergence has been achieved with shorter runs (10 ns) where initial configurations are taken from available crystal structures, while longer runs (50 ns) are required for the solution-NMR derived initial structures. The reduced histograms can also be generated from suitable model initial structures in the absence of PDB structure. However, the equilibration may depend on how the initial conditions are constructed.

As far as the efficiency of the method used to extract ΔS_{conf} from the histograms is concerned, both the Gibbs formula and QH-approximation are computationally comparable when the dihedrals are uncorrelated. Although the Gibbs formula is more accurate, the QH approximation is often used for its simplicity and as a benchmark-tool for analyses with

probability distributions of conformational variables. However, the QH approximation underestimates ΔS_{conf} in our studies. It may be stressed that we use the QH approximation to incorporate the free energy contributions for conformations away from the equilibrium value marked by histogram maxima. Such treatment is meaningful due to low weightage of those conformations compared to the equilibrium conformation.

Experimentally, large amplitude rigid body domain motions have been observed for CaM in time scales much longer than 50 ns⁷⁸. Due to high conservation of the compact structures among all the complexes these domain motions are not expected to vary much from one to another. Such motions of time scale \sim milliseconds⁷⁸, in both free and complex states, would be decoupled from the sub-ns highly localized side-chain motions⁷⁵ that control the conformational thermodynamics. Even if we consider the entropy change associated with such motions, given by the logarithm of the ratio of two high-frequencies in free and complex states, the contribution would be insignificant.

The uncorrelated dihedral angles reduce the computation-cost enormously. However, when the correlations of the conformational variables cannot be neglected, the correlation matrix can be diagonalized to obtain the uncorrelated basis and used for the calculations. For any two conformational variables ξ_i and ξ_j the covariance matrix is symmetric since $C_{ij} = C_{ji}$. Therefore, one can determine a set of uncorrelated variables $\{\tilde{\xi}_i\}$ by diagonalizing the covariance matrix, $\tilde{\xi}_i = \sum_j \lambda_{ij} \xi_j$ where $[\lambda_{ij}]$ is the transformation matrix found by the eigenvalues. The maximum of a sharp histogram of a given variable is essentially equal to its mean and the curvature given by the variance. The mean of the transformed variable, $\langle \tilde{\xi}_i \rangle = \sum_j \lambda_{ij} \langle \xi_j \rangle$, the variance: $\mathbf{Var}(\tilde{\xi}_i) = \lambda_{ii}^2 \mathbf{Var}(\xi_i) + \sum_{j,k} \lambda_{ij} \lambda_{jk} \mathbf{Cov}(\xi_j \cdot \xi_k)$.

5.4 Conformational thermodynamics for Ca²⁺-ion binding to CaM

In this section we consider the thermodynamics of conformational changes for Ca²⁺-ion binding to apo-CaM. The equilibrium dihedral correlations and histograms in apo- and holo-CaM are shown in section 5.4.1. Overall thermodynamics and domain contributions are discussed in 5.4.2. Then we present the contributions of the Ca²⁺ binding loops in detail in 5.4.3. Changes in the linker in CaM are discussed in 5.4.4. We comment on generalization of our observations for other proteins in section 5.4.5.

5.4.1 Dihedral correlations and histograms

To study metal-ion binding to apo-CaM we simulate from the PDB structure 1CFD for apo-state of CaM. The equilibrium correlations (Figure 5.8a-b) among different side-chain dihedrals in both apo- and holo-CaM turn out to be negligible (Figure 5.8a), although the backbone dihedrals show short-ranged correlations (Figure 5.8b). In section 5.3.3 we have shown that one can ignore such correlations in the calculations of the thermodynamic quantities. Accordingly, we treat the dihedrals as independent conformational variables^{80, 83}.

Some sample histograms of apo- and holo-CaM dihedral angles are shown in Figure 5.8c-f. The backbone dihedral histograms generally have one sharp peak typically around the values in PDB structure. This is illustrated in Figure 5.8c-d for ϕ of a loop I residue Glu31 (Figure 5.8c) and ψ of Thr79, residue in the linker (Figure 5.8d). We find significant increase in the histogram peak value with reduction of width from apo- to holo-state indicating increase in rigidity of the protein backbone due to binding to Ca^{2+} . The Ca^{2+} -coordinating side-chains are more prone to changes induced by metal-ions. For instance, the χ_2 -histogram of Ca^{2+} binding residue Asp133 (loop IV) exhibits two broad peaks in apo-state (Figure 5.8e) each indicating a rotamer, while there is one sharp peak in holo-state. For Ser81 in the loop region of the linker helix in apo-CaM (marked in Figure 5.1), the χ_1 -histogram (Figure 5.8f) shows a very similar behaviour as in Figure 5.8e. This observation demonstrates the suppression of side-chain fluctuations induced by the binding of metal-ions.

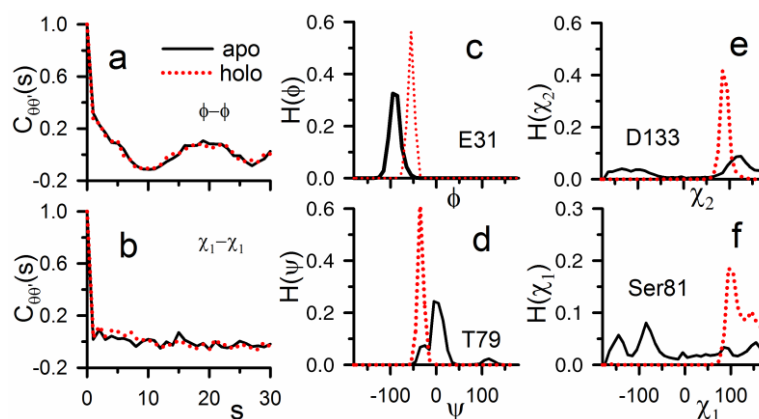


Figure 5.8: Equilibrium dihedral correlations and histograms in apo- and holo-CaM. $C_{\theta\theta'}(s)$ (Eq. 5.5) for (a) $\theta = \theta' = \phi$ and (b) $\theta = \theta' = \chi_1$ in apo- and holo-CaM. Histograms for dihedrals (c) ϕ (Glu31), (d) ψ (Thr79), (e) χ_2 (Asp133) and (f) χ_1 (Ser81) in apo and holo-CaM. Line description for all panels is same as in panel a.

5.4.2 Overall thermodynamics data

The conformational thermodynamic changes have been calculated for the holo-state with respect to the apo-state. A negative value of ΔG_{conf} means stabilization in holo-state than in apo-state, while positive values indicate destabilization. As far as ΔS_{conf} is concerned, a negative value means ordering in holo-state with respect to apo, while positive ΔS_{conf} suggest disordering. We find $\Delta G_{conf}^{tot} = -54.9 \text{ kJ mol}^{-1}$ for binding of four Ca^{2+} , nearly 30% of the experimentally measured binding free energy²⁸². The corresponding $T\Delta S_{conf}^{tot} = -128.7 \text{ kJ mol}^{-1}$ indicating substantial drop in conformational flexibility due to Ca^{2+} binding. In absence of any experimental data, we provide an alternative verification of our estimated $T\Delta S_{conf}^{tot}$ from $\langle \Delta S_{Me}^2 \rangle$ calculated from the simulations⁸³. We estimate $\langle \Delta S_{Me}^2 \rangle = 10.95$ (detailed order parameter data shown in Figure A8-A10 in Appendix). Using the theoretical value of the slope⁸³ (-0.05) of the linear dependence between $T\Delta S_{conf}^{tot}$ and $\langle \Delta S_{Me}^2 \rangle$, we find $T\Delta S_{conf}^{tot} = -169 \text{ kJ mol}^{-1}$ which is close to the estimated $T\Delta S_{conf}^{tot}$ from dihedral histograms.

As far as the domain-specific data are concerned, we find the N-domain of CaM conformationally more stabilized ($\Delta G_{conf} = -26.5 \text{ kJ mol}^{-1}$) in presence of Ca^{2+} ions compared to the C-domain ($\Delta G_{conf} = -15.5 \text{ kJ mol}^{-1}$). This observation matches with the trend of domain-wise binding free energies in earlier grafting experiment¹⁰⁰ and isothermal titration calorimetry measurement¹⁰¹. Entropically both domains get ordered when bound to metal-ions, N-domain being more ordered ($T\Delta S_{conf} = -66.3 \text{ kJ mol}^{-1}$) compared to the C-domain ($T\Delta S_{conf} = -36.1 \text{ kJ mol}^{-1}$).

5.4.3 Conformational changes of the Ca^{2+} binding loops

Figure 5.9 summarizes the loop-wise data on conformational entropy change $T\Delta S_{conf}^L$ ($L=I, II, III$ and IV) (Figure 5.9a) and free energy change ΔG_{conf}^L (Figure 5.9b) of the Ca^{2+} -ion binding to CaM. Loop I, II and IV undergo conformational ordering and stabilization upon Ca^{2+} binding as indicated by negative values of both $T\Delta S_{conf}^L$ and ΔG_{conf}^L . Loop III, however, shows a different trend. The $T\Delta S_{conf}^L$ -value of loop III shows slight disordering upon the metal-ion binding, while the ΔG_{conf}^L value indicates marginal stabilization. The finding of different ΔG_{conf}^L values for the four loops is consistent with the earlier experimental observations^{100, 101} of four different Ca^{2+} binding constants for CaM, indicating different affinities of the four EF-hands.

Figure 5.9 also shows the contributions of different type of residues in these loops towards the respective $T\Delta S_{conf}^L$ (Figure 5.9a) and ΔG_{conf}^L (Figure 5.9b). The trends are very similar in both the panels for all the loops. In all cases except loop III, the main change comes

from the acidic residues, nearly all coordinating to Ca^{2+} . However, the ordering and stabilization of the acidic residues in loop III is nearly half of those observed in loops I and IV. The basic residues in loops I are ordered and stabilized, while that in loop III remains almost unchanged. The residues with hydrophobic side-chains and those with polar side-chains order and stabilize amply in loops I, II and IV.

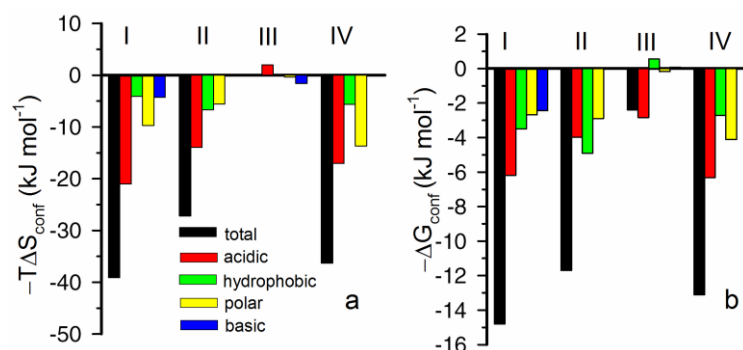


Figure 5.9: Data of the four EF-hand loops. (a) $T\Delta S_{conf}$ and (b) ΔG_{conf} , showing the total changes and contributions of different types of residues. The loop descriptions are: loop I - residues 20-31 (amino acid sequence DKDGDGTITTKKE), loop II - residues 56-67 (sequence DADGNGTIDFPE), loop III - residues 93-104 (sequence DKDGNGYISAAE) and loop IV - residues 129-140 (sequence DIDGDGQVNYEE).

Figure 5.10 presents the residue-wise conformational entropy changes $T\Delta S_{conf}^i$ (Figure 5.10a), i being the residue-index, and conformational free energy changes ΔG_{conf}^i (Figure 5.10b) of the four EF-hand loops using cartoon representations. Earlier studies have shown^{100, 284} that the stabilities of these loops depend heavily on their amino acid compositions and the charge of the binding cation. Although the four Ca^{2+} binding loops of CaM are structurally very similar and all of them show strong sequence conservation at three loop positions 1, 6 and 12, their conformational stabilizations upon binding of Ca^{2+} are different as revealed on closer inspection.

All of the four acidic residues in loop I: Asp20, Asp22, Asp24 and Glu31, coordinate to Ca^{2+} , get ordered and stabilized. The only uncharged Ca^{2+} coordinating residue Thr26 also undergoes high ordering and good stabilization. There are several non-coordinating loop residues as well which show thermodynamic changes. The basic residue Lys21, located between acidic Asp20 and Asp22, also undergo favourable changes. The backbone between Asp20 and Asp22 closes up somewhat upon Ca^{2+} binding. This brings the side-chain of Lys21, projecting outward perpendicularly to the loop-backbone in the apo-state, within the range of electrostatic interactions with the negatively charged side-chains of Asp20 and

Asp22 in the holo-state. The other basic residue Lys30 is also ordered and stabilized, with its side-chain drawn near the polar residue Thr29 undergoing favourable charge-dipole interaction. Among the hydrophobic residues Ile27, the structural linker with loop II¹⁰⁰, gets ordered with a high stabilization.

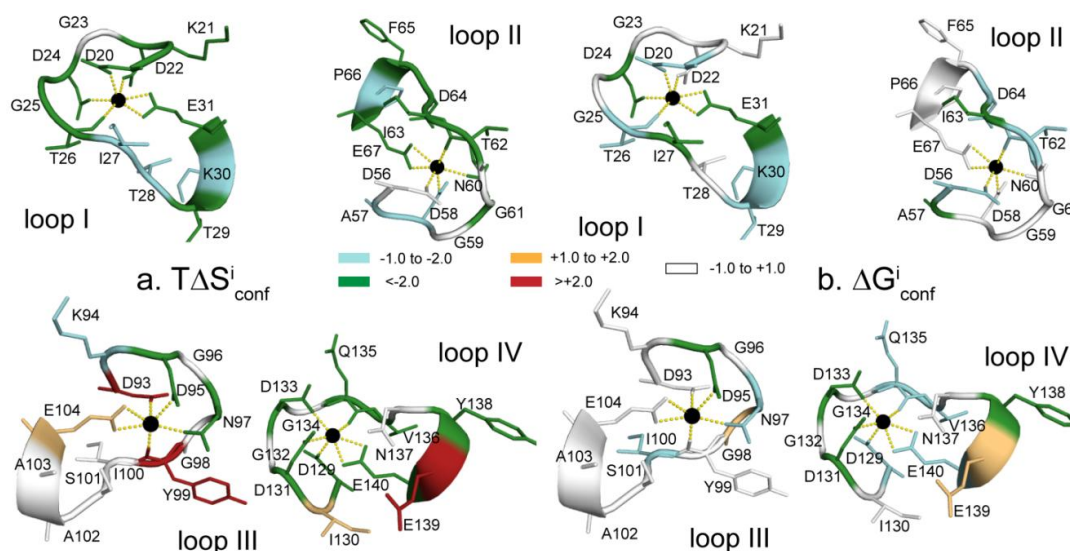


Figure 5.10: Cartoon representations of the EF-hand loops in holo-CaM to show the residue-wise data. (a) $T\Delta S_{conf}^i$ and (b) ΔG_{conf}^i (in kJ mol^{-1}). The colours are described in the figure.

In case of Loop II, the Ca^{2+} coordinating ligands are acidic residues Asp56, Asp58, Glu67 and the polar residues Asn60 and Thr62. All become ordered upon metal-ion binding, but the extent of ordering is less compared to the Ca^{2+} coordinating residues in loop I. Maximum ordering is observed for Glu67, a bidentate Ca^{2+} coordinating ligand like Glu31 in loop I. The smaller $T\Delta S_{conf}^i$ of Asp56 and Asp58, compared to their analogue Asp20 and Asp22 in loop I, is probably due to absence of any basic residue in between them. Interestingly, this is evident from the fact that $T\Delta S_{conf}^i$ values of Lys21 and Lys30 and the excess $T\Delta S_{conf}^i$ of Asp20 and Asp22 over their analogues in loop II add up to $\sim -8.0 \text{ kJ mol}^{-1}$, comparable to the difference in $T\Delta S_{conf}^L$ between loop II and loop I. The fourth acidic residue Asp64 though does not coordinate to Ca^{2+} , gets ordered highly because of the negative charge on its side-chain pointing towards the Ca^{2+} . Among other non-coordinating residues, Ala57, Ile63 and Phe65, all of which are hydrophobic, also become conformationally more ordered and stable compared to the apo-state (Figure 5.10).

The $T\Delta S_{conf}^L$ ($\sim +0.2 \text{ kJ mol}^{-1}$) and ΔG_{conf}^L ($\sim -2.4 \text{ kJ mol}^{-1}$) values of loop III (Figure 5.9) suggest very different Ca^{2+} binding behaviour compared to loops I and II. One reason could be the lack of any fourth negatively charged residue in this loop. This trend is

supported by the enhanced Ca^{2+} binding affinities observed by mutational studies²⁹⁴ via increasing the number acidic residues in loop III. Flexibility of this loop increases upon Ca^{2+} binding, indicated by the high disordering of Ca^{2+} coordinating residues Asp93, Tyr99 and Glu104. Most ordered residue in this loop is Ca^{2+} coordinating Asn97 which occupies the same loop position as Asp24 in loop I and Asn60 in loop II. The other Ca^{2+} coordinating residue Asp95 also undergoes ordering and stabilization which is reflected in the movement of its side-chain, for coordinating to Ca^{2+} , closer to the side-chain of Lys94 for favourable interactions. The ordering of non-coordinating residue I100, the structural link to loop IV, is very small (Figure 5.10a), while its stabilization is significant (Figure 5.10b).

The loop IV, on the other hand, shows similar changes as loops I and II. It has five acidic residues, maximum among the loops. Four of them: Asp129, Asp131, Asp133 and Glu140, coordinate to Ca^{2+} and become highly ordered and stabilized. The disordering and instability of the fifth acidic residue Glu139, which is non-coordinating, is due to the local repulsive strain its side-chain experiences with that of Glu140. Such repulsions lead to somewhat less stabilization of Glu140 compared to its N-domain analogues Glu31 and Glu67. Among other non-coordinating residues in this loop, ordering and stabilization of Gln135 and that of Val136, the structural link to loop III are also significant. The most ordered residue here is Tyr138 (Figure 5.10a) whose stabilization is also high (Figure 5.10b). The ordering factors here are: the reorientation of its side-chain bringing it near Phe89 gaining substantial stacking interaction and favourable charge-dipole interactions with Glu82 and Glu140.

5.4.4 Changes in linker

The most striking conformational change upon Ca^{2+} binding to apo-CaM occurs in the linker (residues 64-92), connecting the two domains, where a loop (the encircled region in Figure 5.1a) becomes helical in holo-state helping CaM to expose its hydrophobic surface for target-binding. The metal-induced changes of the linker helix in CaM are quite substantial: $T\Delta S_{conf} = -44.2$ and $\Delta G_{conf} = -13.3$ kJ mol⁻¹ for all 29 residues in the linker. These values account for ~34% of $T\Delta S_{conf}^{tot}$ and ~25% of ΔG_{conf}^{tot} for the whole protein. The majority of the changes in linker helix come from the loop region that becomes helical upon Ca^{2+} -binding. $T\Delta S_{conf} = -20.5$ and $\Delta G_{conf} = -10.2$ kJ mol⁻¹ for these six residues 76-81 account for ~46% of $T\Delta S_{conf}$ and ~77% of ΔG_{conf} estimated for linker helix.

5.4.5 Generalization of results on metal-ion binding to protein

Due to appreciable similarity in sequence, structure and mode of function among different EF-hand proteins with CaM, our results on CaM can be useful to understand the Ca^{2+} binding activities of the EF-hand proteins in general. It is well known that the EF-hand proteins, just like CaM, possess distinct domains containing EF-hand pairs with different Ca^{2+} binding affinities. For instance, Calbindin D_{9k} has²⁹⁵ two EF-hands, one of which, having higher Ca^{2+} binding affinity than the other, is similar in composition and structure to one of the EF-hands in CaM. The other one is an unconventional EF-hand with the loop containing 14 residues. Both the EF-hands in Parvalbumin²⁹⁶ are homologous to those in CaM and therefore, could be expected to exhibit similar affinities. Calbindin D_{28k} has²⁹⁷ six EF-hands out of which four are high affinity sites for Ca^{2+} . Troponin-C and Centrin both have four EF-hands^{298, 299} distributed over the N- and C- globular domains with a helix linking them, just like CaM. They all undergo conformational changes upon Ca^{2+} binding which are very similar to CaM. Another EF-hand protein S100A1 is, even, known to compete with CaM for binding to the same target³⁰⁰. The conformational entropy and free energy costs of different key residues in CaM for Ca^{2+} induced conformational changes would be helpful for understanding the stabilities and target related activities of analogous residues in these EF-hand proteins.

5.5 Allosteric regulations in Ca^{2+} binding to CaM

In this section we consider the allosteric regulations in apo- to holo-transition of CaM upon binding of Ca^{2+} ions, via the TDCFs of dihedral angles which describe the dynamic correlations. First, we describe in section 5.5.1 the calculations of the TDCFs. The results on TDCFs are presented in 5.5.2. Then we interpret the changes of TDCF pattern in terms of allosteric regulations and connect our method to existing understanding of allostery in 5.5.3.

5.5.1 Dynamic correlations between dihedral angles

We compute the dynamic fluctuations of dihedral angles of the residues in CaM in both the apo- and the holo-states. The dihedral auto-correlation function (DACF) of a dihedral θ of one residue is defined via the TDCF⁸⁰:

$$C_{\theta\theta}(t) = \left\langle \left\langle (\cos[\theta(t)] - \langle \cos \theta \rangle)(\cos[\theta(0)] - \langle \cos \theta \rangle) \right\rangle \right\rangle \quad (5.22)$$

where $\theta(t)$ and $\theta(0)$ are the values of the dihedral at time t and at time $t = 0$, respectively. The dihedral cross-correlation function (DCCF) $C_{\theta\theta'}(t)$ corresponds to the case when θ and θ' are dihedral angles of two different residues. The single angular brackets denote ensemble

average, while double angular brackets represent average over 10000 independent initial conditions¹¹¹ chosen from the equilibrated part of the MD trajectories.

5.5.2 Dihedral auto- and cross correlations in CaM

First, we characterize the nature of fluctuations of the dihedral angles over the simulated MD trajectories with respect to their mean values in the simulated ensemble. Figure 5.11a shows a couple of sample distributions $H(\cos\theta)$ vs. $\cos\theta$ for the dihedral ψ of Ile27 and ϕ of Met76 in apo-(metal-ion free) CaM. Such plots clearly show that the fluctuations about the mean value are Gaussian. The mean values agree to the values of these dihedral angles in the PDB structure.

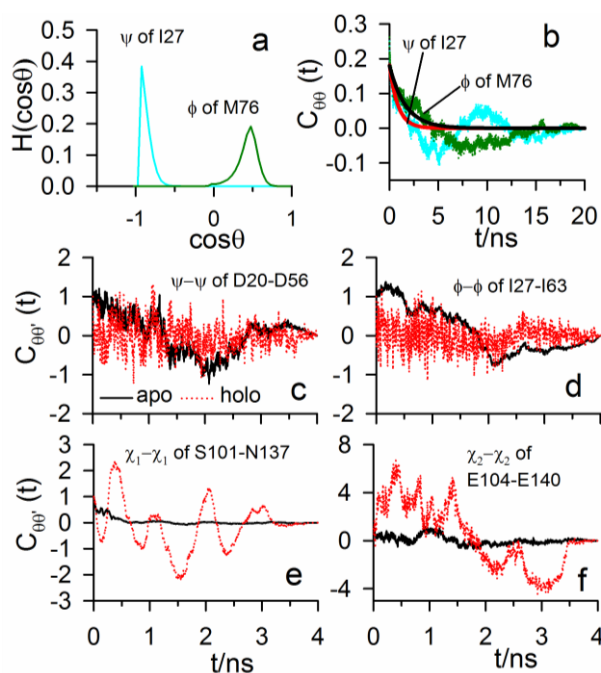


Figure 5.11: Statistics and correlations of dihedral angles. (a) The histograms $H(\cos\theta)$ for the dihedral ψ of Ile27 and ϕ of Met76 in apo-CaM. (b) DACFs $C_{\theta\theta}(t)$ for dihedral ψ of Ile27 and that for ϕ of Met76, along with their exponential fits, all in apo-CaM. DCCFs $C_{\theta\theta'}(t)$ for dihedrals of different pairs of CaM residues in apo (solid) and holo-states (dotted): (a) ψ - ψ of Asp20 and Asp56, (b) ϕ - ϕ of Ile 27 and Ile63, (c) χ_1 - χ_1 of Ser101 and Asn137 and (d) χ_2 - χ_2 of Glu104 and Glu140. All the correlation functions are shown after division with their values at $t=0$.

The majority of the dynamic correlation functions of the dihedrals show usual exponential decay^{111, 254, 285} with short τ (\sim less than 1 ns) which we designate as the absence of dynamic correlation. There are, however, a number of cases where there are large deviations from such behaviour. We show in Figure 5.11b a couple of such cases, namely,

DACF for the same dihedrals for which the fluctuations have Gaussian distributions. The τ for these cases are as long as about 15 ns. The solid lines in this plot exhibit the exponential fits which makes it evident that these DACFs deviate from exponential decay. In particular, both of them show anti-correlations which cannot be captured by the exponential functions. The non-exponential character is exhibited by several θ - θ' DCCFs as can be seen from Figure 5.11c-f and Figure 5.12. The typical τ for the DCCFs is around 3-4 ns. Although these values are smaller than those for the DACFs, they are much larger compared to the timescales of side-chain motions which are predominantly in the sub-ns regime.

It is interesting to compare the DCCFs in the apo- and the holo-states. Probing into the domain-wise behaviour, we first consider the N-domain. Figure 5.11c shows the ψ - ψ DCCF between Asp20 (loop I) and Asp56 (loop II) for which $\tau \sim 3$ ns in apo-state, but the dynamic cross-correlation is absent in holo-form. The ϕ - ϕ DCCF between the structurally linked residues¹⁰⁰ Ile27 (loop I) and Ile63 (loop II) in the apo-state also has $\tau \sim 3$ ns which vanishes in holo-state (Figure 5.11d). In C-domain, only side-chain dihedrals show significant DCCFs. In Figure 5.11e we show the DCCF of one such case: χ_1 - χ_1 DCCF between Ser101 (loop III) and Asn137 (loop IV) with similar τ in apo-state, and dynamically uncorrelated in holo-form. However, opposite trend is shown in Figure 5.11f by χ_2 - χ_2 DCCF between Glu104 (loop III) and Glu140 (loop IV) which is significant in holo, but not in apo.

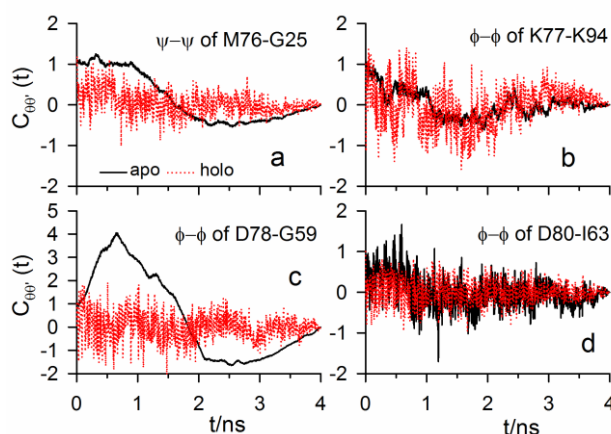


Figure 5.12: Cross-correlations between dihedrals of linker and loops. DCCFs $C_{\theta\theta'}(t)$ for dihedrals of different pairs of CaM residues in apo (solid) and holo-states (dotted): (a) ψ - ψ of Met76 and Gly25, (b) ϕ - ϕ of Lys77 and Lys94 (c) ϕ - ϕ of Asp78 and Gly59, (d) ϕ - ϕ of Asp80 and Ile63.

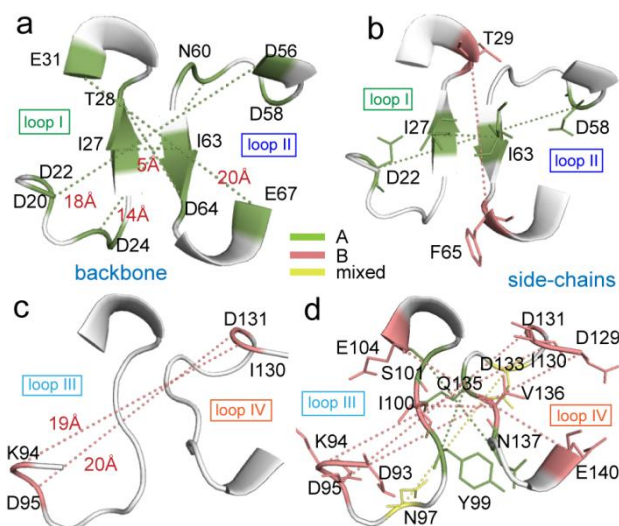


Figure 5.13: Dynamic cross-correlation patterns in the loops. N-domain: (a) backbone and (b) side-chain dihedrals. C-domain: (c) backbone and (d) side-chain dihedrals. Class A (green) includes pairs of dihedrals correlated in apo-state, but not in holo. Class B (red) includes correlated dihedral pairs in holo, but not in apo-state. One residue pair show ‘mixed’ (yellow) behaviour. The dashes, coloured according to the classes, connect the residues correlated to each other. In panels (a) and (c) the distances between the residues in each pair are shown beside the connecting dashes.

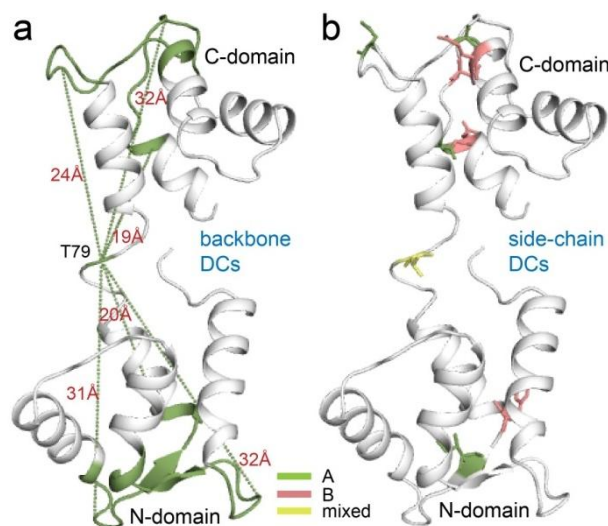


Figure 5.14: Dynamic cross-correlation patterns between the dihedrals of linker and loop residues. (a) Backbone and (b) side-chain dihedrals. The classification and colouring schemes are similar to Figure 5.13.

Next we consider the DCCFs between the dihedrals of the Ca^{2+} binding loop residues and those from residues 76-81 of the linker helix in CaM which undergoes loop to helix transition upon binding of Ca^{2+} ions to CaM (Figure 5.1a). A few typical such DCCFs are shown in Figure 5.12 where θ is a dihedral of one of the six residues 76-81 and θ' is a

dihedral of a loop residue. In Figure 5.12a, we show the ψ - ψ DCCF between Met76 and Gly25 (loop I) which is non-trivial in apo-state, but is negligible in holo-form. Similar behaviour is observed for all other cases: ϕ - ϕ DCCF between Lys77 and Lys94 (loop III) in Figure 5.12b, Asp78 and Gly59 (loop II) in Figure 5.12c and Asp80 and Ile63 (loop II) in Figure 5.12d.

We compare the overall dynamic cross-correlation patterns in N- and C-domains in Figure 5.13 in the apo and the holo states. We find two major classes of dihedral-pairs. Some pair shows non-trivial dynamical cross-correlation in the apo-state which vanish in the holo state, marked as class A (green coloured residues connected by green dots). There is another group of dihedral pairs with opposite behaviour, namely, significant dynamical cross-correlation in the holo state, but not in the apo state, which we mark as class B (coloured red and joined by red dots). Apart from the classes A and B there are cases where the dihedrals show similar or negligible dynamical correlation in both the apo- and the holo-state (uncoloured residues). Figure 5.13a shows the dynamical correlations between backbone dihedrals of loop-residues in the N-domain. We observe the dominance of class A with several pairs of residues, separated by long-distances (5-20 Å) and cross-correlated dynamically via backbone. For instance, the distance between the C_α atoms of Asp20 in loop I and Asp56 in loop II are 18 Å, yet they show non-trivial ψ - ψ DCCF in apo-state. Similarly, significant ϕ - ϕ DCCF is shown in apo-state by Thr28 in loop I and Asp64 in loop II, although C_α distance of these residues is as large as 20 Å. However, among the side-chains in N-domains (Figure 5.13b), there are very few dynamical cross-correlations with two pairs in class A (Asp22 in loop I with Asp58 in loop II and Ile27 in loop I with Ile63 in loop II) and one pair in class B (Thr29 in loop I with Phe65 in loop II). In C-domain, backbones are totally uncorrelated in apo-state shown in Figure 5.13c. In contrast, some long-ranged holo-state dynamical cross-correlations build up here on the backbone (class B): Lys94 in loop III and Ile130 in loop IV with C_α distance 19 Å; and Asp95 in loop III and Asp131 in loop IV with C_α distance 20 Å. Among the side-chain dihedrals in C-domain (Figure 5.13d), we find only two class A pairs: Tyr99 (loop III) and Gln135 (loop IV) with C_α distance 9 Å; and Ser101 (loop III) and Asn137 (loop IV) with C_α distance 11 Å. A good number of side-chain dihedrals belong to class B. The behaviour of side-chains of N97 and Asp133 are mixed, since χ_1 - χ_1 DCCF falls in class A, but χ_2 - χ_2 DCCF in class B.

This linker region is about 20-30 Å away from each of the four loops as shown in Figure 5.14a. We find that most of the backbone dihedrals ϕ and ψ of the residues of this

loop-segment are dynamically cross-correlated in apo-state with the backbone dihedrals of the loop residues, but these correlations are absent in holo CaM (class A). This is clearly shown in Figure 5.14a for the linker residue Thr79 as a representative case. Only a few loop residues show side-chain dynamical correlations with those of Thr79 (Figure 5.14b) of both class A and B types. The situation is very similar for most of the other linker residues as well, except the dihedrals of Ser81 which do not show dynamical cross-correlation at all.

5.5.3 Dynamic dihedral correlations and allosteric regulations

The autocorrelation functions of dynamical variables are known to show exponential decay with time for a stationary, Gaussian and Markovian process according to the Doob's theorem²⁵⁴. Since we construct the DACFs for the dihedral angles from equilibrated MD trajectories the stationarity condition holds good. The histogram of the fluctuations of the cosine of the dihedral angles (Figure 5.11a) shows that these fluctuations obey Gaussian statistics. Thus, the non-exponential character of the DACFs (Figure 5.11b) indicates non-Markovian dynamical process of the dihedral fluctuations. The non-Markovian behaviour indicates persistent memory in the dynamical processes governing the dihedral fluctuations. This should lead to persistence in any dynamically coupled processes, as reflected in the temporally non-exponential and long-ranged DCCFs. In general slower DACFs than the DCCFs would imply the participation of dynamical variables of different timescales in the system.

Our calculations clearly highlight a dynamically coupled network of residues in apo-CaM: the N-domain loops which are primarily correlated via the backbone, the C-domain loops, correlated via side-chains and the linker, correlated with the four loops through the backbone. The estimated τ for different cases of cross correlations, compares well to the signal transmission time of allosteric control¹⁰⁵. Unlike short-ranged correlations building up the long-range correlations²⁶⁹, we find in this network, that there are several cross-correlated residues which are separated by large spatial distances (Figure 5.13 and 5.14). This indicates long-ranged dynamic communication among different regions in the protein. Therefore, if one part of the network is perturbed, other distant parts could be dynamically affected¹⁰³.

Some of the known allosteric events in CaM can be rationalized from the changes in dynamical coupling pattern between distant sites in class A. The consecutive binding of two Ca^{2+} ions to a pair of EF-hands in general show positive cooperativity,^{272, 282, 301} such that Ca^{2+} binding to one EF-hand loop assists the binding on the other. The cooperativity³⁰¹ of consecutive binding of Ca^{2+} ions to a pair of EF-hands is thus an example of allosteric

regulation²⁷². The dihedral angles of class A (green patches in Figure 5.13), belonging to the residues of adjacent EF-hand loops in a given domain of CaM, take part in allosteric cooperativity in Ca²⁺ binding. In case of N-domain, the backbone dihedrals control the cooperativity in binding of Ca²⁺ ions. In the C-domain, on the other hand, class A consists of the side-chain dihedrals indicating side-chain mediated cooperative binding (Figure 5.13d). Thus, the mechanism of allostery is different between two adjacent loops for N- and C-domain in apo-CaM. Due to the dynamic nature of cooperative binding it is not surprising that the equilibrium binding measurements^{282, 301} fail to show significant effect of cooperativity. It is interesting that the loops in both the domains do not show any significant structural change between apo- and the holo-form. This illustrates dynamic allostery without any structural change but via modification in dynamical fluctuations due to Ca²⁺ binding, as observed for a class of protein-ligand binding^{241, 244, 245, 248, 249}.

The dynamic correlations between the loops and the linker suggest that the perturbations at the linker should allosterically regulate binding in the loops. Experimental observations have indeed shown signature of this kind of regulation^{77, 302, 303}. When one of the domains is loaded with Ca²⁺ and the linker wraps a target peptide, the binding affinity in the other unloaded domain increases substantially^{302, 303} compared to holo-CaM. This clearly stands for an instance of allosteric regulation of Ca²⁺ binding in the loops via conformational change in the linker.

Likewise, the changes in the loops would perturb the linker region. Upon binding of Ca²⁺ ions in the EF-hand loops, important conformational changes^{274, 304} occur in the linker of the two domains in CaM (Figure 5.1a) far away from the metal binding sites. In apo-CaM (Figure 5.1a) this linker is broken near the middle with a six-residue (residues 76-81) loop, which becomes helical in holo-CaM (circled region in Figure 5.1a). This transformation enables the CaM molecule to get into an open conformation exposing its hydrophobic residues for binding the targets. Our data on DCCFs indicate that this also in an allosteric regulation²⁶⁵, the signal being transmitted via the backbone. Recent experiments³⁰⁵ suggest that the timescale of loop to helix transition is about 2-5 ns for five to 20 residue peptides which is comparable to the DCCF timescales we observe here. Unlike the Ca²⁺ binding domains, the allosteric regulation in the loop is associated with marked structural changes.

We observe that the dynamic correlation pattern is different in holo-state compared to the apo-state. In particular, there are several dihedrals present in the C-domain belonging to class B (Figure 5.13c and d). Various experimental observations^{69, 306, 307} have shown that

several target peptides, binding to a particular domain of holo-CaM, prefer the C-domain to the N-domain which indicates greater activity of the C-domain. Therefore, the class B dihedrals in C-domain may be signature of its higher-target binding activity compared to the N-domain. This idea is substantiated by the fact that this communication is formed mainly between the dihedrals of side-chains which control the binding processes. The dynamically cross-correlated side-chains in the C-domain loops would have role in any allostery associated with the peptide binding process.

Our studies indicate that the changes in dynamical correlation patterns reflect the allosteric regulations, albeit via non-Markovian processes. The conventional Markovian behaviour may be retrieved only in the large time limit¹⁰⁵ after the dynamical correlations have decayed sufficiently. This clearly shows the limitation of Markovian models to explain allosteric regulation. In particular, the long-time Markovian behaviour of dihedral fluctuations assumed in earlier works^{105, 308} is not necessarily valid as shown by the DACFs in our studies. The allosteric signalling timescale is much shorter (< 10 ns)¹⁰⁵, indicating that the non-Markovian dynamical behaviours, observed in our studies at these timescales, should also be relevant in allosteric regulation. Such non-Markovian dynamics would be ubiquitous in biomacromolecular systems where a host of complex and heterogeneous dynamical processes³⁰⁹ take place. The treatment of non-Markovian dynamics is one of the most challenging problems in non-equilibrium statistical mechanics²⁵⁴. However, since we probe directly the dynamical correlation among the conformational variables, our studies yield a very general picture of allosteric regulation based on the changes of dynamical correlation pattern, even if the underlying dynamical fluctuations may be non-Markovian. Moreover, unlike very long simulation trajectories required to ensure the Markovian process, the non-equilibrium fluctuation of the dihedral angles can be captured with much shorter simulation runs. The novelty of our method lies in the fact that we liberate the microscopic picture of allosteric regulation, with modest computational efforts, from the current Markovian assumptions¹⁰⁵. However, to study the allostery associated with slow domain motions one would require very long simulations, although our method of analysis should hold good in such situations as well. Direct identification of allosterically regulated conformational variables represents significant advancement in microscopic understanding of allostery in biomacromolecules.

5.6 Conclusion

To summarize, we have shown that the entire thermodynamic changes in biomacromolecular conformations can be extracted from the distributions of the dihedral

angles using the HBM. We reproduce the experimentally observed correlation between the conformational and binding entropies and quantify the thermodynamic contributions of different binding regions for a number of CaM-peptide complexes. The histograms would be sensitive to any quantity that undergoes changes upon binding. Hence the present analysis can suitably be extended to calculate thermodynamic changes in the solvent and any other macromolecular complex like protein-protein, protein-DNA or protein-ligand complexes. The detailed thermodynamic information of the binding regions would enable us to identify the prime spots of binding, facilitating the manipulation of the macromolecules required for various applications such as drug design, drug delivery and so forth.

We employed the HBM⁸³ to also study the conformational thermodynamic for Ca²⁺ ion binding to CaM. We estimate the quantitative information of conformational changes at each residue including the different metal binding domains. The N-domain undergoes a higher conformational ordering and stabilization compared to the C-domain. The Ca²⁺ ion binding loops I, II and IV are qualitatively similar with respect to conformational changes, while loop III is significantly different from them undergoing only nominal stabilization and enhanced disorder due to the metal-ion binding. Our results at the level of individual residues indicate that the loop residues including those coordinating to the metal-ions dominate the overall changes in the loops. Apart from the loops, the linker, far away from the metal binding sites, undergoes substantial stabilization and ordering as it becomes a long helix in holo-state. One can readily apply the HBM to understand the microscopic picture of metal-ion binding induced changes in any protein to characterize different metal binding regions.

Finally, we show that the cosine of the dihedral angles for successive equilibrium configurations sampled from MD runs forms a convenient time-series for calculations of the dynamic correlations between the dihedral angles⁸⁰. The dynamical correlation functions yield the microscopic nature of coupling among different degrees of freedom belonging to distant sites in biomacromolecules, highlighting their roles in allosteric regulations. The extraction of dynamical correlation depends on the computation of convenient time-series of the associated dynamical variable. Such correlation functions can be extended to any set of dynamical variables which may provide a unified microscopic insight into non-equilibrium phenomena in biological systems.

Appendices

Calculation of order parameters

In order to calculate the long-axis order parameters S_{Me}^2 of the side-chain methyl groups in CaM-peptide complexes we follow the methods described in Yang et al⁹³ and Krishnan et al²⁹¹. One such methyl group is schematically shown in Figure A2. First, all the backbone CA (α -carbon) atoms in the equilibrium configurations of the complex are fitted to the backbone CA atoms in the average structure calculated over the equilibrium trajectory. This way the effect of rotation of the whole complex is removed. This is done using the VMD program²⁸⁸. The resultant aligned configurations are then subjected to the calculation of S_{Me}^2 values. The generalized order parameter for the methyl long-axis is given by²⁹¹ the following expression:

$$S_{Me}^2 = (3/2) \left[\langle x^2 \rangle^2 + \langle y^2 \rangle^2 + \langle z^2 \rangle^2 + 2\langle xy \rangle^2 + 2\langle yz \rangle^2 + 2\langle zx \rangle^2 \right] - 1/2$$

where $x = \sin(\pi - \alpha) \cos \beta$, $y = \sin(\pi - \alpha) \sin \beta$ and $z = \cos(\pi - \alpha)$, α being the polar angle and β , the dihedral angle as shown in Figure A2. The angular brackets represent ensemble averages over 10000 equilibrium configurations.

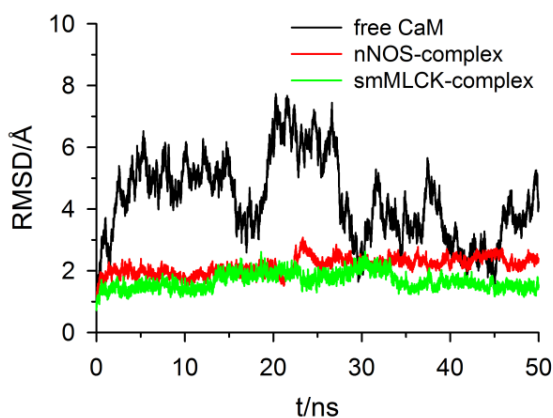


Figure A1: Root mean square deviation (RMSD) during simulations. Free CaM and two representative cases of the nNOS and smMLCK complex. Note the larger fluctuations in case of free CaM as it is free to move in the solution. Fluctuations are suppressed a lot in the complexes due to binding of the peptide which is evident from the RMSDs of the complexes.

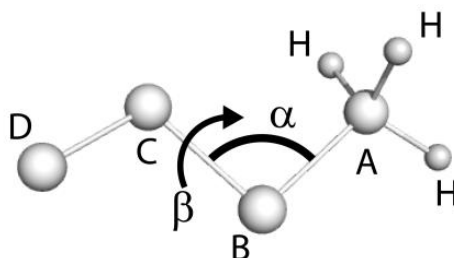


Figure A2: Schematic representation of a side-chain methyl group. The associated polar angle α and dihedral angle β are shown. Here A is the methyl carbon atom (A = CB for Ala, CG or CD for Ile, CD1 or CD2 for Leu, CE for Met, CG2 for Thr and CG1 or CG2 for Val). The other atoms B, C and D represent other heavy atoms which are determined by the residue identity.

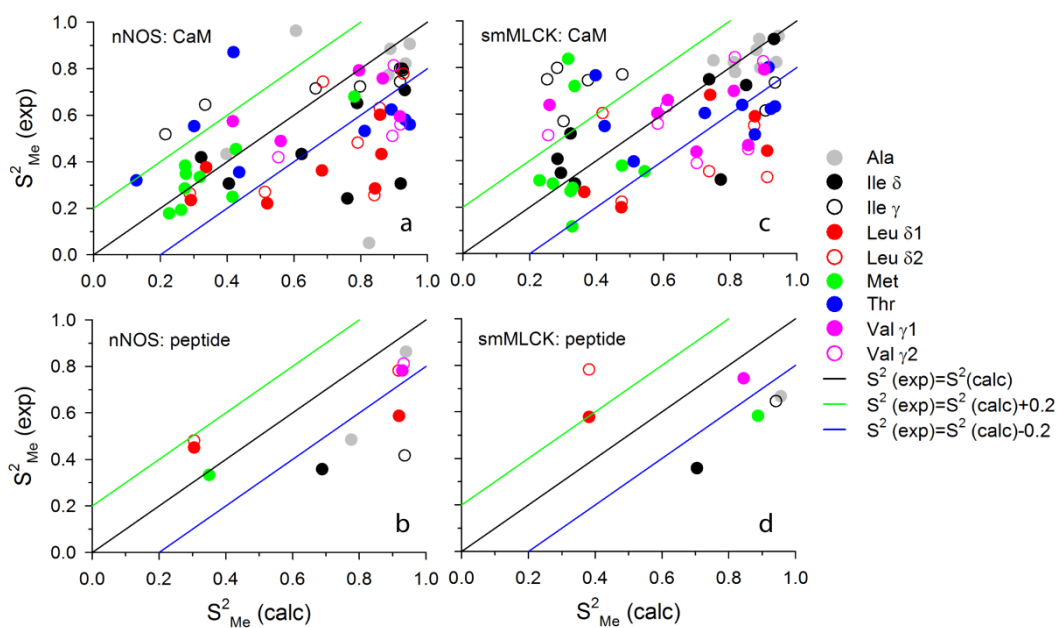


Figure A3: Methyl order parameter data. S^2_{Me} for nNOS complex and smMLCK complex are shown (a,c) for CaM and (b,d) for the peptide. The symbol and line descriptions are the same as those in Figure 5.2.

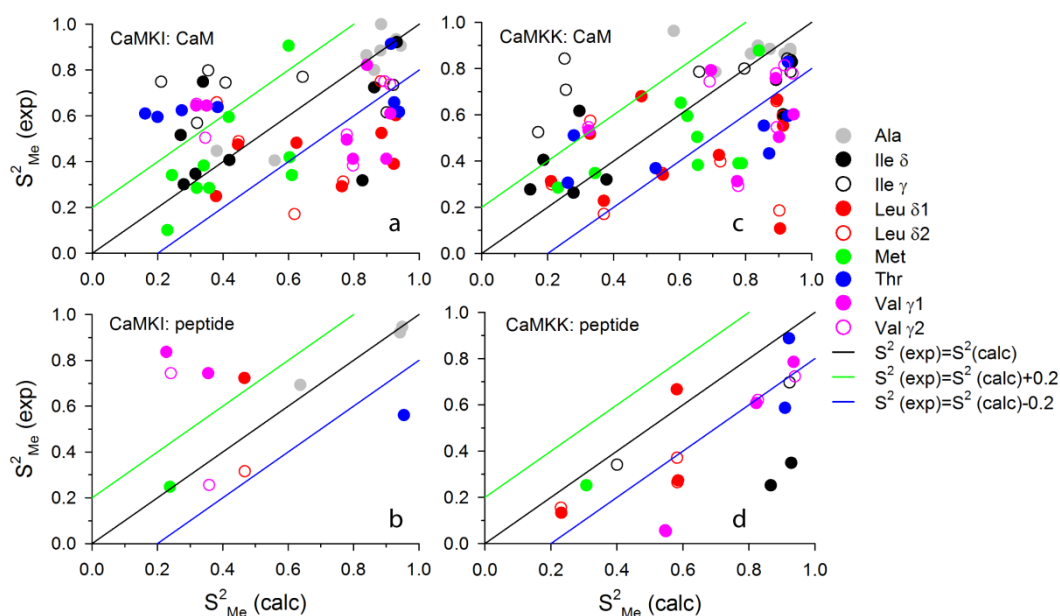


Figure A4: Methyl order parameter data. S^2_{Me} for CaMKI complex and CaMKK complex are shown (a,c) for CaM and (b,d) for the peptide. The symbol and line descriptions are the same as those in Figure 5.2.

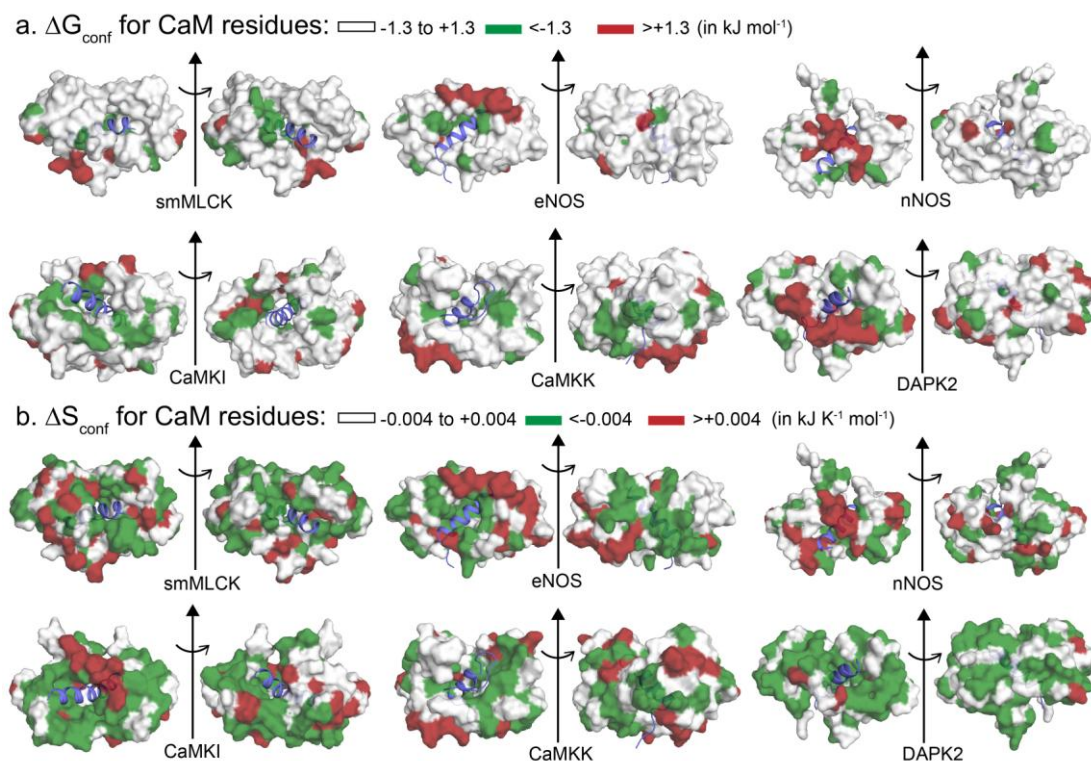


Figure A5: Surface representations of six CaM-peptide complexes showing the residue-wise (a) ΔG_{conf} ; (b) ΔS_{conf} of CaM. Two views separated by 180° rotation are shown in each case. The stabilized residues are green and destabilized ones are red. The residues undergoing minor changes are white. Peptide is in violet cartoon representation.

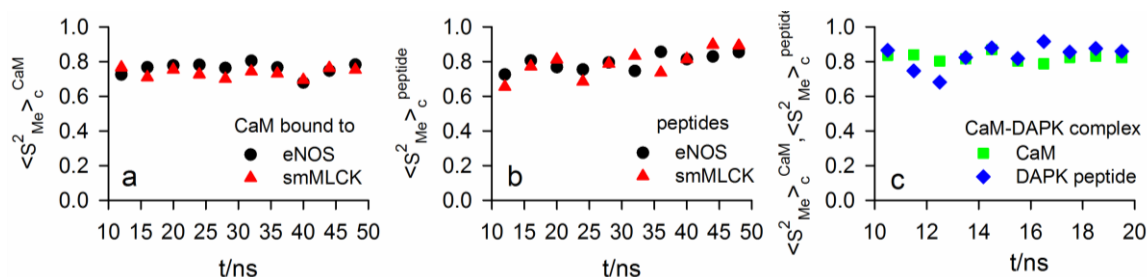


Figure A6: The time-variation of methyl order parameters. $\langle S_{Me}^2 \rangle_{CaM}$ and $\langle S_{Me}^2 \rangle_{peptide}$ (average over available methyl groups) during the simulations for CaM and peptide in several complexes. (a) For CaM in eNOS and smMLCK complexes. These values remain similar throughout the entire equilibrium trajectory in both cases. (b) For the peptides in eNOS and smMLCK complexes. Here convergence is slower than for protein. The convergence in smMLCK is poorer than eNOS. This could be attributed to the fact that this peptide has only 8 methyls, which is fewest among all the peptides considered here. (c) Data for DAPK2-complex. Here, the CaM-data are similar throughout the trajectory, while the peptide-data converge beyond 12 ns.

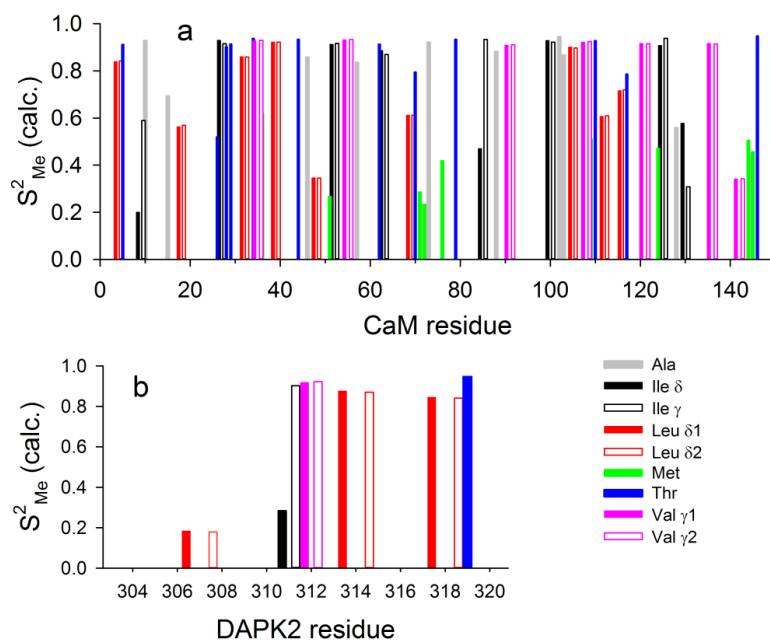


Figure A7: The methyl order parameters of CaM-DAPK2 complex. (a) CaM and the (b) peptide data, predicted from our simulations. The different types of methyl groups are represented by different colours as shown in the legend.

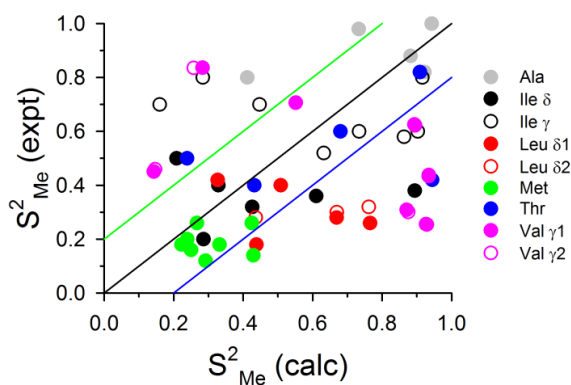


Figure A8: Comparison of methyl order parameters of holo-CaM. The experimental S_{Me}^2 (expt)²⁸¹ vs. calculated S_{Me}^2 (calc) from our simulation. Few overestimations in S^2 are observed due to limitations of the force fields^{291, 292}.

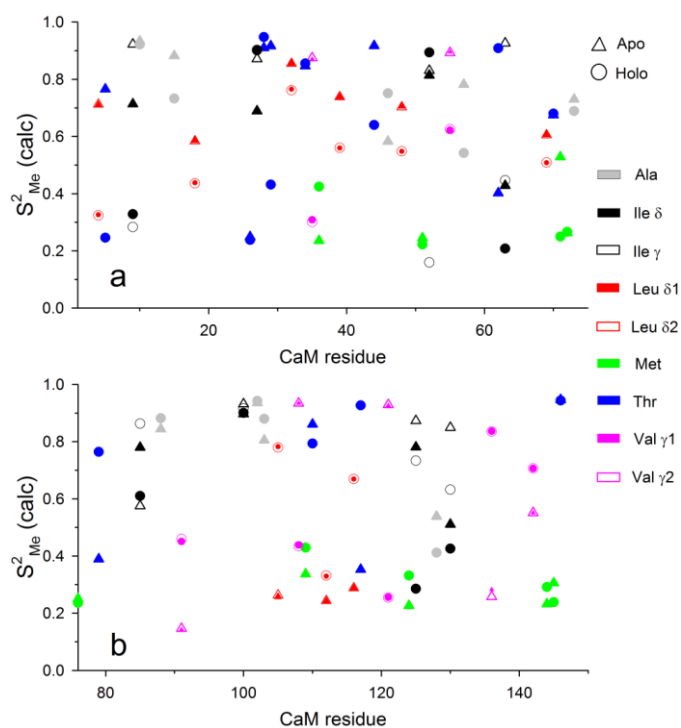


Figure A9: Methyl order parameters in apo- and holo-CaM. Residues (a) 5-75, (b) 76-146.

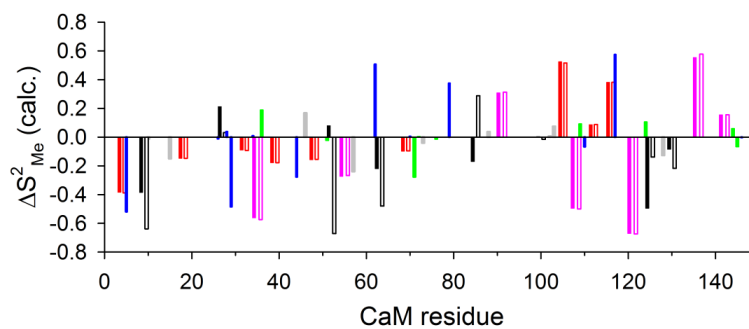


Figure A10: Change in methyl order parameters from apo- to holo-CaM.

$\Delta S_{Me}^2 = S_{Me}^2$ (holo) - S_{Me}^2 (apo) values for different CaM residues.

Chapter 6 Thermodynamics of interfacial changes in a protein-protein complex

6.1 Introduction

Biomacromolecules often share large interfacial area³¹⁰ to facilitate formation of stable complexes. Recent experiments^{75, 106, 311} suggest that structural modifications at the interface play pivotal role at times both in the stability of such complexes and functional activities¹⁰⁶ of the associated biomacromolecules. From structural studies³¹¹⁻³¹³ several qualitative aspects, like formation of salt bridges and water-mediated contacts, changes in secondary-structure elements and so on, associated with the biomacromolecular interfaces have been determined. However, there is hardly any quantification of the thermodynamics of these interfacial changes. Quantitative information about the interface at the microscopic level is of immense importance, not only for understanding the binding mechanism, but also for development of functionally potent biomacromolecules via manipulation of the interfacial interactions^{314, 315}.

The interfacial changes in biomacromolecular complexes are primarily derived from the conformational changes of the binding partners. The advancements with NMR relaxation experiments⁹²⁻⁹⁵ provide a scope of estimating the conformational entropy change for biomacromolecular complexation. These measurements highlight the importance of conformational changes in the binding interface⁷⁵. Similarly, computer simulations offer a very powerful tool to study the microscopic details of the biomacromolecules^{79-81, 83, 86}. In chapter 5, we have shown that the conformational thermodynamics can be extracted from various backbone and side-chain dihedral angles of the amino acid residues in a protein. The equilibrium distributions of different dihedral angles in the complex and the free components are calculated from all-atom MD simulations. Comparing these distributions in the free and the complexed states, one can estimate the changes in conformational entropy (ΔS_{conf}) as well as the conformational free energy (ΔG_{conf}) for binding. Via this histogram based method (HBM)⁸³ a comparable ΔS_{conf} as derived from the NMR experiments, can easily be calculated. The additional advantage of this methodology enables us to quantitative estimation⁸³ of the conformational changes at different binding regions for a number of protein-peptide complexes.

Other than the proteins or nucleic acids, the biomacromolecular interface quite often contains water molecules. These water molecules which could be integral parts of the

interfaces³¹⁶, not only help in the formation of the hydrogen bonding between the biomacromolecular chains¹⁰⁶, but also modulate the specificity and the affinities of binding³¹⁷⁻³²⁰. Sometimes even a small number of water molecules are found to play key role in driving the whole binding process³²¹. The thermodynamics for displacement of waters in a model cavity with specific electrical property by an incoming ligand has been studied in detail³²¹⁻³²³ to reveal significant contribution of these interfacial water molecules in the overall binding thermodynamics. In practice the situation in biomacromolecular interfaces are very complex, with competition between the hydrophobic and hydrophilic interactions.

In the present chapter we apply the HBM⁸³ to quantify the thermodynamics of interfacial conformational changes in a protein-protein complex between an enzyme Nuclease A (NucA)³²⁴ and its specific inhibitor³²⁵ NuiA, a protein (Figure 6.1). NucA, a sugar non-specific nuclease from *Anabaena sp.*, is one of the most active nucleases known^{326, 327} from a class of nucleases containing DRGH structure motif. These nucleases, having the capacity to hydrolyze nucleic acids without any base-preference³²⁷, are very important for their roles in host defence mechanisms³²⁸ providing nutrients to host, DNA-drug binding³²⁹, RNA sequencing³³⁰, cellular apoptosis³³¹ and so on. NuiA, an intrinsic inhibitor, deactivates NucA specifically³²⁶ via formation of a 1:1 complex³³² with a high stability constant ($> 10^9 \text{ M}^{-1}$)^{326, 333}. These enzymes require divalent metal-ion cofactor (like Mn^{2+} , Mg^{2+}) at the active-site to function. The crystal structure data of the NucA-NuiA complex¹⁰⁶ reveals the conformational changes of NucA and NuiA compared to their free forms^{107, 334}. The crystal structure also indicates the presence of water molecule mediated interactions at the interface, accompanied by changes in tertiary structural fold of NuiA. We extend the HBM to estimate the thermodynamic contributions due to the interfacial water molecules present in the NucA-NuiA complex. Here the relevant probability distribution is the pair distribution function¹¹¹ $g(r)$ for the water molecules which gives the probability of finding the centres of mass of a pair of molecules at given separation r .

Our data on ΔS_{conf} and ΔG_{conf} corroborate well with the known structural information^{106, 333} on the enzyme-inhibitor interfacial region (Figure 6.1). The binding is primarily dominated by electrostatic interactions at the interface, as indicated¹⁰⁶ by the high ordering and stabilizations of the basic interfacial residues of NucA and acidic interfacial residues of NuiA. From the generalization of the HBM for interfacial waters we also find that the entropy cost due to the water molecules is substantial. These water molecules are dynamically arrested at the locked jaw interface in NucA-NuiA complex which demonstrates the tight binding of the inhibitor to the enzyme. Our results quantitatively bring out the local

order and stabilities of the enzyme-inhibitor interaction sites due to complexation which has been hitherto known only qualitatively from structural data. Moreover, the complete microscopic picture from our calculation predicts some more residues which could be important in the inhibitor binding to the enzyme.

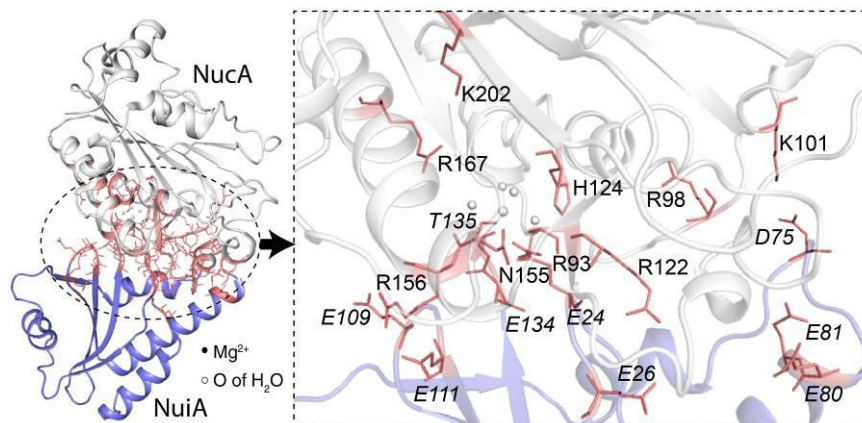


Figure 6.1: Cartoon representation of the NucA (white) - NuiA (violet) complex. The side-chains of the interfacial residues, coloured in purple, are shown using stick representation. The region enclosed by dashed line, representing the interface, is zoomed where the important basic NucA residues (regular labels) and acidic NuiA residues (italicized labels) are shown.

6.2 Methods

6.2.1 Simulation details

MD simulations of free NucA (PDB 1ZM8), free NuiA (PDB 1J57) and the NucA-NuiA complex (PDB 2O3B) are performed with explicit water and counter ions at 300 K using same methods and protocols as described in the previous chapter. The active-site divalent metal-ion of NucA in 1ZM8 is Mn^{2+} , while that in 2O3B is Mg^{2+} . However, hardly any difference is observed¹⁰⁷ in the residue arrangements and coordination geometry around Mg^{2+} or Mn^{2+} . Therefore, we proceed with these available structures. We use 50 ns trajectories for our analyses to compute the normalized histograms of the dihedral angles from equilibrated configurations sampled beyond 10 ns.

6.2.2 Thermodynamics from HBM

Extending Eq. 5.7 for NucA (N) and NuiA (I), the total conformational free energy change for complexation can be written as:

$$\Delta G_{conf}^{tot} = \sum \Delta G_{conf}^N(\theta) + \sum \Delta G_{conf}^I(\tau), \quad (6.1)$$

where $\Delta G_{conf}^N(\theta) = -k_B T \ln[H_{N,max}^c(\theta) / H_{N,max}^f(\theta)]$ and

$\Delta G_{conf}^I(\tau) = -k_B T \ln[H_{I,max}^c(\tau) / H_{I,max}^f(\tau)]$, θ and τ are the dihedral angles of N and I respectively. Here the summations are over all dihedrals and the subscript ‘max’ denotes maximum of histogram. Similarly, the conformational entropy change⁸³, using the Gibbs formula,

$$\Delta S_{conf}(\theta) = -k_B [\sum_i H_i^c(\theta) \ln H_i^c(\theta) - \sum_i H_i^f(\theta) \ln H_i^f(\theta)] \quad (6.2)$$

i being the bin-index of the histograms.

6.2.3 HBM for interfacial water molecules

Next we extend the HBM to estimate the free energy and entropy costs associated with the changes of interfacial water distribution. We calculate $g(r)$ for the interfacial water (iw) molecules within 5 Å of the interfacial residues in the complex ($g^c(r)$), and those within 5 Å of the binding regions of the free enzyme ($g_N^f(r)$) and inhibitor ($g_I^f(r)$). Here r is the separation between the O-atoms of two water molecules. The free energy cost is given by straightforward extension of Eq. 6.1:

$$\Delta G_{iw} = -k_B T \ln[g_{max}^c(r) / \{g_{N,max}^f(r) g_{I,max}^f(r)\}] \quad (6.3)$$

where the peak values in the respective $g(r)$ are used. The corresponding entropy cost ($T\Delta S_{iw}$) is obtained using the Gibbs formula as in Eq. 6.2:

$$\Delta S_{iw} = -k_B [\sum_i g_i^c \ln g_i^c - \sum_i g_{N,i}^f \ln g_{N,i}^f + \sum_i g_{I,i}^f \ln g_{I,i}^f] \quad (6.4)$$

where the the sum has been taken over non-zero bins marked by the index i .

6.2.4 Dynamics of Interfacial water molecules

To capture any change in the dynamics of the active-site waters (asw) we determine their diffusion behavior from the self-part of Van-Hove correlation function (VHCF)¹¹¹ defined at time t as:

$$G_s(r, t) = (1 / N_{asw}) \left\langle \sum_i \delta(\mathbf{r} - \mathbf{r}_i(0) + \mathbf{r}_i(t)) \right\rangle, \quad (6.5)$$

where N_{asw} is the total number of active-site waters and $\mathbf{r}_i(t)$ represents the position vector of the oxygen atom of the i th water molecule. The angular brackets here designate average over 10000 initial configurations. At long-times ($t \sim 100$ times larger than the diffusion time scale required for a tagged water to traverse the length of its diameter) the self-VHCF behaves like

a Gaussian¹¹¹ : $G_s(r, t) \approx (\alpha(t) / \pi)^{3/2} \exp[-\alpha(t)r^2]$ where the time-dependent parameter $\alpha(t) \sim 1/4D_{asw}t$, D_{asw} being the self-diffusion coefficient of the water molecules. We plot $1/\alpha(t)$ as a function of t and D_{asw} is obtained from the slope of the best linear fit.

6.3 Results

The RMSD are followed in each simulation to ensure the equilibration (Figure 6.2). The equilibrium correlations among different dihedral angles in the NucA-NuiA complex turn out to be negligible (Figure 6.3) as in the previous chapter, so that we consider them as independent conformational variables for the calculation of thermodynamics.

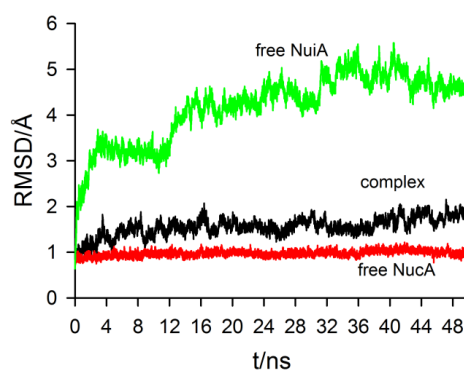


Figure 6.2: RMSD of free NucA, NuiA and the complex as function of simulation time (t).

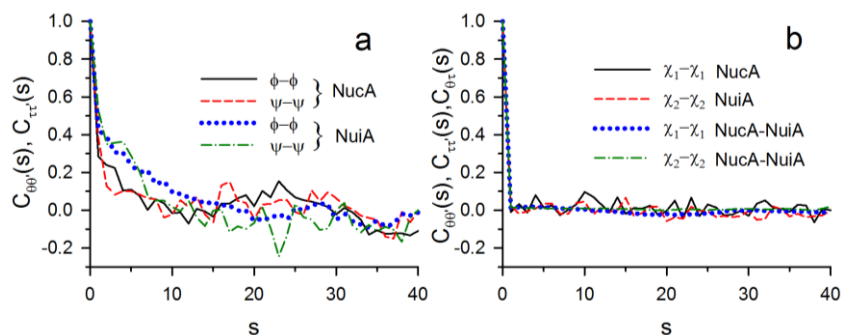


Figure 6.3: Simulation data on NucA-NuiA complex. (a) Variation of RMSD of free NucA, free NuiA and the complex as functions of simulation time (t). (b) Equilibrium $\theta - \theta'$ correlations among dihedral angles given by $C_{\theta\theta'}(s)$ where s denotes the separation between the locations of the residues having dihedrals θ and θ' .

Few sample histograms of dihedral angles are shown in Figure 6.4 showing similar behaviour, as in the previous chapter, for both backbone (Figure 6.4a-b) and side-chain (Figure 6.4c-d) dihedral angles. The peak values of the histograms generally increases upon binding, indicating decrease in fluctuations of the dihedrals from free to the bound state.

Multi-modal histograms are observed here also as illustrated in Figure 6.4d for χ_1 of Thr135 of NuiA which shows two broad peaks in free state, indicating two rotamers, reduce to one sharp peak in the bound state after binding to active-site metal-ion.

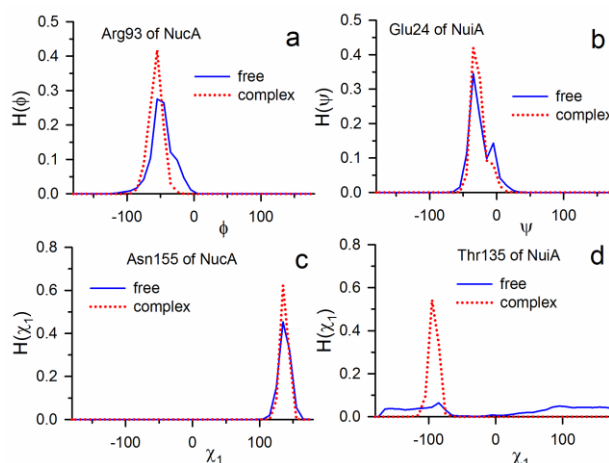


Figure 6.4: Sample histograms of dihedrals of different residues in free and bound states. Histogram of (a) ϕ in NucA residue Arg93, (b) ψ in NuiA residue Glu24, (c) χ_1 in NucA residue Asn155 and (d) histogram of χ_1 in NuiA residue Thr135.

After taking a close look at our data on histograms we elaborate different aspects of the thermodynamic changes in the NucA-NuiA complex. Decrease in free energy indicates gain in stability, whereas drop in entropy suggests ordering.

Overall conformational changes—We estimate the total conformational free energy cost of NucA-NuiA complexation $\Delta G_{conf}^{tot} = -138.2 \text{ kJ mol}^{-1}$. NuiA gets stabilized by $-89.8 \text{ kJ mol}^{-1}$ which is about double the contribution of NucA towards ΔG_{conf}^{tot} . Similarly, the total conformational entropy cost for the NucA-NuiA complexation $T\Delta S_{conf}^{tot} = -471.6 \text{ kJ mol}^{-1}$. The individual contribution by NucA is $-148.3 \text{ kJ mol}^{-1}$ and that by NuiA is $-323.3 \text{ kJ mol}^{-1}$, again almost twice that of NucA as in conformational free energy contributions. The 240 residue protein NucA experiences a very small ΔG_{conf} or $T\Delta S_{conf}$ value per residue ($< 1 \text{ kJ mol}^{-1}$) which quantifies the experimentally observed¹⁰⁶ little conformational change of NucA upon inhibitor binding. On the other hand, for the 135 residue inhibitor protein NuiA, the ΔG_{conf} value per residue is small ($< 1 \text{ kJ mol}^{-1}$) but the $T\Delta S_{conf}$ per residue is quite large ($\sim -2.4 \text{ kJ mol}^{-1}$).

A large contribution to the $T\Delta S_{conf}^{tot}$ in NuiA is due to the striking difference between the tertiary structures of bound NuiA (Figure 6.5a) and free NuiA (Figure 6.5b), reflected in the lowered spatial separation across the hinge-like structure of the molecule in the bound state. This occurs via rotation of the longest helix in NuiA around the normal to its helical axis to facilitate (i) coordination with the active-site of NucA via one end of the hinge and (ii) formation of a salt-bridge with NucA at the other end. The two helices constituting the hinge-like structure become heavily ordered in the enzyme-bound form (Figure 6.5a): $T\Delta S_{conf} = -19.7 \text{ kJ mol}^{-1}$ for the 12-residue shorter helix (residues 5-16) and $T\Delta S_{conf} = -74.5 \text{ kJ mol}^{-1}$ for the 20-residue longer helix containing residues 79-98. This stabilization is because of the formation of a hydrophobic core in the space between these two helices in bound NuiA by the side-chains of six residues as shown in Figure 6.5a. Each of these six residues participating in this hydrophobic region undergoes huge ordering ($T\Delta S_{conf}^i = -4$ to -11 kJ mol^{-1}) to result in a total entropy change of $T\Delta S_{conf} = -48.3 \text{ kJ mol}^{-1}$, further stabilizing the hinge.

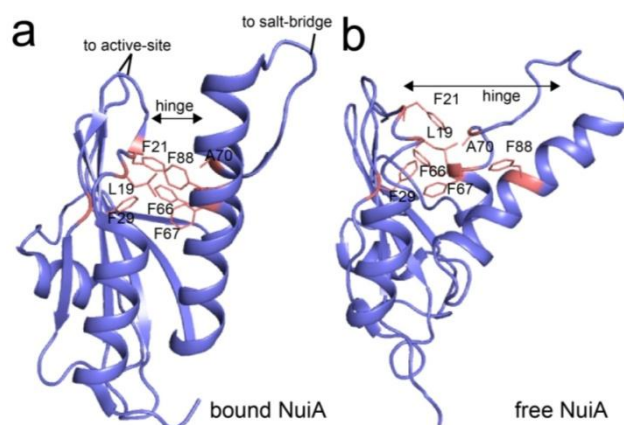


Figure 6.5: Cartoon representations of bound and free NuiA. (a) Enzyme bound NuiA and (b) free NuiA showing the changes in the hinge-like region. The side-chains of the residues forming a hydrophobic core between the two helices in the hinge are also shown using stick representations.

Conformational changes at interface—If we now consider the conformational changes associated with complexation, the region which will definitely require attention is the interface (Figure 6.1). The enzyme-inhibitor interface consists of the residues of NucA and NuiA within 5 \AA separations. This is an open-jaw like interface, consisting of: (i) the active-site of NucA, (ii) the second interaction-site containing the salt-bridge and (iii) other NucA and NuiA residues in contact through either direct or water-bridged hydrogen bonding

interactions¹⁰⁶. The conformational entropy and free energy changes of all interfacial residues are shown in Figure 6.6a-b.

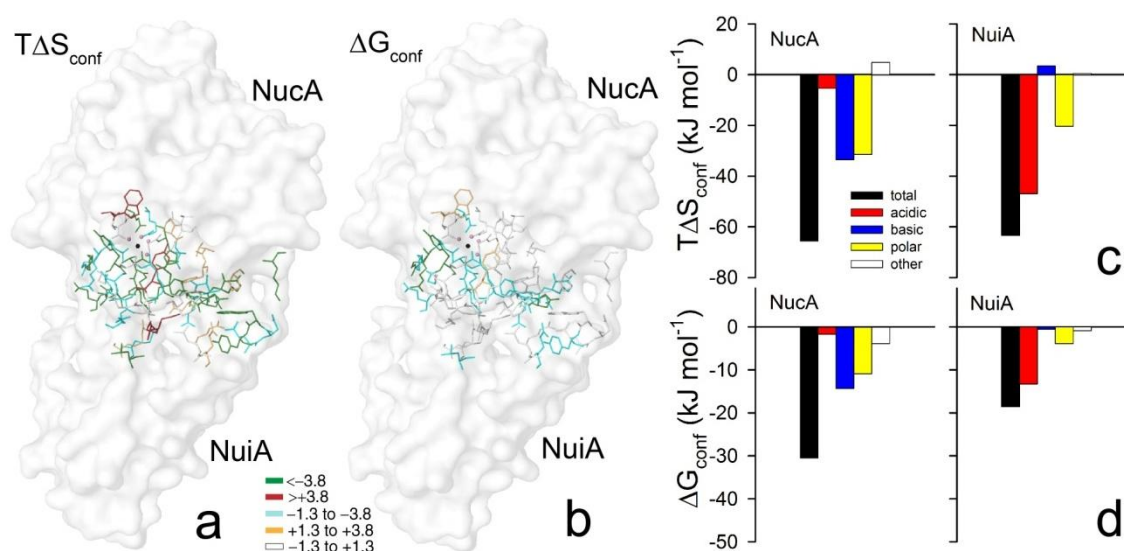


Figure 6.6: Surface representations of the complex showing the interfacial thermodynamics data and contributions of different types of residues. (a) conformational entropy and (b) free energy costs of all the interfacial residues (only side-chains shown via sticks). Colour description: residues coloured green if $T\Delta S_{conf}^i$ or $\Delta G_{conf}^i < -3.8 \text{ kJ mol}^{-1}$, cyan for ~ -1.3 to -3.8 kJ mol^{-1} , yellow for $\sim +1.3$ to $+3.8 \text{ kJ mol}^{-1}$, red for $> +3.8 \text{ kJ mol}^{-1}$ and left uncoloured for negligible changes. (c) The conformational entropy and (d) free energy changes of different types of residues at NucA-NuiA interface are shown along with the total interfacial contributions of the respective system.

The conformational entropy and free energy contributions of the different types of residues in the interfacial region are shown in Figure 6.6c and d. The basic residues of NucA and acidic residues of NuiA undergo maximum stabilization and ordering out of all interfacial residues. In Table 6.1, we list the $T\Delta S_{conf}^i$ and ΔG_{conf}^i of these interfacial charged residues whose locations are shown in Figure 6.1. The stabilizations and ordering of the polar side-chain containing residues at the interface are also significant, while the changes in any other type of interfacial residues are negligible. All these observations quantitatively confirm that the enzyme-inhibitor interaction is predominantly electrostatic as suggested from the crystal structure of the complex¹⁰⁶. We now take a close look at the interface.

The active-site region is shown in Figure 6.7a-b where the side-chains of different metal-ion coordinating and neighbouring residues are labelled according to their $T\Delta S_{conf}^i$ (Figure 6.7a) and ΔG_{conf}^i (Figure 6.7b) values. Here, four water molecules coordinate to the

metal-ion Mg^{2+} along with the side-chain of Asn155 ($T\Delta S_{conf}^i = -3.0 \text{ kJ mol}^{-1}$ and $\Delta G_{conf}^i = -1.3 \text{ kJ mol}^{-1}$) of NucA and the terminal residue of NuiA, Thr135 ($T\Delta S_{conf}^i = -8.0 \text{ kJ mol}^{-1}$ and $\Delta G_{conf}^i = -2.1 \text{ kJ mol}^{-1}$). A neighbouring NucA residue Arg93, believed to participate in transition state stabilization, undergoes a significant rearrangement of its side-chain¹⁰⁶ and experiences high ordering and stabilization. A few more highly stabilized and ordered residues in the active-site are tabulated in Table 6.1. They are mostly the hydrogen bonded residues involved in nucleolytic activity or its inhibition such as His124, Arg156, Glu163 of NucA and Glu24 of the inhibitor. The roles of Arg93, His124 and Glu163 in substrate binding to NucA have already been emphasized earlier via mutational studies³³³ where significant decrease in enzymatic activity have been observed upon mutation of any of these residues. Furthermore, Glu24 (NuiA) induced decrease in inhibition has also been reported earlier¹⁰⁶.

Table 6.1: The conformational entropy and free energy changes (in kJ mol^{-1}) of interfacial basic residues of NucA and acidic residues of NuiA. Lys202 is a non-interface residue, but included here for its large entropy change.

NucA residue	$T\Delta S_{conf}^i$	ΔG_{conf}^i	NuiA residue	$T\Delta S_{conf}^i$	ΔG_{conf}^i
Arg93	-5.2	-1.7	Glu24	-17.3	-3.4
Arg98	-11.7	-3.4	Glu26	-2.9	-0.7
Lys101	-5.9	-0.9	Asp75	-3.6	-0.6
Arg122	-7.2	-7.1	Glu80	-0.2	-0.2
His124	-8.2	-1.6	Glu81	+1.3	-1.8
Arg156	-3.0	-4.9	Glu109	-6.4	-0.9
Arg167	-3.5	-0.4	Glu111	-9.4	-3.4
Lys202	-13.8	-2.6	Glu134	-8.3	-2.2

The second interaction-site in the open-jaw type NucA-NuiA interfacial structure is shown in Figure 6.7c-d. The side-chains of the salt-bridge forming Lys101 (NucA) and Asp75 (NuiA) are marked along with those of some neighbouring residues. Both of these residues are highly ordered (Table 6.1) indicating the strong attractive interaction. Several neighbouring residues in NuiA Gln74 ($T\Delta S_{conf}^i = -3.1 \text{ kJ mol}^{-1}$), Trp76 ($T\Delta S_{conf}^i = -4.1 \text{ kJ}$

mol⁻¹) and Tyr77 ($T\Delta S_{conf}^i = -6.9$ kJ mol⁻¹) get ordered as well which have also been proved important for inhibition.

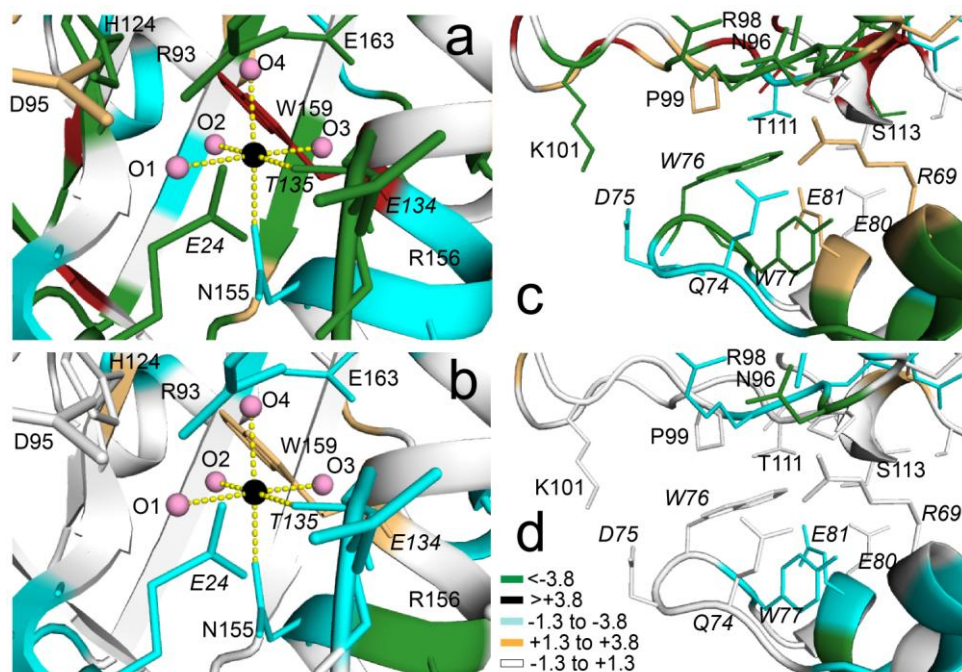


Figure 6.7: Changes of the active-site and neighbouring residues. (a) The conformational entropy and (b) conformational free energy. The O-atoms of the four water molecules at the active-site are shown in pink, while the Mg²⁺ ions is shown by black sphere. (c) The conformational energy and (d) conformational free energy changes of the residues in the second NucA-NuiA interaction site.

Hydrogen bond mediated interaction sites include other NucA and NuiA residues at the interface, apart from those in the above two binding regions as indicated in Table 2 of Ghosh et al¹⁰⁶. These residues within the hydrogen bonding distance are found to be highly ordered in the complexed state. For instance, Gln94 of NucA, with a polar side-chain undergo huge ordering ($T\Delta S_{conf}^i = -9.6$ kJ mol⁻¹) after coming close to Arg69 of NuiA. Arg122 (Table 6.1), polar Ser128 ($T\Delta S_{conf}^i = -2.6$ kJ mol⁻¹) and Arg167 (Table 6.1) of NucA, having water-mediated interactions with metal coordinating NuiA residue Thr135, also undergo substantial ordering. Interestingly, earlier mutations³³³ on Arg122 and Arg167 have also lead to significant drop in enzymatic activity of NucA.

Interfacial water—The $g(r)$ for the interfacial water molecules is shown in Figure 6.8a along with those for the waters present around the binding surfaces of free NucA and free NuiA. The gross behaviour of these water distributions is the same in all three cases, except the peak value being maximum in case of the complex (inset Figure 6.8a). This indicates the high localization of the water molecules at the interface due to tight inhibitor-binding. Such

localization leads to a substantial drop of entropy ($T\Delta S_{iw} \sim -10.2 \text{ kJ mol}^{-1}$ for about 300 interfacial waters) with respect to the free components. However, the free energy cost turns out to be negligible ($\Delta G_{iw} \sim -0.6 \text{ kJ mol}^{-1}$). It is interesting to compare our results to those of an earlier study³²² where the thermodynamics of cavity-ligand association for different systems has been reported with particular emphasis on water contributions. The free energy associated with the water molecules depends very sensitively on the property of the cavity and the ligand. For instance, neutral ligand in positively charged cavity shows a marginal decrease in water free energy, whereas a negatively charged ligand in a positively charged cavity shows a large change in the water free energy³²². In our system, the electrical properties of different residues are highly non-uniform having both positively and negatively charged as well as polar side-chains. Such a complicated interfacial environment brings in compensatory changes in the water free energy leading to only a marginal change.

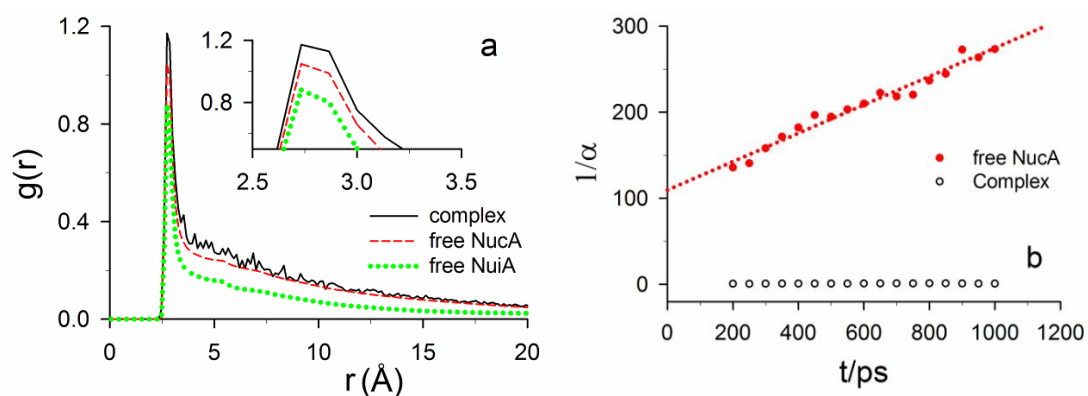


Figure 6.8: Data on interfacial water molecules. (a) The oxygen-oxygen pair distribution function $g(r)$ s of the water molecules at the protein-protein interface of the complex and around the binding regions of NucA and NuiA are shown. Inset, a close view of the peaks in $g(r)$ -plots. (b) The plot of $1/\alpha$ as a function of time t along with the best fit line through the points for the active-site water in complex and free NucA.

The immobilization of the water molecules at the active site of NucA in the inhibitor-bound state is reflected in the VHCFs as well. In Figure 6.8b, we show the long-time-behaviour of $1/\alpha$ for the active-site waters in free (the filled circles) and inhibitor-bound NucA (the open circles). Clearly, the metal-ion coordinating water molecules move away from the active-site of free NucA as indicated by the increase in $1/\alpha$. The slope of the best linear fit through the filled circles gives us the self-diffusion coefficient D_{asw} of the active-site waters. We find $D_{asw} \sim 0.4 \text{ cm}^2 \text{ s}^{-1}$ which is 5 times smaller compared to the self-diffusion coefficient in bulk water³³⁵, but resembles the values reported for water diffusion near a protein or a biomolecular surface³³⁵⁻³³⁷. On the other hand, we observe no change of the value

of α for the active-site waters in the complex, indicating that they are arrested dynamically with practically no diffusion.

6.4 Interpretation of results

Our results on the thermodynamic changes at the biomolecular interface of NucA-NuiA complex shed lights on several microscopic aspects of NucA-NuiA binding:

Importance of interfacial changes—It is known¹⁰⁶ from experimental observations that enzymatic activity of NucA diminishes dramatically upon binding to NuiA. Therefore, it is expected that NuiA binds either exactly or adjacent to the substrate binding sites, blocking the binding of the substrate to the enzyme. However, isolation of substrate-bound NucA has been unsuccessful so far due to its high activity¹⁰⁶. Consequently, comparison of inhibitor-bound NucA structure has been done earlier¹⁰⁶ with a DNA-bound NucA model structure. The comparison reveals¹⁰⁶ that several atoms of Glu24 and Thr135 of NuiA occupy the positions where key atoms of DNA could have been. In our calculations, we find large ordering and stabilization for both these NuiA residues Glu24 (Table 6.1) and Thr135.

More importantly, the fact that NucA hardly shows any activity in inhibitor-bound form indicates that the inhibitor binding to NucA is tighter compared to the substrate binding. Both DNA and RNA carry high negative charges. Therefore, they would prefer to interact with the positively charged basic residues of the enzyme. From the structure^{106, 107} it turns out that the binding surface of NucA offers at least seven basic residues (Table 6.1). In The NucA-NuiA complex there are eight interfacial acidic residues of NuiA (Table 6.1) which could satisfy all the interfacial positive charges of NucA. A DNA substrate, on the other hand, is unlikely to satisfy all the seven positive charges on NucA interface. This is because of the fact that in order to access the phosphate groups the DNA would have bound to the enzyme surface through its minor groove. The space covered by NuiA at the NucA-NuiA interface, about 31 Å in width, could be accessed at most by 4-5 phosphates present on the approaching minor groove of the DNA, as seen from a docking of a DNA double helix on NucA using HADDOCK³³⁸. Similar situation also has been observed earlier in the DNA-bound structure of Vvn nuclease (PDB 1OUP)³³⁹ where only 4 phosphates bind with the enzyme. Thus, it is quite possible that the better electrostatic stabilization factor is responsible for the preferential binding of the NuiA to NucA in presence of nucleic acid molecules.

Second interaction site—Another very important interaction site, other than the active site, between NucA and NuiA is the possible salt-bridge interaction¹⁰⁶ between Lys101 (NucA)-Asp75 (NuiA) shown in Figure 6.7c and d. Measurements of the inhibition constants with several NuiA-mutants have shown¹⁰⁶ that the looser binding is observed when Asp75 is replaced by an Asn or even Glu. This may be indicating that the salt-bridge is formed possibly at an optimum separation between Lys101 (NucA) and Asp75 (NuiA) which is altered by the mutations. Interestingly, a very similar effect is observed when there is a double mutation¹⁰⁶ at two adjacent residues of Asp75 (NuiA) to replace both Gln74 and Trp76 by Ala. From our results, we find that both Lys101 (NucA) and Asp75 (NuiA) are well ordered indicating strong attractive interaction between their side-chains. We find that several neighbouring residues of Asp 75 (NuiA) undergo substantial ordering as well via van der Waals interaction among their side-chains, as shown in Fig, 6.7c-d, to stabilize the loop structure around this region. Such stabilization may lead to proper orientation of Asp75 (NuiA) to be at the optimum distance to form the salt-bridge with Lys101 (NucA).

Conformational entropy and methyl order parameters—It has been observed via NMR relaxation experiments⁷⁵ and detailed molecular simulations⁸³ that the generalized order parameters for methyl groups (S_{Me}^2) can provide a measure of total conformational entropy cost of complexation $T\Delta S_{conf}^{tot}$. For several calmodulin-peptide complexes⁷⁵, ΔS_{conf}^{tot} has been observed to vary linearly with the residue weighted average changes in methyl order parameter^{75, 83} given by $\langle \Delta S_{Me}^2 \rangle$. Here we check whether the same linear scaling is present here. The plot of individual conformational entropy changes of NucA ($\Delta S_{conf}^N = -0.49 \text{ kJ K}^{-1} \text{ mol}^{-1}$) and NuiA ($\Delta S_{conf}^I = -1.08 \text{ kJ K}^{-1} \text{ mol}^{-1}$) against their respective $\langle \Delta S_{Me}^2 \rangle$, computed from our simulations using earlier methods⁸³, yields a slope $m = -0.06$ which is close to the m calculated earlier^{75, 83}.

Contribution of interfacial waters—The immobilization of the active-site water molecules in the inhibitor-bound form during the entire simulation clearly demonstrates the extent of tight-binding of the inhibitor to NucA and hence justifies the drop in interfacial water-entropy. The binding of inhibitor leads to sufficiently heavy packing of the side-chains at the interface of NucA and NuiA, so that the water molecules cannot escape from within or come in from outside. These observations also support the proposed catalytic mechanism of NucA to hydrolyze a DNA or RNA molecule¹⁰⁷ that the water required for hydrolysis is provided from the coordination sphere of the active-site metal-ion, not from the bulk or the hydration shells around the protein surface.

Predictions on possible mutations—We have already pointed out several interfacial residues of NucA and NuiA which undergo large ordering and stabilization upon complexation. Roles of many of them, like, Arg93, Arg122, His124 and Arg167 have already been explored³³³ by studying the changes in enzymatic activity of NucA after mutations of those residues. In addition to these we predict some other interfacial residues whose roles have not been explored via mutational studies. These are basic residue Arg98 of NucA and acidic residues of NuiA, like, Glu109, Glu111 and Glu134. All of these residues, shown in Figure 6.1, undergo heavy ordering upon complexation (Table 6.1). According to Table 6.1 ordering of Lys202 is also very large. This is a non-interfacial residue which is part of the six stranded β -sheet of NucA (Figure 6.1), making it an interesting candidate for such mutational studies. Here Arg98 can have very important role in substrate binding to NucA and others may be important in the inhibition mechanism.

6.5 Conclusion

Our studies might be the first report on the quantitative thermodynamics data of the interfacial changes, highlighting both the conformational contributions as well as the water contributions, due to binding of inhibitor protein NuiA to the enzyme NucA using the HBM⁸³. We show that the interfacial changes are governed by the electrostatic interactions. This supports quantitatively the idea that the inhibitor mimics the way different nucleic acid substrates bind to NucA. The tight inhibitor binding to the enzyme leads to a heavily packed interface with bound water molecules undergoing a large change in entropy. The HBM depends on the shift in distributions of different degrees of freedom upon binding and should be applicable to any biomacromolecular interface. Our study thus provides a novel route to microscopic understanding of biomacromolecular interfaces which would help the manipulations of interfacial properties to regulate biomacromolecular activities in general.

References

1. J. Ross and A. P. Arkin, *Proc. Nat. Acad. Sci., USA* **106**, 6433 (2009).
2. B. Bagchi and C. Chakravarty, *J. Chem. Sci.* **122**, 459 (2010).
3. C. J. Mundy, S. M. Kathmann, R. Rousseau, G. K. Schenter, J. VandeVondele and J. Hutter, in *SciDAC Review* (USA, 2010), pp. 10-21.
4. D. G. Truhlar, *J. Am. chem. Soc* **130**, 16824 (2008).
5. P. M. Chaikin and T. C. Lubensky, *Principles of Condensed Matter Physics*. (Cambridge University Press, Cambridge, 1995).
6. M. Plischke and B. Bergersen, *Equilibrium statistical physics*, 3 ed. (World Scientific, Singapore, 2006).
7. M. G. Kurnikova, N. Balabai, D. H. Waldeck and R. D. Coalson, *J. Am. Chem. Soc.* **120**, 6121 (1998).
8. M. L. Horng, J. A. Gardecki and M. Maroncelli, *J. Phys. Chem. A* **101**, 1030 (1997).
9. M. Maroncelli, *J. Chem. Phys.* **106**, 1545 (1997).
10. G. S. Jas, Y. Wang, S. W. Pauls, C. K. Johnson and K. Kuczera, *J. Chem. Phys.* **107**, 8800 (1997).
11. J. R. Lakowicz, *Principles of Fluorescence Spectroscopy*. (Kluwar Academic/Plenum Publishers, New York, USA, 1999).
12. G. B. Dutt and T. K. Ghanty, *J. Chem. Phys.* **116**, 6687 (2002).
13. G. B. Dutt and T. K. Ghanty, *J. Phys. Chem. B* **107**, 3257 (2003).
14. L. A. Philips, S. P. Webb and J. H. Clark, *J. Chem. Phys.* **83**, 5810 (1985).
15. R. Noyori, in *Chem. Rev.* (1999), Vol. 99, pp. 353-634.
16. M. P. Heitz and F. V. Bright, *J. Phys. Chem.* **100** (1996).
17. R. Biswas, K. Dahl and M. Maroncelli, *J. Phys. Chem. B* **106** (2002).
18. N. Kometani, Y. Hoshihara, Y. Yonezawa, O. Kajimoto, K. Hara and N. Ito, *J. Phys. Chem. A* **108** (2004).
19. M. P. Heitz and M. Maroncelli, *J. Phys. Chem. A* **101**, 5852 (1997).
20. R. D. Rogers and K. R. Seddon, *Science* **302**, 792 (2003).
21. C. F. Chapman and M. Maroncelli, *J. Phys. Chem.* **95**, 9095 (1991).
22. J. L. Dote, D. Kivelson and R. N. Schwartz, *J. Phys. Chem.* **85**, 2169 (1981).
23. H. Jin, G. A. Baker, S. Arzhantsev, J. Dong and M. Maroncelli, *J. Phys. Chem. B* **111**, 7291 (2007).
24. B. Halle and M. Davidovic, *Proc. Natl. Acad. Sci. USA* **100** (2003).
25. A. Das, R. Biswas and J. Chakrabarti, *J. Phys. Chem. A* **115**, 973 (2011).

26. A. Das, R. Biswas and J. Chakrabarti, *J. Chem. Phys.* **136**, 014505 (2012).
27. A. Das, R. Biswas and J. Chakrabarti, *Chem. Phys. Lett.* **558**, 36 (2013).
28. T. W. Nee and R. Zwanzig, *J. Chem. Phys.* **52**, 6353 (1970).
29. A. Papazyan and M. Maroncelli, *J. Chem. Phys.* **102**, 2888 (1995).
30. K. Bhattacharyya, *Chem. Commun.* **2008**, 2848 (2008).
31. B. Bhushan, J. N. Israelachvilli and U. Landman, *Nature* , **374**, 607 (1995).
32. L. Bureau, *Phys. rev. lett* **104**, 218302 (2010).
33. T.-S. Kim and R. H. Dauskardt, *Nano Lett.* **10**, 1955 (2010).
34. T. K. Nielsen, U. Bosenberg, R. Gosalawit, M. Dornheim, Y. Cerenius, F. Besenbacher and T. R. Jensen, *ACS Nano* **4**, 3903 (2010).
35. R. Biswas, N. Rohman, T. Pradhan and R. Buchner, *J. Phys. Chem. B* **112**, 9379 (2008).
36. L. Jiang, Y. Sun and X. Chen, *Small* **8**, 333 (2012).
37. X. Pan and X. Bao, *Acc. Chem. Res.* **44** 553 (2011).
38. C. Li, H. Zhang, D. Jiang and Q. Yang, *Chem. Commun.*, 547 (2007).
39. P. K. Verma, A. Makhal, R. K. Mitra and S. K. Pal, *Phys. Chem. Chem. Phys.* **11**, 8467 (2009).
40. K. Ishikawa, N. Kameta, M. Aoyagi, M. Asakawa and T. Shimizu, *Adv. Funct. Mater.* **23**, 1677 (2013).
41. C. F. Lopez, S. O. Nielsen, P. B. Moore and M. L. Klein, *Proc. Natl. Acad. Sci. USA* **101**, 4431 (2004).
42. A. Calvo, M. C. Fuertes, B. Yameen, F. J. Williams, O. Azzaroni and G. J. A. A. Soler-Illia, *Langmuir* **26**, 5559 (2010).
43. M. Fichtner, *Phys. Chem. Chem. Phys.* **13**, 21186 (2011).
44. S. Granick, S. C. Bae, S. Kumar and C. Yu, *Physics* **3**, 73 (2010).
45. W. H. Thompson, *Annu. Rev. Phys. Chem.* **62**, 599 (2011).
46. M. Heuberger, M. Zach and N. D. Spencer, *Science* **292**, 905 (2001).
47. S. H. Khan, G. Matei, S. Patil and P. M. Hoffmann, *Phys. Rev. Lett* **105**, 106101 (2010).
48. T.-D. Li, J. Gao, R. Szoszkiewicz, U. Landman and E. Riedo, *Phys. Rev. B* **75**, 115415 (2007).
49. J. K. Holt, H. G. Park, Y. Wang, M. Stadermann, A. B. Artyukhin, C. P. Grigoropoulos, A. Noy and O. Bakajin, *Science* **312**, 1034 (2006).
50. J. D. Simon, *Pure & Appl. Chem.* **62**, 2243 (1990).

51. M. D. Elola, J. Rodriguez and D. Laria, *J. Phys. Chem. B* **115**, 12859 (2011).
52. A. A. Vartia and W. H. Thompson, *J. Phys. Chem. B* **116**, 5414 (2012).
53. W. H. Thompson, *J. Chem. Phys.* **120**, 8125 (2004).
54. Z. Gemici, P. I. Schwachulla, E. H. Williamson, M. F. Rubner and R. E. Cohen, *Nano Lett.* **9** 1064 (2009).
55. E. Shahraeeni and D. Or, *Phys. Rev. E* **85**, 016317 (2012).
56. P. P. Singh and M. D. A. Saldaña, *Food Res. Int.* **44**, 2452 (2011).
57. X. Amashukeli, C. C. Pelletier, J. P. Kirby and F. J. Grunthaler, *J. Geophys. Res.* **112**, G04S16 (2007).
58. I. Rodríguez-Meizoso, L. Jaime, S. Santoyo, F. J. Señoráns, A. Cifuentes and E. Ibáñez, *J. Pharm. Biomed. Anal.* **51**, 456 (2010).
59. I. Brovchenko and A. Oleinikova, *J. Phys. Chem. B* **115**, 9990 (2011).
60. D. R. Bérard, P. Attard and G. N. Patey, *J. Chem. Phys.* **98**, 7236 (1993).
61. K. Leung, A. Luzar and D. Bratko, *Phys. Rev. Lett.* **90**, 065502 (2003).
62. M. C. Stewart and R. Evans, *Phys. Rev. E* **86**, 031601 (2012).
63. R. Evans, U. M. B. Marconi and P. Tarazona, *J. Chem. Phys.* **84**, 2376 (1986).
64. P. Graf and A. Nitzan, *Chem. Phys.* **235**, 297 (1998).
65. A. Das and J. Chakrabarti, *Phys. Rev. E* **85**, 050601(R) (2012).
66. A. Das and J. Chakrabarti, Microscopic mechanisms of confinement induced slow solvation **Communicated** (2013).
67. A. Das and J. Chakrabarti, Solvation in nanoscale solvophobic confinement near liquid-gas phase coexistence **Communicated** (2013).
68. E. Charlaix and M. Ciccotti, in *Handbook of Nanophysics*, edited by K. D. Sattler (CRC Press, USA, 2011), Vol. 1.
69. R. D. Brokx, M. M. Lopez, H. J. Vogel and G. I. Makhatadze, *J. Biol. Chem.* **276**, 14083 (2001).
70. I. Andre, T. Kesvatera, B. Jonsson, K. S. Akerfeldt and S. Linse, *Biophys. J.* **87**, 1929 (2004).
71. S. W. Vetter and E. Leclerc, *Eur. J. Biochem.* **270**, 404 (2003).
72. J. K. Soukup and G. A. Soukup, *Curr. Opin. Struct. Biol.* **14**, 344 (2004).
73. W. P. Hall, J. Modica, J. Anker, Y. Lin, M. Mrksich and R. P. V. Duyne, *Nano Lett.* **11**, 1098 (2011).
74. D. Dell'Orco, S. Sulmann, S. Linse and K.-W. Koch, *Anal. Chem.* **84**, 2982 (2012).

75. M. S. Marlow, J. Dogan, K. K. Frederick, K. G. Valentine and A. J. Wand, *Nature Chem. Biol.* **6**, 352 (2010).
76. E. S. Price, M. Aleksiejew and C. K. Johnson, *J. Phys. Chem. B* **115**, 9320 (2011).
77. H. Y. Park, S. A. Kim, J. Korlach, E. Rhoades, L. W. Kwok, W. R. Zipfel, M. N. Waxham, W. W. Webb and L. Pollack, *Proc. Natl. Acad. Sci., USA* **105**, 542 (2008).
78. N. J. Anthis, M. Doucleff and G. M. Clore, *J. Am. Chem. Soc.* **133**, 18966 (2011).
79. B. J. Killian, J. Y. Kravitz and M. K. Gilson, *J. Chem. Phys.* **127** (2007).
80. D.-W. Li, S. A. Showalter and R. Brüschweiler, *J. Phys. Chem. B* **114**, 16036 (2010).
81. H. Meirovitch, *Curr. Opin. Struct. Biol.* **17**, 181 (2007).
82. M. Spichty, M. Cecchini) and M. Karplus, *J. Phys. Chem. Lett.* **1**, 1922 (2010).
83. A. Das, J. Chakrabarti and M. Ghosh, *Biophys. J.* **104**, 1274 (2013).
84. B. Jayaram, K. J. McConnell, S. B. Dixit and D. L. Beveridge, *J. Comp. Phys.* **151**, 333 (1999).
85. M. Ghosh, G. Meiss, A. M. Pingoud, R. E. London and L. C. Pedersen, *J. Biol. Chem.* **282**, 5682 (2007).
86. J. Wereszczynski and J. A. McCammon, *Quarterly Reviews of Biophysics* **45**, 1 (2012).
87. W. L. Jorgensen, *Nature* **466**, 42 (2010).
88. T. Dudev and C. Lim, *Ann. Rev. Biophys.* **37**, 97 (2008).
89. C. Branden and J. Tooze, *Introduction to Protein Structure*, 2 ed. (Garland Publishing, Inc., New York, 1999).
90. R. Mendez and U. Bastolla, *Phys. Rev. Lett.* **104**, 228103 (2010).
91. P. Atkins and J. d. Paula, *Atkins' Physical Chemistry*, 8 ed. (Oxford University Press, New York, 2006).
92. M. Akke, R. Brüschweiler and A. G. Palmer, *J. Am. Chem. Soc.* **115**, 9832 (1993).
93. D. Yang and L. E. Kay, *J. Mol. Biol.* **263**, 369 (1996).
94. Z. Li, S. Raychaudhuri and A. J. Wand, *Protein Sci.* **5**, 2647 (1996).
95. T. I. Igumenova, K. K. Frederick and A. J. Wand, *Chem. Rev.* **106**, 1672 (2006).
96. L. Ma, Z. Ahmed, A. V. Mikhonin and S. A. Asher, *J. Phys. Chem. B* **111**, 7675 (2007).
97. N. Trbovic, J.-H. Cho, R. Abel, R. A. Friesner, M. Rance and A. G. Palmer, *J. Am. Chem. Soc.* **131**, 615 (2009).
98. K. H. DuBay and P. L. Geissler, *J. Mol. Biol.* **391**, 484 (2009).
99. A. Das, J. Chakrabarti and M. Ghosh, *Chem. Phys. Lett.* **In Press** (2013).

100. Y. Ye, H.-W. Lee, W. Yang, S. Shealy and J. J. Yang, *J. Am. Chem. Soc.* **127**, 3743 (2005).
101. G. Wu, Z. Gao, A. Dong and S. Yu, *Int. J. Biol. Macromol.* **50** 1011 (2012).
102. A. Das, M. Ghosh and J. Chakrabarti, Dynamic correlation among allosterically regulated conformational variables in biomacromolecules **Communicated** (2013).
103. V. J. Hilser, J. O. Wrabl and H. N. Motlagh, *Annu. Rev. Biophys.* **41**, 585 (2012).
104. K. Gunasekaran, B. Ma and R. Nussinov, *Prot. Struct. Func. Bioinf.* **57**, 433 (2004).
105. D. Long and R. Bruschweiler, *J. Am. Chem. Soc.* **133**, 18999 (2011).
106. M. Ghosh, G. Meiss, A. Pingoud, R. E. London and L. C. Pedersen, *J. Biol. Chem.* **282**, 5682 (2007).
107. M. Ghosh, G. Meiss, A. Pingoud, R. E. London and L. C. Pedersen, *J. Biol. Chem.* **280**, 27990 (2005).
108. A. Das, J. Chakrabarti and M. Ghosh, Thermodynamics of interfacial changes in a protein-protein complex **Communicated** (2013).
109. R. Biswas, J. E. Lewis and M. Maroncelli, *Chem. Phys. Lett.* **310** (1999).
110. W. Song, N. Patel and M. Maroncelli, *J. Phys. Chem. B* **106** (2002).
111. J. P. Hansen and I. R. McDonald, *Theory of Simple Liquids*, 3 ed. (Academic, San Diego, 2006).
112. C. G. Gray and K. E. Gubbins, *Theory of Molecular Fluids*. (Oxford University Press, New York, 1984).
113. N. Balabai, A. Sukharevsky, I. Read, B. Strazisar, M. Kurnikova, R. S. Hartman, R. D. Coalson and D. H. Waldeck, *J. Mol. Liq.* **77**, 37 (1998).
114. P. V. Kumar and M. Maroncelli, *J. Chem. Phys.* **112** (2000).
115. M. G. Kurnikova, D. H. Waldeck and R. D. Coalson, *J. Chem. Phys.* **105**, 628 (1996).
116. Y. Marcus, *Chem. Rev.* **88**, 1475 (1988).
117. J. L. deGrazia, T. W. Randolph and J. A. O'Brien, *J. Phys. Chem. A* **102** (1998).
118. T. A. Betts, J. Zagrobelny and F. V. Bright, *J. Am. Chem. Soc.* **114** (1992).
119. F. Ingrosso, B. M. Ladanyi, B. Mennucci and G. Scalmani, *J. Phys. Chem. B* **110** (2006).
120. N. Kometani, S. Arzhantsev and M. Maroncelli, *J. Phys. Chem. A* **110** (2006).
121. J. E. Lewis, R. Biswas, A. G. Robinson and M. Maroncelli, *J. Phys. Chem. B* **105** (2001).
122. T. Gaskell, U. Balucani, M. Gori and R. Vallauri, *Phys. Scr.* **35** (1987).

123. M. P. Allen and D. J. Tildsley, *Computer Simulation of Liquids*. (Clarendon Press, Oxford, 1987).
124. R. Biswas and J. Chakrabarti, *Journal of Physical Chemistry B* **111**, 13743 (2007).
125. M. L. Horng, J. A. Gardecki, A. Papazyan and M. Maroncelli, *J. Phys. Chem.* **99**, 17311 (1995).
126. C. R. Cantor and P. R. Schimmel, *Biophysical Chemistry*. (W. H. Freeman, New York, 1980).
127. A. Mukherjee and B. Bagchi, *Curr. Sci.* **91** (2006).
128. R. Ramirez, R. Gebauer, M. Mareschal and D. Borgis, *Physical Review E* **66** (2002).
129. A. Mukherjee and B. Bagchi, *Chem. Phys. Lett.* **404**, 409 (2005).
130. J. B. Hubbard and P. G. Wolynes, *J. Chem. Phys.* **69**, 998 (1978).
131. P. Madden and D. Kivelson, *J. Phys. Chem.* **86**, 4244 (1982).
132. G. v. d. Zwan and J. T. Hynes, *J. Phys. Chem.* **89**, 4181 (1985).
133. P. Brito and P. Bordewijk, *Mol. Phys.* **39**, 217 (1980).
134. D. S. Alavi and D. H. Waldeck, *J. Chem. Phys.* **94**, 6196 (1991).
135. D. S. Alavi, R. S. Hartman and D. H. Waldeck, *J. Chem. Phys.* **94**, 4509 (1991).
136. D. S. Alavi, R. S. Hartman and D. H. Waldeck, *J. Chem. Phys.* **95**, 6770 (1991).
137. B. Bagchi and R. Biswas, *Adv. Chem. Phys.* **109** (1999).
138. R. Biswas, S. Roy and B. Bagchi, *Phys. Rev. Lett.* **75**, 1098 (1995).
139. R. Biswas and B. Bagchi, *J. Chem. Phys.* **106**, 5587 (1997).
140. R. Biswas and B. Bagchi, *J. Am. Chem. Soc.* **119**, 5946 (1997).
141. B. Bagchi and R. Biswas, *Acc. Chem. Res.* **31**, 181 (1998).
142. H. K. Kashyap, T. Pradhan and R. Biswas, *J. Chem. Phys.* **125**, 174506 (2006).
143. S. Daschakraborty and R. Biswas, *Chem. Phys. Lett.* **510**, 202 (2011).
144. H. Jin, B. O'Hare, J. Dong, S. Arzhantsev, G. A. Baker, J. F. Wishart, A. J. Benesi and M. Maroncelli, *J. Phys. Chem. B* **112**, 81 (2008).
145. L. Karve and G. B. Dutt, *J. Phys. Chem. B* **115**, 725 (2011).
146. K. Fruchey and M. D. Fayer, *J. Phys. Chem. B* **114**, 2840 (2010).
147. K. Iwata, M. Kakita and H. Hamaguchi, *J. Phys. Chem. B* **111**, 4914 (2007).
148. D. C. Khara and A. Samanta, *PCCP* **12**, 7671 (2010).
149. T. R. Kirkpatrick, *Phys. Rev. Lett.* **53**, 1735 (1984).
150. T. R. Kirkpatrick, *J. Non. Cryst. Solids* **75** () 437 (1985).
151. E. G. D. Cohen, B. Kamgar-Parsi and I. M. D. Schepper, *Phys. Lett.* **114**, 241 (1986).
152. H. Kovacs, J. Kowalewski, A. Maliniak and P. Stilbs, *J. Phys. Chem.* **93**, 962 (1989).

153. D. J. Evans and G. P. Morriss, *Statistical Mechanics of Nonequilibrium Liquids*. (Academic Press, London London, 1990).
154. A. Legendijk, *Physica B* **83**, 283 (1976).
155. L. X. Dang, *J. Chem. Phys.* **110**, 10113 (1999).
156. D. W. McCall, D. C. Douglass and E. W. Anderson, *J. Chem. Phys.* **31**, 1555 (1959).
157. G. Guevara-Carrion, C. Nieto-Draghi, J. Vrabec and H. Hasse, *J. Phys. Chem. B* **112**, 16664 (2008).
158. S. Girard and F. Muller-Plathe, *Mol. Phys.* **101**, 779 (2003).
159. Y. Marcus, *The Properties of Solvents*. (John Wiley & Sons Ltd, Chichester, England, 1999).
160. L. X. Dang and T.-M. Chang, *J. Chem. Phys.* **119**, 9851 (2003).
161. S. Patel and C. L. BrooksIII, *J. Chem. Phys.* **123**, 164502-1 (2005).
162. A. B. Roney, B. Space, E. W. Castner, R. L. Napoleon and P. B. Moore, *J. Phys. Chem. B* **108**, 7389 (2004).
163. L.-M. Wang and R. Richert, *J. Chem. Phys.* **120**, 11082 (2004).
164. J. A. Ingram, R. S. Moog, N. Ito, R. Biswas and M. Maroncelli, *J. Phys. Chem. B* **107**, 5926 (2003).
165. N. Ito, S. Arzhantsev, M. Heitz and M. Maroncelli, *J. Phys. Chem. B* **108**, 5771 (2004).
166. P. V. Kumar and M. Maroncelli, *J. Chem. Phys.* **103** (1995).
167. D. Y. C. Chan, D. J. Mitchell and B. W. Ninham, *J. Chem. Phys.* **70**, 2946 (1979).
168. C. S. Santos, N. S. Murthy, G. A. Baker and E. W. Castner-Jr, *J. Chem. Phys.* **134**, 121101 (2011).
169. O. Russina, A. Triolo, L. Gontrani, R. Caminiti, D. Xiao, L. G. Hines, R. A. Bartsch, E. L. Quitevis, N. Plechkova and K. R. Seddon, *J. Phys.: Condens. Matter* **21** 424121 (2009).
170. O. Borodin and G. D. Smith, *J. Phys. Chem. B* **110**, 11481 (2006).
171. L. J. A. Siqueira and M. C. C. Ribeiro, *J. Phys. Chem. B* **111**, 11776 (2007).
172. H. K. Kashyap, C. S. Santos, H. V. R. Annapureddy, N. S. Murthy, C. J. Margulis and E. W. Castner-Jr, *Faraday Discuss.* **154**, 133 (2012).
173. S. Li, J. L. Bañuelos, J. Guo, L. Anovitz, G. Rother, R. W. Shaw, P. C. Hillesheim, S. Dai, G. A. Baker and P. T. Cummings, *J. Phys. Chem.Lett.* **3**, 125 (2012).
174. H. Tokuda, K. Ishii, M. A. B. H. Susan, S. Tsuzuki, K. Hayamizu and M. Watanabe, *J. Phys. Chem. B* **110**, 2833 (2006).

175. M.-M. Huang, Y. Jiang, P. Sasisanker, G. W. Driver and H. Weingartner, *J. Chem. Eng. Data* **56**, 1494 (2011).
176. H. Tokuda, K. Hayamizu, K. Ishii, M. A. B. H. Susan and M. Watanabe, *J. Phys. Chem. B* **108**, 16593 (2004).
177. K. Hoshino, *J. Phys. F: Metal Physics* **13**, 1981 (1983).
178. T. Pradhan and R. Biswas, *J. Phys. Chem. A* **111**, 11514 (2007).
179. H. J. Wang and S. Miller, *Journal of American Chemical Society* **74**, 1611 (1952).
180. R. Gopal and S. J. Jha, *J. Phys. Chem.* **78**, 2405 (1974).
181. P. K. McCarthy and G. J. Blanchard, *J. Phys. Chem.* **97**, 12205 (1993).
182. G. B. Arfken and H. J. Weber, *Mathematical Methods for Physicists*, 5 ed. (Academic Press: A Harcourt Science and Technology Company, San Diego, 2001).
183. N. W. Ashcroft and D. C. Langreth, *Phys. Rev.* **156**, 685 (1967).
184. J. N. Israelachvili, *Intermolecular and Surface forces*, 2 ed. (Academic Press, 1998).
185. A. McBride, M. Kohonen and P. Attard, *J. Chem. Phys.* **109** (1998).
186. M. Erko, G. H. Findenegg, N. Cade, A. G. Michette and O. Paris, *Phys. Rev. B* **84**, 104205 (2011).
187. N. E. Levinger, *Science* **298**, 1722 (2002).
188. M. Schoen, D. J. Diestler and J. H. Cushman, *J. Chem. Phys.* **87**, 5464 (1987).
189. B. Go'tzelmann and S. Dietrich, *Phys. Rev. E* **55**, 2994 (1997).
190. Y. Liu, A. Z. Panagiotopoulos and P. G. Debenedetti, *J. Chem. Phys.* **132**, 144107 (2010).
191. S. K. Singh, J. K. Singh, S. K. Kwak and G. Deo, *Chem. Phys. Lett.* **494**, 182 (2010).
192. R. L. C. Vink, K. Binder and J. Horbach, *Phys. Rev. E* **73**, 056118 (2006).
193. S. Y. Reece and D. G. Nocera, *Annu. Rev. Biochem.* **78**, 673 (2009).
194. N. E. Levinger and L. A. Swafford, *Annu. Rev. Phys. Chem.* **60**, 385 (2009).
195. H. Shirota and H. Segawa, *Langmuir* **20**, 329 (2004).
196. R. Baumann, C. Ferrante, E. Kneuper, F.-W. Deeg and C. Brauchle, *J. Phys. Chem. A* **107**, 2422 (2003).
197. S. K. Pal, D. Sukul, D. Mandal, S. Sen and K. Bhattacharyya, *J. Phys. Chem. B* **104**, 2613 (2000).
198. N. Sarkar, K. Das, A. Datta, S. Das and K. Bhattacharyya, *J. Phys. Chem.* **100**, 10523 (1996).
199. R. Jimenez, G. R. Fleming, P. V. Kumar and M. Maroncelli, *Nature* **369**, 471 (1994).

200. R. Baumann, C. Ferrante, F. W. Deeg and C. Bräuchle, *J. Chem. Phys.* **114**, 5781 (2001).
201. J. Chakrabarti, S. Chakrabarti and H. Lowen, *J. Phys.: Condens. Matter* **18**, L81 (2006).
202. J. Chakrabarti and H. Lowen, *J. Chem. Phys.* **129**, 134507 (2008).
203. A. J. Patel, P. Varilly, S. N. Jamadagni, M. F. Hagan, D. Chandler and S. Garde, *J. Phys. Chem. B* **116**, 2498 (2012).
204. N. Giovambattista, P. J. Rossky and P. G. Debenedetti, *J. Phys. Chem. B* **113**, 13723 (2009).
205. D. J. Adams, *Mol. Phys.* **29**, 307 (1975).
206. T. Fehr and H. Lowen, *Phys. Rev. E* **52**, 4016 (1995).
207. N. B. Wilding, *Am. J. Phys.* **69**, 1147 (2001).
208. S. Stapf, R. Kimmich and T. Zavada, *Appl. Magn. Reson.* **12**, 199 (1997).
209. O. Beckstein and M. S. P. Sansom, *Proc. Natl. Acad. Sci. USA* **100**, 7063 (2003).
210. S. R.-V. Castrillón, N. s. Giovambattista, I. A. Aksay and P. G. Debenedetti, *J. Phys. Chem. B* **113**, 7973 (2009).
211. L. Zarkova, U. Hohm and M. Damyanova, *Int. J. Thermophys* **25**, 1775 (2004).
212. V. Tran and B. J. Schwartz, *J. Phys. Chem. B* **103**, 5570 (1999).
213. M. M. Martins and H. Stassen, *J. Chem. Phys.* **118**, 5558 (2003).
214. E. Bernardi, M. M. Martins and H. Stassen, *Chem. Phys. Lett.* **407**, 171 (2005).
215. P. Larre´garay, A. Cavina and M. Chergui, *Chem. Phys.* **308** 13 (2005).
216. L. Reynolds, J. A. Gardecki, S. J. V. Frankland, M. L. Horng and M. Maroncelli, *J. Phys. Chem.* **100**, 10337 (1996).
217. S. L. Chang and T.-M. Wu, *Chem. Phys. Lett.* **324** 381 (2000).
218. H. Kim, J. K. Saha and J. Jang, *J. Phys. Chem. C* **116**, 19233 (2012).
219. R. Godawat, S. N. Jamadagni and S. Garde, *Proc. Natl. Acad. Sci. USA* **106**, 15119 (2009).
220. D. Thirumalai, Z. Liu, E. P. O’Brien and G. Reddy, *Curr. Opin. Struct. Biol.* **23**, 22 (2013).
221. J. Min, T. Lee, S.-M. Oh, H. Kim and J.-W. Choi, *Biotechnol. Bioprocess Eng.* **15**, 30 (2010).
222. J. J. Prompers and R. Bruschiweiler, *J. Phys. Chem. B* **104**, 11416 (2000).
223. H. Schafer, A. E. Mark and W. F. v. Gunsteren, *J. Chem. Phys.* **113**, 7809 (2000).

224. R. Baron, P. H. Huñnenberger and J. A. McCammon, *J. Chem. Theory Comput.* **5**, 3150 (2009).
225. E. Suarez, N. Díaz and D. Suarez, *J. Chem. Theory Comput.* **7**, 2638 (2011).
226. B. Brooks and M. Karplus, *Proc. Natl. Acad. Sci. USA* **80**, 6571 (1983).
227. M. Karplus and J. N. Kushick, *Macromolecules* **14**, 325 (1981).
228. M. M. Gromiha and K. Fukui, *J. Chem. Inf. Model.* **51**, 721 (2011).
229. S. Samanta, J. Chakrabarti and D. Bhattacharyya, *J. Biomol. Struct. Dyn.* **27**, 429 (2010).
230. C.-E. Chang, W. Chen and M. K. Gilson, *J. Chem. Theory Comput.* **1**, 1017 (2005).
231. D.-W. Li, D. Meng and R. Brüschweiler, *J. Am. Chem. Soc.* **131**, 14610 (2009).
232. D.-W. Li and R. Brüschweiler, *Phys. Rev. Lett.* **102**, 118108 (2009).
233. K. K. Frederick, M. S. Marlow, K. G. Valentine and A. J. Wand, *Nature* **448**, 325 (2007).
234. F. M. Ytreberg and D. M. Zuckerman, *J. Chem. Phys.* **124**, 104105 (2006).
235. M. Cecchini, S. V. Krivov, M. Spichty and M. Karplus, *J. Phys. Chem. B* **113**, 9728 (2009).
236. S. Park, A. Y. Lau and B. Roux, *J. Chem. Phys.* **129**, 134102 (2008).
237. P. Maragakis, M. Spichty and M. Karplus, *J. Phys. Chem. B* **112**, 6168 (2008).
238. P. I. Zhuravlev, S. Wu, D. A. Potoyan, M. Rubinstein and G. A. Papoian, *Methods* **52**, 115 (2010).
239. P. Weinkama, J. Ponsb and A. Sali, *Proc. Natl. Acad. Sci., USA* **109**, 4875 (2012).
240. J. L. Vinkenborg, N. Karnowski and M. Famulok, *Nat. Chem. Biol.* **7**, 519 (2011).
241. W. Stacklies, F. Xia and F. Gräter, *PLoS Comput. Biol.* **5**, e1000574 (2009).
242. S. Kim, E. Broströmer, D. Xing, J. Jin, S. Chong, H. Ge, S. Wang, C. Gu, L. Yang, Y. Q. Gao, X.-d. Su, Y. Sun and X. S. Xie, *Science* **339**, 816 (2013).
243. I. R. Kleckner, P. Gollnick and M. P. Foster, *J. Mol. Biol.* **415**, 372 (2012).
244. N. Popovych, S. Sun, R. H. Ebright and C. G. Kalodimos, *Nat. Struct. Mol. Biol.* **13**, 831 (2006).
245. C. G. Kalodimos, *Ann. N.Y. Acad. Sci.* **1260** 81 (2012).
246. B. F. Volkman, D. Lipson, D. E. Wemmer and K. D., *Science* **291**, 2429 (2001).
247. V. A. Jarymowycz and M. J. Stone, *Biochemistry* **47**, 13371 (2008).
248. A. Zhuravleva, D. M. Korzhnev, S. B. Nolde, L. E. Kay, A. S. Arseniev, M. Billeter and V. Y. Orekhov, *J. Mol. Biol.* **367**, 1079 (2007).

249. C. M. Petit, J. Zhang, P. J. Sapienza, E. J. Fuentes and A. L. Lee, *Proc. Natl. Acad. Sci., USA* **106**, 18249 (2009).
250. C.-J. Tsai, A. d. Sol and R. Nussinov, *Mol. BioSyst.* **5**, 207 (2009).
251. G. Manley and J. P. Loria, *Archives of Biochemistry and Biophysics* **519** 223 (2012).
252. A. Bhattacharya, A. V. Kurochkin, G. N. B. Yip, Y. Zhang, E. B. Bertelsen and E. R. P. Zwietering, *J. Mol. Biol.* **388**, 475 (2009).
253. R. Selvaratnam, S. Chowdhury, B. VanSchouwen and G. Melacini, *Proc. Natl. Acad. Sci., USA* **108**, 6133 (2011).
254. N. G. V. Kampen, *Stochastic Processes in Physics and Chemistry*, third ed. (Elsevier, Amsterdam, The Netherlands, 2007).
255. A. Pandini, A. Fornili, F. Fraternali and J. Kleinjung, *FASEB J.* **26**, 868 (2012).
256. C. Chennubhotla and I. Bahar, *PLoS Comput. Biol.* **3**, 1716 (2007).
257. W. Zheng, B. R. Brooks and D. Thirumalai, *Proc. Natl. Acad. Sci., USA* **103**, 7664 (2006).
258. A. T. VanWart, J. Eargle, Z. Luthey-Schulten and R. E. Amaro, *J. Chem. Theory Comput.* **8**, 2949 (2012).
259. Z. Yang, P. Majek and I. Bahar, *PLoS Comput. Biol.* **5**, e1000360 (2009).
260. E. Laine, C. Auclair and L. Tchertanov, *PLoS Comput. Biol.* **8**, e1002661 (2012).
261. A. Ghosh, R. Sakaguchi, C. Liu, S. Vishveshwara and Y.-M. Hou, *J. Biol. Chem.* **286**, 37721 (2011).
262. E. Marcos, R. Crehuet and I. Bahar, *PLoS Comput. Biol.* **7**, e1002201 (2011).
263. F. Chiappori, I. Merelli, G. Colombo, L. Milanesi and G. Morra, *PLoS Comput. Biol.* **8**, e1002844 (2012).
264. G. Morra, G. Verkhivker and G. Colombo, *PLoS Comput. Biol.* **5**, e1000323 (2009).
265. K. Itoh and M. Sasai, *J. Chem. Phys.* **134**, 125102 (2011).
266. R. A. Estabrook, J. Luo, M. M. Purdy, V. Sharma, P. Weakliem, T. C. Bruice and N. O. Reich, *Proc. Natl. Acad. Sci., USA* **102**, 994 (2005).
267. A. Cembran, L. R. Masterson, C. L. McClendon, S. S. Taylor, J. Gao and G. Veglia, *Biochemistry* **51**, 10186 (2012).
268. S. W. Lockless and R. Ranganathan, *Science* **286**, 295 (1999).
269. D. Long and R. Bruschweiler, *J. Phys. Chem. Lett.* **3**, 1722 (2012).
270. K. H. DuBay, J. P. Bothma and P. L. Geissler, *PLoS Comput. Biol.* **7**, e1002168 (2011).

271. Y. S. Babu, J. S. Sack, T. J. Greenhough, C. E. Bugg, A. R. Means and W. J. Cook, *Nature* **315**, 37 (1985).
272. M. R. Nelson, E. Thulin, P. A. Fagan, S. Forsén and W. J. Chazin, *Protein Sci.* **11**, 198 (2002).
273. H. Kuboniwa, N. Tjandra, S. Grzesiek, H. Ren, C. Klee and A. Bax, *Nat Struct Biol.* **2**, 768 (1995).
274. M. Zhang, T. Tanaka and M. Ikura, *Nature Struct. Biol.* **2**, 758 (1995).
275. K. T. O'Neil, H. R. Wolfe-Jr, S. Ericksen-Vitanen and W. F. Degrado, *Science* **236**, 1454 (1987).
276. C. R. Kahl and A. R. Means, *Endocr. Rev.* **24**, 719 (2003).
277. P. L. Wintrode and P. L. Privalov, *J. Mol. Biol.* **266**, 1050 (1997).
278. M. Zhang and H. J. Vogel, *J. Biol. Chem.* **269**, 981 (1994).
279. M. Osawa, H. Tokumitsu, M. B. Swindells, H. Kurihara, M. Orita, T. Shibanuma, T. Furuya and M. Ikura, *Nature struct. Mol. Biol.* **6**, 819 (1999).
280. J. L. Gifford, H. Ishida and H. J. Vogel, *J. Biomol. NMR* **50**, 71 (2011).
281. A. L. Lee, S. A. Kinnear and A. J. Wand, *Nature Struct. Biol.* **7**, 72 (2000).
282. S. Linse, A. Helmersson and S. Forsen, *J. Biol. Chem* **266**, 8050 (1991).
283. C. Kobayashi and S. Takada, *Biophys. J.* **90**, 3043 (2006).
284. M. Lepsik and M. J. Field, *J. Phys. Chem. B* **111**, 10012 (2007).
285. D. A. McQuarrie, *Statistical Mechanics*. (University Science Books, Sausalito, California, USA, 2000).
286. M. K. Gilson, J. A. Given, B. L. Bush and J. A. McCammon, *Biophys. J.* **72**, 1047 (1997).
287. J. C. Phillips, R. Braun, W. Wang, J. Gumbart, E. Tajkhorshid, E. Villa, C. Chipot, R. D. Skeel, L. Kale and K. Schulten, *J. Comp. Chem.* **26**, 1781 (2005).
288. W. Humphrey, A. Dalke and K. Schulten, *J. Molec. Graphics* **14**, 33 (1996).
289. B. R. Brooks, C. L. B. III, A. D. Mackerell, L. Nilsson, R. J. Petrella, Y. W. B. Roux, G. Archontis, C. Bartels, S. Boresch, A. Caflisch, L. Caves, Q. Cui, A. R. Dinner, M. Feig, S. Fischer, J. Gao, M. Hodoscek, K. K. W. Im, T. Lazaridis, J. Ma, V. Ovchinnikov, E. Paci, R. W. Pastor, C. B. Post, J. Z. Pu, M. Schaefer, B. Tidor, R. M. Venable, H. L. Woodcock, X. Wu, W. Yang, D. M. York and M. Karplus., *J. Comp. Chem.* **30**, 1545 (2009).
290. U. Essmann, L. Perera, M. L. Berkowitz, T. Darden, H. Lee and L. G. Pedersen, *J. Chem. Phys.* **103**, 8577 (1995).

291. M. Krishnan and J. C. Smith, *J. Phys. Chem. B* **116**, 4124 (2012).
292. R. B. Best, J. Clarke and M. Karplus, *J. Mol. Biol.* **349** (2005).
293. K. Kuczera and P. Kursula, *J. Biomol. Struct. Dyn.* **30**, 45 (2012).
294. X. Wu and R. E. Reid, *Biochemistry* **36**, 8649 (1997).
295. M. andersson, A. malmendal, S. linse, I. ivarsson, S. forsen and L. A. svensson, *Prot. Sci.* **6**, 1139 (1997).
296. M. S. Cates, M. B. Berry, E. L. Ho, Q. Li, J. D. Potter and G. N. Phillips, *Structure* **7**, 1269 (1999).
297. U. V. Nagerl, D. Novo, I. Mody and J. L. Vergara, *Biophys. J.* **79**, 3009 (2000).
298. J. Gulati, A. Babu, H. Su and Y. u.-F. Zhang, *J. Biol. Chem* **268**, 11685 (1993).
299. H. Hu, J. H. Sheehan and W. J. Chazin, *J. Biol. Chem* **279**, 50895 (2004).
300. N. T. Wright, B. L. Prosser, K. M. Varney, D. B. Zimmer, M. F. Schneider and D. J. Weber, *J. Biol. Chem* **283**, 26676 (2008).
301. W. S. VanScyoc, R. A. Newman, B. R. Sorensen and M. A. Shea, *Biochemistry* **45**, 14311 (2006).
302. Z. Xia and D. R. Storm, *Nat Rev Neurosci* **6** (2005).
303. J. M. Shifman, M. H. Choi, S. Mihalas, S. L. Mayo and M. B. Kennedy, *Proc. Natl. Acad. Sci., USA* **103**, 13968 (2006).
304. Z. Qin and T. C. Squier, *Biophys. J.* **81**, 2908 (2001).
305. O. F. Mohammed, G. S. Jas, M. M. Lin and A. H. Zewail, *Angew. Chem. Int. Ed.* **48**, 5628 (2009).
306. B. Elshorst, M. Hennig, H. Försterling, A. Diener, M. Maurer, P. Schulte, H. Schwalbe, C. Griesinger, J. Krebs, H. Schmid, T. Vorherr and E. Carafoli, *Biochemistry* **38**, 12320 (1999).
307. Y. Liu, X. Zheng, G. A. Mueller, M. Sobhany, E. F. DeRose, Y. Zhang, R. E. London and L. Birnbaumer, *J. Biol. Chem.* **287**, 43030 (2012).
308. N.-V. Buchete and G. Hummer, *J. Phys. Chem. B* **112**, 6057 (2008).
309. F. Demmel and C. Morkel, *Phys. Rev. E* **85**, 051204 (2012).
310. S. J. d. Vries and A. M. J. J. Bonvin, *Curr. Prot. Pept. Sci.* **9**, 394 (2008).
311. R. B. Russell, F. Alber, P. Aloy, F. P. Davis, D. Korkin, M. Pichaud, M. Topf and A. Sali, *Curr. Opin. Struct. Biol.* **14**, 313 (2004).
312. F. Ferrage, K. Dutta, A. Shekhtman and D. Cowburn, *J. Biomol. NMR* **47**, 41 (2010).
313. M. J. Hartl, B. M. Burmann, S. J. Prash, C. Schwarzinger, K. Schweimer, B. M. Wöhrl, P. Rösch and S. Schwarzinger, *J. Biomol. Struct. Dyn.* **29**, 793 (2012).

314. L. S. Wong, C. V. Karthikeyan, D. J. Eichelsdoerfer, J. Micklefield and C. A. Mirkin, *Nanoscale* **4**, 659 (2012).
315. F. Rechfeld, P. Gruber, J. Hofmann and J. Kirchmair, *Curr. Top. Med. Chem.* ;(11):. **11**, 1305-1319 (2011).
316. Z. Li, Y. He, L. Cao, L. Wong and J. Li, *Int. J. Bioinform. Res. Appl.* **8**, 228 (2012).
317. F. A. Quioco, D. K. Wilson and N. K. Vyas, *Nature* **340**, 404 (1989).
318. N. A. G. Meenan, A. Sharma, S. J. Fleishman, C. J. MacDonald, B. Morel, R. Boetzel, G. R. Moore, D. Baker and C. Kleanthous, *Proc. Natl. Acad. Sci., USA* **107**, 10080 (2010).
319. C. K. Reddy, A. Das and B. Jayaram, *J. Mol. Biol.* **314**, 619 (2001).
320. S. B. A. d. Beer, N. P. E. Vermeulen and C. Oostenbrink, *Curr. Top. Med. Chem.* **10**, 55 (2010).
321. G. Hummer, *Nature Chem.* **2**, 906 (2010).
322. R. Baron, P. Setny and J. A. McCammon, *J. Am. Chem. Soc.* **132**, 12091 (2010).
323. R. Baron and V. Molinero, *J. Chem. Theory Comput.* **8**, 3696–3704 (2012).
324. A. M. Muro-Pastor, Flores, E., Herrero, A. & Wolk, C. P., *Mol. Microbiol.* **6**, 3021 (1992).
325. A. M. Muro-Pastor, Herrero, A., Flores, E., *J. Mol. Biol.* **268**, 589 (1997).
326. G. Meiss, Franke, I., Gimadutdinow, O., Urbanke, C., and Pingoud, A., *Eur. J. Biochem.* **251**, 924 (1998).
327. E. S. Rangarajan and V. Shankar, *FEMS Microbiol. Rev.* **25**, 583 (2001).
328. K.-C. Hsia, C.-L. Li and H. S. Yuan, *Curr. Opin. Struct. Biol.* **15**, 126 (2055).
329. K. R. Fox and M. J. Waring, *Biochim. Biophys. Acta.* **909**, 145 (1987).
330. G. Krupp and H. J. Gross, *Nucleic Acids Res.* **6**, 3481 (1979).
331. M. Varecha, J. Amrichova, M. Zimmermann, V. 1. Ulman, E. Lukasova and M. Kozubek, *Apoptosis* **12**, 1155 (2007).
332. C. Korn, G. Meiss, F.-U. Gast, O. Gimadutdinow, C. Urbanke and A. Pingoud, *Gene* **253**, 221 (2000).
333. G. Meiss, Gimadutdinow, O., Haberland, B., Pingoud, A., *J. Mol. Biol.* **297**, 521 (2000).
334. T. W. Kirby, G. A. Mueller, E. F. DeRose, M. S. Lebetkin, G. Meiss, A. Pingoud and R. E. London, *J. Mol. Biol.* **320**, 771 (2002).
335. C. D. Eccles, P. T. Callaghan and C. F. Jenner, *Biophys. J.* **53**, 77 (1988).
336. J. Fitter, R. E. Lechner and N. A. Dencher, *J. Phys. Chem. B* **103**, 8036 (1999).

337. J. H. Ortony, C.-Y. Cheng, J. M. Franck, R. Kausik, A. Pavlova, J. Hunt and S. Han, *New J. Phys.* **13** 015006 (2011).
338. S. J. d. Vries, M. v. Dijk and A. M. J. J. Bonvin, *Nature Protocols* **5**, 883 (2010).
339. C.-L. Li, L.-I. Hor, Z.-F. Chang, L.-C. Tsai, W.-Z. Yang and H. S. Yuan, *Embo J.* **22**, 4014 (2003).

List of Publications

1. **A. Das**, R. Biswas and J. Chakrabarti, Dipolar Solute Rotation in a Supercritical Polar Fluid, *J. Phys. Chem. A* **115**, 973 (2011).
2. **A. Das**, R. Biswas and J. Chakrabarti, Solute rotation in polar liquids: Microscopic basis for the Stokes-Einstein-Debye model, *J. Chem. Phys.* **136**, 014505 (2012).
3. **A. Das**, R. Biswas and J. Chakrabarti, Dipolar solute rotation in ionic liquids, electrolyte solutions and common polar solvents: Emergence of universality, *Chem. Phys. Lett.* **558**, 36 (2013).
4. **A. Das** and J. Chakrabarti, Dimensional crossover in fluids under nanometer-scale confinement, *Phys. Rev. E* **85**, 050601(R) (2012).
5. **A. Das**, J. Chakrabarti and M. Ghosh, Conformational contribution to thermodynamics of binding in protein-peptide complexes through microscopic simulation, *Biophys. J.* **104**, 1274 (2013).
6. **A. Das**, J. Chakrabarti and M. Ghosh, Conformational thermodynamics of metal-ion binding to a protein, *Chem. Phys. Lett.* **In Press** (2013).
7. **A. Das** and J. Chakrabarti, Microscopic mechanisms of confinement induced slow solvation. *Communicated* (2013).
8. **A. Das** and J. Chakrabarti, Solvation in nanoscale solvophobic confinement near liquid-gas phase coexistence. *Communicated* (2013).
9. **A. Das**, M. Ghosh and J. Chakrabarti, Dynamic correlations among allosterically regulated conformational variables in biomacromolecules, *Communicated* (2013).
10. **A. Das**, J. Chakrabarti and M. Ghosh, Thermodynamics of interfacial changes in a protein-protein complex, *Communicated* (2013).